Mechanical instabilities in the blistering and buckling of polymer-supported two-dimensional materials: Graphene and beyond

Ph.D. Thesis

by

Mukesh Pandey

Department of Physics
Indian Institute of Technology Ropar
Rupnagar, Punjab 140001, India
December 2023

A Ph.D. thesis
submitted in fulfillment of the requirements
for the Degree of

DOCTOR OF PHILOSOPHY

by

Mukesh Pandey
2018PHZ0002

to the

Department of Physics

Indian Institute of Technology Ropar
Rupnagar, Punjab 140001, India
December 2023

©Indian Institute of Technology Ropar - 2023
All rights reserved.

To

the almighty authority,

my grandparents, and family

DECLARATION BY THE CANDIDATE

I hereby declare that the work contained in the Ph.D. thesis entitled "**Mechanical instabilities in the blistering and buckling of polymer-supported two-dimensional materials: Graphene and beyond**" submitted for the degree of **Doctor of Philosophy** in **Physics** from the **Indian Institute of Technology Ropar** has been carried out under the supervision of A/Prof. **Dr. Rakesh Kumar**. The work is original and has not been submitted in part or full elsewhere for a degree.

Mukesh.

Place: IIT Ropar
Date: 12/01/2024

Mukesh Pandey
Research Scholar

CERTIFICATE

It is certified that the work contained in the Ph.D. thesis entitled "**Mechanical instabilities in the blistering and buckling of polymer-supported two-dimensional materials: Graphene and beyond**" by **Mr. Mukesh Pandey**, a research scholar in the **Department of Physics, Indian Institute of Technology Ropar** for the award of the degree of **Doctor of Philosophy**, has been carried out under my supervision and this work has not been submitted elsewhere for a degree.

Rakesh Kumar

Place: IIT Ropar
Date: 12/01/2024

Dr. Rakesh Kumar
Research Supervisor

Acknowledgements

First of all, I want to express my gratitude to the almighty authority for everything I have and for the wonderful people I have in my life. I convey heartfelt thanks to my late grandfather *Shri Prayag Dutt Pandey*, whose pioneer efforts and motivation led me toward intellectual growth. I also thank my parents *Mr. and Mrs. Suresh Chandra Pandey* for supporting me with whatever I needed for fulfilling my dreams. I thank my favored god '*Shri Hanuman Ji*' for ultimate bliss and for being an tremendous source of positivity, internal peace, and motivation.

I heartily thank and appreciate the valuable guidance of my research supervisor, *Dr. Rakesh Kumar*, who also gave me the freedom to pursue my own interests and ideas on my own. His ability to address the reviewers' criticism of a manuscript is excellent. His humble yet forward-thinking demeanor, inspiring attitude, and faith in me enabled to excel in my research career. The fact that our insightful conversations frequently lead to new developments in the breadth of knowledge makes me delighted. From him, I learned, 'To achieve high, target higher'; and 'Research resides in the vicinity of keen scientific observation, not around a sophisticated instrument'.

As the group's first experimentalist to seek a doctorate, I had the opportunity to start from scratch and learn everything. Thanks to the 'Graphene Science and Technology' course in the edX online learning environment (Course Code: ChalmersX ChM001x), which sparked my curiosity on the subject. Since I was amused by the physical properties of two-dimensional (2D) materials that are highly sensitive to strain, I thoroughly analyzed the straining techniques for strain engineering applications, concentrating on the bending of 2D materials.

I heartily express my sincere gratitude to the Director of my parent institute, *Prof. Rajeev Ahuja* as my co-advisor for whatever I could learn from him. He is a brilliant intellectual who has been there as a constant source of inspiration for me to realize my full potential. His realization of the various straining techniques as vital tools for nanoscale straintronic technologies and of the viscous fingering in 2D material blisters as a multidisciplinarily emerging field led us to foster new avenues. As a reviewer, his insightful critiques of the research projects are recommendable.

I would also like to thank my colleague and a chemical engineer *Dr. Chandra Shekhar* for the interesting discussions on viscous fingering instabilities. I would also like to acknowledge my doctoral committee members *Prof. C. C. Reddy, Dr. Asoka Biswas, Dr. Sandeep Gautam, & Dr. Vishwa Pal* for their constant support during my Ph.D. tenure. I used to get motivated and learned a lot from the casual discussions with *Dr. Vishwa, & Dr. Sandeep* related to my Ph.D. journey.

I would like to thank my former lab colleagues *Dr. Payal Wadhwa, & Dr. Anita Yadav* in particular for establishing a pleasant working atmosphere and culture in the lab, which was continued and upheld by my current lab partners, *Mr. Sahil Dani, Ms. Prarena Jamwal, Ms. Renu, Mr. Vikash Singh, Ms. Shikha, Mr. Gagandeep Singh, & Mr. Sayed Mohammed.* I genuinely appreciate how my spiritual and mental alignment with *Dr. Payal Wadhwa* helped me stay motivated and goal-focused. The lively and welcoming lab environment enabled me to effortlessly advance in my skills. Here, I especially mention my classmate and friend *Mr. Sahil Dani*, in particular for accompanying me in setting up the experimental lab, which was really helpful to me during my PhD journey. I am also very happy with what I shared with *Mr. Cheeranjiv Pandey*, who got associated with me for his M.Sc. Thesis work. In addition, I thank all my near & dear friends, whoever directly or indirectly connected with me on the journey.

I am happy with what I shared with *Dr. Basanta K. Parida, Dr. Mukesh Ranjan & Ms. Rakhi*, regarding ion-beam irradiation assisted nano-patterning of polymeric substrates. I would also like to thank some of the important persons, especially, *Dr. Binod Kumar, Mr. Harsimran Singh, Mr. Damninder Singh, Mr. Amit Kausal, & Mr. Abhishek Sharma*, who helped me in instrumental training on central research instruments. I also thank *Dr. Rajendra P. Joshi* for providing me with an opportunity to work on an industry-academia project. In addition, I would also like to thank *Prof. Saroj Prasad Dash* from Chalmers University, Sweden for providing us the hBN crystals for a joint research work. A special thanks goes out to *Prof. Guorui Wang & Prof. Zhaohe Dai*, respectively, from USTC China and Peking University China, for inspiring me to pursue the thesis topic through their insightful research works and for agreeing to engage with me on ongoing research initiatives.

Moreover, I thank my family members and teachers for everything I learned and for every bit of help throughout the journey.

Abstract

Keywords: Graphene, 2D materials, bending, blisters, wrinkles, adhesion, nanomechanics, viscous fingering, water confinement, elastic wetting, instabilities.

Graphene is the zero band gap semimetal though it has remarkable electronic, optical, and mechanical properties. Researchers started to look for ways to open its band gap. In 2008, researchers showed the opening of the band gap of graphene by applying tensile strain. Thereafter, such strain engineering techniques have constantly been searched for, which have significant implications in tunable electronics. The strain engineering in 2D materials offers a versatile toolbox for tailoring their physical properties to suit specific applications. It enables researchers and engineers to explore new avenues for device design, fundamental research, and technological innovation. Blistering and wrinkling of 2D materials are the most efficient techniques to tailor their physical properties. Moreover, the formation of such nano/microstructures of 2D elastic sheets has huge implications for fundamental research. Blistering occurs when a 2D material detaches from its substrate due to the accumulation of strain resulting from the confinement of molecules or lattice-mismatch. Blistering can lead to localized areas of high strain, which can significantly alter the electronic and optical properties of the material within the blister region. This provides a means to create strain gradients and non-uniform strain patterns, which are desirable for engineering specific electronic and optoelectronic properties. The accumulated strain gets relaxed by the formation of blisters, potentially leading to a local change in its lattice structure and band gap. This can be exploited to create locally engineered properties within the material. On the other hand, wrinkling occurs when a 2D material forms periodic or irregular folds or wrinkles due to the relaxation of applied strain. These wrinkles can have various sizes and orientations, and they can be controlled to achieve specific strain distributions. The wrinkling can introduce controlled strain patterns in a 2D material, enabling precise manipulation of its electronic properties. The resulting strain-induced modifications can be used to tailor band gaps, carrier mobility,

and other characteristics for specific applications. It increases the surface area of the 2D material, which can be advantageous for applications in catalysis, sensing, and energy storage. The increased surface area provides more active sites for chemical reactions and interactions. Moreover, the mechanical properties of wrinkled 2D materials can be different from their flat counterparts, offering enhanced flexibility and stretchability. This is important for applications in flexible electronics and wearable devices. In summary, both blistering and wrinkling are manifestations of how 2D materials respond to applied strain, and they provide unique opportunities for strain engineering. Researchers can exploit these effects to create tailored strain distributions and modify the electronic, optical, and mechanical properties of 2D materials. By carefully designing and controlling blistering and wrinkling, scientists can develop novel devices and materials with customized functionalities for various technological applications, ranging from electronics and photonics to sensors and energy conversion.

In the presented thesis work, we mainly focus on the blistering and wrinkling of 2D materials: graphene and beyond. The 2D material blisters are formed by the confinement of molecules. The blisters form either spontaneously or intentionally. We utilized a polymer curing-assisted technique to form optically visible sub-micron blisters of 2D materials spontaneously. A suitable blister-test model is used by taking into account the shape profile, thickness, and aspect ratio of the blister to deduce the mechanical properties of 2D material. We also strategically investigated the instabilities that arose while blister formation. The instabilities could be either based on the 2D material or the substrate. The choice of a viscoelastic substrate in this blistering process led to the emergence of an unconventional phenomenon i.e., viscous fingering. Besides this, we offer intriguing insights into the formation of wrinkles, buckles, and folds in 2D elastic nanosheets over a soft substrate under a prestretch-release process. The acquired information would advance our understanding of the mechanics of 2D materials adhering to various solid or soft substrates, which is potentially advantageous in nanopatterning and strain engineering of 2D materials.

List of Abbreviations

PVA	(Poly)vinyl alcohol
PAE	PVA-assisted exfoliation
PDMS	(Poly)dimethylsiloxane
vdW	van der Waals
PPC	(Poly)propylene carbonate
PMMA	(Poly)methylmethacrylate
IRM	Interference reflection microscopy
AFM	Atomic force microscopy
FESEM	Field emission scanning electron microscopy
PL	Photoluminescence
t-BG	twisted-bilayer graphene
RT	Room temperature
MLG	Multilayer graphene
FvK	Föpple von Kármán
3D	Three-dimensional
MME	Micromechanical exfoliation
MHE	Micromechanical hot exfoliation

List of Publications

1. Mukesh Pandey, Cheeranjiv Pandey, Rajeev Ahuja*, Rakesh Kumar*, Straining techniques for strain engineering of 2D materials towards flexible straintronic applications Nano Energy **109**, 108278 (2023).
2. Mukesh Pandey, Rakesh Kumar*, Polymer curing assisted formation of optically visible sub-micron blisters of multilayer graphene for local strain engineering J. Phys.: Condens. Matter **34**, 245401 (2022).
3. Mukesh Pandey, Rajeev Ahuja, Rakesh Kumar*, Hoop compression driven instabilities in spontaneously formed multilayer graphene blisters over a polymeric substrate Nanotechnology **34**, 175301 (2023).
4. Mukesh Pandey, Rajeev Ahuja*, Rakesh Kumar*, Viscous fingering instabilities in spontaneously formed blisters of MoS_2 multilayers, Nanoscale Advances **5**, 6617-6625 (2023).
5. Mukesh Pandey, B. K. Parida, M. Ranjan, Rajeev Ahuja, Rakesh Kumar*, Pinning of graphene for conformal wrinkling over a soft corrugated substrate through prestretch-release process Applied Surface Science Advances **16**, 100433 (2023).

Contents

Acknowledgements v

Abstract vii

List of Abbreviations ix

List of Publications xi

List of Figures xvii

Introduction 1

1 Prologue 3

1.1 2D materials: graphene and beyond 3
1.2 Synthesis techniques 4
  1.2.1 Top-down approach 4
    1.2.1.1 Tape-assisted mechanical exfoliation techniques . . . 5
      1.2.1.1.1 Micromechanical exfoliation (ME) 5
      1.2.1.1.2 Micromechanical hot exfoliation (MHE) . . 7
      1.2.1.1.3 PVA-assisted exfoliation (PAE) 7
      1.2.1.1.4 Metal-assisted exfoliation (MAE) 8
    1.2.1.2 Electrostatic Hot Exfoliation (EHE) or Anodic bonding technique 8
    1.2.1.3 Liquid-phase exfoliation (LPE) technique 9
  1.2.2 Bottom-up approach 10
1.3 Transfer techniques and 2D material-based heterostructure fabrication 10
1.4 Characterization techniques 13
  1.4.1 Microscopy 13
    1.4.1.1 Optical microscopy 13
      1.4.1.1.1 Interference reflection microscopy (IRM) . . 14

1.4.1.2 Atomic force microscopy (AFM) 15
1.4.1.3 Electron microscopy 15
1.4.2 Spectroscopy 15
1.4.2.1 Raman spectroscopy 15
1.4.2.2 Fourier transform infrared (FT-IR) spectroscopy . . 16
1.4.2.3 Photoluminescence (PL) spectroscopy 18
1.5 Strain engineering and straining techniques 20
1.5.1 Fundamentals of Strain Engineering 20
1.6 Adhesion mechanics of 2D materials 25
1.6.1 Strained nano/microstructures of 2D materials 26
1.6.1.1 Blisters 26
1.6.1.2 Wrinkles and Buckles 26
1.6.1.2.1 Methods for nano/micro-structuring of 2D materials 27
1.6.2 Blistering instabilities in elastomeric sheets and 2D materials . 34
1.6.3 Buckling instabilities in 2D materials 40
1.7 Applications 41

2 Blistering of a 2D crystal over a viscoelastic substrate 45
2.1 Introduction 45
2.2 Experimental methods 47
2.2.1 Preparation of PVA-coated substrates 47
2.2.2 2D material exfoliation and PVA curing assisted blistering . . 47
2.2.3 Characterizations 48
2.3 Results and Discussion 49
2.4 Summary 66

3 Elastic solid- and viscoelastic substrate-based instabilities in spontaneously formed multilayer Graphene blisters 69
3.1 Introduction 69
3.2 Experimental methods 72
3.2.1 Ice-water adsorption assisted PVA-curing induced blistering of MLG flakes 72
3.2.2 Characterizations 73
3.3 Results and Discussion 73
3.3.1 Interference from a thin film of varying thickness (confined water inside a blister) due to reflected light 73

3.3.2 Significance of h/τ in blistering the MLG flakes 78
3.3.3 vdW interactions affect the aspect-ratio of the blisters 78
3.3.4 Effect of hoop compression 81
3.3.5 Partial elastic wetting analogy for the liquid-drop model . . . 82
3.3.6 Elastic solid- and viscoelastic substrate-based instabilities . . . 85
3.4 Summary 99

4 Dynamical evolution of viscous fingering instability underneath spontaneously formed blisters of MoS_2 crystal 101
4.1 Introduction 101
4.2 Experimental methods 104
4.2.1 PVA-curing-induced blistering of MoS_2 multilayers in different synthesis and processing conditions 104
4.2.2 Characterizations 104
4.3 Results and Discussion 105
4.4 Summary 114

5 Pinning of graphene for conformal wrinkling over a soft corrugated substrate via snap-through transition 117
5.1 Introduction 117
5.2 Experimental methods 121
5.2.1 Fabrication of PDMS substrates 121
5.2.2 Ion-beam bombardment assisted rippling of PDMS substrates 121
5.2.3 Sample fabrication and PVA-assisted wet transfer process . . . 121
5.2.4 Characterizations 122
5.3 Results and Discussion 122
5.4 Summary 134

6 Conclusions and Outlook 135
6.1 Conclusions 135
6.2 Scope and Outlook 135

Appendix A Review of previous analytical blister-test models 137
A.1 Analysis of previous analytical models for liquid-filled blisters 137
A.1.1 Membrane model[1] for liquid-filled blisters with quadratic form of radial displacement 137

A.1.2 Membrane model by Sanchez *et al.*[2], for liquid-filled nanoblisters with cubic form of radial displacement 138
A.1.3 Nonlinear elastic plate model[1] for liquid-filled blisters with cubic form of radial displacement 140

Appendix B Adhesion mechanical model for conformal wrinkles of graphene on a corrugated soft substrate 143
B.1 Corrugation of graphene membrane induced by sinusoidal ripples on PDMS substrate 143

Bibliography 205

List of Figures

1.1 Schematic representation of graphene exfoliation from layered graphitic flake (ore) with corresponding band structure diagrams. Graphene is shown by scanning electron micrograph showing the crystal's faces in zigzag (blue line) and armchair (red line) directions[3]. Adapted with permission: ©2007, Springer Nature Ltd. 4

1.2 (i) Optical micrograph of graphene and its bilayer captured in transmittance mode[4]. Adapted with permission: ©2008, AAAS. (ii) Ambipolar electric field effect in single-layer graphene, showing the shifting of Fermi energy E_F with gate voltage V[3]. Adapted with permission: ©2007, Springer Nature Ltd. The single and bilayer graphene consists of 2 and 4 atoms in each unit cell, respectively. The hopping between nearest neighbor atom sites A and B results in linear dispersive relation whereas the hopping between A1 and B2 in bilayer graphene results in two parabolic electronic bands[5]. Adapted with permission: ©2012, WILEY-VCH Verlag GmbH & Co. KGaA, Weinheim. 5

1.3 Schematic representations of graphene synthesis techniques[6]. Adapted with permission: ©2012, Elsevier Ltd. 6

1.4 Tape-assisted mechanical exfoliation techniques[7]: (i) micromechanical exfoliation[8]. Adapted with permission: ©2015, RSC Publishing Ltd. (ii) Micromechanical hot exfoliation[9,10]. Adapted with permission: ©2015, ACS Publishing Ltd. (iii) PVA-assisted graphene exfoliation[11]. Adapted with permission: ©2020, Springer Nature Ltd. (iv) Metal-assisted exfoliation of 2D materials[12]. Adapted with permission: ©2018, ACS Publishing Ltd. 7

1.5 2D flakes' deposition yield for different mechanical exfoliation techniques: (a) mechanical hot exfoliation, (b) PVA-assisted graphene exfoliation, and (c) electrostatic hot exfoliation. 8

1.6 (a) A schematic diagram of the electrostatic hot exfoliation (anodic bonding) process, and (b) the experimental set-up used in exfoliation step[13]. Adapted with permission: ©2015, Theses, Université Pierre et Marie Curie - Paris VI. (c) The deposition yield with (d) blisters of MoS_2 flake over a borosilicate glass substrate (Pyrex). 9

1.7 Transfer techniques and 2D material-based heterostructure fabrication. (1) PDMS-based dry transfer process[14]. Adapted with permission: ©2018, RSC Publishing Ltd. (2) PDMS/PPC-based pick up-release dry transfer process[14]. Adapted with permission: ©2018, RSC Publishing Ltd. (3) PMMA carrier layer-based wet transfer process[6]. Adapted with permission: ©2012, Elsevier Ltd. 11

1.8 (a) Schematic diagram of confocal optical microscope[15]. Adapted with permission: ©2015, Elsevier Ltd. (b) Schematic representation of atomic force microscope (AFM)[16]. Adapted with permission: ©2008, IOP Publishing Ltd. (c) Schematic diagram of scanning electron microscope (SEM)[17]. Adapted with permission: ©2016, Elsevier Ltd. . 14

1.9 (a, b) Raman spectroscopy of graphene and origin of peaks in the spectrum[18]. Adapted with permission: ©2013, Nova Science Publishers Hauppauge NY. (c, d) Identification of number of layers in MoS_2 using Raman spectrocopy[19]. Adapted with permission: ©2013, American Chemical Society. 17

1.10 Band diagram for direct and indirect band gap semiconductors[20]. Adapted with permission: ©2016, Theses, Université de Strasbourg. (c) The 'funneling effect' observed at the wrinkled site of monolayer MoS_2 (shown in (d)), and (e) photoluminescence spectroscopy of flat and wrinkled region of monolayer MoS_2[19]. Adapted with permission: ©2013, ACS Publishing Ltd. 19

1.11 The straining techniques enabling the utilization of 2D materials in flexible straintronic applications[21]. Adapted with permission: ©2023, Elsevier Ltd. 21

1.12 (i) Gaseous air molecules, confining underneath the graphene monolayer over a smooth SiO_2/Si substrate, form graphene bubble during the micromechanical hot exfoliation process[22]; Adapted with permission: ©2018, American Physical Society. (ii-iii) Bending of a multilayered flake follows either membrane or elastic plate like profile[23]; Adapted with permission: ©2019, American Physical Society. (iv) Work of adhesion with respect to a given substrate as a function of the characteristic aspect ratios of the blisters of different 2D materials and heterostuctures[2]; Adapted with permission: ©2018, AAAS. 25

1.13 (a-b) Schematics and corresponding scanning electron microscope images of nano/microstructures of 2D materials, and (c-d) bending profile of 2D multilayer with perfectly glued and ultralubricated interfaces, respectively[23]. Adapted with permission: ©2019, American Physical Society. 26

1.14 Techniques for nano/microstructuring of 2D materials[21]. (i) Pressurized bulging; (ii-iii) Thermal-mismatch-induced blisters and wrinkles, respectively; (iv-v) AFM cantilever tip-assisted indentation; (vi) Straining from patterned substrate; (vii) Funneling effect observed at the blister or buckle regions; (viii) Buckling-induced delamination through prestretch-release process; (ix-x) Blister formation due to molecular confinement. Adapted with permission: ©2023, Elsevier Ltd. . . 31

1.15 (I) Blistering techniques utilized for 2D materials[24]: (A) trapping matter by layering, (B) intercalation of molecules, (C) manipulation of trapped matter, (D) deformation of atomically thin drumheads. Adapted with permission: ©2021, Elsevier Ltd. (II) Blistering techniques utilized for elastomeric or plastic sheets: (A) pressurized bulging[25], adapted with permission: ©2021, Elsevier Ltd., (B) mechanical force indentation[26], adapted with permission: ©2020, Elsevier Ltd., (C) fluid-flux driven debonding (two-phase fluid flow model)[27], adapted with permission: ©2013, American Physical Society, (D) spontanesously formed air-filled bubbles on a screen-protector plastic sheet, adapted from internet. 34

1.16 Blistering instabilities in elastic/plastic sheets. (I) Elastic solid-based instability. (i-ii) Mechanical force indentation induced instability: (i) The liquid blister test, where a plastic sheet is subjected to a mechanical force indentation. (ii) The solid-based instability arise in the blister depending on the indentation height to sheet thickness ratio[28]. Adapted with permission: ©2008, The Royal Society. (II) Viscous fluid-based mechanical instabilities. (iii-iv) Pressurized blistering: (iii) Viscous fingering patterns in the Hele-Shaw cell can be suppressed by replacing the upper-bounding rigid plate with an elastic membrane[29]. The transition from an unstable interface to stable interface ($c \to b \to a$) occurs under the variable elasticity of the latex sheet. Adapted with permission: ©2012, Americal Physical Society. (iv) The dynamical evolution of viscous fingering patterns can be visualized in elastic-walled Hele-Shaw cell under varying injected Nitrogen gas flux-driven pressure[30]. Adapted with permission: ©2018, Cambridge University Press. (v) Vertical mechanical debonding of upper bounding rigid plate from a viscous medium results in the development of viscous fingering patterns at the interface[31]. Adapted with permission: ©2016, American Chemical Society. (vi) Peeling of an upper-bounding elastic cover sheet from a viscoelastic surface develops viscous fingering pattern, which depends on the bending rigidity of the elastic sheet. The finger-length increases with the bending rigidity of the cover sheet[32]. Adapted with permission: ©2000, American Physical Society. 36

1.17 Crumpling and wrinkling instabilities in daily-life examples: (I) transition from grapes to raisins due to mass-loss as a result of drying, adapted from internet, and (II) wrinkles in the apple-skin due to mass-loss (a), and wrinkles in human-skin due to compression[33] (b), adapted with permission: ©2003, Americal Physical Society. 37

1.18 Blistering instabilities in 2D elastic nanosheets. (i) AFM images of graphene bubbles of different shapes on bulk hBN substrate resulting from the annealing process (at ∼ 150°C for 20-30 min), scale bars: 500 nm, 100 nm, and 500 nm, respectively for a, b, and c[34]. Adapted with permission: ©2016, Springer Nature Ltd. (ii) AFM amplitude images of a bilayer graphene bubble and a multilayer graphene tent, which result from the micromechanical hot exfoliation process[25]. Adapted with permission: ©2021, Elsevier Ltd. (iii) AFM deflection image of ethanol nanopockets formed due to confinement of ethanol molecules in between two monolayers of graphene, scale bar: 100 nm[35]. Adapted with permission: ©2021, Springer Nature Ltd. (iv) AFM topographic images showing wrinkle patterns around the perimeter of bubbles of hBN and MoS_2 flakes on graphite substrate[36]. Adapted with permission: ©2021, AAAS. 38

1.19 (I) Viscous fingering instability in an elastic-walled Hele-Shaw cell resulting from two-phase fluid flow. (II) Coupled instability (concurrence of elastic solid-based wrinkling instability and viscous fingering instability) in elastic-walled Hele-Shaw cell, which is driven by fluid-structure interaction parameter[37]. Adapted with permission: ©2014, AIP Publishing. 39

1.20 Buckling instabilities in 2D elastic nanosheets (SEM images). (i) Conformal graphene wrinkles on CF_x-coated PDMS substrate. Graphene is transferred to a prestretched PDMS substrate (30% prestrain) coated with a CF_x layer, and then the prestrain is released to form the conformal wrinkles[38]. The CF_x layer prevents the interfacial contact failure in the graphene layer under larger compressions. Adapted with permission: ©2020, American Chemical Society. (ii) Buckling-induced delamination or buckles of MoS_2 monolayer over PDMS substrate (initial prestrain level ∼ 50%))[19]. Adapted with permission: ©2013, American Chemical Society.(iii) Graphene folds over the PDMS substrate resulting from the prestretch-release process (prestrain level ∼ 50%)[39]. Adapted with permission: ©2015, Elsevier Ltd. 40

1.21 Development of wrinkling instability in 2D elastic nanosheets over smooth elastomeric substrate as a result of compression while releasing the prestrain. (i) Buckling-induced delamination in graphene through the prestretch-release process[39]. Adapted with permission: ©2015, Elsevier Ltd. (ii) Buckle to fold transition in graphene under compression[40]. Adapted with permission: ©2017, RSC Publishing. (iii) Topographical evolution of graphene ($\sim$ 4 layers) on PDMS substrate during uniaxial compression[41]. Adapted with permission: ©2023, Wiley-VCH GmbH. (iv) Evolution of a simply supported graphene membrane on PMMA substrate under uniaxial compression. The buckles collapse to form folds due to interfacial slippage. Beyond a critical compressive strain, the mosaic patterns form[42]. Adapted with permission: ©2019, Springer Nature Ltd. (v) Topographical evolution of MoS_2 folds under increasing compression (scale bar: 1 μm)[43]. Adapted with permission: ©2020, American Chemical Society. 41

1.22 (i) Superimposed AFM height and phase data showing the conformal wrinkling of few layer graphene (FLG) on a corrugated PDMS substrate (a), schematic showing the interaction of FLG with the corrugations while downward pushing, which leads to conformal adhesion of FLG in stressed condition (b). This illustrates the ‘snap-through transition’ in FLG, where FLG snaps between two distinct states, i.e., conformal and nearly flat on the substrate surface under the effect of external stress. (ii) AFM phase image showing the conformally adhered bilayer graphene, and less conformed 13-layer graphene, which depicts the suppression of ‘snap-through instability’ for thicker graphene flakes[44]. Adapted with permission: ©2011, AIP Publishing. (iii) Adhesion factor (A), i.e. ratio of peak-to-peak amplitudes of the graphene and substrate, where A = 1 represents the fully conformal state whereas A = 0 represents the flat state. For the number of layers $\sim$ 61, a sharp transition between the states occurs[45]. Adapted with permission: ©2012, AIP Publishing. (iv) Hierarchical patterned graphene wrinkles (SEM image) having conformal adhesion with polystyrene (PS) substrate coated with a soft CF_x layer formed by CHF_3 plasma-mediated polymerization of the PS substrate using double masking process[46]. Adapted with permission: ©2016, American Chemical Society. 42

1.23 A graphical representation depicting the experimentally achieved applied strain limits for different straining techniques before device failure, and the theoretical intrinsic strain limits of 2D materials[21]. Adapted with permission: ©2023, Elsevier Ltd. 43

2.1 Schematic representation of PVA curing assisted blistering technique. 48

2.2 [(a)-(f)] Optical images of multilayer graphene blisters (encircled in red) over PVA-coated Pyrex substrate. 50

2.3 FESEM image of multilayer graphene blisters, which follow elastic-plate profile. 50

2.4 Deflation of a PVA-curing induced air-filled sub-micron MLG blister with time: a color optical image captured (with white light source) (a) just after the deposition via PAE technique, (b) after time-lapse of 24 h, and [(c), (d)] AFM topographic images, confirming the deflation. . 51

2.5 Multilayer graphene circular blister: (a) optical image, (b) AFM topographic image (inset: location of AFM tip operated in tapping mode), (c) Fourth-order polynomial fitting of AFM height profile of the circular blister, (d) Room temperature Raman spectra recorded at the points marked in the optical image along the diameter of the circular blister. Note a red-shift of $\sim 1.63\ cm^{-1}$ at the center of the blister w.r.t. the unstrained flat region. 52

2.6 Multilayer graphene elliptical blister: (a) optical image, (b) AFM topographic image, (c) 3D height profile, (d) Room temperature Raman spectra recorded at the points marked in the optical image across the elliptical blister. Note a red-shift of $\sim 6.6\ cm^{-1}$ at the center of the blister w.r.t. the unstrained flat region. 53

2.7 AFM 3D topographic images of the PVA-curing induced liquid-filled circular sub-micron blister of MLG over a period of 58 days, which show a negligible deflation rate with time. 54

2.8 [(a)-(d)] Real-time optical images showing the deformation of the elliptical blister under thermal annealing process, (e) Temperature-dependent Raman spectra at the center of the elliptical blister. The Raman spectra from RT to 175°C superpose on each other, which shows the absence of polymer degradation. 55

2.9 Temperature-dependent Raman spectra, measured at the center of the elliptical blister, showing a change in G-peak position with temperature. The vertical dashed lines are drawn as a reference for comparison of the Raman peak positions for selected temperatures. 56

2.10 Optical & AFM images of the elliptical blisters captured at room temperature, before and after the heat treatment (up to 200°C). 57

2.11 (a) Optical image, (b) AFM topographic image of the encircled area showing thermal-expansion mismatch induced graphene wrinkles on PVA-coated glass (Pyrex) substrate. 58

2.12 [(a)-(d)]AFM topographic images of the approximately circular sub-micron MLG blisters on flakes of different thicknesses (number of layers: N), (e) Interfacial adhesion energy & confining pressure as a function of aspect-ratio of the MLG blisters at room temperature. 65

2.13 PVA-curing induced sub-micron blisters: (a) and (d) are optical images; (b) and (e) are AFM topographic images; (c) and (f) are AFM thickness profiles along the marked black lines in the AFM images. 66

3.1 The high-resolution optical images, showing (a) face-up oriented graphene flakes, and (b) face-down oriented graphene flakes deposited over PVA-coated Pyrex substrate under monochromatic-light illumination (Inset: the optical images under white-light illumination). The optical contrast for the PVA-supported 2D flakes (in upside-down or face-down orientation) is sufficiently higher than that for the face-up orientation of the flakes, which significantly helps in the identification of single to few-layer flakes[47,48]. Further, the different kinds of shapes of MLG flakes can be easily characterized with the help of the interference patterns (rings or fringes), optically visible at the 'flake-PVA' interfaces. 74

3.2 The optical images, showing the time-lapse deflation of the MLG blisters, when optically visualized in [i:(a-f)] face-up orientation, and [ii:(g-l)] face-down orientation; the optical images (a,b,g,h) are captured at the beginning just after the deposition, (c,d,i,j) are captured after a time-lapse of $\sim$ 12 hours, and (e,f,k,l) are captured after a time-lapse of $\sim$ 24 hours with (m & n), depicting the corresponding AFM topographic 3D images of the blisters (shown by red squares in (k & l), respectively) (scale bar: 50 μm). The Newton's rings or interference patterns over a blister change as the confined matter releases with time. The time-lapse deflation of the blisters can be easily detected by analyzing the change in the interference patterns. Therefore, any bulk or surface events (e.g. deflation, folds, fingering etc.) can be visualized by just focusing the laser light beam at the interface of the MLG blister and the supporting layer of PVA. 74

3.3 (a) Optical image, showing the MLG sub-micron blisters with located AFM-tip; (b) AFM topographic image captured at the edge of the MLG flake (shown by a red square in (a)) for deducing the thickness of the flake (measured from the PVA surface); [(c), (d)] AFM topographic 3D images, showing negligible deflation of the blister (encircled in red in (a)) even after a period of 80 days; and (e) Raman mapping of the G-peak position along a line (marked in red) across the blister, showing the accumulation of tensile strain at the center of the blister with a red-shifting of $\sim 5.4\text{cm}^{-1}$ with respect to the flat region of the MLG flake[49]. The deflation-free nature of the blisters, as depicted by their time-lapse AFM topographic images (captured with standard Silicon cantilever in tapping mode with consistent parameters) allow us to consider the confinement of water (liquid) inside the sub-micron blisters[2]. 75

3.4 Optical images (with incident white light) of a few-layer graphene blister in (a) face-up and (b) face-down orientation (scale bar: 20 μm). The complementary Newton's rings in the cases (a) & (b) are formed by the light beams, reflected from the confined water inside the blister. 76

3.5 (a) Schematic of the Newton's ring model & optical ray-diagram for the interference from a tiny gap of varying height (blister) due to reflected light, and (b) schematic representation of the curved geometry. 77

3.6 Schematic representation of the 'blister-collapse model': (a) water-vapor pressure driven blistering of MLG flake, (b) the tapered region of the MLG flake around the blister-edge collapses downwards due to phase-transition of water-vapor into water droplets and thereby, generating a pretension, which induces the hoop compression, (c) the suppression of hoop compression results into the development of elastic solid-based instabilities in the blister. 81

3.7 AFM topographic images of the tent-like MLG blisters (having a pointed tip at the center, where a maximum tensile strain accumulates). The AFM 3D profile of a circular blister (bubble) is presented for reference. 83

3.8 Graphical representation of the scheme employed for the determination of the height and the radius of the axisymmetric (circular) MLG blisters, following either the elastic-plate profile or the elastic-tent profile. The parameters are evaluated by fitting the shape of a blister with an appropriate profile. For determining the taper angle of a blister, the slope of the blister is fitted with a line profile. The radius a and the central deflection h of the blister is estimated by fitting the height profile of the spherical/ conical cap obtained from the atomic force microscopy (AFM) image in tapping mode. If the AFM height profile of a blister fits well with the fourth order polynomial function of radial distance r (elastic-plate profile) as, $\mathrm{w(r) = B_0 + B_1r + B_2r^2 + B_3r^3 + B_4r^4}$; then the characteristic parameters: central deflection or height h and the radius a of the blister are determined as $\mathrm{B_0}$ and $\left(-2\frac{\mathrm{B_0}}{\mathrm{B_2}}\right)^{\frac{1}{2}}$, respectively. But, if the AFM height profile of a blister fits well with the $\frac{2}{3}^{rd}$ power function of radial distance r (elastic-tent profile) as, $\mathrm{w(r) = A - Br^{2/3}}$; then the characteristic parameters: central deflection or height h and the radius a of the blister are determined as A and $\left(\frac{\mathrm{A}}{\mathrm{B}}\right)^{\frac{3}{2}}$, respectively. 85

3.9 (a) The interference reflection microscopy (IRM) set-up, (b) optical image of interference fringes at the MLG blister interface, when illuminated with monochromatic light ($\lambda \sim 605$nm), (c) AFM topographic 2D image & (d) 3D image of the blister, placed in upside-down orientation to optically visualize the interface using the IRM set-up, and (e) comparison of the height profile obtained using optical analyses of the interference fringe pattern with the height profile of the blister measured using AFM, across a line marked in (d). 86

3.10 A graphical representation of the solid-based instabilities in the blisters: showing the variation in the shape-profiles of the MLG blisters (optical and AFM topographic images) with respect to their respective aspect-ratios (h/a for axisymmetric (circular) or h/L for asymmetric blisters) and the blister-height to flake-thickness ratios (h/τ). The side length L of the typical triangular pyramidal blister was experimentally determined as $L = \sqrt{\frac{4A}{\sqrt{3}}}$; the side length L of the typical trapezoidal blister was measured as $L = \sqrt{A}$; the side length L of the typical pentagonal pyramidal blister was measured as $L \simeq \sqrt{\frac{1.74V}{h}}$; and the side length L of the typical hexagonal pyramidal blister was measured as $L = \sqrt{\frac{2V}{\sqrt{3}h}}$, where V is the measured volume of the blister, A is the measured base-area of the blister, and h is the maximum vertical deflection for an asymmetric MLG blister[34]. However, for an axisymmetric (circular) blister, the characteristic parameters: height (h) and radius (a), are deduced by fitting the AFM height profile of the blister with an appropriate profile, e.g. elastic plate, tent, etc. Red stars represent the circular MLG blisters (following the elastic plate profile with a stable interface) from a recent work[49]. 87

3.11 Schematic representation of the 'blister-collapse model', governing the solid-based instabilities in the blisters. The tapered region of the MLG flake around the blister-edge collapses downwards as the water-vapor condenses into the liquid phase. (a & b) AFM topographic phase and height profile of the MLG blister (top-view), (c & d) side and top schematic views of the MLG blister before collapse, and (e & f) side and top schematic views of the MLG blister after collapse. The single-headed arrows represent the elastic stresses or interfacial tensions acting at the perimeter of the blister, whereas the double-headed arrows represent the azimuthal (hoop) stress components, distributed across the blister. 90

3.12 Schematic representation of the (i) formation process of viscous fingering instabilities, (ii) axisymmterically growing MLG blister with other involved parameters, and (iii) fingering pattern at the edge of the blister, having a typical finger wavelength λ. 91

3.13 [a-e] Optical images of the viscous fingering patterns under the MLG blisters (number of layers (N) is increasing order from left-to-right), with [f-j] the AFM topographic 3D images and [k-o] amplitude images. The scale bar is 10 μm. 93

3.14 A graphical representation, depicting the tapering-controlled viscous fingering under sub-micron MLG blisters as a function of blister-height to flake-thickness ratio (h/τ). The number of layers in MLG flakes typically decreases with increasing h/τ. The scale bar is 10 μm. Inset shows the schematic representation of the transition from 'peeling by bending' regime to 'peeling by tension' regime. 94

3.15 The interfacial viscous fingering instability is noticeably observed in the bending-dominated regime in spontaneous blistering of the MLG flakes over the viscoelastic PVA substrate (a), however, the tension-dominated regime is highly susceptible to the elastic solid-based instability (c). We also come across an intermediate transition between the two, where both types of instabilities occur concurrently (b). However, it is also possible that a circular blister with interfacial viscous fingering instability, being prone to the elastic-solid based instability, leads to the tent-like shape of the blister with modulated fingering pattern at the interface under phase-transition (resulting from dropwise condensation of the confined water-vapor on cooling) driven collapse of the blister, depicting the transition from a $\rightarrow$ b. 95

3.16 Heating assisted reshaping of the MLG blisters for corroboration of the interfacial nature of the viscous fingering. The optical images (captured continuously with rising temperature) and the AFM topographic 3D images (captured at room temperature) of the MLG sub-micron blisters having viscous fingering instabilities at the interface, during heat-treatment up to ~200°C in upside-down or face-down orientation (scale bar: 50 μm). The interfacial nature of the viscous fingering instabilities have been confirmed by analyzing the temperature-dependent dynamics of the fingering patterns under the MLG blisters. The rapid & unstable axisymmetric in-plane propagation of the more viscous PVA (viscoelastic in nature) in the less viscous medium of water-vapor (gaseous in nature) results into the development of interfacial viscous fingering patterns. 96

3.17 Aspect-ratio of the MLG blisters (having viscous fingering instabilities) as a function of the taper angle. As the taper angle is increased the fingering pattern tries to concentrate at the edges only and thereby tends to stabilize the interface. This depicts the tapering controlled viscous fingering instabilities under the 2D material blisters (scale bar: 10 μm). 98

4.1 (a) Nanoblisters of multilayer MoS_2, having the number of layers N = 39, formed spontaneously through conventional PVA-curing-induced blistering process. (b) The interfacial adhesion energy and the net confinement pressure as a function of the blister aspect ratio for 14 different nano-blisters across the flake. 105

4.2 Blisters of MoS_2 multilayers having viscous fingering instability underneath. The scale bar is 20 μm. 106

4.3 (a) AFM topographic 2D map of the blister with coupled instability; (b) AFM height profiles along the lines marked in (a). (c, d) AFM topographic 2D height image and the line profile across the periphery of the blister shown by a red dotted circle, respectively, and (e, f) optical image captured at the interface of the blister using interference reflection microscopy, depicting three zones of the blister, and the gray value plot profile across the periphery of the blister shown by a blue dotted circle, respectively. 107

4.4 Multilayer MoS_2 blister with coupled instability: (a) AFM topographic 3D image, (b) optical image (scale bar: 10 μm), (c, d) Raman and PL spectra acquired at a point (red-colored, as shown in (b)) located at the center of the blister, respectively, (e, f) AFM topographic 2D and 3D image of the viscous fingering pattern on the PVA surface, (g, h) top-view and side-view of the polymeric fingers, respectively, and (i) Raman spectrum acquired at the center of the pattern, indicating no degradation of the polymer. 110

4.5 (a, c) The AFM 3D height images, and (b, d) the 2D amplitude images of a blister with coupled instability. The onset of wrinkling instability around the perimeter of a bubble of thin 2D flake is attributed to the phase transition of the confined water vapor during the cooling process[36]. The negligible time-lapse deflation of the polymer-curing-induced blisters at the ambient atmosphere indicates the liquid phase of the confined matter[2]. The blisters can sustain more than a period of 90 days. No new wrinkles were observed after the time-lapse, however, a few of the wrinkles vanish due to deflation. 111

4.6 (a) Surface plot of the optical image; (b) AFM topographic 3D image of the blister; the arrow indicates the direction of the line map of the PL spectrum; (c, d) the line maps for the position and the PL intensity of the A-exciton peak, respectively. The optical band gap evolves across the curvature of the blister. The fluctuating line profile is because of the presence of wrinkles along the periphery of the blister. 112

4.7 Graphical representation of circular blisters showing the dynamical evolution of interfacial viscous fingering instability with respect to the effective interfacial radial velocity (U^*) and the interfacial adhesion energy (Γ). The scale bar is 10 μm. 113

5.1 Schematics showing (i) the buckling-induced folds and delaminations of a 2D elastic membrane over a flat & smooth surface of PDMS, and (ii) the conformal wrinkling of a 2D elastic membrane over a corrugated surface of PDMS, resulting from the conventional prestretch-release process. 123

5.2 AFM topographic 3D images of (a) the flat & smooth surface of a pristine PDMS substrate and (b, c, and d) rippled PDMS surfaces obtained through IB irradiation at angles of incidence of 0°, 30°, and 60°, respectively, with respect to a normal to the PDMS substrate's surface. 124

5.3 (a, b) Optical and corresponding AFM height image of a fewlayer graphene flake having folds (standing and fallen) over a smooth PDMS substrate, (c, d) Optical and corresponding AFM height image of a hetero-fewlayer MoS_2/graphene flake having folds (standing and fallen) over a smooth PDMS substrate. The folds are optically visible and appear as white belts. The applied prestrain level is ∼40%. 124

5.4 (a, b) Optical and corresponding AFM height image of a mechanically exfoliated fewlayer graphene flake over a smooth PDMS substrate that is partially suspended to the graphite substrate. The prestretch-release process results in the formation of folds and buckle delaminations; (c) AFM line profiles across the lines marked in (b), where the line profiles 1 and 2, respectively correspond to the folds and buckle delaminations of fewlayer graphene flake over smooth PDMS and graphite substrate, respectively. This infers that the degree of mechanical folding instability depends on the substrate roughness and interfacial adhesion, in addition to the elastic properties of the 2D material, the thickness of the 2D nanosheet, and the amount of compressive stress, as reported by Jaehyung Yu *et al*[50]. The more slippery the interface, the larger will be the height of the folds. 125

5.5 Optical, AFM phase, 2D & 3D height images, and corresponding line profiles across the lines marked in red (respectively, from left to right in a row) of the graphene flakes (single to few layers) over the smooth (i-v), and rippled PDMS surfaces obtained through IB irradiation at the angles of incidence of 0° (vi-x), and 60° (xi-xv). The optically visible white belts across the graphene flakes depict the buckling-induced folds. The shaded portions in graphs represent the graphene folds distinguishing it from the PDMS surface corrugations. 126

5.6 (a) Optical image of graphene folds over an ion-beam irradiated PDMS surface having serpentine ripples, (b) the corresponding FESEM image, and (c) the zoomed-in FESEM image depicting the folds of graphene over the rippled PDMS substrate. 127

5.7 The topographic line profiles, across the lines marked in the corresponding AFM images (at the right), across the corrugations over the rippled (at 0° (a), 30° (b), and 60° (c)) PDMS surfaces. 128

5.8 AFM-based amplitude images of the single to few-layer graphene flakes over the PDMS substrates((a) flat, and (b-d) patterned at different angles of incidence: (b) 0°, (c) 30°, & (d) 60°). The folds are inevitably observed (as shown in a, b, and d) in the prestretch-release process except for the trenched PDMS substrate (as shown in (c)). 128

5.9 (i) Pinning of graphene membrane over the corrugated PDMS substrate via snap-through transition under the prestretch-release process. (ii) AFM topographic 3D image of the wrinkled graphene over a corrugated PDMS substrate having trenches, obtained through IB irradiation at an angle of incidence of 30°. (iii) Zoomed-in AFM topographic 3D image of the wrinkled graphene over trenches. (iv) FESEM image of the wrinkled graphene on the corrugated PDMS substrate (the red point indicates the wrinkled graphene region, and the yellow point indicates the corrugated PDMS region). (v) Topographic pinned configuration of the graphene membrane over a periodic depression. The line profiles correspond to the lines marked in black (for PDMS trench) and blue (for graphene wrinkle) in figure (iii). (vi) A schematic representation of the pinned configuration. 129

5.10 Optical, AFM phase, superimposed height & amplitude, zoomed-in 3D height images, and corresponding line profiles, across the lines marked in red, (respectively, from left to right in a row) of the wrinkled graphene (SLG (a, p) & FLG (f, k)) flakes over the trenched PDMS substrates obtained through IB irradiation at an angle of incidence of 30°. Note that the mechanical folding instabilities are suppressed effectively. 131

5.11 (a) Optical image of wrinkled single-layer graphene over a trenched PDMS substrate, and (b) the corresponding Raman spectrum taken at a point. (c) AFM 3D height image of the wrinkled graphene flake, (d) a two-point uniaxial straining tool; (e, f) Raman maps of 2D peak position for the area indicated by the green square in figure (a) under the applied tensile strain-level of (e) 0%, and (f) 40%, respectively. . . 133

6.1 Schematic depicting the scope of the blistering and buckling of 2D elastic nanoshhets. 136

Introduction

The strain-modulated electronic properties of 2D materials make them promising candidates for tunable electronics. Several techniques have been deduced to develop or induce strain in 2D materials. Chapter 1 provides a prologue, which includes insights into the fundamental and experimental background. We have extensively reviewed and presented one-to-one analyses of all the existing straining techniques. We emphasized the uniqueness, strength, and applicability criteria of the various straining techniques in order to upgrade flexible straintronic devices (such as gas sensors, photodetectors, and strain/pressure sensors). The strained nano/microstructures of the elastic 2D nanosheets, such as blisters and wrinkles, play intriguing roles in the strain engineering of 2D materials. The blisters form due to the confinement of molecules (liquid, gas, nanoparticles, etc.) spontaneously or intentionally whereas the wrinkles usually form due to a mismatch in thermal expansion coefficient or Young's modulus.

In Chapter 2, the physics and chemistry behind the spontaneous formation of multilayered graphene blisters over a polymeric substrate through a polymer-curing-assisted technique have been discussed. This method not only produces circular blisters but also complex-shaped (triangular, tetragonal, pentagonal, and star-like) blisters. Such an elastic solid-based instability in the 2D material bubbles is driven by the parameter h/τ, i.e., the ratio of blister height to flake thickness (Chapter 3). In addition to the elastic solid-based instability, we also observed the viscous fingering instability in the 2D material bubbles over a viscoelastic substrate. The thickness-dependent elasticity of the 2D material makes it possible to see the evolution of the viscous fingering patterns underneath the blisters. These viscous fingering patterns sometimes couple with elastic solid-based wrinkling instabilities around the perimeter of a bubble. In Chapter 4, the parameters and conditions governing such a coupling of instabilities have been discussed in detail. Further, the parameters responsible for the dynamical evolution of the viscous fingering patterns underneath the blisters have been extensively analyzed. We observed that the presence of instability in the blisters creates an anomaly in modeling the blisters using the blister-test model.

The nano/microstructures, such as blisters, wrinkles, buckles, etc., can provide intriguing insights into the adhesion mechanical behavior of 2D materials. The strong adhesion and static nature of the 2D elastic nanosheet over a flexible substrate are highly desired for strain engineering applications. The weak adhesion and super-hydrophobicity of (poly)dimethyl siloxane (PDMS) substrate, made from Sylgard-184 by mixing the elastomer and curing agent in a 10:1 ratio, results in low deposition yield of graphene flakes over it. Therefore, the folding instabilities in the 2D elastic nanosheets of graphene are inevitably observed at larger compressions under a stress loading-unloading cycle. In Chapter 5, we show an efficient surface engineering technique to suppress the folding instabilities by increasing the conformal adhesion of the graphene membrane over a PDMS substrate. The conformal adhesion results from the pinning of the monolayer graphene via snap-through transitions. At last, in Chapter 6, we discuss the conclusion and outlook as a take-home message, which includes a brief discussion on future directions.

Chapter 1

Prologue

1.1 2D materials: graphene and beyond

Graphene emerged as the ultimate wonderful material after its discovery in 2004 by Prof. A. K. Geim and Prof. K. S. Novoselov at the University of Manchester[51]. According to Prof. Geim, graphene has literally been there in front of our eyes for a very long time, but it has never been fully isolated and identified[52]. In 1859, a British chemist Benjamin Brodie obtained the liquid suspension of tiny crystals of graphite oxide by exposing graphite to strong acids[53]. In 1947, P. R. Wallace gave the band theory of Graphite to understand its electronic properties[54]. In 1948, G. Ruess and F. Vogt utilized transmission electron microscopy (TEM) to characterize the flakes with a thickness of only a few nm after drying a droplet of a graphitic oxide solution on a TEM grid[55]. In 1962, Ulrich Hofmann and Hanns-Peter Boehm searched for the thinnest flakes of reduced graphitic oxide and identified some of them as monolayers[56]. In 1986, Boehm *et al* introduced the term 'graphene', which they derived by combining the prefix of the word 'graphite' and the suffix 'ene' that is used for polycyclic aromatic hydrocarbons[57]. For the first time, Geim *et al* reported a simple and straightforward Scotch tape-assisted exfoliation technique, which led to the isolation and identification of single-layer graphene nanosheets (see Figure 1.1). Moreover, exceptionally high mobility of the few-layer graphene at room temperature $\mu \approx 10,000\ \mathrm{cm^{-2}V^{-1}s^{-1}}$ drew significant attention of the researchers worldwide[51]. After the discovery of graphene that is a semimetal, having optical transmittance of $\sim 97.7\%$, relativistic speed of charge carriers, and ultrahigh conductivity (see Figure 1.2), several other classes of two-dimensional (2D) layered van der Waals (vdW) materials emerged, e.g. 2D semiconductors (transition metal dichalcogenides (TMDCs), etc.), 2D insulators (hexagonal Boron Nitride (hBN), etc.), and 2D superconductors

(Bismuth Telluride (BiTe), Iron Selenide (FeSe), etc.)[58]. Transition metal dichalcogenides have chemical formula MX_2 having layered nature in bulk form, where M is a transition metal and X is a chalcogen atom. A hexagonally-ordered M atoms are sandwiched between two another hexagonally-ordered X atoms in single layer[59]. The monolayer TMDCs are direct band gap semiconductors whereas multilayer TMDCs are of indirect band gap. Single layer TMDCs are found in three poly-types: 2H, 1T and 1T′ phases. 2H (Hexagonal) phase is semiconductor phase, while 1T (Tetragonal) and 1T′ are metallic phases.

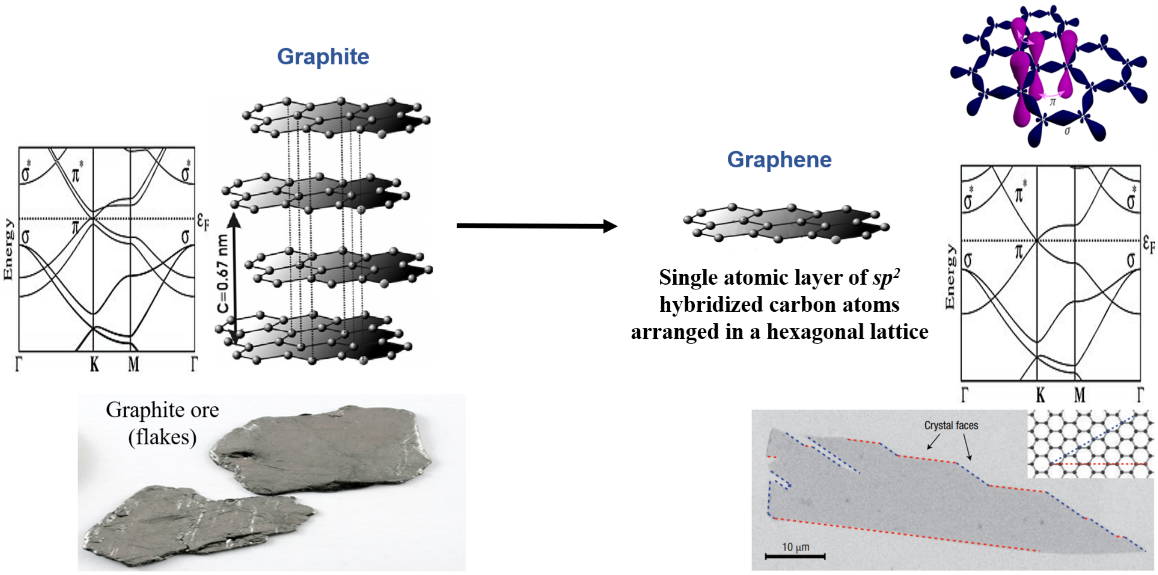

Figure 1.1: Schematic representation of graphene exfoliation from layered graphitic flake (ore) with corresponding band structure diagrams. Graphene is shown by scanning electron micrograph showing the crystal's faces in zigzag (blue line) and armchair (red line) directions[3]. Adapted with permission: ©2007, Springer Nature Ltd.

1.2 Synthesis techniques

The 2D materials can be synthesized using either chemical or mechanical processes (see Figure 1.3). They can be obtained either from atomic nucleation and reconstruction or by miniaturizing their bulk counterparts. The synthesis techniques are categorized as the following:

1.2.1 Top-down approach

In this approach, 2D materials can be obtained from their bulk counterparts through physical or chemical treatment. The physical processes include mechanical force or ultrasonic energy for exfoliating the layers from the bulk form of layered vdW materials. In contrast, the chemical treatment is based on chemical reactions, which

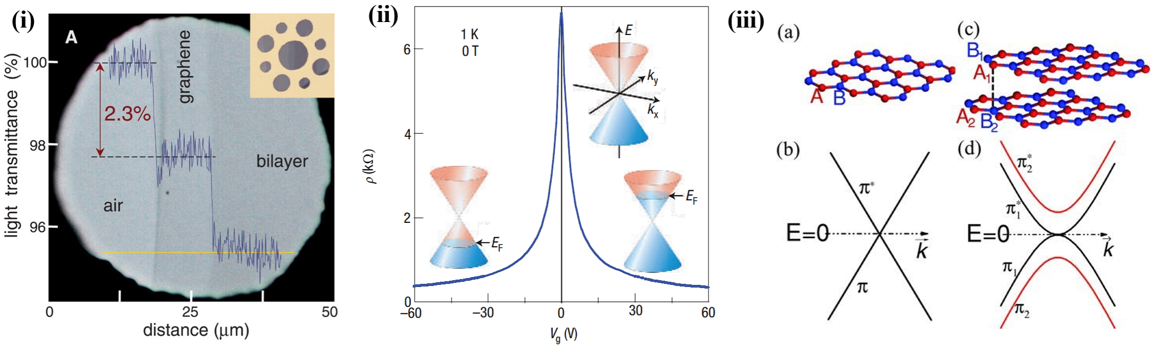

Figure 1.2: (i) Optical micrograph of graphene and its bilayer captured in transmittance mode[4]. Adapted with permission: ©2008, AAAS. (ii) Ambipolar electric field effect in single-layer graphene, showing the shifting of Fermi energy E_F with gate voltage V[3]. Adapted with permission: ©2007, Springer Nature Ltd. The single and bilayer graphene consists of 2 and 4 atoms in each unit cell, respectively. The hopping between nearest neighbor atom sites A and B results in linear dispersive relation whereas the hopping between A1 and B2 in bilayer graphene results in two parabolic electronic bands[5]. Adapted with permission: ©2012, WILEY-VCH Verlag GmbH & Co. KGaA, Weinheim.

result in charge or heat exchange for chemical changes to overcome the interlayer vdW interactions, which is followed by miniaturization of the bulk counterparts using mechanical treatment. During exfoliation, the imposed mechanical force can be normal or lateral. The normal mechanical force is utilized in tape-assisted exfoliation techniques (see Figure 1.4), whereas the lateral or shear force assists in exfoliating 2D crystals in the liquid-phase exfoliation method.

1.2.1.1 Tape-assisted mechanical exfoliation techniques

1.2.1.1.1 Micromechanical exfoliation (ME)

The tape-assisted micromechanical exfoliation is the mother technique for producing 2D monolayers, first employed by the discoverers of graphene Prof.(s) Geim and Novoselov[51,60]. This technique produces 2D monolayers of the highest quality. Since the discovery of graphene, tape exfoliation has constantly evolved in order to obtain a large-area single to few-layer deposition yield of 2D materials. The disadvantages of this technique are as follows: it produces a random distribution (location) of deposited flakes, and it can not be scaled up for the mass production of 2D monolayer flakes.

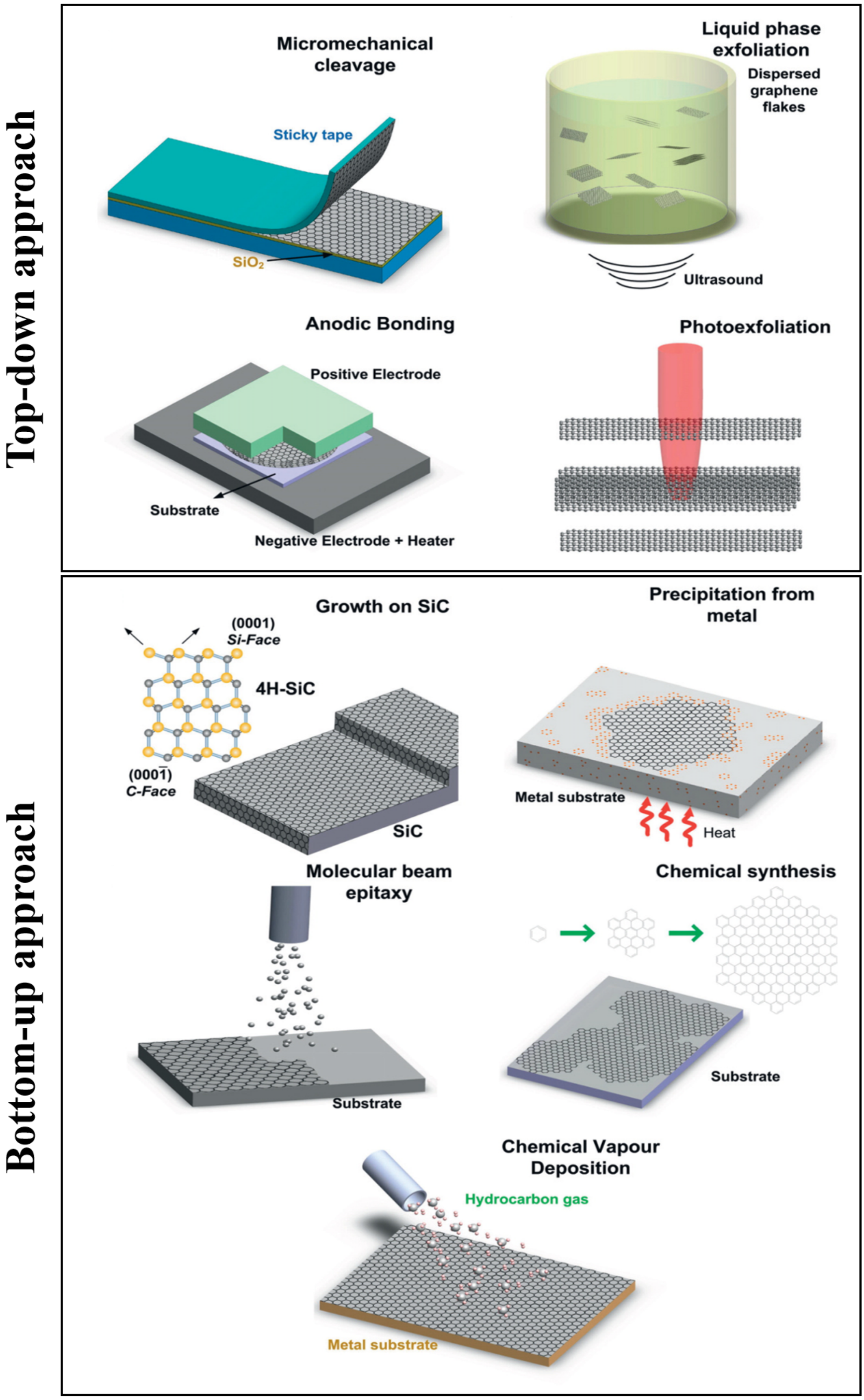
Top-down approach
Micromechanical cleavage
Sticky tape
SiO_2
Liquid phase exfoliation
Dispersed graphene flakes
Ultrasound
Anodic Bonding
Positive Electrode
Substrate
Negative Electrode + Heater
Photoexfoliation
Bottom-up approach
Growth on SiC
(0001)
Si-Face
4H-SiC
(000$\bar{1}$)
C-Face
SiC
Precipitation from metal
Metal substrate
Heat
Molecular beam epitaxy
Substrate
Chemical synthesis
Substrate
Chemical Vapour Deposition
Hydrocarbon gas
Metal substrate

Figure 1.3: Schematic representations of graphene synthesis techniques[6]. Adapted with permission: ©2012, Elsevier Ltd.

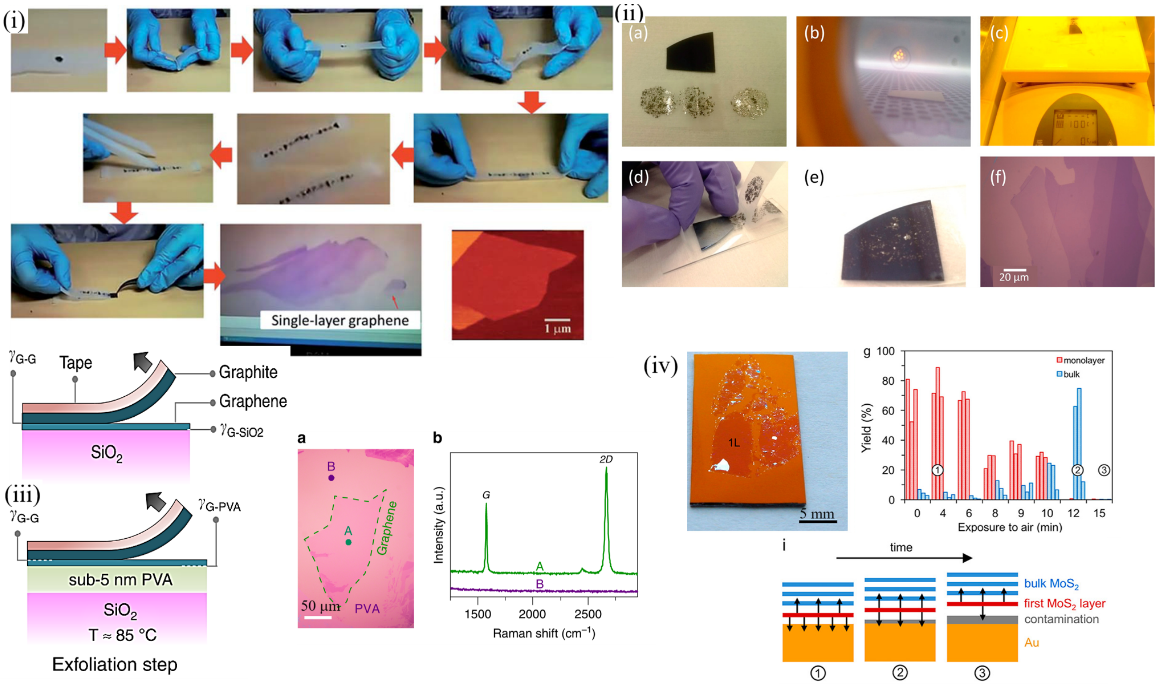
(i)
Single-layer graphene
1 µm
(ii)
(a)
(b)
(c)
(d)
(e)
(f)
20 µm
$\gamma_{G\text{-}G}$
Tape
Graphite
Graphene
$\gamma_{G\text{-}SiO2}$
SiO_2
(iii)
$\gamma_{G\text{-}G}$
$\gamma_{G\text{-}PVA}$
sub-5 nm PVA
SiO_2
T ≈ 85 °C
Exfoliation step
a
B
A
Graphene
50 µm
PVA
b
Intensity (a.u.)
G
2D
A
B
1500
2000
2500
Raman shift (cm^{-1})
(iv)
1L
5 mm
g
Yield (%)
100
80
60
40
20
0
monolayer
bulk
①
②
③
0
4
6
8
9
10
12
15
Exposure to air (min)
i
time
bulk MoS_2
first MoS_2 layer
contamination
Au
①
②
③

Figure 1.4: Tape-assisted mechanical exfoliation techniques[7]: (i) micromechanical exfoliation[8]. Adapted with permission: ©2015, RSC Publishing Ltd. (ii) Micromechanical hot exfoliation[9,10]. Adapted with permission: ©2015, ACS Publishing Ltd. (iii) PVA-assisted graphene exfoliation[11]. Adapted with permission: ©2020, Springer Nature Ltd. (iv) Metal-assisted exfoliation of 2D materials[12]. Adapted with permission: ©2018, ACS Publishing Ltd.

1.2.1.1.2 Micromechanical hot exfoliation (MHE)

A Nitto tape decorated with mechanically cleaved thinner 2D flakes, obtained by repeated sticking-detaching method, is placed in conformal contact with a silicon substrate (or, SiO_2/Si, Pyrex, etc.). For a better deposition yield with large-area monolayer regions, the silicon substrate is first treated with oxygen plasma to remove surface adsorbates and increase surface wettability. The stack is then, placed on a heater plate at a temperature of 100 °C for ∼2 min. Thereafter, the tape is peeled off gradually starting from one of its ends once the sample cools down to room temperature[9,10]. This technique may produce blisters of 2D flakes due to aggregation of adsorbed gas molecules/contamination, which has significant implications in fundamental research on the bending of layered 2D materials[2,61].

1.2.1.1.3 PVA-assisted exfoliation (PAE)

A good wettability and debonding rigidity of polyvinyl alcohol(PVA) with single-crystalline 2D flakes (mostly hydrophobic by nature) helps in achieving a good deposition yield with larger area single to few-layer flakes[11,62,63] (see Figure 1.5(b)). In this technique, a tiny amount of PVA solution (mostly, prepared in water) is spin-coated over a solid substrate, which is then cured at a raised temperature to result in a thin film of PVA over the substrate. Thereafter, the 2D flakes' exfoliation-cum-deposition step is performed using the Nitto tape at the ambient atmosphere. The water-soluble nature of PVA is also helpful for the transfer of 2D flakes from the parent substrate to a hydrophobic substrate like polydimethylsiloxane (PDMS)[64], which otherwise needs to be treated with oxygen plasma prior to the exfoliation step to increase its wettability for a better deposition yield.

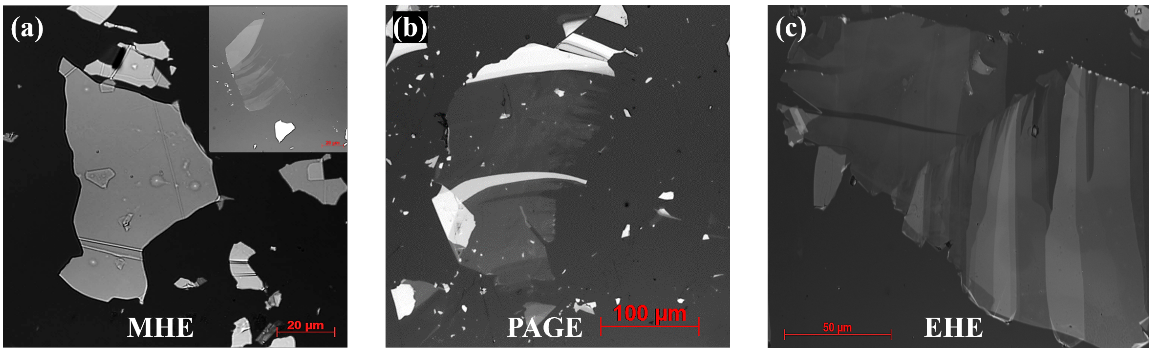

Figure 1.5: 2D flakes' deposition yield for different mechanical exfoliation techniques: (a) mechanical hot exfoliation, (b) PVA-assisted graphene exfoliation, and (c) electrostatic hot exfoliation.

1.2.1.1.4 Metal-assisted exfoliation (MAE)

The strong adhesion of 2D materials with metal substrates allows the exfoliation of layered vdW crystals[65,66]. Nickel (Ni) and Gold (Au) have been extensively utilized for depositing 2D flakes with single to few layers. A large-area 'deposition yield' of MoS_2 monolayer is obtained on freshly sputtered gold (Au), but it reduces with the time of air exposure of gold (Au) before the exfoliation and deposition step[12].

1.2.1.2 Electrostatic Hot Exfoliation (EHE) or Anodic bonding technique

Anodic bonding is a technique to bond two glass or silicon substrates with the help of an intermidiate Pyrex (Na_2O doped glass) layer. Abhay Shukla *et al* experimentally exploited this technique for the large-area deposition of single-layer graphene[67–72]. Figure 1.5(c) depicts the single-to-few layers of graphene exfoliated using this technique. In this technique, a thin graphitic flake on a Pyrex substrate is sandwiched between two metallic electrodes. A high electric DC voltage ($\sim$ 1 kV) is applied across the electrodes at a raised temperature of $\sim 200 - 300$°C (see Figure 1.6(a, b)). The temperature is sufficient to dissociate Na_2O molecules into Na^+ and O^{2-} ions. Under the effect of electric field, the Na^+ ions, being smaller in size and more mobile, move towards the cathode terminal whereas the O^{2-} ions create negative space charge at the top of the Pyrex substrate. This negative space charge induces positive charge at the bottom layer of the graphitic flake (precursor), which gets adhered on the surface of Pyrex substrate due to attractive electrostatic forces. A humid environmental condition may give rise to the formation of 2D material blisters in the electrostatic hot exfoliation process (see Figure 1.6(d)).

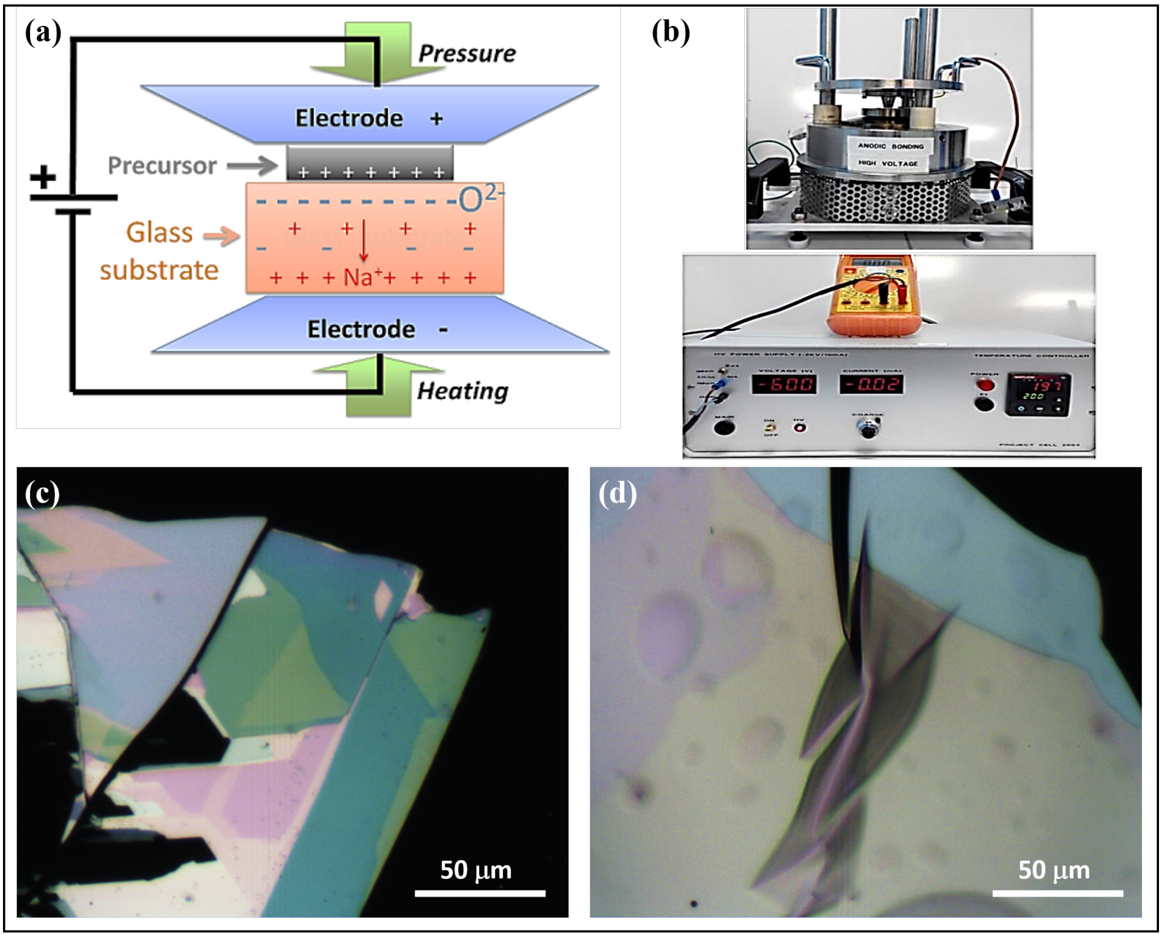

Figure 1.6: (a) A schematic diagram of the electrostatic hot exfoliation (anodic bonding) process, and (b) the experimental set-up used in exfoliation step[13]. Adapted with permission: ©2015, Theses, Université Pierre et Marie Curie - Paris VI. (c) The deposition yield with (d) blisters of MoS_2 flake over a borosilicate glass substrate (Pyrex).

1.2.1.3 Liquid-phase exfoliation (LPE) technique

The graphite flakes are dispersed in solvents like N-Methyl-2-pyrrolidone (NMP), Dimethylformamide (DMF), etc. and the prepared solution is subjected to sonication in an ultrasonic bath. During ultrasonic vibration, the sonication ruptures large graphitic flakes and forms kinks (deformations) on the flakes[73,74]. These kinks lead to cracks from where the solvent molecules pass through and intercalate, which increases the interlayer separation and leads to the unzipping of thin graphitic flakes into single-layer graphene nanosheets. The (modified) Hummers method has been extensively utilized for the liquid-phase exfoliation of graphitic flakes[75].

1.2.2 Bottom-up approach

Figure 1.3 illustrates the bottom-up approaches for producing graphene. In the 'Chemical vapor deposition' (CVD) process, the vapor of one or more volatile precursors is transported to decompose on a heated substrate in an ultra-vacuum reaction chamber[76]. For the growth of graphene, methane (CH_4) and hydrogen (H_2) gases are made to flow through a furnace kept at a high temperature, where a metal substrate (Copper (Cu) or Nickel (Ni)) is placed in an inert gas (Argon (Ar)) environment. The metal substrate acts as a catalyst, which allows the dissociation of methane gas into carbon atoms at a temperature of ~ 1000 °C lower than the graphitization temperature (~ 3000 °C). As a result of the chemical reactions, the graphene film form by the nucleation and aggregation of carbon atoms on the metal substrate in the reaction chamber.

In addition to that, epitaxial growth of graphene on Silicon Carbide (SiC) has gained significant interest among other graphene production techniques[77]. Graphene grows on the insulating SiC surface through an ultravacuum high-temperature annealing process. The vacuum decomposition of SiC leads to desorption of Si atoms from the heated surface leaving behind the carbon atoms which form graphitic layers, also called few-layer graphene (FLG) that consists of small grains with varying thickness ($30 - 200$ nm)[78]. By annealing the SiC sample in an argon atmosphere at high temperatures above ~ 1650 °C, the rate of silicon evaporation can be reduced to produce larger domains of graphene[79].

1.3 Transfer techniques and 2D material-based heterostructure fabrication

Two-dimensional (2D) materials show extraordinary electronic, optical, and mechanical properties, which make them worthy for optoelectronic applications[80,81]. The thinnest 2D material Graphene can withstand strain up to ~20% before rapture[3,82], in addition, it shows remarkable optical transparency of 97.7%[83]. The ultra-high flexibility and stretchability of 2D materials make them mechanically reliable and compliant with polymers for their applications in transparent and flexible electronics[84–86]. However, the constraints of growth conditions limit the direct growth/synthesis of 2D flakes (single or few layers) over a flexible polymer substrate[87].

The scotch-tape-based micromechanical exfoliation method produces the highest quality 2D flakes amongst other known deposition or growth techniques[88], but is incapable of selective transfer of 2D flakes from the scotch tape to the desired substrate. However, the mechanically cleaved 2D flakes are the best for prototype development for fundamental intrinsic studies. 2D layered materials similar to graphene have strong in-plane covalent bonding and weak inter-planar Van der Waals (vdW) bonding, therefore single or few layered flakes can be transferred to a substrate using polymer-assisted transfer techniques[89]. The polymer-assisted transfer techniques (see Figure 1.7) employed for the 2D flakes prepared using the bottom-up approach may also be reliable and effective for the transfer of 2D flakes prepared using the top-down approach[90].

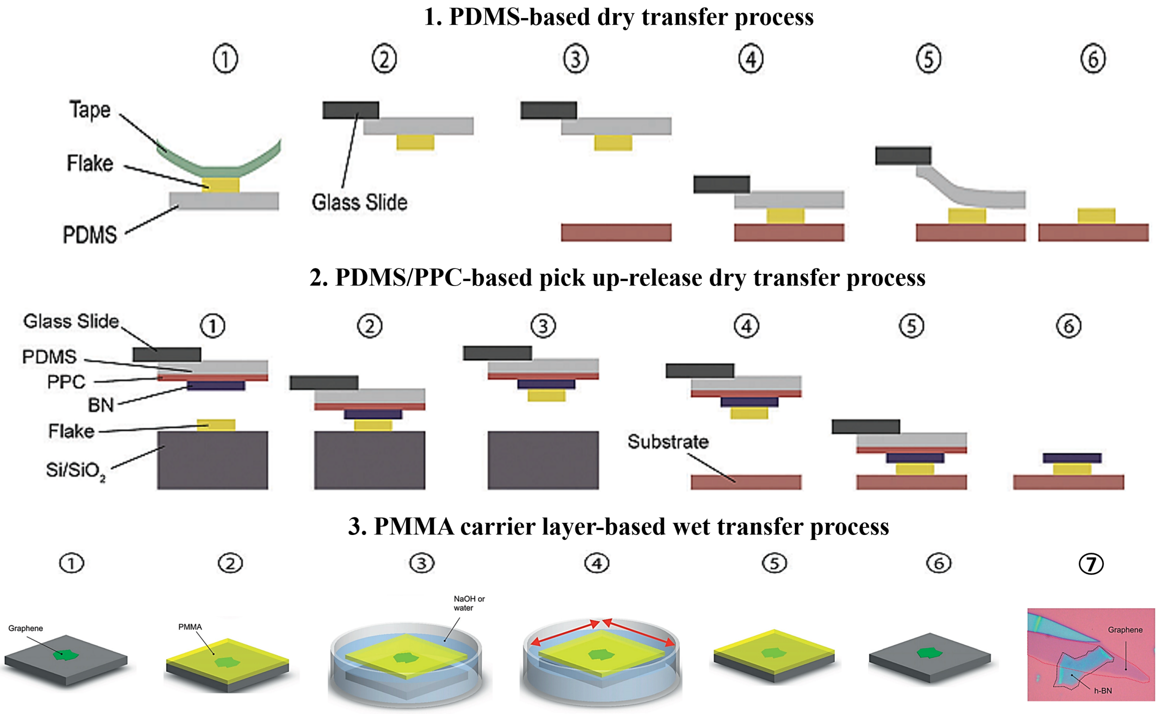
1. PDMS-based dry transfer process

2. PDMS/PPC-based pick up-release dry transfer process

3. PMMA carrier layer-based wet transfer process

Figure 1.7: Transfer techniques and 2D material-based heterostructure fabrication. (1) PDMS-based dry transfer process[14]. Adapted with permission: ©2018, RSC Publishing Ltd. (2) PDMS/PPC-based pick up-release dry transfer process[14]. Adapted with permission: ©2018, RSC Publishing Ltd. (3) PMMA carrier layer-based wet transfer process[6]. Adapted with permission: ©2012, Elsevier Ltd.

Several earlier reports show the use of harsh chemical etchants for the transfer of 2D flakes from the growth platform to an arbitrary substrate[91,92]. The chemical etching of the substrate is a destructive technique, which may also degrade the quality of 2D flakes. In the widely used PMMA carrier layer-assisted transfer processes such as ultrasonic-bubbling transfer[93], O_2-bubbling transfer[94], PVA film-based transfer[95], wedging transfer[96–98], and chemical etching (of the growth/deposition substrate) based transfer process[90,99–103], there is a very common problem of polymer contamination and folding of the transferred 2D flakes. However, the PMMA carrier layer-based techniques can transfer larger area flakes. Even the 2D flakes protected by a pressure-sensitive polymeric film face a significant amount of ripples and residues when transferred to a target substrate using a chemical etching-based method[104]. A significant amount of buckles or folds are observed in the wet wedging transfer of graphene onto a hydrophilic substrate due to water intercalation[105]. Room temperature transfer processes have also been attempted to avoid strain development due to harsh heat treatment. A polymeric layer of low molecular weight has 'medium-range' interfacial interactions with the supported 2D flakes, which helps in their cleaner transfer at room temperature with fewer folds in comparison to other high molecular weight polymer scaffolds[92,106].

The selective & direct transfer of 2D flakes from the scotch tape onto the desired substrate is impractical. However, a transfer process plays a crucial or even detrimental role in the performance of the 2D material-based electronic devices[107–111]. The wet transfer of 2D flakes by chemical etching of the rigid/ solid growth substrate is a destructive technique, which often degrades the quality of the 2D flakes, and may even result in damage, polymeric residual contamination, and folding of the transferred 2D flakes[90,93,99–103].

Furthermore, the direct transfer of 2D flakes from a growth or deposition substrate onto flexible polymeric substrates has also been attempted. The electrostatic hot transfer[112] and thermal-assisted direct transfer[113,114] techniques facilitate alternatives to the transfer of graphene from a copper substrate directly onto a flexible polymer substrate placed in ultra conformal contact. The direct transfer of single crystalline 2D flakes from a Nitto tape onto a pristine PDMS substrate results in several delamination regions[115,116]. However, the transfer process is probabilistic, non-deterministic, and unselective, and requires wettability of the PDMS substrate, which can be obtained by its oxygen plasma treatment before deposition[117]. It has been observed that oxygen-plasma treatment time has a substantial effect on the surface roughness of the PDMS substrate as extended plasma treatment induces unwanted surface deformation and cracks[118].

It is an ultimate task to combine the best of different ingredients into a single material, which is actually a motivation behind the formation of 2D material-based heterostructures. There is no constraint of lattice-mismatch in stacking distinct 2D layers over each other to form a heterostructure as the 2D layers are bonded with weak vdW interlayer forces. Strain engineering can play a vital role in further modulating the physical properties of the heterostructures. The strain can modulate the interlayer interactions in the heterostructure as the inter-layer distance decreases under tensile strain whereas it increases under compression. The PDMS-based dry transfer technique has also been extensively utilized for transferring mechanically cleaved 2D flakes onto a rigid/solid substrate that already has another 2D material lying over it, for making the 2D material-based heterostructure. This is an easier, fast, and cleaner transfer technique. In a recent work of Achint Jain *et al.*[119], PDMS film with MoS_2 flake is firstly aligned and placed in contact with hBN flake on Si/SiO_2 substrate, and then detached slowly after a short heat treatment, which leaves behind the MoS_2/hBN heterostructure on the Si/SiO_2 substrate. The hot pick-up & release of 2D flakes utilizes a temperature-dependent polymer-softening and hardening approach but with a finite probability of polymeric residual contamination as well as the development of folds or blisters on the 2D flakes[120,121]. For picking up a few-layer sample, a smooth surface of the substrate is highly needed (substrate selection) because any corrugation in the surface helps the flake conform properly. The larger the flake-to-surface adhesion, the stronger the vdW force and difficult to pick it using a polymer. The thick flakes are easily picked up because they do not conform to the substrate and their inter-layer interaction is more than the flake-surface interaction[14]. However, the manual stacking of 2D flakes onto a flexible substrate is still a challenge in the way of flexible electronics using the dry transfer technique as the elastomeric nature of the target substrate may cause mechanical damage or incomplete transfer of the 2D flakes.

1.4 Characterization techniques

1.4.1 Microscopy

1.4.1.1 Optical microscopy

The optical transmittance of monolayer graphene is 97.3%, which decreases with increasing number of layers. Therefore, the optical contrast increases with the thickness of the 2D flake, helping in the identification of the number of layers. The optical contrast is the relative intensity of reflected light from the substrate with and without the 2D flake[122–124]. The difference in optical contrast helps to distinguish the number of layers by analyzing optical images. The contrast $C(\lambda)$ of a 2D flake on a substrate

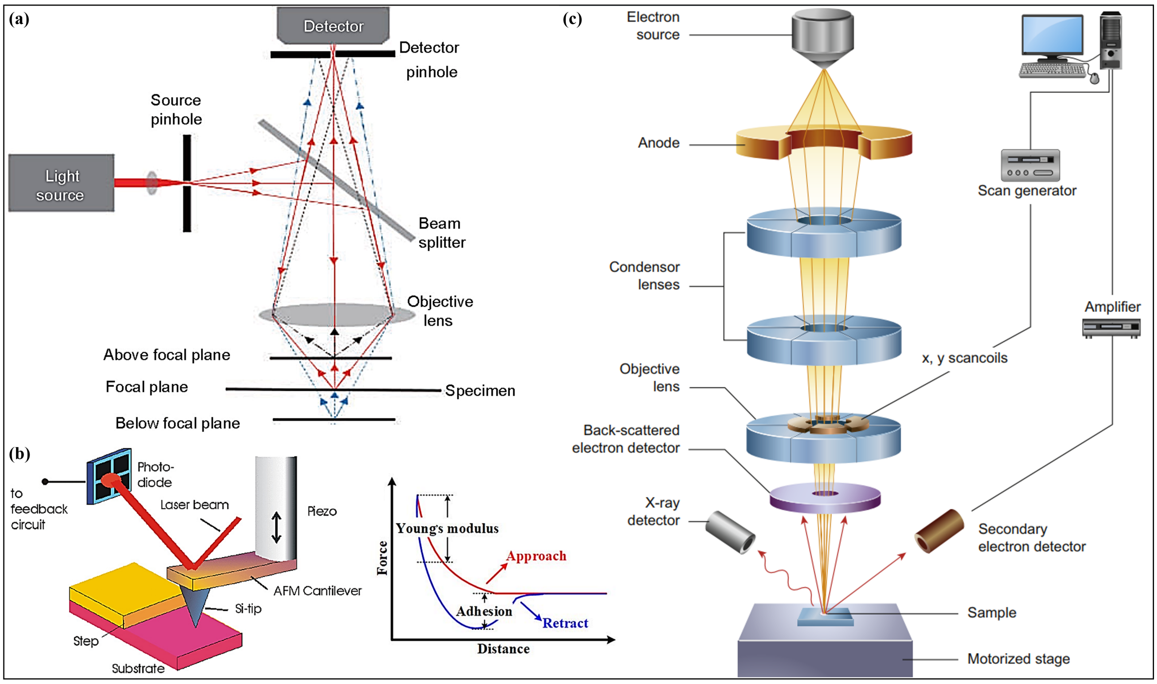
(a)
Detector
Detector pinhole
Source pinhole
Light source
Beam splitter
Objective lens
Above focal plane
Focal plane
Specimen
Below focal plane
(b)
to feedback circuit
Photo-diode
Laser beam
Piezo
AFM Cantilever
Si-tip
Step
Substrate
Force
Young's modulus
Approach
Adhesion
Retract
Distance
(c)
Electron source
Anode
Scan generator
Condensor lenses
Amplifier
x, y scancoils
Objective lens
Back-scattered electron detector
X-ray detector
Secondary electron detector
Sample
Motorized stage

Figure 1.8: (a) Schematic diagram of confocal optical microscope[15]. Adapted with permission: ©2015, Elsevier Ltd. (b) Schematic representation of atomic force microscope (AFM)[16]. Adapted with permission: ©2008, IOP Publishing Ltd. (c) Schematic diagram of scanning electron microscope (SEM)[17]. Adapted with permission: ©2016, Elsevier Ltd.

is found using

$$C(\lambda) = \frac{I_s(\lambda) - I(\lambda)}{I_s(\lambda)} \tag{1.1}$$

where $I_s(\lambda)$ is the intensity of the light reflected from the substrate and $I(\lambda)$ is the intensity of the light reflected from the 2D flake.

1.4.1.1.1 Interference reflection microscopy (IRM)

Interference reflection microscopy (IRM) is the optical imaging obtained as a result of interference of reflected light beams from a reflecting layers of a 2D flake. With this method, the optical contrast of the 2D layers can be significantly enhanced, which helps in the rapid and low-cost characterization of the number of layers in 2D materials[47]. Moreover, the interference of reflected light beams from the 2D material bubbles or buckles can produce interference patterns like Newton's rings, which can effectively characterize the topographical features of the microstructures[63].

1.4.1.2 Atomic force microscopy (AFM)

This is a type of scanning probe microscopy (SPM). It is a proficient tool for imaging, measuring, and manipulating matter at the nanoscale. It can provide resolution down to the atomic scale. AFM is an essential tool for confirming the number of layers in a 2D material[125]. The topographic information is gathered by scanning the surface with a mechanical probe that is a sharp-tip cantilever of silicon or silicon nitride. A focused laser spot gets reflected from the top surface of the cantilever into a position-sensitive photodetector (see Figure 1.8(b)). Therefore, the phase (path) difference between the reflected beams, resulting from the deflection of the cantilever while scanning the surface, is acquired to map the topographic profile of the surface. The electrostatic Coulombic and vdW forces affect the movement of the AFM tip. AFM can be used for mapping the topographic profile of the 2D material surface, whether flat or patterned; moreover, the AFM cantilever tip can be used for nanoindentation experiments to deduce the mechanical properties of the 2D elastic sheets.

1.4.1.3 Electron microscopy

Scanning electron microscopy (SEM) imaging produces the surface morphology of 2D materials through contrast mapping. The focused electron beam interacts with the matter and produces back-scattered, secondary, and auger electrons, which are selectively collected to generate images. The electrons can be produced either through thermionic emission or field emission. On the other hand, high-resolution transmission electron microscopy (HR-TEM) imaging produces atomically resolved images of the specimen, which provide the structural and atomic arrangement of the specimen. Both SEM and TEM operate in ultravacuum conditions[126,127].

1.4.2 Spectroscopy

1.4.2.1 Raman spectroscopy

Raman spectroscopy is a vital non-destructive tool to gain insights into the quality, disorder, edge and grain boundaries, thickness, doping, strain, and thermal conductivity of graphene and other 2D materials. Raman signals (or, phonon-modes) are the fingerprints for the 2D monolayer, bilayer, trilayer, and so on. When light propagates through a medium, most of it is either transmitted or absorbed, but a very fraction is scattered in all directions due to inhomogeneities inside the medium. If these inhomogeneities are static (such as defects in crystals), then this corresponds to elastic scattering of light (i.e., without frequency change) and is called Rayleigh scattering. Else if the inhomogeneities are dynamic like atomic vibrations or fluctuations in the charge or spin density in crystals, then it corresponds to inelastic scattering of light (i.e., with frequency change) and is called Raman scattering[18]. Raman scattering is a result of photon-electron interaction via emission (stokes) or absorption (anti-stokes) of a phonon.

The incident light (E_{in}) affects the atomic charge distribution (electron clouds), which induces the microscopic dipole moments. The sum of all these induced dipole moments constitutes the macroscopic polarization ($P = \alpha E_{in}$), where the molecular polarizability (α) is the deformability of the electron cloud about the molecule by an electric field. This polarization produces a secondary electromagnetic field, which causes scattering of the light. The scattered photons are mostly composed of Rayleigh scattered photons and a very small amount of Raman scattered photons[128]. Rayleigh and Raman are two-photon processes, which involve the scattering of an incident photon from a "virtual state". A typical Spectrum is composed of three features: the Stokes, anti-Stokes, and Rayleigh lines. The first two are symmetrically located from both sides of the Rayleigh line.

- If the induced electric field oscillates with the same frequency as that of the incident light ω, the polarization term is responsible for the elastic Rayleigh scattering.
- If the induced electric field oscillates with a frequency $\omega + \Omega$, the polarization term is responsible for the blue-shifted (w.r.t. incident light) scattered light (anti-stokes line). This scattered light is due to the annihilation of a phonon.
- If the induced electric field oscillates with a frequency $\omega - \Omega$, the polarization term is responsible for the red-shifted scattered light (Stokes line). This process corresponds to the creation of a phonon.

In the case of graphene, the characteristic Raman peaks are: D peak (at 1350 cm^{-1}), G peak (at 1580 cm^{-1}), and 2D peak (at 2690 cm^{-1}). The high-quality and defect-free nature of graphene is confirmed on the basis of: (i) lack of D band, (ii) $\mathrm{I}_{2\mathrm{D}}/\mathrm{I}_{\mathrm{G}}$ ratio, and (iii) full width at half maximum (FWHM) of the 2D band (see Figure 1.9(a,b)). For MoS_2 flakes, the frequency difference between the characteristic $\mathrm{E}^1_{2\mathrm{g}}$ and $\mathrm{A}_{1\mathrm{g}}$ modes increases monotonically with the number of layers from $\sim$ 19 cm^{-1} for single layer to $\sim$ 25.5 cm^{-1} for bulk MoS_2 (see Figure 1.9(c,d))[19].

1.4.2.2 Fourier transform infrared (FT-IR) spectroscopy

Fourier transform infrared spectroscopy (FT-IR) is based on infrared (IR) radiation-matter interactions. The vibrational modes of the molecules modulate due to the

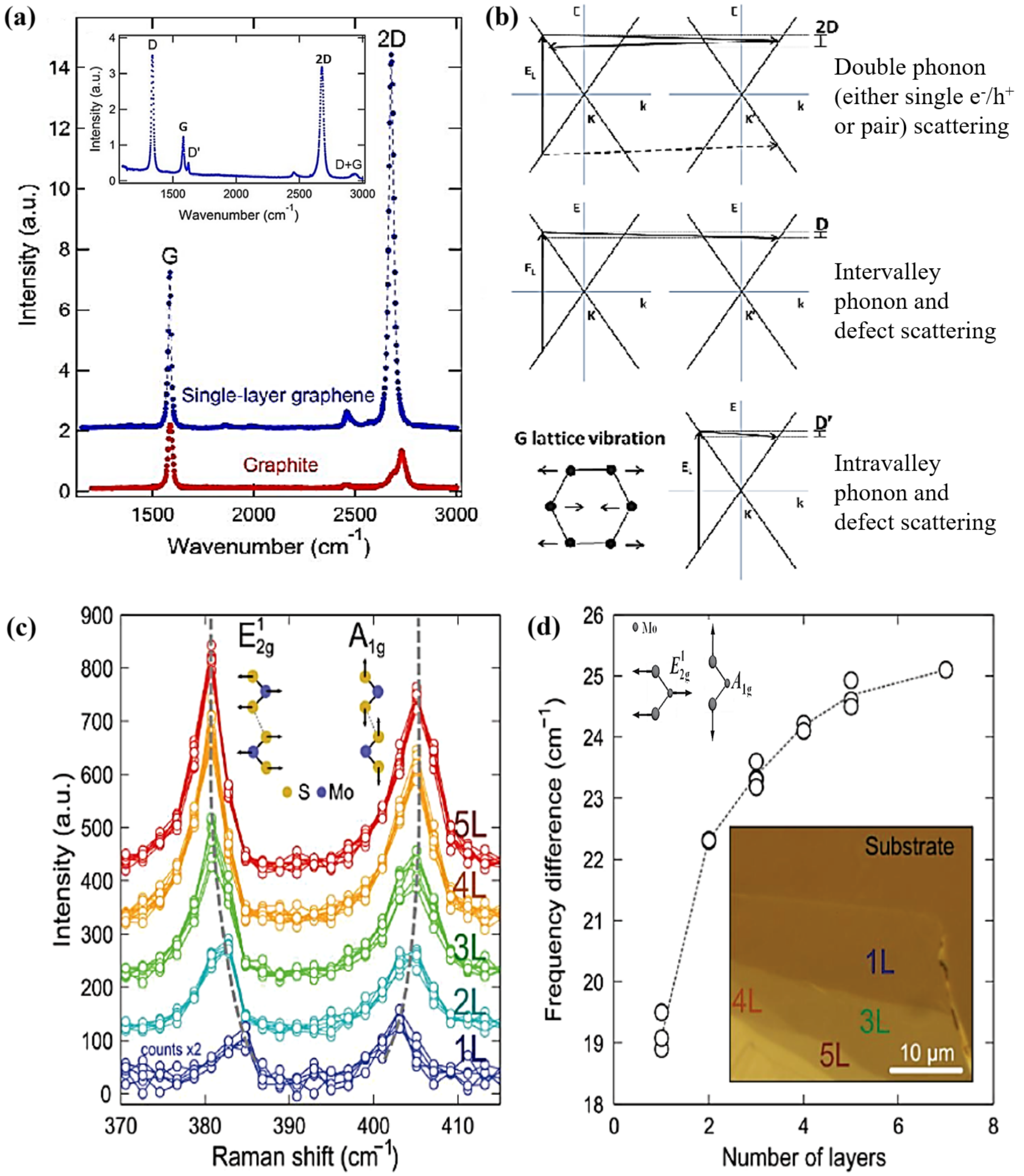

Figure 1.9: (a, b) Raman spectroscopy of graphene and origin of peaks in the spectrum[18]. Adapted with permission: ©2013, Nova Science Publishers Hauppauge NY. (c, d) Identification of number of layers in MoS_2 using Raman spectrocopy[19]. Adapted with permission: ©2013, American Chemical Society.

absorption of IR radiation. The absorbed IR light wavelength resembles the type of bonds and functional groups present in the specimen[129]. An FT-IR microscope comprises an FT-IR spectrometer and an optical microscope. The image captured using an IR microscope contains a spectrum for each pixel, which is collected to map the intensity at any wavelength.

The molecules of a crystal follow a resonance condition, where they have a tendency to interact with radiation having oscillating dipoles of a specific frequency that matches the natural vibrational frequency of a particular mode of the crystal. In the IR absorption process, the absorbed energy by the molecule causes a change in the dipole moment, which results in a change in the vibrational energy level. Homonuclear diatomic molecules such as H_2, N_2, and O_2 have no dipole moment and are IR inactive (but Raman active) whereas heteronuclear diatomic molecules such as HCl, NO, and CO do have dipole moments and have IR active vibrations[128].

1.4.2.3 Photoluminescence (PL) spectroscopy

'Luminescence' is the process of spontaneous emission of light by excited atoms in a crystal, which involves only real states, and therefore, the energy and momentum are conserved in real transitions. The atoms can be excited by different means e.g., by absorbing light (photoluminescence), by heat (thermoluminescence), etc.

In semiconductors, optical absorption is dominated by inter-band absorption, i.e., electrons are excited from the valence band to the conduction band. The excited electron leaves an unoccupied state in the valence band which is described as a hole. Hence, the inter-band absorption process creates an electron-hole pair. The oppositely charged particles are created at the same point in space and can attract each other through Coulomb interactions. Such interactions can lead to the formation of a bounded electron-hole pair which is called an exciton. The emission process corresponds to radiative/non-radiative electron-hole recombination and is the opposite process of inter-band absorption. The electron-hole pair can recombine non-radiatively by emitting phonons or by transferring its energy to impurities or defects. In general, the incoming photon has much higher energy than the band gap so that the excited electrons (holes) are promoted to states well above (below) the conduction (valence) band edges. The electrons (the holes) relax to the bottom (top) of the conduction (valence) band before radiatively recombining and forming a thermal distribution with a width of $\sim k_BT$.

Intrinsic photoluminescence (PL) spectrum, resulting from the radiative recombination within $\sim k_BT$ of C.B edge and V.B edge, consists of a peak of energy E_g with a width $\sim k_BT$. Hence, PL spectroscopy is a technique to measure the band

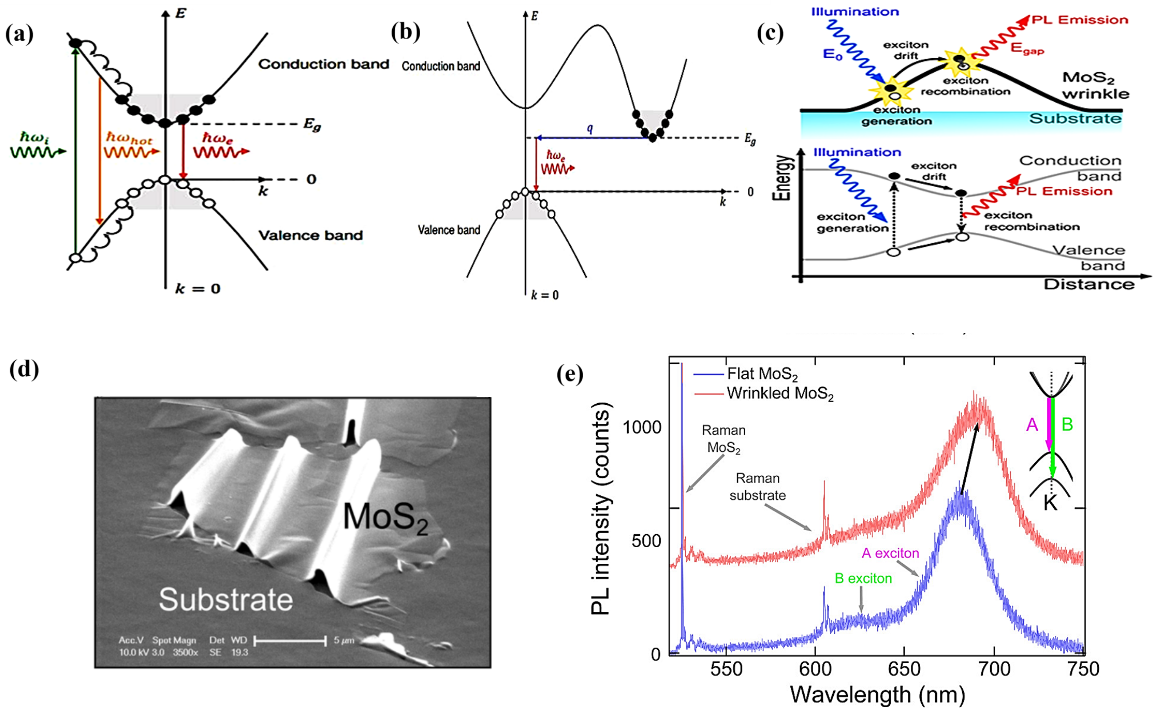
(a)
E
Conduction band
$\hbar\omega_i$
$\hbar\omega_{hot}$
$\hbar\omega_e$
E_g
0
k
Valence band
k = 0
(b)
E
Conduction band
q
E_g
$\hbar\omega_e$
0
k
Valence band
k = 0
(c)
Illumination
E_0
exciton drift
PL Emission
E_{gap}
exciton recombination
exciton generation
MoS2 wrinkle
Substrate
Energy
Illumination
exciton drift
Conduction band
PL Emission
exciton generation
exciton recombination
Valence band
Distance
(d)
MoS2
Substrate
Acc.V Spot Magn Det WD 5 µm
10.0 kV 3.0 3500x SE 19.3
(e)
Flat MoS2
Wrinkled MoS2
Raman MoS2
Raman substrate
A exciton
B exciton
A
B
K
PL intensity (counts)
0
500
1000
550
600
650
700
750
Wavelength (nm)

Figure 1.10: Band diagram for direct and indirect band gap semiconductors[20]. Adapted with permission: ©2016, Theses, Université de Strasbourg. (c) The 'funneling effect' observed at the wrinkled site of monolayer MoS_2 (shown in (d)), and (e) photoluminescence spectroscopy of flat and wrinkled region of monolayer MoS_2[19]. Adapted with permission: ©2013, ACS Publishing Ltd.

gap of a semiconductor. The PL intensity is proportional to ηN, where η is the quantum yield which is the ratio of the number of emitted photons to the number of absorbed ones. PL peaks at lower energies than the band gap E_g are also possible due to excitonic effects even if no impurities or defects states are present in the gap. The exciton is a neutral particle that can be regarded as a hydrogenic system. The excitonic energy levels lie in the gap and are indicated by the binding energy $E_X^{(n)}$, where $n = 1, 2, 3, ..., \infty$, which follows a Rydberg-like series. The lowest excitonic feature i.e., $E_g - E_X^{(1)}$ resembles the 'optical band gap', which dominates the photoluminescence (PL) or emission spectrum. Therefore, PL spectroscopy always reveals the optical band gap. The sum of the optical band gap ($\hbar\omega_e$) and the excitonic binding energy $E_X^{(1)}$ gives the electronic band gap E_g. Single-layer TMDCs are direct band gap semiconductors whereas their bulk counterparts are mostly indirect band gap semiconductors. The indirect band-gap semiconductors have their conduction band minimum at a different wave vector than their valence band maximum. Therefore, additional momentum usually provided by a phonon is required for a radiative transition to take place at the band edges. Such indirect band gap transition is a second-order process in contrast to the direct band gap transition which is a first-order process. Since the second-order process is less probable than the first-order process, the PL intensity of an indirect band gap semiconductor is much weaker than that of a direct band gap one[20] (see Figure 1.10(a,b)).

1.5 Strain engineering and straining techniques

2D materials' high mechanical flexibility and strain-bearing ability make it easier to tailor their physical characteristics when subjected to external strain[3,60,130,131]. It is highly desirable to have a higher degree of control over the tunability of the vibrational, electronic, and optical properties of 2D materials for flexible electronics (see Figure 1.11). This can be achieved by applying various straining modes, either in-plane or out-of-plane[132]. Doping engineering has already been very successful in three-dimensional (3D) or bulk materials for the semiconductor industry, but mechanical strain engineering has certain limitations on them. For instance, silicon typically breaks at a strain level of only $\sim 1.5\%$. On the other hand, 2D materials can sustain a tensile strain up to $\sim 30\%$, therefore there has been a great surge of interest in developing strain-engineered 2D materials[133,134]. Engineering the physical properties of 2D materials under strain also takes into account their anisotropic behavior owing to finite interlayer sliding (induced by the weak van der Waals (vdW) coupling) and the flake thickness-dependent elastic as well as adhesive capabilities. Since the strain-enabled band gap engineering in 2D materials has intriguing implications for both fundamental research and commercial applications, a solid grasp of the straining techniques is a prerequisite[135]. The straining techniques have been formulated with motivation from naturally occurring phenomena (e.g. human skin-based strains) or robotic or mechanical processes.

1.5.1 Fundamentals of Strain Engineering

The first and foremost requirement is the reversibility of the straining effects on 2D materials. Therefore, 2D material is strained to the elastic limit beyond which the plastic region starts, where irreversibility enters through the development of the permanent deformation of the 2D material, followed by the breaking point. The external mechanical strain affects the interatomic separation in the atomically thin 2D material, which modulates its intrinsic properties. The interatomic distance or the chemical bond length increases (decreases) with the application of tensile (compressive) strain. The bond strength becomes weaker (stronger) as the bond length increases (decreases). Since the natural vibrational frequency (ω) is directly proportional to the bond strength (or, force constant (k)), i.e. $\omega = \sqrt{\frac{k}{m}}$, the vibrational frequency

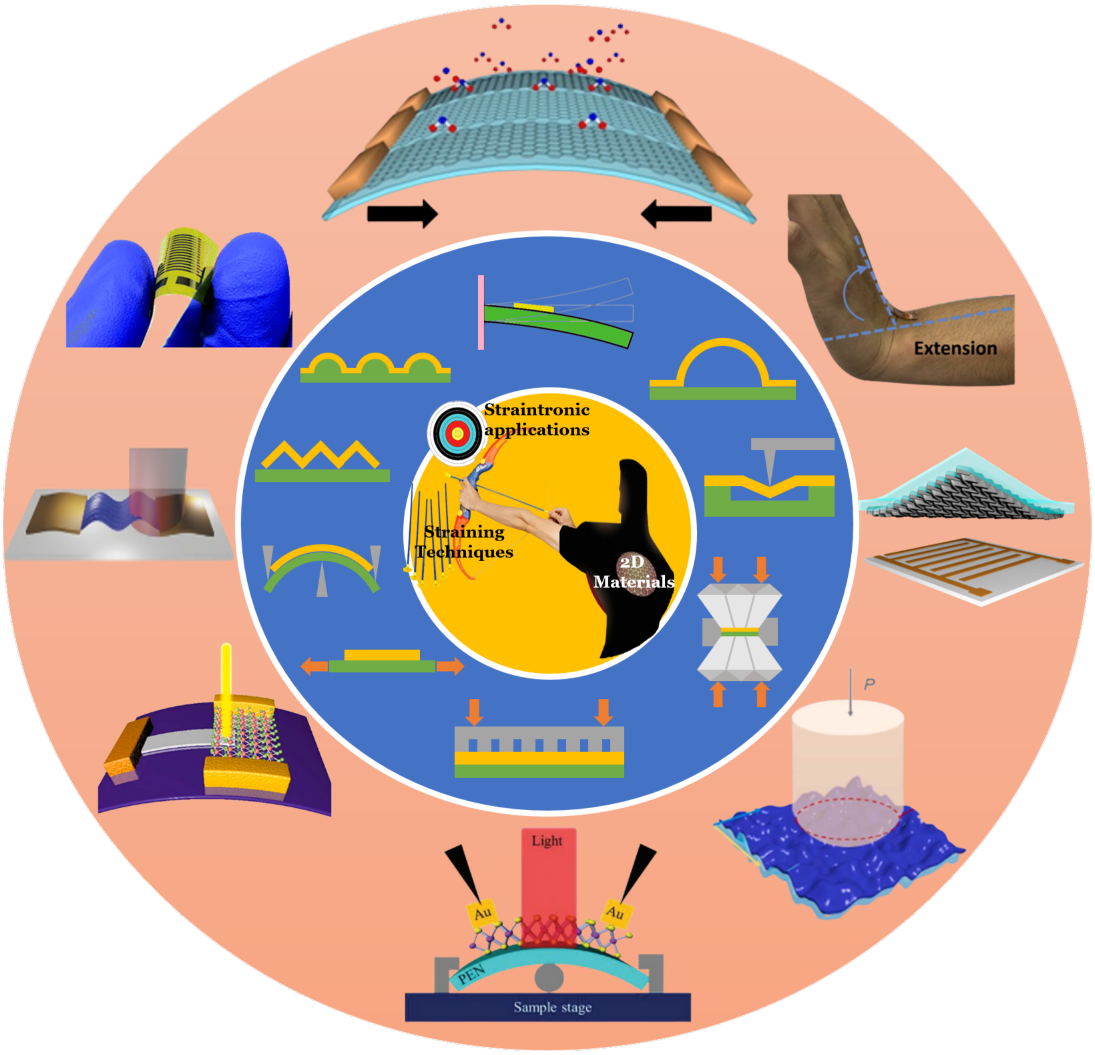

Figure 1.11: The straining techniques enabling the utilization of 2D materials in flexible straintronic applications[21]. Adapted with permission: ©2023, Elsevier Ltd.

decreases (increases) by applying tensile (compressive) strain to the 2D material[134]. The shifting in the crystal vibrational frequency of the strained 2D material can be easily detected using the μ-Raman spectroscopy[136]. The red (blue) shifting of the Raman peaks corresponds to the softening (hardening) of the phonon modes. Hence, the modulation of the physical properties of a 2D material is the direct & straightforward consequence of the mechanical straining on the crystal lattice.

The 2D transition metal dichalcogenides (TMDCs) are semiconducting (SC) by nature, differing from graphene, which is a zero-band gap semimetal. In 2D semiconductors, the electrons are excited from the valence band (V.B.) to the conduction band (C.B.) by absorbing energy that is equal to or greater than the electronic band gap, leaving behind unoccupied states (holes) in the V.B.[137] An electron-hole pair bounded by a Coulombic force of attraction is called an exciton. The radiative recombination of the electron-hole pairs results in the emission of light, which is called 'photoluminescence' (PL). The energy corresponding to a photon, emitted as a result of the recombination of electron-hole pair, is called an 'optical band gap'[20]. Due to the finite binding energy of the electron-hole pair, the optical band gap is slightly less than the electronic band gap. The electronic band gap decreases (increases) with an increase (decrease) in the lattice parameter under tensile (compressive) strain due to the phenomenon of quantum confinement. Since the electronic band gap is the direct sum of the optical band gap and the excitonic binding energy (which is negligibly affected by the external strain)[138–142]. Therefore, the optical band gap of the 2D semiconductor also decreases (increases) under the tensile (compressive) strain[143,144]. An indirect band gap semiconductor has the C.B. minima and V.B. maxima at the different wave vectors, which require additional momentum for the radiative transitions. Therefore, the indirect band gap transition is a second-order process in contrast to the direct band gap transition, which is a first-order process. Due to the lower probability of indirect band-gap transitions, the PL intensity is much weaker than that for direct band-gap transitions[137]. In 2D SCTMDCs, there is a transition from indirect band gap to direct band gap, going from multilayer to monolayer[145]. However, a multilayer 2D SCTMDC has been demonstrated to exhibit a transition from an indirect to a direct band gap with a dramatic increase in PL intensity under the application of strain[146].

For strain engineering research, the 2D flakes are usually prepared by using the micromechanical exfoliation (MME) technique, as this assures that the prepared flakes are defect-free and of the highest quality[7,147]. Since 2D materials are highly flexible and stretchable, owing to the strong in-plane covalent bonding and the weak interplanar van der Waals (vdW) bonding, it is always preferred to transfer them onto flexible polymeric substrates for strain engineering purposes by using any polymer-assisted wet or dry transfer technique. In general, the wet transfer techniques demand the chemical etching of the deposition/growth substrate[90,103], while the dry transfer techniques utilize thermal softening and hardening of the polymeric stamps for hot pick-up and release of the 2D flakes[14,120,121]. The dangling bonds-free surface of 2D materials enables the direct fabrication of the heterostructures on the flexible substrates, adding more degrees of freedom for strain engineering applications.

The strain value, developed at the strained sites of a 2D material, can be deduced using the "Grüneisen parameters", which describe the effect of a change in the lattice structure on its vibrational and optical properties. The application of strain alters the electron and phonon band structures of a lattice, which is characterized by the amount of shifting in the Raman and PL peak positions. The Grüneisen parameters only deal with the strain-dependent spectral response of the 2D material, regardless of the applied straining technique. To probe the uniaxial or biaxial strain in a 2D material, Raman spectroscopy has been proven to be a powerful and nondestructive tool, as the Raman active mode shifts and/or splits under the application of strain. Group theory establishes a functional dependence of the peak positions on the strain tensor. The Raman and PL peaks shift under a uniaxial strain[148], as

$$\omega_{A'} = \omega^0_{A'} \left[1 - \gamma_{A'}(1-\nu)\varepsilon\right] \tag{1.2}$$

where A' is a rotationally invariant point-group representation of the crystal symmetry, $\omega^0_{A'}$ is the zero strain frequency, $\gamma_{A'}$ is the Grüneisen parameter, ν is the Poisson's ratio, and ε is the amount of the uniaxial strain. On the other hand, a degenerate phonon peak E', which splits into two peaks: the + peak and the − peak, shifts under the uniaxial strain, as

$$\omega^{\pm}_{E'} = \omega^0_{E'} \left\{1 - \left[\gamma_{E'}(1-\nu) \mp \frac{\beta_{E'}}{2}(1+\nu)\right]\varepsilon\right\} \tag{1.3}$$

where $\omega^0_{E'}$ is the zero strain frequency, $\gamma_{E'}$ is the Grüneisen parameter, and $\beta_{E'}$ is the shear deformation potential. The ± sign in the equation 1.3 denotes the lifting of the degeneracy under uniaxial strain. The following reasons lead to the discrepancies in the values of the Grüneisen parameters among the reported experimental findings related to uniaxial straining[148,149]: (i) the Grüneisen parameters behave anisotropically, as the frequency-shifts of the splitted phonon modes vary with the direction of the uniaxial strain, (ii) the higher Poisson's ratio of the underlying substrate than that of the 2D material induces errors in the uniaxial straining experiments, (iii) the Grüneisen parameters decrease with increasing uniaxial or biaxial strain within the elastic limit, and (iv) the Poisson's ratio is valid for the isotropic straining through the substrate with good interfacial adhesion, but there is always a possibility of finite interfacial slippage during the strain-transfer process. However, in case of biaxial strain[1,149], the Grüneisen parameter is given by,

$$\gamma_{A'} = -\left(\omega_{A'} - \omega^0_{A'}\right) / \left(2\omega^0_{A'}\varepsilon\right) \tag{1.4}$$

where ε is the equi-biaxial strain. As the biaxial strain value does not depend upon Poisson's ratio, therefore, the same biaxial strain value develops for both freely suspended graphene and simply supported graphene over a substrate under isotropic out-of-plane deformation. Therefore, the biaxial strain is more reliable for deducing the Grüneisen parameter from the straining experiments. However, any discrepancy, in this case, may be attributed to the intrinsic strains already present in the 2D material before performing the experiments[149].

Over and above that, strain engineering also has a crucial role to play in tuning the strongly correlated electronic states of the moiré superlattices with twisted 2D homo- or hetero-bilayers[150–152]. In twisted bilayer graphene (t-BG), the positions of Fermi energy E_{F} (Dirac point, where the density of states (DOS) vanishes) and the van Hove singularities vHSs (saddle points, where DOS is very large) in the electronic band structure, can be controlled by electrostatic gating and relative rotation of the 2D layers, respectively. By introducing a small rotation between the stacked graphene layers, the moiré patterns form, and the vHSs come closure to E_{F}, which results in the emergence of exciting new phases of matter[153]. The relative angle of rotation is directly related to the period of the moiré superlattice, which can help in evaluating the local strain fields in the t-BG[154]. As the twist angle becomes smaller ($\theta < 3.5°$), the interlayer coupling strengthens and the quasi-particle velocity at the Dirac point begins to decrease. However, for larger twist angles ($\theta > 5.5°$), the electronic spectra of the graphene layers become identical to that of a single-layer graphene, resembling the electronic decoupling of the layers[155]. The unconventional superconductivity at 1.7 K has been realized in t-BG, where two graphene layers are relatively twisted at a so-called 'magic angle' $\sim 1.05°$. At the magic angle, the bands of the two graphene layers hybridize and exhibit strong interlayer coupling, which results in the modulation of the physical properties. The strong interlayer coupling in the magic-angle t-BG can be further fine-tuned under the applied strain or pressure[156,157]. The band flattening has been found to emerge in t-BG with a relative twist angle of $\sim 1.25°$ under a small uniaxial heterostrain (interlayer relative strain) of 0.35%[158]. The heterostrain may also produce higher-order vHSs in the moiré superlattice, which offers a vital platform for enhancing the correlation effects[159]. Therefore, an interplay between strain and twist might open new pathways to control the flattening of the moiré bands and, thus, the conductivity of the t-BG[159–161]. Recently, Marwa Mannaï *et al*[162] showed a way to find the direction and the amplitude of the applied strain in the t-BG and t-BTMDC superlattices at a given twist angle, such that the twist angle approaches the magic angle. Furthermore, the strain engineering of 2D TMD-based 'kirigami' (an ancient Japanese art of paper cutting) patterns on a flexible polymeric substrate have been employed for tunable and reversible photoresponsivity, as the Kirigami architectures significantly improve the reversible stretchability as well as flexibility[163,164]. The fundamental advances in strain engineering of 2D materials have a major impact on the development of cutting-edge technologies for the future.

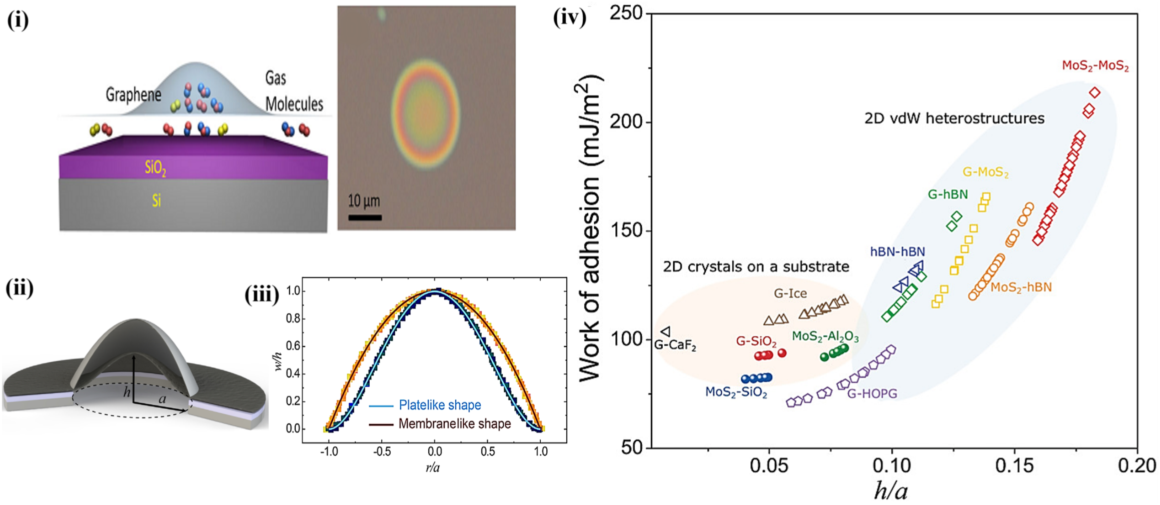

Figure 1.12: (i) Gaseous air molecules, confining underneath the graphene monolayer over a smooth SiO_2/Si substrate, form graphene bubble during the micromechanical hot exfoliation process[22]; Adapted with permission: ©2018, American Physical Society. (ii-iii) Bending of a multilayered flake follows either membrane or elastic plate like profile[23]; Adapted with permission: ©2019, American Physical Society. (iv) Work of adhesion with respect to a given substrate as a function of the characteristic aspect ratios of the blisters of different 2D materials and heterostuctures[2]; Adapted with permission: ©2018, AAAS.

1.6 Adhesion mechanics of 2D materials

The adhesion mechanical behavior of the 2D elastic nanosheets over any substrate can be understood by analyzing the topographic profiles of bubbles or buckles formed on their surfaces. The presence of blisters on 2D material surfaces has a detrimental role in their electronic properties. However, the topographic features of the blisters can indirectly probe their mechanical response over the given substrate as the presence of bubbles on an elastic sheet over a substrate ensures a finite amount of interfacial adhesion. The measure of work of adhesion is a prerequisite for the selection of a substrate to fabricate electronic devices based on 2D materials or their heterostructures. The elastocapillarity of 2D materials results from the competitive interplay between the elastic strain energy and the surface/interface energy, which constitute the minimized potential energy of the system. The relative dominance of the bending stiffness and the stretching stiffness (governed by the ratio of blister height to flake thickness, i.e. h/τ) determines the shape-profile of a 2D material blister either membrane-like or elastic plate-like (see Figure 1.12). On the contrary, the wrinkles form in 2D material over an elastomeric substrate due to a finite mismatch in Young's modulus or thermal expansion coefficient in a prestretch-release process or thermal annealing process, respectively. The minimization of net potential energy yields the interfacial adhesion energy or exfoliation energy of the 2D material over a substrate. The elastocapillary properties of 2D materials are responsible for the formation of various nano/microstructures of 2D elastic nanosheets (see Figure 1.13).Such strained nano/microstructures of 2D materials have significant implications in fundamental research as well as strain engineering applications.

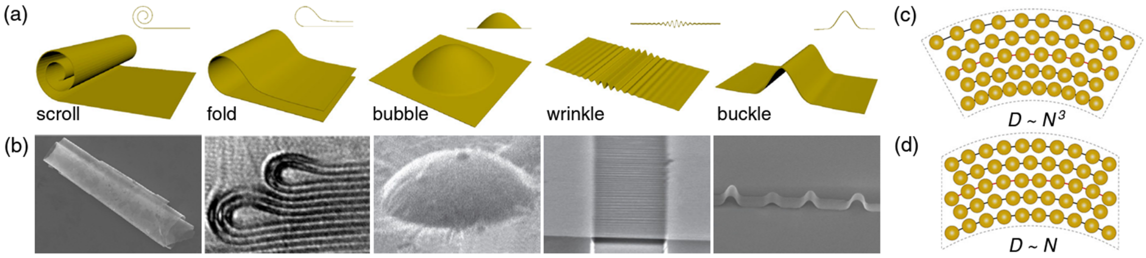

Figure 1.13: (a-b) Schematics and corresponding scanning electron microscope images of nano/microstructures of 2D materials, and (c-d) bending profile of 2D multilayer with perfectly glued and ultralubricated interfaces, respectively[23]. Adapted with permission: ©2019, American Physical Society.

1.6.1 Strained nano/microstructures of 2D materials

1.6.1.1 Blisters

The out-of-plane deformation of 2D elastic nanosheets due to the confinement of gas/liquid/nanoparticles results in the formation of bubbles, domes, tents, pyramids, etc., which are commonly termed 'blisters'[24]. The competitive interplay between the in-plane elastic stiffness and out-of-plane bending stiffness determines the parameter h/τ, which governs the membrane or elastic plate-like behavior of the 2D elastic sheet.

1.6.1.2 Wrinkles and Buckles

When 2D elastic nanosheets are adhered to a pre-stretched elastomeric substrate, and then, it is released controllably, the wrinkles of the 2D elastic nanosheets form as a result of Young's modulus mismatch. Initially, at smaller compression levels while releasing the pre-strain of the substrate, conformal wrinkles form, which starts delaminating from the substrate's surface to form the buckles with increasing compression level. At sufficiently larger compressions, the buckles collapse to form the folds due to interfacial contact failure[64].

1.6.1.2.1 Methods for nano/micro-structuring of 2D materials

There are several techniques to form the various nano/microstructures of 2D materials, e.g., blisters, buckles, wrinkles, folds, etc. Some of the major techniques are shown in Figure 1.14.

Pressurized Blistering A flexible polymeric film carrying 2D elastic nanosheets is suspended over a circular cavity patterned on a silicon substrate, and then, pressurized to blow it in an out-of-plane direction. The pressurized bulging generates biaxial strain at the center of the "blown-bubble". The positive or negative pressure difference ($p_{int} - p_{ext}$) results in upward or downward deflection of the membrane, which develops tensile or compressive strain, respectively, at the center of the pressurized bubble[165,166].

The bulging or out-of-plane bending of the 2D membrane, and hence the induced biaxial tensile strain is controlled by altering the pressure difference. As the central deflection of the pressurized blister increases, the accumulated tensile strain at the center also increases, which results in the red-shifting of the phonon modes and reduction of the band gap. Using Hencky's model and considering unity strain-transfer efficiency, the biaxial strain developed at the center of the bulged 2D membrane with negligible bending stiffness is defined as follows[165]:

$$\varepsilon = \sigma(\nu)\left(\frac{\delta}{a}\right)^2 \tag{1.5}$$

where $\sigma(\nu)$ is a constant prefactor, which depends only on Poisson's ratio (ν), δ is the upward deflection of the membrane, and a is the radius of the circular hole. Alternatively, the biaxial strain on the 2D material can also be calculated using the Grüneisen parameter (γ) for Raman or PL peaks, as[166–170] $\varepsilon = [\omega - \omega_0] / [2\gamma\omega_0]$, where ω and ω_0 are the frequencies of the Raman/PL peaks at finite strain and zero strain, respectively. Further, the investigation of the pressurized blisters in terms of the upward deflation height, radius, and in-plane as well as out-of-plane elasticity of the membrane is exploited for measuring the mechanical properties (such as Young's modulus, interfacial adhesion energy, confinement pressure, etc.) of the 2D material-substrate system[1,170].

Thermal-Mismatch Induced buckling The differing thermal expansion response of a 2D material with respect to the underlying substrate can be exploited as a robust tool to induce controlled in-plane equi-biaxial strain for modifying the band structure of the 2D material. By selecting a substrate with a highly positive thermal expansion coefficient (TEC), the deposited 2D flakes can be subjected to a biaxial tensile (or compressive) strain effectively by heating (or cooling) the underlying substrate locally or globally. The strain in the deposited 2D flakes arises due to (i) the mismatch in the thermal expansion coefficient with respect to the substrate, and (ii) the interfacial shear stress, transferred from the substrate. The strain transfer efficiency can be increased significantly by choosing a substrate having a high Young's modulus[171], therefore flexible substrates are preferred in comparison to the rigid/ solid substrates. In general, the 2D material-substrate system is mounted on a Peltier element or a temperature-controlled stage (inside a vacuum chamber) for detecting the altered vibrational & optical responses of the 2D material as a function of temperature through in-situ micro-Raman/PL spectroscopy. Periodic features are marked on the surface of the flexible polymeric substrate for measuring the relative change in the length of the 2D flake as a result of the thermal-mismatch effect, which is confirmed by continuously monitoring the optical images with varying temperature[171–173]. The thermal-mismatch induced equi-biaxial strain applied to the 2D material or the relative spacing ($\Delta L/L$) of the periodic features over the polymeric substrate varies linearly with the temperature, as

$$\varepsilon = \frac{\Delta L}{L} = \alpha_{sub}(T - T_0) \tag{1.6}$$

where α_{sub} is the thermal-expansion coefficient of the substrate, T is the temperature at a particular strain-level, and T_0 is the room temperature. The linear relationship between the strain and the temperature is valid up to a threshold temperature (T_{th}), beyond which the vdW interactions are unable to hold the 2D flake in the conformal contact with the underlying substrate, thereby causing the interfacial slippage. Therefore, once the sample is cooled down from the raised temperature ($T > T_{th}$) to room temperature, the nanoscale blisters, wrinkles, or buckles form in the 2D material[174,175].

Molecular confinement induced blistering 2D materials can be strained locally by confining the liquid/gas molecules or nanoparticles at the 2D material/substrate interface. The 2D material blisters are either induced spontaneously or formed intentionally[24]. The spontaneously formed blisters inevitably form on transferring the 2D material onto a flat[2,22,176–178] or patterned substrate[179] as a result of the aggregation & confinement of naturally adsorbed surface-matter or interfacial contaminants into the blisters. On the contrary, the intentionally induced blisters result from the intercalation of molecules by diffusion[180,181] or charged particle irradiation[182–186], physical manipulation of confined matter[63,133,187–192] and pressurized bulging of atomically thin 2D nanosheets[165,193,194]. The adhesion mechanics (studies related to interfacial adhesion, confinement pressure, etc.) of the 2D nanosheets depends on the nature of the confined fluid inside the blisters, owing to the different fluid-structure interactions[34,195]. There are several direct and indirect ways to get compositional insights into the blisters, such as AFM-tip-assisted poking, scratching, bursting, and time-dependent deflation of the blisters. The strain profile of an axisymmetric blister can be used to deduce the interfacial adhesion energy & the confinement pressure inside it using a relevant blister-test model (nonlinear elastic plate model/ membrane model/ tent model)[1,133,196]. The out-of-plane deflation of a blister (h) with respect to the thickness of the 2D nanosheet (τ) helps in selecting an appropriate model. The nonlinear elastic plate model and the membrane model are applicable for $\frac{h}{\tau} \lesssim 1.5$ and $\frac{h}{\tau} > 2$, respectively[1]. The vdW interactions, acting among the 2D nanosheet, the substrate, and the confined matter, play a crucial role in stabilizing the blister system and thereby determining the work of adhesion & the confining pressure. For air-filled blisters of 2D nanosheets, the 'fluid-structure interaction term' is ignored, which gives rise to the work of adhesion $\Gamma \propto E_{2D}(\frac{h}{a})^4$ and the confinement pressure $p \propto E_{2D}\frac{h^3}{a^4}$, where E_{2D} is the 2D elastic stiffness of the 2D nanosheet and h & a are the height and radius of the blister, respectively[1].

The Raman spectroscopy is used to measure the local strain in a 2D material, induced due to the blister formation. For a 2D material under strain with two principal strain components ε_r (radial) and ε_θ (azimuthal), the frequency shift of each phonon mode is given by[1],

$$\Delta\omega = -\gamma\omega_0\left(\varepsilon_r + \varepsilon_\theta\right) \pm \frac{1}{2}\beta\omega_0\left(\varepsilon_r - \varepsilon_\theta\right) \tag{1.7}$$

where ω_0 is the phonon frequency at zero strain, γ is the Grüneisen parameter, and β is the shear-deformation potential. The shear component of the strain corresponds to the phonon mode splitting, similar to the G peak of graphene under uniaxial strain. At the center of the bubble, ($\varepsilon_r = \varepsilon_\theta$), the strain is equibiaxial with no splitting in the phonon-mode. For modulating the electronic band structure remarkably, a relatively large strain (>5%) is needed to be developed at the center of a graphene bubble[1,197], which requires the adhesion energy of ~ 1.2 J/m^2. However, the graphene has comparatively less interfacial adhesion with SiO$_2$[198,199] or any other rigid/ solid substrates[200]. Polymeric support or encapsulation may help to achieve larger interfacial adhesion, even for multilayer graphene flakes, for the formation of the blisters of larger aspect-ratio (h/a)[133]. The pressure-difference-driven diffusion of gas molecules along the interface results in the merger of small blisters into bigger ones[182]. Since, an equibiaxial strain develops at the center of a pressurized 2D membrane, viz. given by[165,176]: $\varepsilon = \sigma(\nu)\left(\frac{h}{a}\right)^2$. Therefore, the equibiaxial strain at the center of an air-filled blister of a 2D membrane would vary, as $\varepsilon_{center} \propto \sqrt{\Gamma / E_{2D}}$, and the confinement pressure inside the blister can be given by the following expression:

$$p \propto \frac{E_{2D}}{a} (\varepsilon_{center})^{3/2}. \tag{1.8}$$

A stable out-of-plane deformation of a 2D flake is attained as a result of the competition among the in-plane elasticity (elongation/compression) of the flake, interlayer & interfacial sliding, and the surface tension of the confined matter. Several attempts have been made to understand the out-of-plane bending of the multilayered 2D flakes[23]. The weak vdW interactions between the layers of a 2D multilayer improve its super-lubricity behavior, which thereby stimulates the out-of-plane bending of the flakes in comparison to their in-plane straining. Therefore, the phenomenon of blistering of the multilayered 2D flakes is currently a great surge of interest due to the deterministic but crucial roles of the in-plane elastic stiffness and out-of-plane bending stiffness[24,35,63,133]. Some exciting phenomena on the 2D material blisters, such as the funneling effect and the optical standing waves have also been observed recently[22,177,185,201]. The funneling effect is commonly observed in the blisters of 2D semiconductors (e.g. TMDCs, hBN, GaSe, etc.), wherein the photo-induced excitons drift towards the tip of the blister before recombining radiatively. The 2D semiconductor funnel traps the electron-hole pairs (excitons) and increases their lifetime remarkably against recombination, making them promising candidates for single-photon emission applications[202]. On the other hand, the standing waves (oscillations in Raman G and 2D band intensities and frequencies) form across a graphene bubble due to the interference of incident and reflected laser beams, which generates a series of interference maxima & minima with a distance of $\frac{\lambda}{2}$ between the two maxima. The formation of optical standing waves implies the nonuniform heat distribution in the graphene bubble when illuminated by a laser beam[22].

Indentation with AFM-tip The AFM (atomic force microscopy) tip can be used as a nanoindentation probe to deform the 2D membranes (suspended over patterned substrates, micro-cavities, or metal electrodes) in a controlled manner, which induces a non-homogeneous localized strain. The *in-situ* Raman/PL and electrical measurements are carried out for analyzing the modulated properties of the 2D material upon bending or poking with the AFM tip. While poking a few-layer graphene (FLG) flake suspended over patterned holes on SiN/Si chips with an AFM tip, a continuous redshift in the G and 2D peak frequencies is observed on gradually increasing

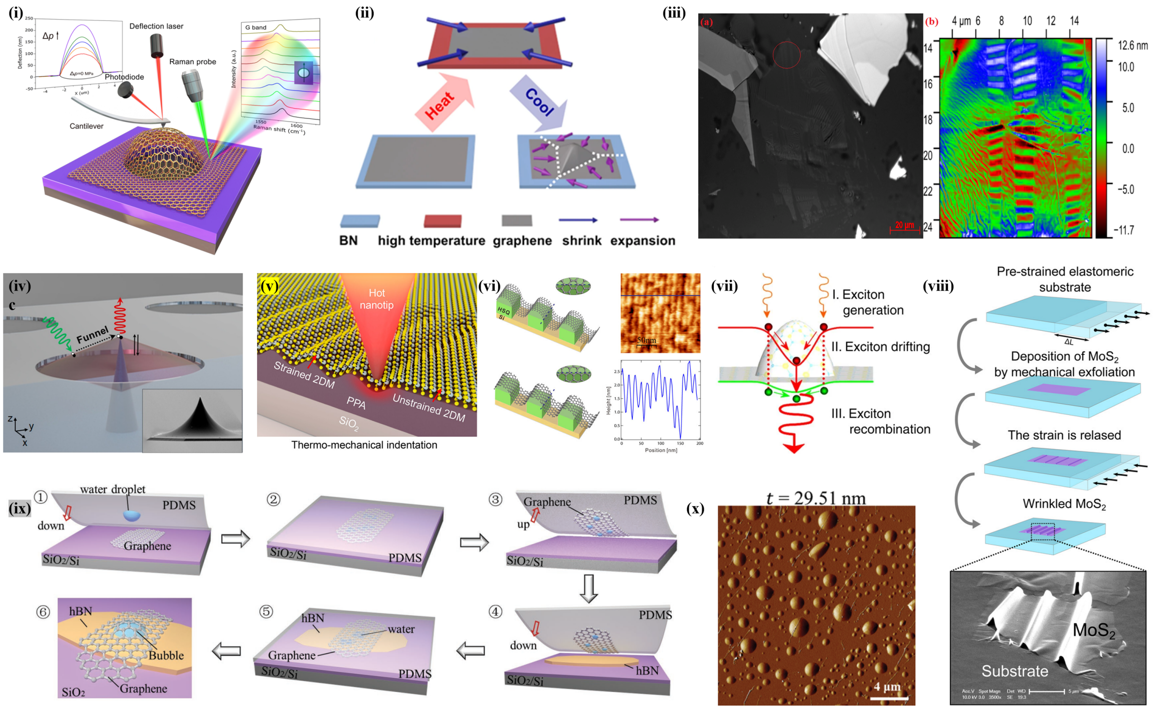
(i)
Deflection laser
Raman probe
Photodiode
Cantilever
G band
(ii)
Heat
Cool
BN
high temperature
graphene
shrink
expansion
(iii)
(a)
(b)
12.6 nm
10.0
5.0
0.0
−5.0
−11.7
(iv)
Funnel
(v)
Hot nanotip
Strained 2DM
Unstrained 2DM
PPA
SiO₂
Thermo-mechanical indentation
(vi)
(vii)
I. Exciton generation
II. Exciton drifting
III. Exciton recombination
(viii)
Pre-strained elastomeric substrate
Deposition of MoS2 by mechanical exfoliation
The strain is relased
Wrinkled MoS2
MoS2
Substrate
(ix)
① water droplet
PDMS
down
Graphene
SiO2/Si
②
PDMS
③ Graphene
up
④ PDMS
down
hBN
⑤ hBN
water
Graphene
⑥ hBN
Bubble
SiO2
Graphene
(x)
t = 29.51 nm
4 µm

Figure 1.14: Techniques for nano/microstructuring of 2D materials[21]. (i) Pressurized bulging; (ii-iii) Thermal-mismatch-induced blisters and wrinkles, respectively; (iv-v) AFM cantilever tip-assisted indentation; (vi) Straining from patterned substrate; (vii) Funneling effect observed at the blister or buckle regions; (viii) Buckling-induced delamination through prestretch-release process; (ix-x) Blister formation due to molecular confinement. Adapted with permission: ©2023, Elsevier Ltd.

the deflection of the FLG membrane, which gets reverted to its original values after the AFM tip is withdrawn[203]. Therefore, AFM-tip-induced straining is highly precise and reversible, provided the membrane is deformed within its elastic limit.

In addition to the local band gap tuning, the out-of-plane deformation of a suspended 2D membrane through nanoindentation with an AFM tip has also been utilized to extract information about its mechanical properties (e.g., Young's modulus, fracture limit, adhesion strength, etc.)[204–208]. It is also possible to control the piezoresistive effect[209] & the exciton funneling effect (mostly in 2D TMDCs) through AFM tip-assisted bending[210]. In addition, a nano-tip can also be used to pattern and deform the 2D flakes (deposited over polymeric[211] as well as SiO_2/Si[212] substrates) in a controlled & precise manner through the application of high mechanical stress. The deformed 2D flake remains in the strained condition even after the removal of the tip-induced mechanical stress, which can be attributed to the strong interfacial adhesion of the 2D flakes to the substrate. However, the mechanical stress can be severely reduced in order to deform a 2D material deposited over a thermosensitive polymer by heating the nanotip. The well-controlled and permanent strain features can be written on different 2D TMDCs and graphene flakes, viz., deposited over thermosensitive deformable polymers, such as polyphthalaldehyde (PPA) and poly(methyl methacrylate) (PMMA), through thermal scanning probe lithography (t-SPL) at a temperature above the glass transition temperature of the respective polymeric substrates[213]. More interestingly, it is possible to control the depth of each indent by adjusting the temperature and the force of the nano-tip.

Substrate induced patterning Any corrugation or roughness on the substrate helps 2D materials conform more closely due to their remarkable stretchability & bendability (flexibility). Therefore, it is difficult to peel off or transfer the adhered 2D flakes from an underlying corrugated substrate. However, this behavior of the 2D flakes is advantageous in terms of transferring the strain from a patterned substrate. Different strained configurations of 2D materials (suspended or supported) can be achieved by using different patterned substrates, as the strain (in accordance with the strain profile of the corrugated substrate) is imposed onto the adhered 2D material from the underlying substrate. As a consequence, the alteration in the physical properties of the 2D material is observed up to the extent of local deformation in its lattice structure. It has been observed that a clean array of periodically strained single atomic layers of MoS_2 on SiO_2/Si pillars, forming the pinched isolated tents of MoS_2 with an unprecedentedly high local atomic biaxial strain value of 3%, shows a direct-to-indirect band gap transition as well as a strong reduction of the band gap[214]. The semimetal-to-semiconductor transition of monolayer graphene with significant shifting in G and 2D Raman modes has also been obtained by its periodic nano-modulation from periodic grid-like nanostructured hydrogen silesquioxane (HSQ)/Si substrate[215]. The development of high biaxial tensile strain values in the highly strained MoS_2 layers over the SiO_2 nanocones leads to an increment in the absorption bandwidth, which enables broadband light absorption[216]. The point-like strain accumulation sites of the atomically thin 2D semiconductor flakes, obtained by transferring the flakes onto the lithographically patterned nanopillar array, result in the local modulation of the band gap as well as the emergence of the exciton funneling effect. The photogenerated excitons funnel from the nanopillar valley (larger band gap regions) towards the nanopillar crest (smaller band gap regions), thereby enhancing the exciton lifetime against recombination, which is highly beneficial for the photodetector applications[217]. The nanopillar crests act as isolated quantum emitters that exhibit high-purity single photon emission[218].

Wrinkling through prestretch-release process The mismatch of elastic modulus between the 2D material and the substrate is utilized to generate an inhomogeneous strain in the 2D material through a prestretch-release process. A desired 2D flake is transferred or deposited onto a highly elastomeric polymer substrate, viz. already pre-stretched by up to ∼ 50% along in-plane[19] or out-of-plane direction[219,220]. The interfacial interactions get modified due to the redistribution of strain on releasing the previously exerted strain in the substrate, which results in the development of the wrinkles of the 2D flake through buckling-induced delamination[221]. The prestretching-induced strain in the elastomeric substrate is defined as $\varepsilon_{pre} = \Delta L/L \times 100\%$, where ΔL is the change in the length of the substrate on stretching with respect to its original length. Using the linear elastic theory, the local strain ε induced at the crest of the wrinkles is related to the height profile, as[19,219,222]

$$\varepsilon \sim \pi^2 h\delta / \left(1-\nu^2\right) \lambda^2 \tag{1.9}$$

where ν is the Poisson's ratio of the 2D flake, h is the thickness of the flake, and δ & λ are the height & width of the wrinkle respectively, which are measured using the atomic force microscopy (AFM). The wavelength of the wrinkles increases linearly with the increasing thickness of the 2D flake[220]. The red-shifting of the positions of Raman peaks (due to localized & accumulated tensile strain) with enhancement in their individual intensities (due to optical interference between the light beam scattered from the sample and the substrate) is observed at the top of the wrinkled structures when compared to that from the flat regions. In addition, an enhancement in the PL intensity is observed at the wrinkled regions of 2D semiconductors, which can be explained by the "funneling effect"[201]. Most of the photogenerated excitons drift towards the crest of the wrinkles, where the local strain (tensile) is maximum and the optical band gap is minimum. Since, the majority of the excitons funnel towards the top of the wrinkle and because of a lesser optical band gap, they recombine to produce the PL emission light with lesser energy. Therefore, the red-shifting of the PL peak position occurs with enhanced PL intensity, which thereby, locally modulates the electronic structure of the 2D semiconductor[222]. Direct tuning of interlayer-coupling in TMDCs hetero-bilayer is possible through the wrinkling process[223]. The interlayer exciton PL intensity decreases nonmonotonically with both the increasing tensile and compressive strains in the wrinkled TMDCs hetero-bilayers in contrast to the monotonic funneling effect observed in the case of the individual single atomic layers during intralayer transitions[223]. The conformal wrinkling technique can modulate the local properties of a 2D material by changing the wavelength and switching the orientation of the nano-wrinkles with reversible tensile strain[38,224].

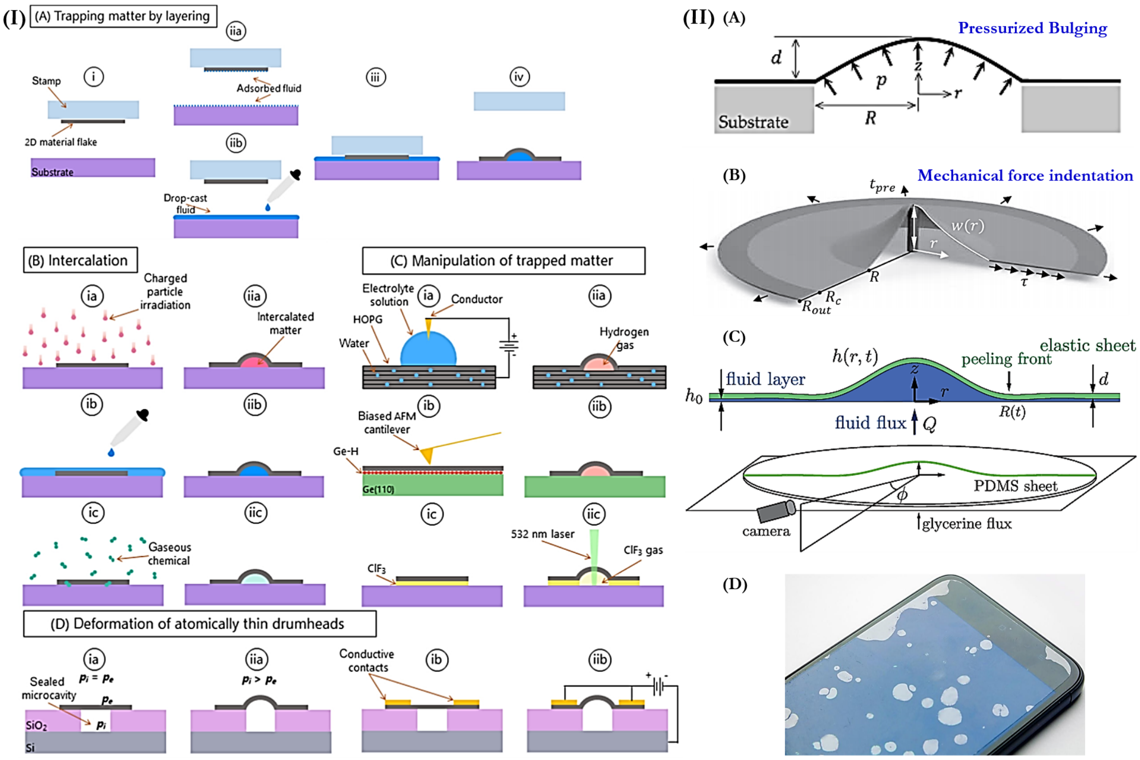
(I)
(A) Trapping matter by layering
Stamp
2D material flake
Substrate
Adsorbed fluid
Drop-cast fluid
(B) Intercalation
Charged particle irradiation
Intercalated matter
Gaseous chemical
(C) Manipulation of trapped matter
Electrolyte solution
Conductor
HOPG
Water
Hydrogen gas
Biased AFM cantilever
Ge-H
Ge(110)
532 nm laser
ClF_3
ClF_3 gas
(D) Deformation of atomically thin drumheads
Sealed microcavity
$p_i = p_e$
$p_i > p_e$
p_e
p_i
SiO_2
Si
Conductive contacts
(II) (A)
Pressurized Bulging
d
p
z
r
R
Substrate
(B)
Mechanical force indentation
t_{pre}
$w(r)$
r
R
R_c
R_{out}
τ
(C)
$h(r,t)$
elastic sheet
peeling front
fluid layer
h_0
z
r
d
fluid flux
Q
$R(t)$
PDMS sheet
ϕ
camera
glycerine flux
(D)

Figure 1.15: (I) Blistering techniques utilized for 2D materials[24]: (A) trapping matter by layering, (B) intercalation of molecules, (C) manipulation of trapped matter, (D) deformation of atomically thin drumheads. Adapted with permission: ©2021, Elsevier Ltd. (II) Blistering techniques utilized for elastomeric or plastic sheets: (A) pressurized bulging[25], adapted with permission: ©2021, Elsevier Ltd., (B) mechanical force indentation[26], adapted with permission: ©2020, Elsevier Ltd., (C) fluid-flux driven debonding (two-phase fluid flow model)[27], adapted with permission: ©2013, American Physical Society, (D) spontanesously formed air-filled bubbles on a screen-protector plastic sheet, adapted from internet.

1.6.2 Blistering instabilities in elastomeric sheets and 2D materials

The techniques for blistering of elastomeric sheets are similar to that of 2D materials (see Figure 1.15). In the micromechanical hot exfoliation process, there is a finite probability of the formation of bubbles (circular blisters) in 2D flakes at the raised temperature, however, the bubbles continue to change their shapes due to the phase-transition of the confined gas molecules with temperature as a result of condensation or intake of water molecules from humid environment[2,36]. Consequently, the instabilities may arise in the bulged elastic sheet over a rigid substrate, which is, therefore, called elastic solid-based instability[34,195]. The mechanical indentation-induced blister of a plastic sheet over a liquid layer (the liquid blister-test) shows a dynamical evolution of the blister shape by varying the indentation height keeping the thickness of the sheet constant (see Figure 1.16(i-ii)). There are several daily-life examples having the wrinkling or crumpling instabilities, occurring either due to mass-loss or physical compression (see Figure 1.17). Recently, Ares *et al* reported the wrinkling instability around the perimeter of 2D material bubbles over 2D crystal substrates[36] (see Figure 1.18(iv)). It became possible to induce a substrate-based instability in 2D material blister systems by replacing the solid substrate with a viscoelastic substrate[62,63,225]. The viscoelastic substrate-based instabilities develop due to displacement of more viscous fluid by a less viscous fluid while debonding of a rigid or elastic sheet. The pressurized or mechanical debonding of a rigid or elastomeric sheet from a viscous surface may give rise to onset of viscous fluid-mechanical instabilities (see Figure 1.16(iii-vi)). The competitive interplay between the viscous stresses and the bending stresses determines the strength of fluid-structure interactions, which plays a crucial role in the onset of viscous fingering instabilities in 2D material blisters over a viscoelastic substrate[63].

Viscous fingering is a fluid dynamical phenomenon that occurs when a less viscous fluid displaces a more viscous fluid in a confined space. In the context of an elastic-walled Hele-Shaw cell[27,30,226], which is a simplified experimental setup used to study fluid flows, this phenomenon leads to the development of intricate and branching patterns resembling fingers or fractals. The viscous fingering patterns mostly arise in out-of-plane debonding of a stiff plate from a viscous surface by different ways such as the vertical mechanical delamination, peeling-off, pressurizing at the interface, etc. In this case, the less viscous fluid, i.e., air displaces the more viscous fluid during the movement of the upper-bounding plate.

The viscous fingering instability can be suppressed by replacing the stiff plate with an elastic membrane in a Hele-Shaw cell[227] (see Figure 1.16(iii, iv)). An elastic-walled Hele-Shaw cell is utilized in order to investigate the evolution of viscous fingering patterns in the two-phase fluid flow model by varying the elasticity of the plate and the flux-driven pressure. An elastic-walled Hele-Shaw cell consists of two parallel, closely spaced transparent plates or walls. These walls can deform or move in out-of-plane direction under the effect of flux-driven pressure due to their elasticity. The narrow gap between the walls represents the confined space where the displacement of the viscous fluid takes place. The cell is usually filled with two immiscible fluids: a more viscous fluid (e.g., oil) and a less viscous fluid (e.g., air or water). When the less viscous fluid is injected into the Hele-Shaw cell, it displaces the more viscous fluid. Due to the confinement between the walls, the fluids flow in the narrow gap

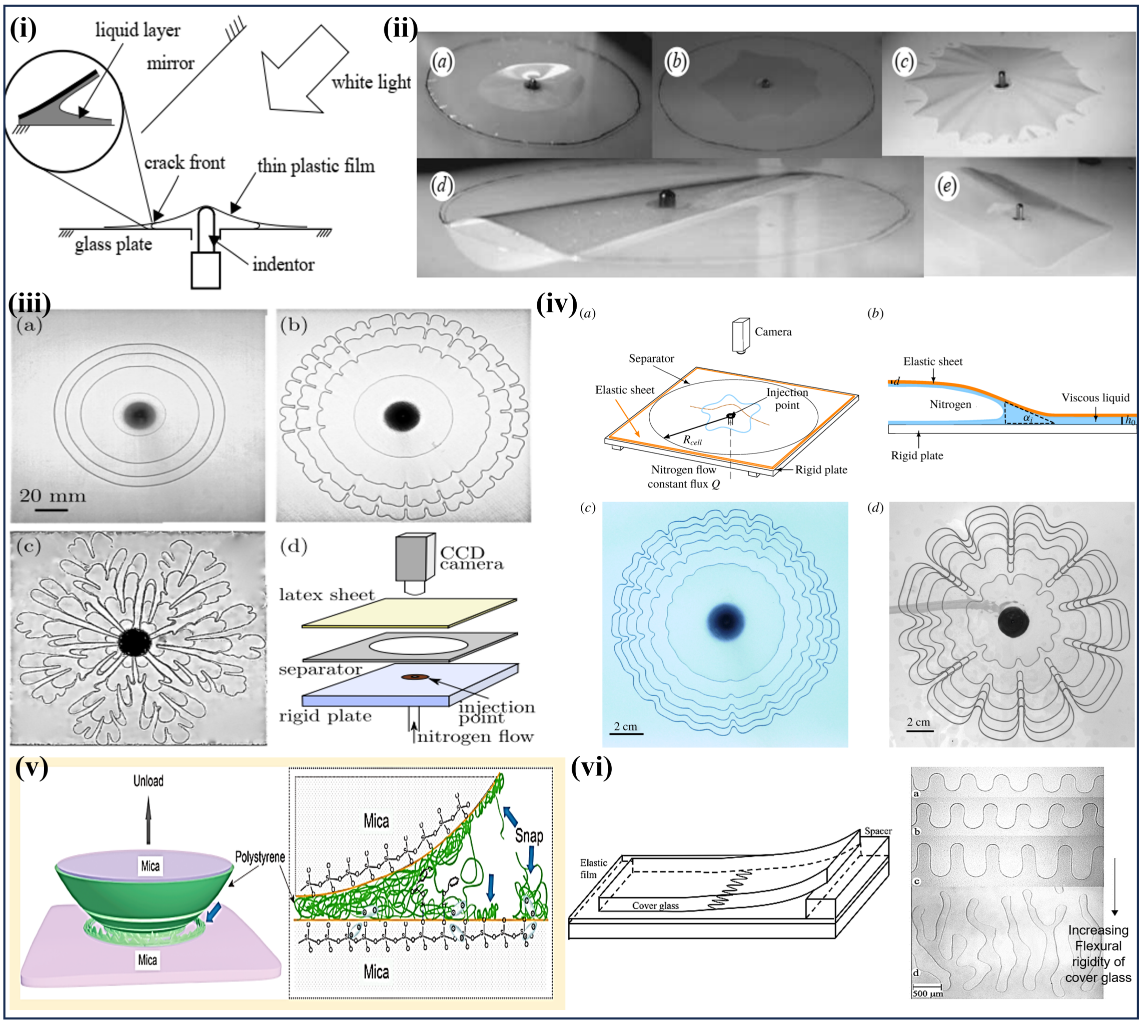
(i)
liquid layer
mirror
white light
crack front
thin plastic film
glass plate
indentor
(ii)
(a)
(b)
(c)
(d)
(e)
(iii)
(a)
20 mm
(b)
(c)
(d)
CCD camera
latex sheet
separator
rigid plate
injection point
nitrogen flow
(iv)
(a)
Camera
Separator
Elastic sheet
Injection point
R_{cell}
Nitrogen flow constant flux Q
Rigid plate
(b)
Elastic sheet
Nitrogen
Viscous liquid
α
h_0
Rigid plate
(c)
2 cm
(d)
2 cm
(v)
Unload
Mica
Polystyrene
Mica
Mica
Snap
Mica
(vi)
Elastic film
Cover glass
Spacer
a
b
c
d
500 μm
Increasing Flexural rigidity of cover glass

Figure 1.16: Blistering instabilities in elastic/plastic sheets. (I) Elastic solid-based instability. (i-ii) Mechanical force indentation induced instability: (i) The liquid blister test, where a plastic sheet is subjected to a mechanical force indentation. (ii) The solid-based instability arise in the blister depending on the indentation height to sheet thickness ratio[28]. Adapted with permission: ©2008, The Royal Society. (II) Viscous fluid-based mechanical instabilities. (iii-iv) Pressurized blistering: (iii) Viscous fingering patterns in the Hele-Shaw cell can be suppressed by replacing the upper-bounding rigid plate with an elastic membrane[29]. The transition from an unstable interface to stable interface ($c \to b \to a$) occurs under the variable elasticity of the latex sheet. Adapted with permission: ©2012, Americal Physical Society. (iv) The dynamical evolution of viscous fingering patterns can be visualized in elastic-walled Hele-Shaw cell under varying injected Nitrogen gas flux-driven pressure[30]. Adapted with permission: ©2018, Cambridge University Press. (v) Vertical mechanical debonding of upper bounding rigid plate from a viscous medium results in the development of viscous fingering patterns at the interface[31]. Adapted with permission: ©2016, American Chemical Society. (vi) Peeling of an upper-bounding elastic cover sheet from a viscoelastic surface develops viscous fingering pattern, which depends on the bending rigidity of the elastic sheet. The finger-length increases with the bending rigidity of the cover sheet[32]. Adapted with permission: ©2000, American Physical Society.

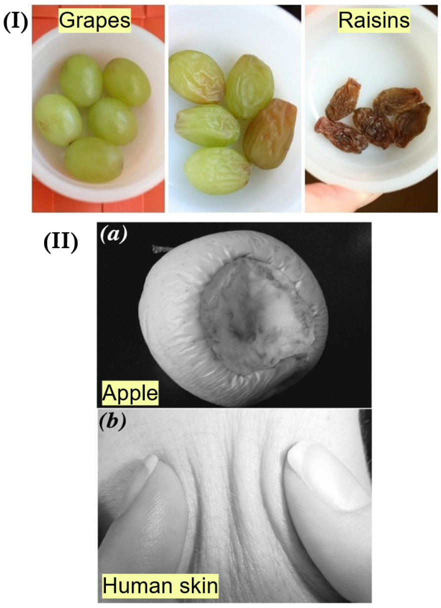

Figure 1.17: Crumpling and wrinkling instabilities in daily-life examples: (I) transition from grapes to raisins due to mass-loss as a result of drying, adapted from internet, and (II) wrinkles in the apple-skin due to mass-loss (a), and wrinkles in human-skin due to compression[33] (b), adapted with permission: ©2003, Americal Physical Society.

between the plates. However, the flow is not always smooth and uniform; instead, it can become unstable and form patterns[225]. The instability arises from the difference in viscosity between the two fluids and the confinement of the cell. As the less viscous fluid advances into the more viscous fluid, it tends to penetrate faster along certain paths, creating finger-like protrusions. These fingers grow and branch out over time, leading to complex patterns[228] (see Figure 1.16). The instability can be understood through a competition between viscous forces and capillary forces. Viscous forces tend to spread the fluids uniformly because of viscosity difference, while capillary forces, which are related to surface tension, tend to pinch off the less viscous fluid into fingers. The elasticity of the cell walls plays a crucial role in enhancing the instability. As the less viscous fluid pushes against the cell walls, it can cause the walls to deform slightly. This deformation can amplify the fingering instability, leading to even more pronounced patterns. The deformable walls due to their elasticity introduce an additional degree of complexity to the system, affecting the way the fingers grow and interact.

The thickness-dependent elasticity of the 2D materials is beneficial for the dynamical evolution of the viscous fingering patterns. The elastic solid- as well as viscoelastic substrate-based instabilities have been observed in the spontaneously formed blisters

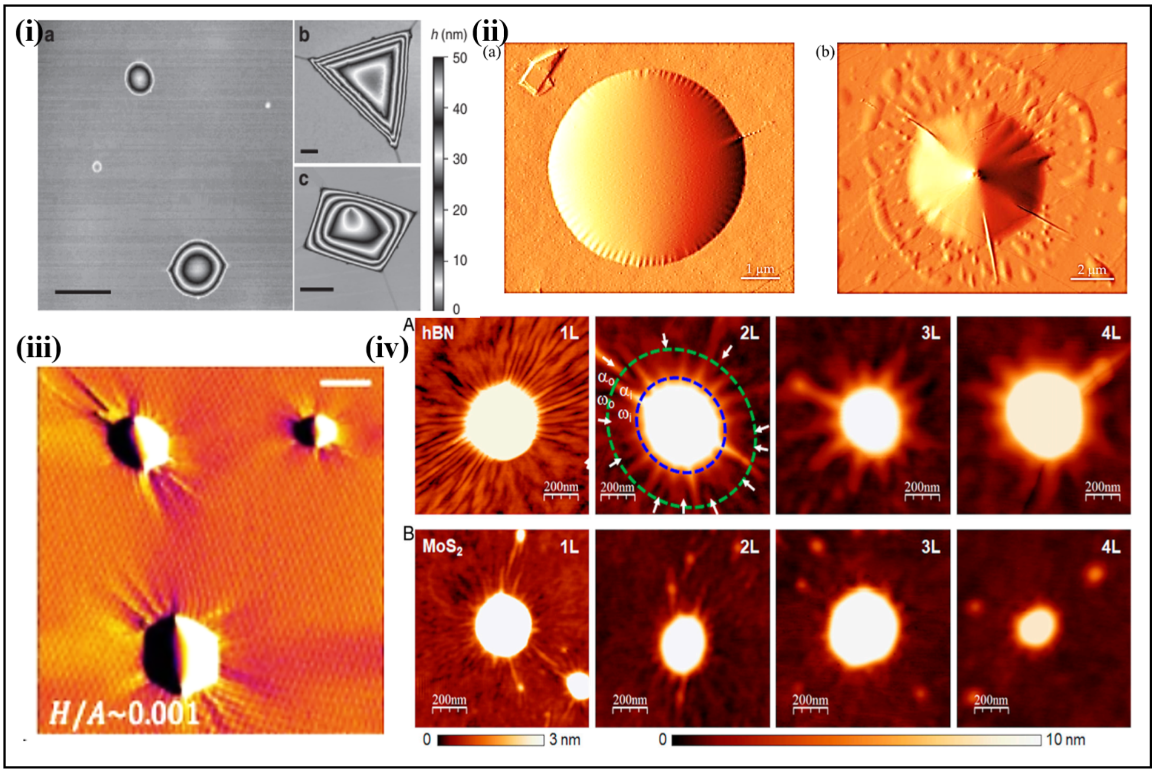

Figure 1.18: Blistering instabilities in 2D elastic nanosheets. (i) AFM images of graphene bubbles of different shapes on bulk hBN substrate resulting from the annealing process (at ∼ 150°C for 20-30 min), scale bars: 500 nm, 100 nm, and 500 nm, respectively for a, b, and c[34]. Adapted with permission: ©2016, Springer Nature Ltd. (ii) AFM amplitude images of a bilayer graphene bubble and a multilayer graphene tent, which result from the micromechanical hot exfoliation process[25]. Adapted with permission: ©2021, Elsevier Ltd. (iii) AFM deflection image of ethanol nanopockets formed due to confinement of ethanol molecules in between two monolayers of graphene, scale bar: 100 nm[35]. Adapted with permission: ©2021, Springer Nature Ltd. (iv) AFM topographic images showing wrinkle patterns around the perimeter of bubbles of hBN and MoS_2 flakes on graphite substrate[36]. Adapted with permission: ©2021, AAAS.

of graphene multilayers[63]. It is also possible to see the concurrence of both types of instabilities in the 2D material blisters[229]. It is to be noted that the coupling of the both types of instabilities in the blistering of thin elastic/plastic sheets has already been modelled numerically, but not realized experimentally[37] (see Figure 1.19). Therefore, such a phenomenon is extremely unique and novel for the 2D material blisters.

The wrinkling of a 2D elastic sheet depends on the its bending stiffness and the substrate-induced stiffness or the interfacial tension. As per the available literature reports, Zhaohe Dai *et al* observed the wrinkling instability for the first time in 2D

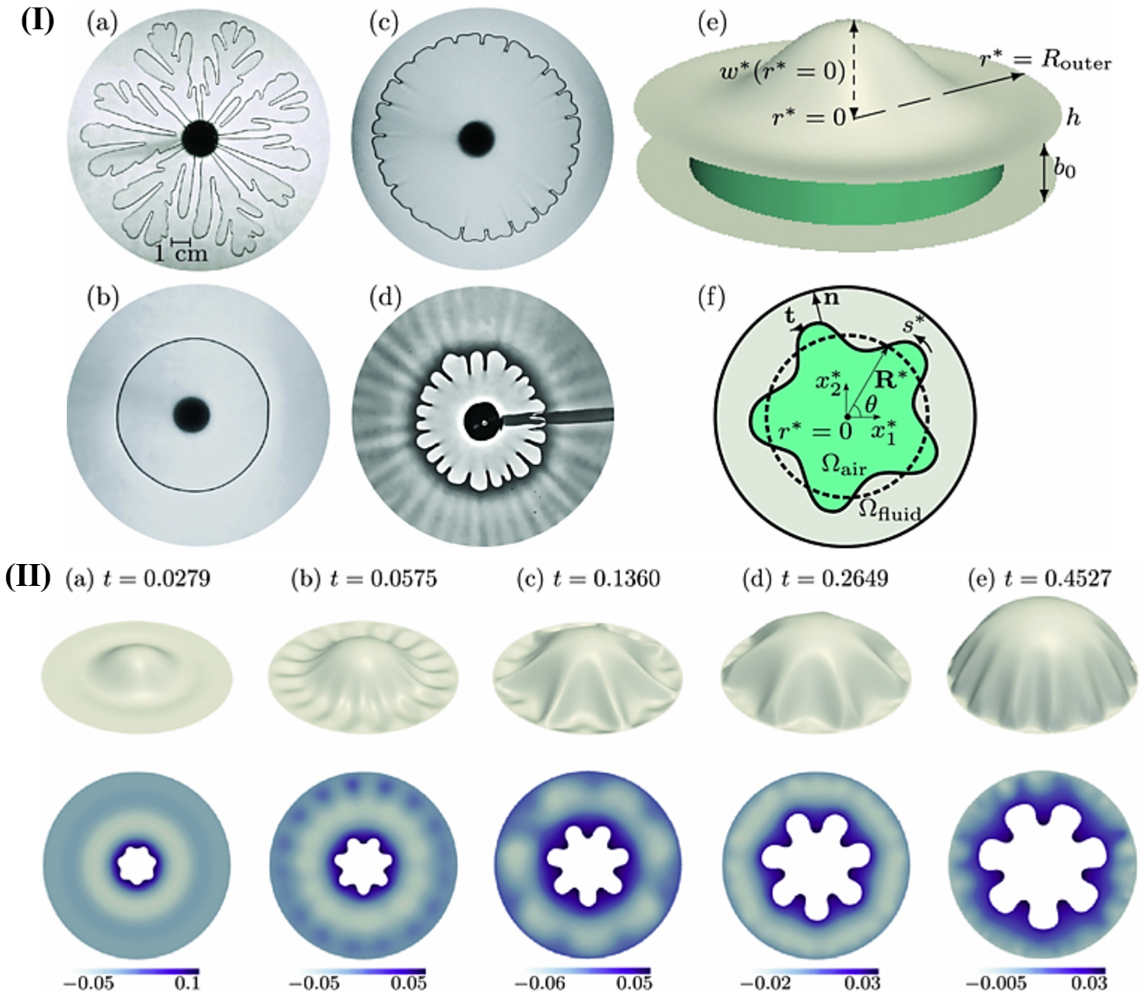
(I)
(a)
1 cm
(c)
(e)
$w^*(r^*=0)$
$r^* = R_{\text{outer}}$
$r^*=0$
h
b_0
(b)
(d)
(f)
$\mathbf{t}$
$\mathbf{n}$
s^*
x_2^*
$\mathbf{R}^*$
θ
$r^*=0$
x_1^*
Ω_{air}
Ω_{fluid}
(II)
(a) $t = 0.0279$
(b) $t = 0.0575$
(c) $t = 0.1360$
(d) $t = 0.2649$
(e) $t = 0.4527$
−0.05 0.1
−0.05 0.05
−0.06 0.05
−0.02 0.03
−0.005 0.03

Figure 1.19: (I) Viscous fingering instability in an elastic-walled Hele-Shaw cell resulting from two-phase fluid flow. (II) Coupled instability (concurrence of elastic solid-based wrinkling instability and viscous fingering instability) in elastic-walled Hele-Shaw cell, which is driven by fluid-structure interaction parameter[37]. Adapted with permission: ©2014, AIP Publishing.

material blisters[196], however, the study of the mechanism behind the onset of such an instability remained unexplored. Recently, Ares *et al* investigated the physics and mechanics behind such an observation in hBN and MoS_2 blisters over another 2D crystal as a substrate[36]. The variation in the environmental conditions acts as a crucial factor for the onset of the wrinkling instability. Diffusion of water molecules from a humid atmosphere could be a possible reason. It has been observed that the wrinkling instability in the 2D material blisters is more pronounceable for single-to-few layers of the 2D material[25,36,196]. Such an instability disappears for the larger number of layers due to increased bending stiffness. However, in the 2D material blisters with larger number of layers, the tent-like or pyramidal instabilities are observed[196,230].

It is therefore, interesting to understand the mechanism behind the onset of such instabilities.

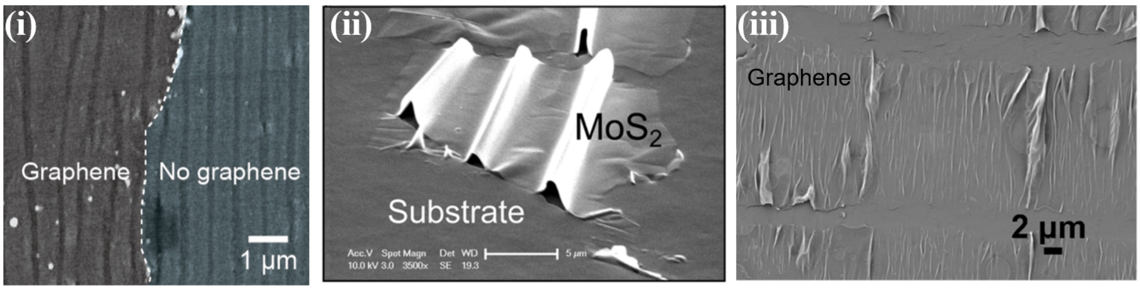

Figure 1.20: Buckling instabilities in 2D elastic nanosheets (SEM images). (i) Conformal graphene wrinkles on CF$_x$-coated PDMS substrate. Graphene is transferred to a prestretched PDMS substrate (30% prestrain) coated with a CF$_x$ layer, and then the prestrain is released to form the conformal wrinkles[38]. The CF$_x$ layer prevents the interfacial contact failure in the graphene layer under larger compressions. Adapted with permission: ©2020, American Chemical Society. (ii) Buckling-induced delamination or buckles of MoS$_2$ monolayer over PDMS substrate (initial prestrain level $\sim$ 50%))[19]. Adapted with permission: ©2013, American Chemical Society.(iii) Graphene folds over the PDMS substrate resulting from the prestretch-release process (prestrain level $\sim$ 50%)[39]. Adapted with permission: ©2015, Elsevier Ltd.

1.6.3 Buckling instabilities in 2D materials

Wrinkles usually form at lower compression levels during the prestretch-release process due to Young's modulus mismatch between 2D material and the underlying flexible substrate (see Figure 1.20(i)). However, at larger compressions, the wrinkles delaminate to form the buckles, which thereby collapse to form the folds[43,231,232] (see Figures 1.20(ii-iii), and 1.21). Therefore, folding instability is inevitably observed in 2D elastic nanosheets under larger compressions[64,233]. Such buckling instabilities result from the interfacial sliding and the contact failure. Suppression of non-conformal folding instabilities in 2D material monolayer over a soft substrate in the buckling process may be beneficial for flexible electronic applications.

The conformal adhesion of 2D elastic nanosheets over the rough or corrugated soft substrates can be achieved easily in comparison to similar rigid/solid substrates. The mechanically induced pressure during the tape-assisted deposition of a 2D elastic membrane (likewise few layer graphene flake, shown in Figure 1.22(i)) deforms the corrugated soft substrate such that its corrugation amplitude decreases and the corrugated wavelength increases making the soft substrate shallower. Such a morphology of the elastomeric substrate favors the snap-through transition (a kind of instability, which allows a flat state of an elastic membrane over a corrugated substrate to

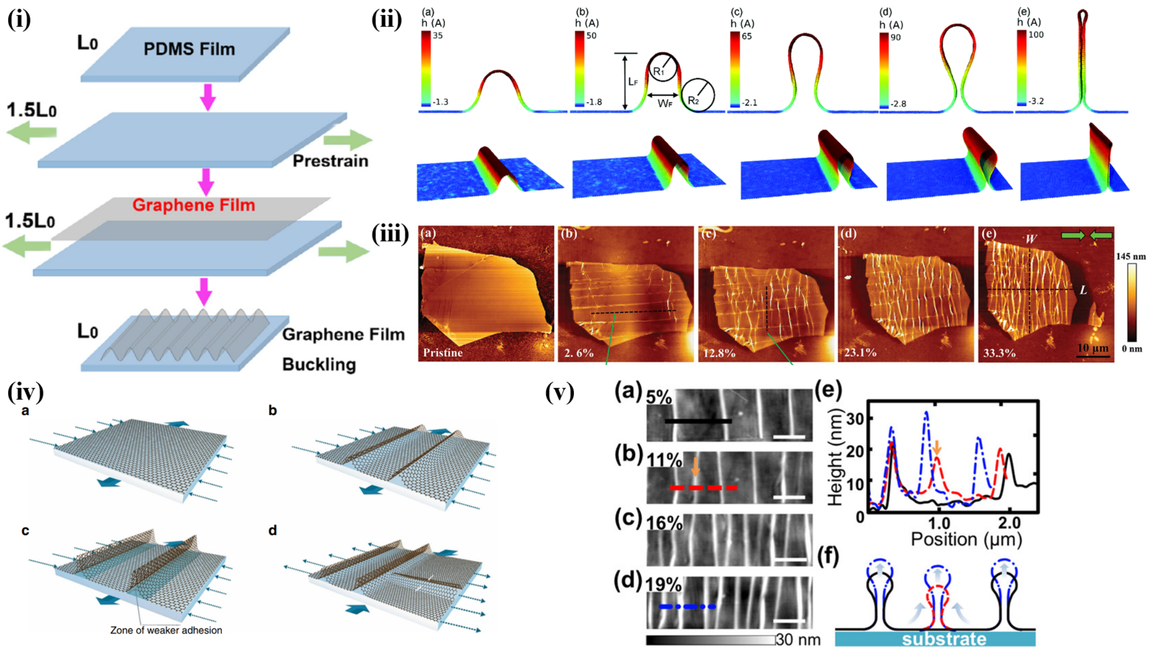
(i)
L0
PDMS Film
1.5L0
Prestrain
Graphene Film
1.5L0
L0
Graphene Film
Buckling
(ii)
(iii)
Pristine
2. 6%
12.8%
23.1%
33.3%
10 μm
145 nm
0 nm
(iv)
Zone of weaker adhesion
(v)
(a) 5%
(b) 11%
(c) 16%
(d) 19%
30 nm
(e)
Height (nm)
Position (μm)
(f)
substrate

Figure 1.21: Development of wrinkling instability in 2D elastic nanosheets over smooth elastomeric substrate as a result of compression while releasing the prestrain. (i) Buckling-induced delamination in graphene through the prestretch-release process[39]. Adapted with permission: ©2015, Elsevier Ltd. (ii) Buckle to fold transition in graphene under compression[40]. Adapted with permission: ©2017, RSC Publishing. (iii) Topographical evolution of graphene (~ 4 layers) on PDMS substrate during uniaxial compression[41]. Adapted with permission: ©2023, Wiley-VCH GmbH. (iv) Evolution of a simply supported graphene membrane on PMMA substrate under uniaxial compression. The buckles collapse to form folds due to interfacial slippage. Beyond a critical compressive strain, the mosaic patterns form[42]. Adapted with permission: ©2019, Springer Nature Ltd. (v) Topographical evolution of MoS_2 folds under increasing compression (scale bar: 1 μm)[43]. Adapted with permission: ©2020, American Chemical Society.

transition into a slightly conformal but wavy state), thereby increasing the interfacial adhesion of the membrane. However, the adhesion decreases with increasing number of layers (or, the bending stiffness). The suppression of buckling or folding instability is advantageous for various practical applications such as strain sensors.

1.7 Applications

The straining techniques utilized to form the strained nano/microstructures of 2D materials have huge scope to achieve the maximum strain limits for the larger degree of freedom towards strain engineering applications[21] (see Figure 1.23). The strain-engineered 2D materials have potential applications in the efficient detection of light, strain/pressure, or gas molecules. Furthermore, the strained nano/micro-

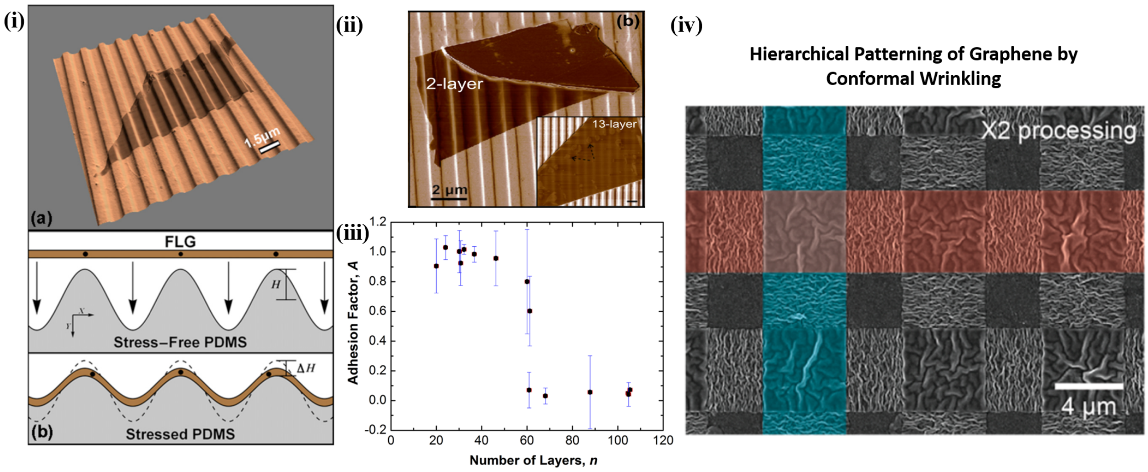

Figure 1.22: (i) Superimposed AFM height and phase data showing the conformal wrinkling of few layer graphene (FLG) on a corrugated PDMS substrate (a), schematic showing the interaction of FLG with the corrugations while downward pushing, which leads to conformal adhesion of FLG in stressed condition (b). This illustrates the 'snap-through transition' in FLG, where FLG snaps between two distinct states, i.e., conformal and nearly flat on the substrate surface under the effect of external stress. (ii) AFM phase image showing the conformally adhered bilayer graphene, and less conformed 13-layer graphene, which depicts the suppression of 'snap-through instability' for thicker graphene flakes[44]. Adapted with permission: ©2011, AIP Publishing. (iii) Adhesion factor (A), i.e. ratio of peak-to-peak amplitudes of the graphene and substrate, where A = 1 represents the fully conformal state whereas A = 0 represents the flat state. For the number of layers ∼ 61, a sharp transition between the states occurs[45]. Adapted with permission: ©2012, AIP Publishing. (iv) Hierarchical patterned graphene wrinkles (SEM image) having conformal adhesion with polystyrene (PS) substrate coated with a soft CF_x layer formed by CHF_3 plasma-mediated polymerization of the PS substrate using double masking process[46]. Adapted with permission: ©2016, American Chemical Society.

structures of 2D materials can be utilized as tools to probe their mechanical as well as adhesion properties. The adhesion characteristics of 2D materials with various solid or soft substrates must be known prior to the micro/nanofabrication of (opto)electronic devices utilizing 2D materials and their heterostructures. By analyzing the nano/microstructures of 2D materials over the desired substrates, such information can be retrieved.

Strain-engineered piezoelectric 2D materials can be widely used for flexible piezo-(photo)tronic devices with improved performance. The merger of straintronics with twistronics in 2D vdW homo- and hetero-bilayers offers a plethora of opportunities to design new exciting magic angle superlattices having exotic properties. The strain engineering of a 2D bilayer at an arbitrary relative angle of rotation helps in attaining

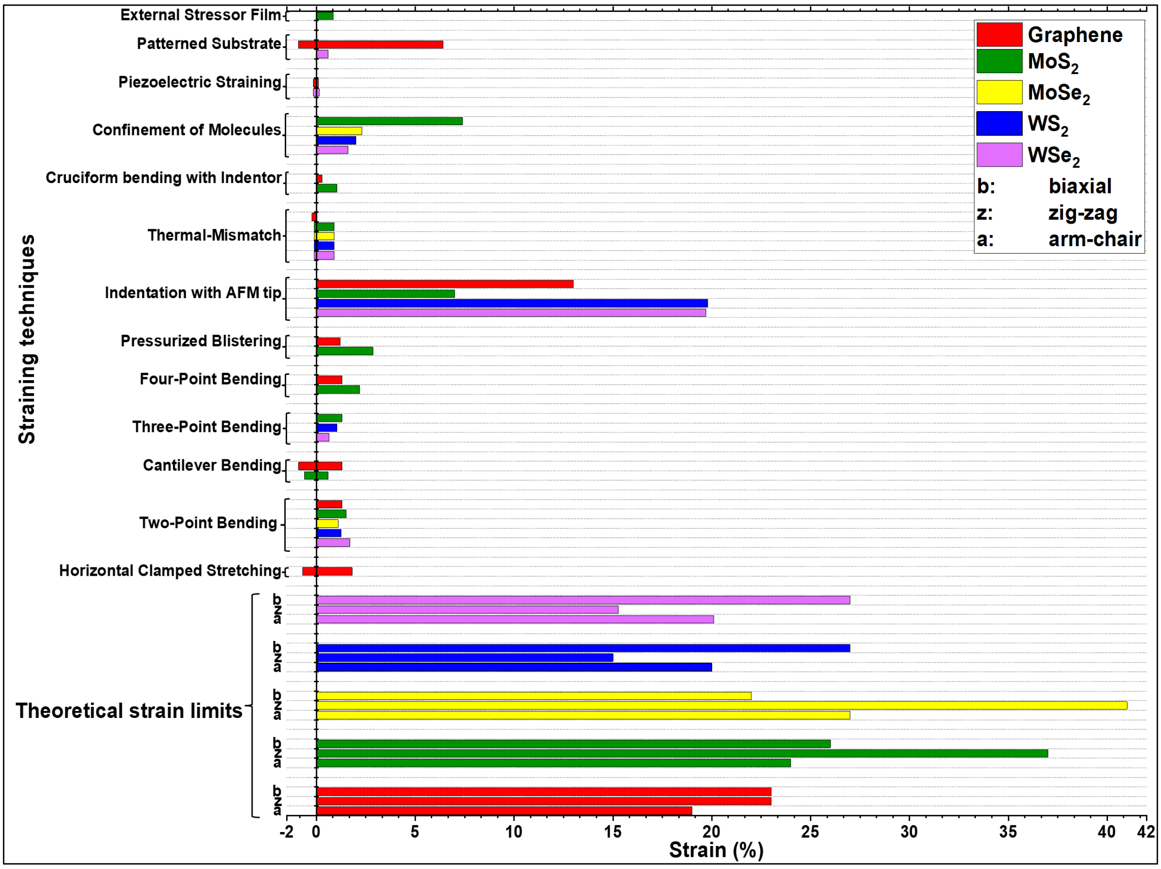

Figure 1.23: A graphical representation depicting the experimentally achieved applied strain limits for different straining techniques before device failure, and the theoretical intrinsic strain limits of 2D materials[21]. Adapted with permission: ©2023, Elsevier Ltd.

the relatively small magic angle, where the exotic states of strongly correlated electronic systems emerge. Furthermore, the strain-engineered kirigami patterns of 2D materials on soft substrates provide enormous potential for tunable optoelectronics.

The strained (wrinkled, crumpled, or buckled) sites of 2D materials provide more active sites for the extruding agents (strain/pressure) or the analyte gas molecules. In addition, the lifetime of photo-generated charge carriers against the recombination also increases at the strained sites, which enhances the photo-current under photo-illumination. The strain engineering of 2D materials can also be exploited for improving the performance of the photovoltaic cells[234–236] as well as energy storage devices[237]. Moreover, the strained 2D semiconductors can also be exploited for single-photon emitters, where the enhancement in spontaneous emission of light is attributed to the ‘funneling effect’[218,238]. The most promising candidates for broadening the light absorption range of solar cell devices are tunable band gap materials. The strain-driven absorption coefficient modulates the photon-electron interactions in order to achieve improved energy conversion efficiency[239]. Feng *et al*[240] showed that the locally strained MoS_2 monolayers, forming the ‘artificial atoms’, absorb a wide range of the solar spectrum (2-1.1 eV) under varying biaxial strain ranging from 0-9%. As a proof-of-concept, Hong Li *et al*[216] reported a broadband light absorption from 677 nm (pristine MoS_2) to 905 nm (highly strained MoS_2) in a photovoltaic device based on MoS_2 ‘artificial atoms’. The physical insights into the local strain development and the instabilities in blistering and buckling would be beneficial for both fundamental research and meticulous applications of strained 2D materials[132,241].

Chapter 2

Blistering of a 2D crystal over a viscoelastic substrate

2.1 Introduction

Graphene is the most flexible material having remarkable electronic and optical properties, which can sustain an in-plane elastic tensile strain up to $\sim$ 25%, whereas silicon typically breaks even at a strain level of $\sim$ 1.5%[60,242,243]. Because of highly strain-sensitive properties and large strain-bearing capacity, the global and local strain engineering of 2D materials has undergone tremendous interest[238,244]. There are many ways to apply global strain in 2D materials using different straining techniques such as uniaxial straining[245], cantilever bending[246], horizontal[247] & vertical pushing[109,248] etc., but local strain engineering in 2D materials is more challenging[19]. However, several techniques like laser-induced local heating[249], bending with AFM tip[203], and pressurized bulging[250] techniques have been employed for local straining, which show significant modulations in the physical properties of the 2D materials.

The everlasting demand for mechanically exfoliated graphene or similar 2D flakes has driven a search for efficient 2D material exfoliation techniques. The PVA-assisted exfoliation (PAE) and the modified conventional or micromechanical hot exfoliation (MHE) techniques are the most promising candidates in terms of the deposition yield, which consists of large areas of single or few-layer graphene flakes[88,251]. The synthesis & processing, as well as the atmospheric conditions, while using an exfoliation/transfer technique, play a key role in the formation of the blisters on the surface of the exfoliated 2D flakes. The 2D material blisters are either formed intentionally or induced spontaneously[24]. The spontaneously formed blisters are inevitably observed while transferring 2D materials onto a flat[2,22,176–178] or patterned substrate[179] due to aggregation and trapping of naturally adsorbed surface matter or interfacial contamination into the blisters. On the other hand, intentionally induced blisters are formed in different ways such as intercalation of molecules by diffusion[180,181] or charged particle irradiation[182–184], physical manipulation of confined matter[187,189–192,252] and pressurized bulging of atomically thin drumheads[165,193,194].

Blisters may be formed in 2D flakes by trapping a matter at the interface of the flake and a substrate supporting the 2D flakes. Since, the shape of the 2D material blisters depends on the nature of the trapped substance[195,253], therefore the investigation of the confined material inside the blister is essential to understand the involved physics and chemistry. Several efforts to investigate the phase (liquid/ gas) of the contents confined inside the blisters are reported in the literature, mostly on the basis of synthesis and atmospheric conditions under which the blisters form and deflate[34,120,254–256]. Furthermore, the time-dependent deflation rate[193,194,257] and AFM tip assisted scratching & bursting of the blisters[258] are noticeable approaches to get the compositional insights of the confined matter. However, direct characterization of the blister content is still a big challenge. Recently, Beng hau Tan *et al* strategically ruptured a blister using AFM tip to investigate the internal composition of MoS_2 nanoblisters[259].

In the 2D material blisters, the elasticity of the 2D material and the van der Waals (vdW) interactions between the adjoining surfaces help in pressurizing the confined matter appreciably, which can be utilized for exploring the high-pressure physics[35,193]. The interlayer slippage, adhesion energy & shear strength of the 2D material-substrate interface, and the bending & stretching stiffness of the 2D material affect the mechanical response of the 2D material-blister system. The locally strained 2D material or pressurized blisters have been extensively exploited for deducing the mechanical properties (such as bending rigidity, Young's modulus, interfacial adhesion energy, etc.) of the graphene or any other 2D material using membrane and non-linear plate theories[260–262]. The membrane model is employed for the bubbles with $\frac{h}{\tau} \gtrsim 2$ (h: height of the bubble & τ: thickness of the flake) while the nonlinear plate model for $\frac{h}{\tau} \lesssim 1.5$. The out-of-plane bending stiffness dominates over the in-plane stiffness of an elastic film or vice versa, are treated as a non-linear elastic plate or a membrane, respectively[1,23].

In general, the presence of blisters on the surface of 2D materials affects the device performance severely, and this issue has enabled new opportunities for deducing the origin and physics behind the role and significance of the blisters. The properties of the 2D material can be tuned by engineering the shape & size of the blisters by trapping different types of liquids of different surface energies[195]. The blister density can severely modify the carrier transport properties of the 2D flakes[263]. The mechanism of obtaining locally strained 2D structures or blisters is utilized for obtaining light-emitting "artificial atoms"[264]. The graphene nanobubbles also demonstrate strain-induced enormous pseudo-magnetic field greater than 300 Tesla, which shows a method to control the electronic structure of graphene even at room temperature[265]. Furthermore, a circular blister with a controllable shape is a possible candidate for its use in optical lenses with variable focal length[253]. Recently, the elasticity of the confining membrane and the capillarity of the confined fluid in the nanopockets have been utilized to develop self-cleaning ability in the vdW material interfaces[35]. Despite extensive efforts, the study of out-of-plane deformation behavior of multilayer van der Waals (vdW) materials under a local strain is currently a great surge of interest[23,196,266].

In this chapter, we focus on a simple but strategic approach to develop sub-micron blisters by thermally manipulating the supporting polymeric-layer content underneath mechanically exfoliated single-crystal multilayer graphene flakes for modulating their vibrational properties. The detailed optical, morphological, and spectroscopic investigations along with the temperature-dependent dynamics[192] of the blisters reveal the nature of the confined matter inside the sub-micron blisters. Our technique provides a vital platform for local strain engineering of 2D multilayer, where the bending rigidity plays a crucial role in determining its interfacial adhesion energy.

2.2 Experimental methods

2.2.1 Preparation of PVA-coated substrates

Prior to the exfoliation experiments, borosilicate glass or Pyrex (Borofloat®, RMS Roughness < 1 nm) substrates are thoroughly cleaned in trichloroethylene, acetone, and methanol, each for 10 min at their respective boiling temperatures and then rinsed in isopropyl-alcohol and DI water. The glass substrates are placed overnight in a vacuum desiccator for drying and, thereafter, cleaned with oxygen plasma for ~ 5 min. A cleaned borosilicate glass substrate is spin-coated with 4% w/w PVA solution (prepared by dissolving PVA powder (Alfa Aesar™, 86-89% hydrolyzed, av. Mw $\sim$ 10,000) in DI water) at a spin speed of 1600 rpm for 60 s.

2.2.2 2D material exfoliation and PVA curing assisted blistering

A Nitto tape decorated with thin flakes of graphite is placed in a conformal contact and pressed softly on the PVA(uncured)-coated glass substrate at room temperature, followed by a brief heat treatment at ∼ 120°C for 60 s on a hot plate. Thereafter, the sample is allowed to cool down to room temperature. The Nitto tape is then peeled off slowly, starting from one end of the substrate (Figure 2.1).

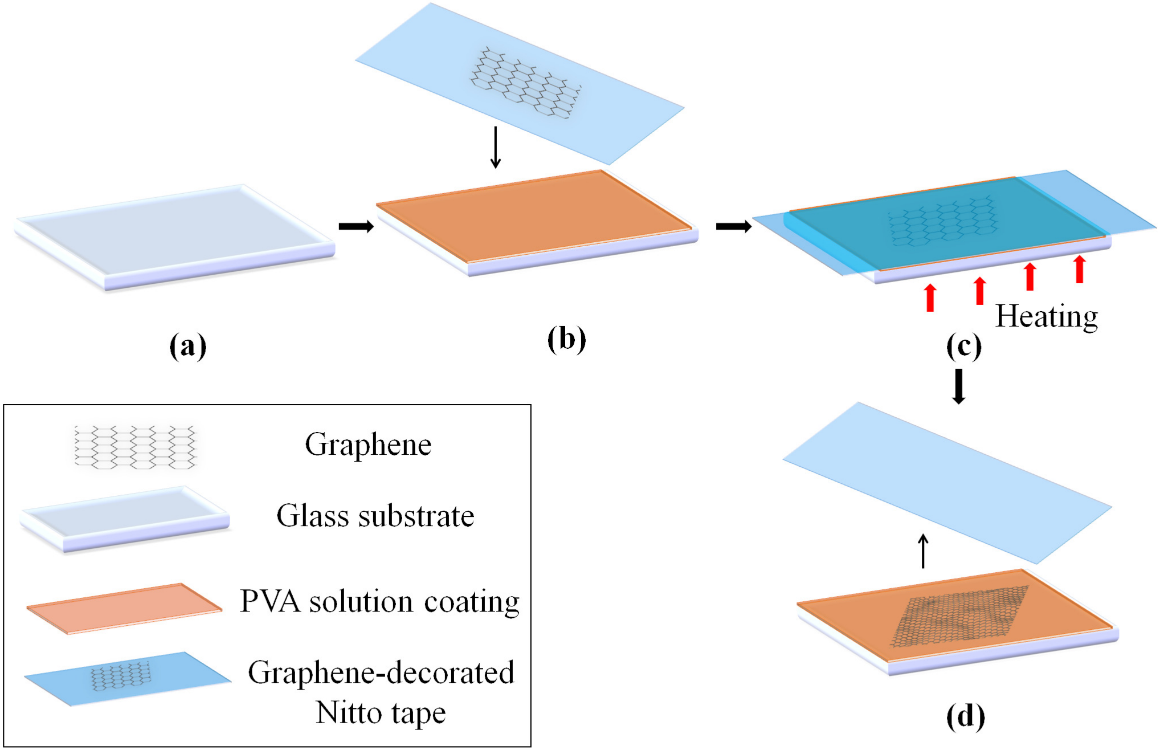

Figure 2.1: Schematic representation of PVA curing assisted blistering technique.

2.2.3 Characterizations

Optical identification of graphene flakes is carried out under a high-resolution optical microscope (Zeiss Axio Imager-M2m). The temperature-dependent Raman spectroscopy is carried out using a HORIBA LabRAM HR Evolution system on the identified multilayer graphene blisters, placing the sample on a LINKAM THMS600 heating stage. The output power of laser light is kept low at ∼ 1 mW for the laser excitation wavelength of 532 nm using a 50X air objective lens (NA=0.5) in a confocal microscopy set-up. The acquisition time is kept 20 s with a detector grating of 600 lines mm^{-1}, which provides a spectral resolution of 1.65 cm^{-1}. The heating process has been carried out with a ramp rate ∼ 100°C/ minute with a dwell of ∼ 2 min at each set temperature for attaining a state of thermal equilibrium before performing the Raman measurements. The Raman line-scan of blister profiles is obtained with the same set-up with 100X air objective lens (NA=0.8), taking the acquisition time of 10 s at room temperature under ambient conditions with a detector grating of 1800 lines

mm^{-1}, which provides a spectral resolution of $\sim 0.47\ cm^{-1}$. Atomic force microscopy (AFM) measurements in tapping mode have been taken with Bruker MultiMode-8 AFM set-up. The Raman peaks are fitted with a single Lorentzian function for analyzing the data.

2.3 Results and Discussion

We used PVA-assisted exfoliation (PAE) technique as a tool for the formation of optically visible sub-micron blisters having size of radius a $\sim$ 10 μm & height h $\sim$ 0.1 μm on the surface of multilayer graphene flakes deposited over the PVA-coated borosilicate glass substrate, possibly due to the pressure-difference driven merger of small blisters into bigger ones[35]. In the PAE technique, a Nitto tape decorated with thin graphitic flakes is first placed onto the PVA solution (prepared in DI water) coated glass substrate at room temperature (RT), and thereafter kept for a brief heat treatment at a raised temperature of $\sim$ 120°C. It should be noted that the PVA film is not cured just after the spin-coating and prior to the exfoliation step, rather a brief heat treatment process is carried out to cure the PVA and exfoliation of the 2D flakes simultaneously, which helps in the formation of blisters on the surface of the 2D material. However, the blisters do not form if the PVA is cured just after the spin-coating and prior to the deposition of the MLG flakes. This suggests that the water vapor from the PVA solution possibly gets trapped between the graphene flakes and the PVA-coated glass substrate to form the blisters, where the PVA layer acts as an interfacial hydration layer. The AFM topographic imaging and micro-Raman spectroscopy have been carried out on the graphene sub-micron blisters to investigate the corresponding number of layers in the 2D flakes. It is observed that the intensity of the deconvoluted $2D_2$ peak is twice that of $2D_1$ peak, which shows the signature of multilayer graphene (MLG) flakes[267]. The PAE technique dominates over the conventional hot exfoliation/ MHE technique in terms of the deposited large area single or few-layer graphene flakes, but along with a moderate density of optically visible MLG sub-micron blisters.

The optical and FESEM images of the sub-micron blisters of multilayer graphene flakes obtained via the PAE technique are shown in Figures 2.2 and 2.3, respectively. In the PAE technique, we realized that both (i) the variation of imposed mechanical pressure on graphene flakes during the deposition, and (ii) the vaporization of the water solvent from the PVA during its curing, play key roles in the formation of differently shaped blisters. In addition, the thickness of the polymer coating, the curing temperature, and the curing time are other crucial operating parameters for the

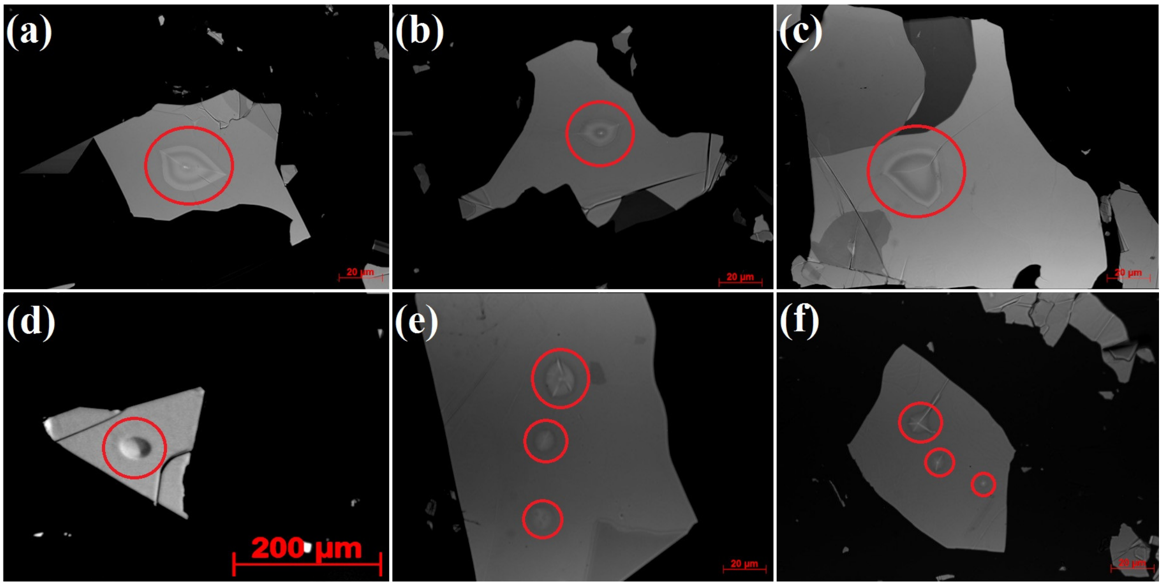
(a)
(b)
(c)
(d)
(e)
(f)
20 µm
200 µm

Figure 2.2: [(a)-(f)] Optical images of multilayer graphene blisters (encircled in red) over PVA-coated Pyrex substrate.

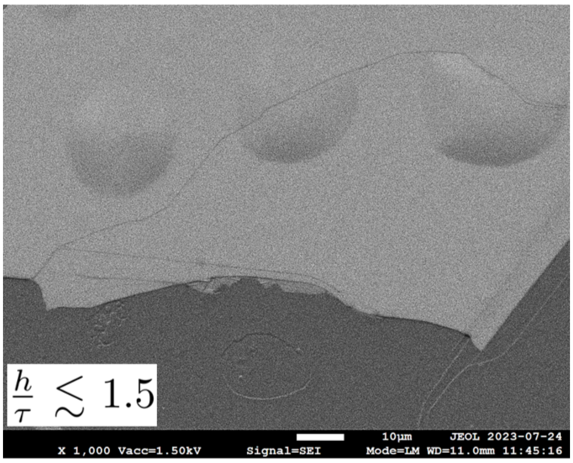
$\frac{h}{\tau} \lesssim 1.5$
X 1,000 Vacc=1.50kV Signal=SEI 10µm JEOL 2023-07-24 Mode=LM WD=11.0mm 11:45:16

Figure 2.3: FESEM image of multilayer graphene blisters, which follow elastic-plate profile.

formation of the blisters. In order to investigate PVA curing-assisted blister formation further, we varied the curing temperature as well as the thickness of the PVA coating (inversely proportional to the spinning speed & time[268]). On increasing the polymer curing temperature, the deposition yield on the PVA-coated glass substrate as well as the probability of getting blisters increases. However, the MLG blisters formed due to simultaneous polymer curing and deposition processes at relatively high temperatures are mostly seen to deflate within a few hours (see Figure 2.4).

In our work, we have only analyzed the deflation-free sub-micron blisters for further studies. We observed a moderate density of deposited SLG & FLG flakes, and MLG

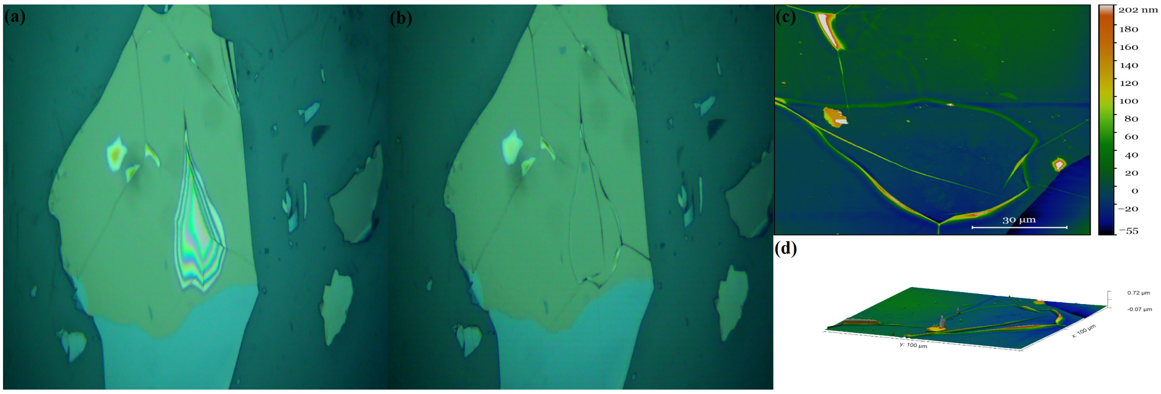

Figure 2.4: Deflation of a PVA-curing induced air-filled sub-micron MLG blister with time: a color optical image captured (with white light source) (a) just after the deposition via PAE technique, (b) after time-lapse of 24 h, and [(c), (d)] AFM topographic images, confirming the deflation.

sub-micron blisters on a thin film of PVA (spin-coated at 800 rpm for 40 s in step 1 and 2400 rpm for 20 s in step 2) cured at ∼ 120°C for 60 s on a hot plate. On the other hand, a relatively large quantity of MLG sub-micron blisters are obtained on a thicker film of PVA (spin-coated at 1600 rpm for 60 s) under the same processing conditions, which has relatively more water content. It indicates that the vaporization of the water solvent during the heat treatment helps in the formation of the blisters. The results show that the optimization of the synthesis & processing conditions are crucial for the deposition of graphene flakes, and the formation of the optically visible sub-micron blisters. We observed circular, triangular, and elliptical sub-micron blisters (Figure 2.2) in optical and AFM topographic images, which are most likely filled with the water solvent of the PVA. The different geometries of the blisters result from the competing interfacial energies[24], while the stable shape of the blisters by van der Waals (vdW) interactions acting among the graphene flake, the PVA-coated substrate, and the confined matter inside the blister.

The strain distribution across the blister has been investigated using Raman spectroscopy. A significant red-shift is observed in the Raman G-peak at the center of a circular (Figure 2.5) as well as elliptical (Figure 2.6) MLG blister in comparison to the edge of the blisters. The detailed analyses of the Raman spectra show an accumulation of tensile strain at the center of the blisters. The G-peak position at the center of the circular blister is 1577.41 ± 0.05 cm^{-1}, which is redshifted by ∼ 1.63 cm^{-1} due to relatively more tensile strain in comparison to the flat area having G-peak at 1579.04 ± 0.05 cm^{-1} (Figure 2.5). In a circular blister (bubble), the circumferential strain (ε_θ) varies linearly from the center to the edge of the bubble, while the radial strain (ε_r) varies non-linearly across the bubble, but the equi-biaxial strain ($\varepsilon_r = \varepsilon_\theta$) remains

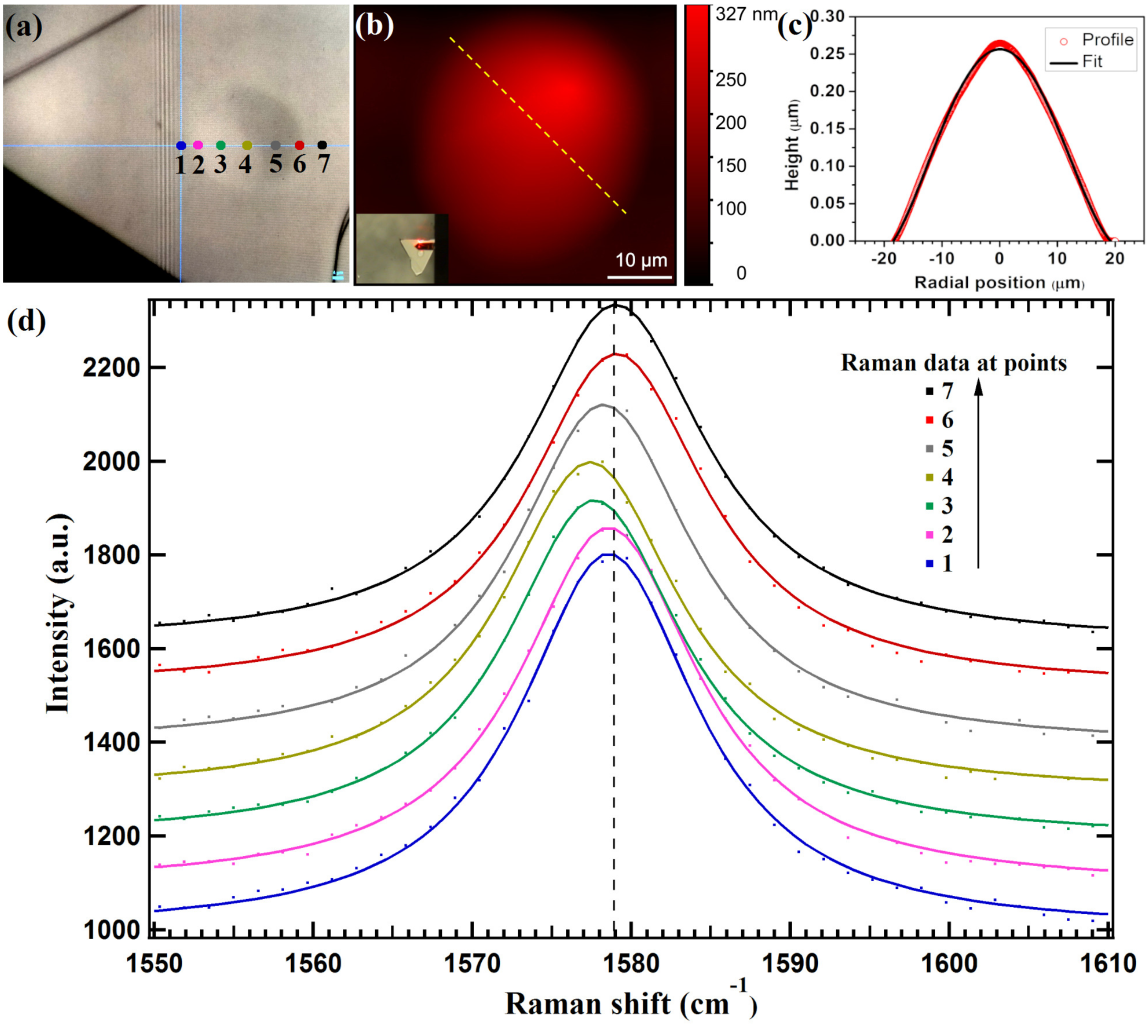

Figure 2.5: Multilayer graphene circular blister: (a) optical image, (b) AFM topographic image (inset: location of AFM tip operated in tapping mode), (c) Fourth-order polynomial fitting of AFM height profile of the circular blister, (d) Room temperature Raman spectra recorded at the points marked in the optical image along the diameter of the circular blister. Note a red-shift of $\sim 1.63\ cm^{-1}$ at the center of the blister w.r.t. the unstrained flat region.

constant at the center of the bubble (r = 0). The Raman peak shifts linearly under a biaxial strain ε^{biax} at the center of a bubble according to the following equation[269]

$$\Delta\omega_G = -2\gamma_G^{biax}\omega_G^0\Delta\varepsilon^{biax} \tag{2.1}$$

where γ_G^{biax} is the Grüneisen parameter and ω_G^0 is the unstrained peak position for the G-peak in case of the multilayer graphene. The Raman shift corresponds to a biaxial strain value of

$$\Delta\varepsilon^{biax} = \frac{\Delta\omega_G}{2\gamma_G^{biax}\omega_G^0} \approx 0.05\%$$

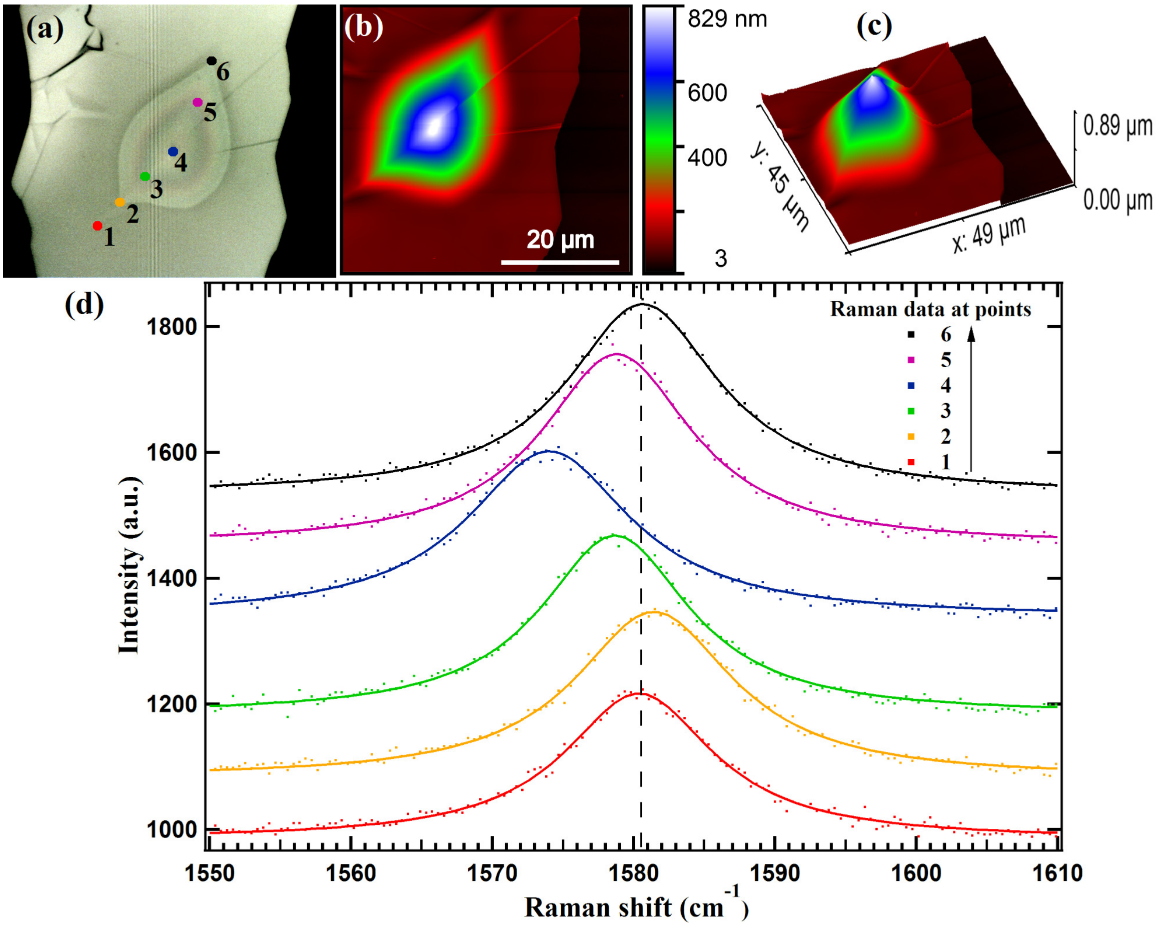

Figure 2.6: Multilayer graphene elliptical blister: (a) optical image, (b) AFM topographic image, (c) 3D height profile, (d) Room temperature Raman spectra recorded at the points marked in the optical image across the elliptical blister. Note a red-shift of $\sim 6.6\ cm^{-1}$ at the center of the blister w.r.t. the unstrained flat region.

where the value of γ_G^{biax} has been taken as 1.06[270,271] for quantitative analysis of the circular sub-micron blister of MLG. The relatively smaller laser-spot size ($\sim$ 1 μm) in comparison to the size of the circular sub-micron blister (bubble) assures the reliability of the biaxial strain value estimated at the center. The higher the biaxial strain at the center of the blister, the more would be the confining pressure inside the circular blister (bubble)[22,194,250]. In addition, the red-shift of the G-peak at the center of a typical elliptical blister (Figure 2.6) is $\sim 6.6\ cm^{-1}$, which is $\sim$ 4 times larger than the red-shift observed for the circular blister. The results indicate that manipulation of the vibrational properties or softening of the phonon modes may be achieved by subjecting the graphene flake to a local strain, engineered by the formation of the blisters of different geometries.

To investigate the phase (liquid/gas) of the confined matter inside the sub-micron

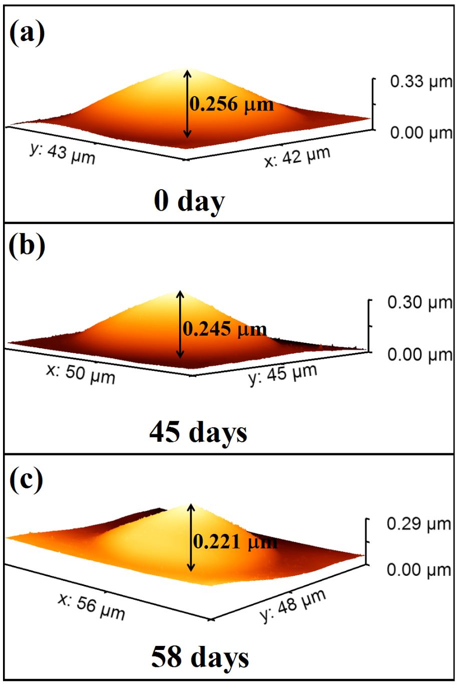

Figure 2.7: AFM 3D topographic images of the PVA-curing induced liquid-filled circular sub-micron blister of MLG over a period of 58 days, which show a negligible deflation rate with time.

blisters, we carried out time-lapse AFM topographic imaging using the same scanning parameters, where the deflation rates were measured in terms of a change in the height or radius of the blisters with time. We did not observe any appreciable change in the height profile of the blisters even after a period of 58 days (see Figure 2.7), which indicates that the blisters are filled with a liquid. The conclusion is supported by the literature, where no appreciable deflation rate (w.r.t. time) has been reported for the liquid-filled blisters, in contrast to that for gas-filled blisters[2,24]. H_2 and N_2 filled blisters at graphene-SiO_2 interface deflate within a few hours to a week time, respectively,[193] inspite of the fact that the graphene layer is mostly impermeable to all gases and liquids[272]. Further, it should be noted that the polymeric solution of PVA is prepared by dissolving PVA powder in DI water, which is spin-coated over the glass substrate, followed by simultaneous curing and exfoliation of the graphene flakes at $\sim$ 120°C (close to the boiling point of water as well as glass-transition temperature of PVA) for the formation of blisters. Since, the PVA melts at a temperature of $\sim$ 200°C, therefore the possibility of confinement of the hydrocarbon vapor inside the blisters, and any contamination from the polymeric residue is ruled out. Hence, most likely the confined liquid inside the sub-micron blisters is water. From this observation, we infer that the water vapor or gas molecules condense into a liquid state when

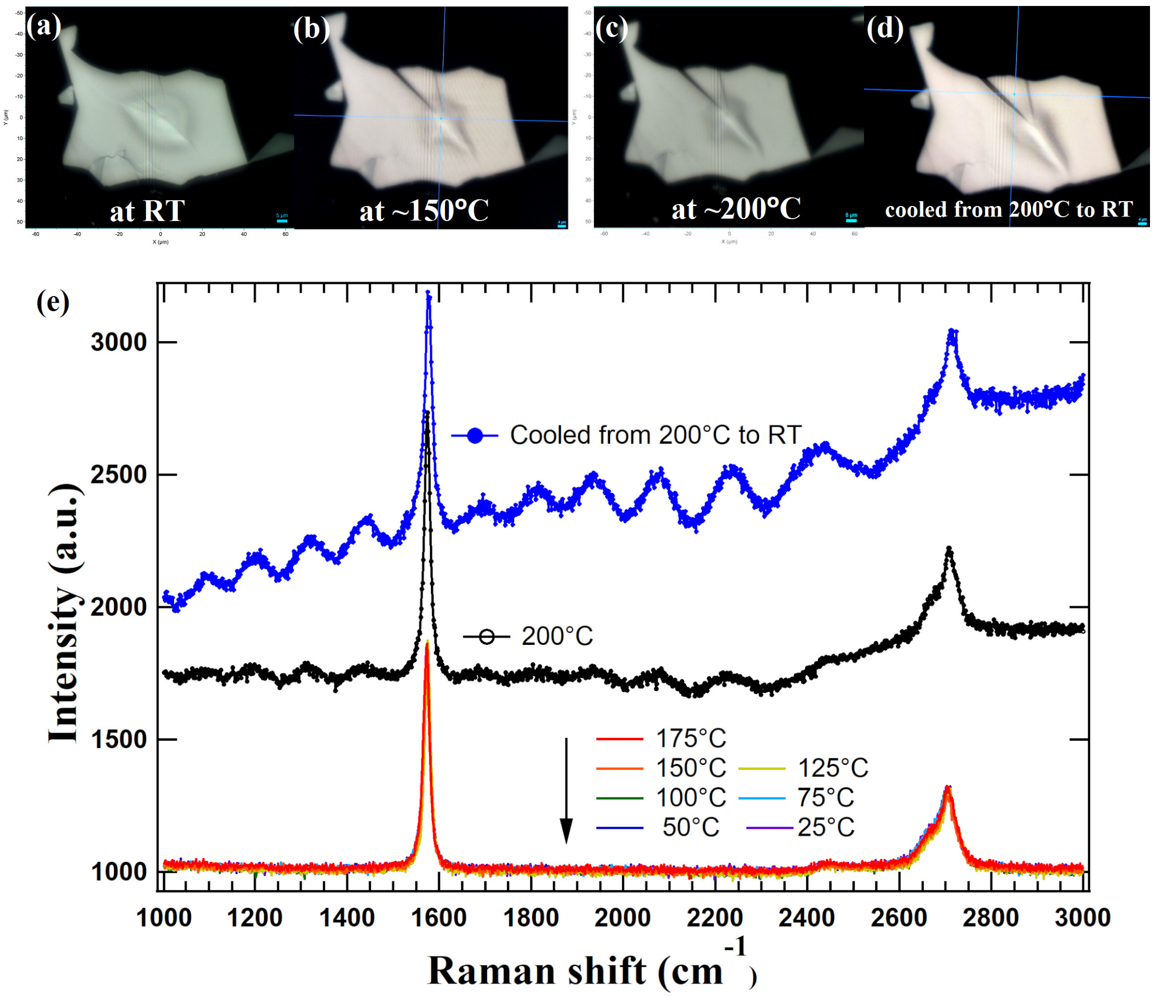

Figure 2.8: [(a)-(d)] Real-time optical images showing the deformation of the elliptical blister under thermal annealing process, (e) Temperature-dependent Raman spectra at the center of the elliptical blister. The Raman spectra from RT to 175°C superpose on each other, which shows the absence of polymer degradation.

the stack is cooled down to room temperature during the exfoliation process, which causes the formation of liquid-filled sub-micron blisters. The water is trapped inside the sub-micron blisters as it does not find any escape route but may come out by rupturing or heating the graphene blisters at higher temperatures[35,192,259]. We found that the over-heat treatment while deposition of 2D flakes results in a relatively lower density of liquid-filled sub-micron blisters. The optically visible sub-micron blisters of different geometrical shapes (circular, triangular, elliptical, etc.) are formed far away from the edges in multilayer graphene flakes of different thicknesses, which may be attributed to different residual strain imposed on the 2D flakes while deposition (Figure 2.2). However, most of the blisters are of broken axial symmetry near the edges of the 2D flakes because of more sliding and less confinement[2,273].

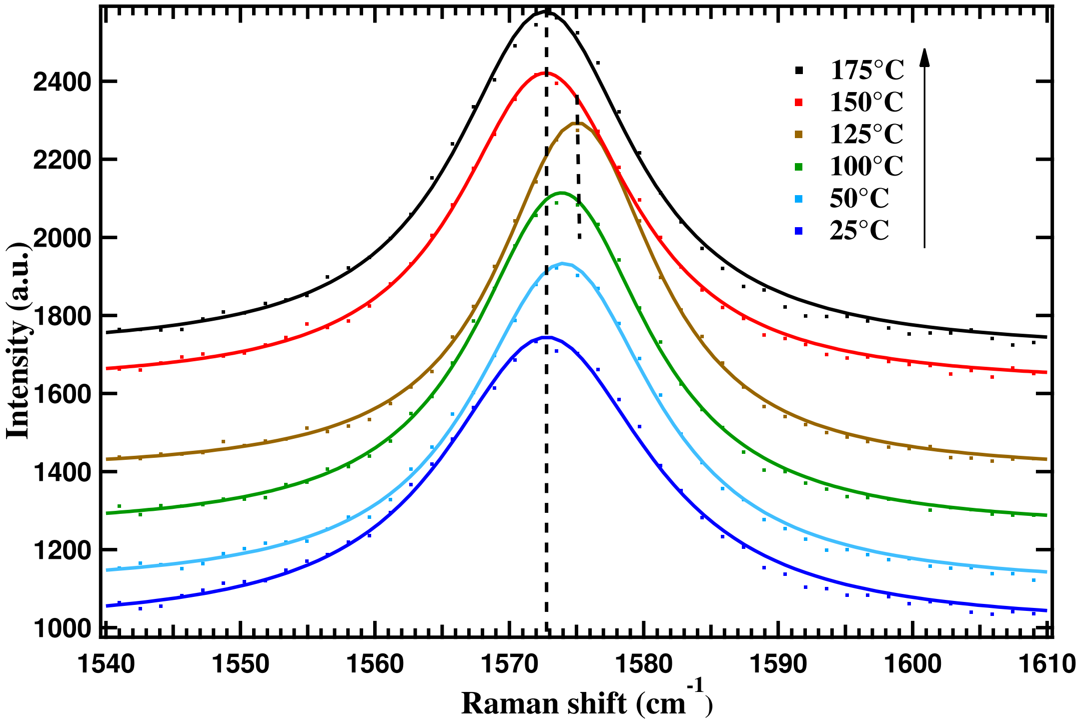

Figure 2.9: Temperature-dependent Raman spectra, measured at the center of the elliptical blister, showing a change in G-peak position with temperature. The vertical dashed lines are drawn as a reference for comparison of the Raman peak positions for selected temperatures.

To gain insights into the dynamics of the sub-micron blisters, we carried out temperature-dependent Raman spectroscopy at the center of an elliptical sub-micron blister. The shape of the blister was imaged and tracked continuously during the thermal treatment process under normal atmospheric conditions (Figure 2.8). A blue shift in the G-peak is observed on raising the temperature from 25°C up to 125°C (Figure 2.9), which indicates a release of the accumulated strain or flattening at the center of the sub-micron blister. A horizontal expansion is observed in the elliptical sub-micron blister on increasing the temperature, which results in a continuous decrement in the aspect ratio (ratio of the height of the blister to its radius, i.e., h/a) of the sub-micron blister. The horizontal expansion of the sub-micron blister with temperature is due to softening of the PVA (glass transition temperature $\sim$ 100°C) layer as well as the increasing kinetic energy of the confined water molecules, which would result into a decrease in the pressure inside the blister. However, we observed a noticeable sudden red shift in the G-peak as well as a change in the shape of the

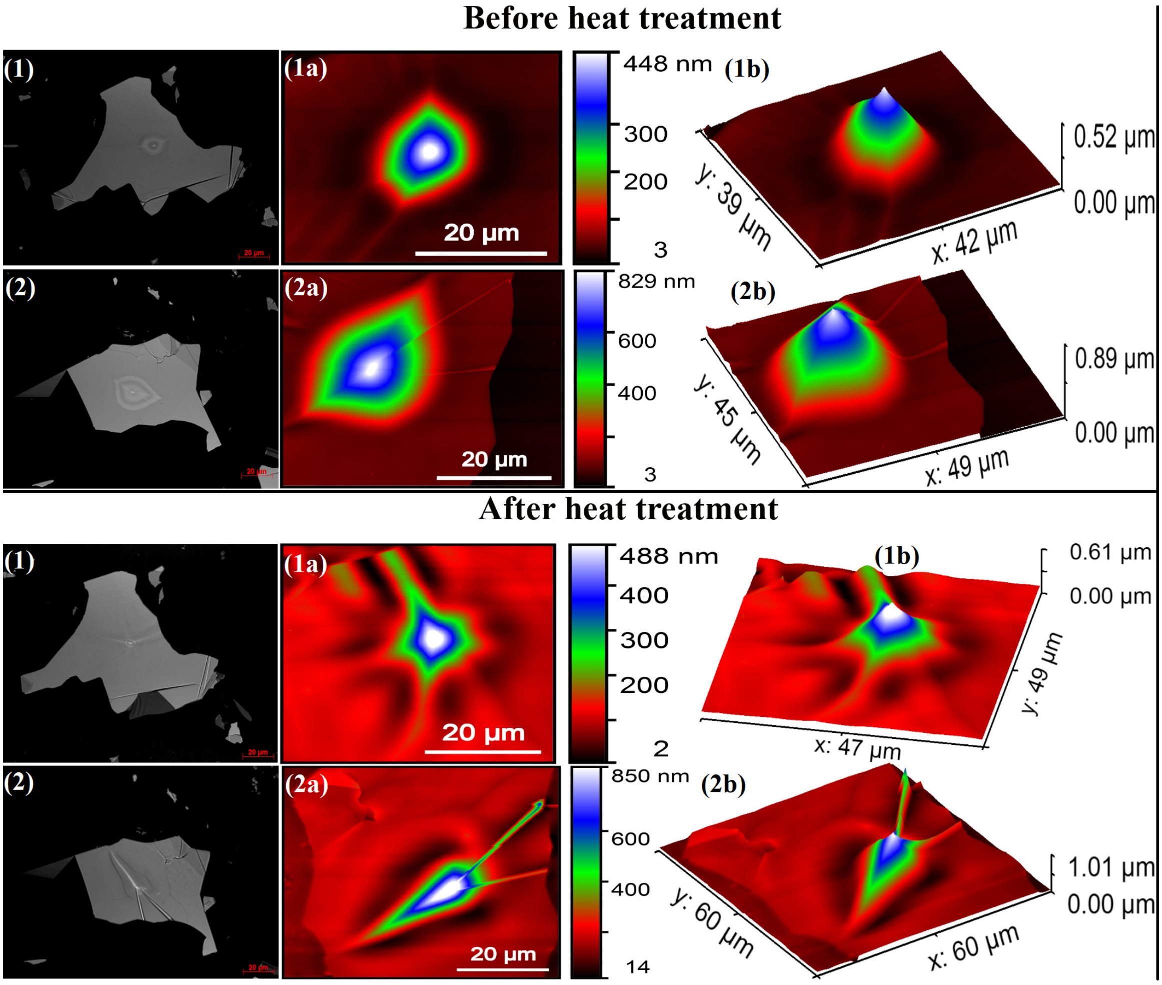
Before heat treatment
(1)
(1a)
20 µm
448 nm
300
200
3
(1b)
y: 39 µm
x: 42 µm
0.52 µm
0.00 µm
(2)
(2a)
20 µm
829 nm
600
400
3
(2b)
y: 45 µm
x: 49 µm
0.89 µm
0.00 µm
After heat treatment
(1)
(1a)
20 µm
488 nm
400
300
200
2
(1b)
0.61 µm
0.00 µm
y: 49 µm
x: 47 µm
(2)
(2a)
20 µm
850 nm
600
400
14
(2b)
y: 60 µm
x: 60 µm
1.01 µm
0.00 µm

Figure 2.10: Optical & AFM images of the elliptical blisters captured at room temperature, before and after the heat treatment (up to 200°C).

blister above 125°C possibly due to boiling of the confined water, which was undergoing only evaporation at the temperatures < 125°C. The raised boiling point of the confined water (> 100°C) indicates a pressure greater than the atmospheric pressure inside the blister. To estimate the pressure, we considered (i) water-filled MLG blister on PVA-coated glass substrate as an adiabatic system (as PVA and the surrounding air are dielectrics by nature), and (ii) boiling of the trapped water at ~ 125°C, where it converts into the vapor phase. The mathematical equation used for estimating water vapor pressure inside the MLG blister under a reversible adiabatic process is $(p_0)^{1-\gamma}(T_0)^{\gamma} = (p_1)^{1-\gamma}(T_1)^{\gamma}$; where $\mathrm{p_0}$ (0.1013 MPa) is normal atmospheric pressure and $\mathrm{T_0}$ (373.15 K) is the corresponding boiling temperature of water. It gives a pressure $p_1 \simeq 0.13$ MPa inside the sub-micron blister for adiabatic constant of water vapor (steam) γ as 1.324[274]. The blister above 125°C reshapes, possibly due to the softening of PVA and the water vapor leakage (making the strain profile stable thereafter).

At 150°C, we see a sudden red shift in the G-peak position (with respect to that of 125°C), but the same as that at RT. It indicates that the redistribution of the strain in the MLG blisters occurs in accordance with their initial shapes. The leakage of water vapor or gas molecules releases the pressure inside the blister, which gives it a final shape, therefore no appreciable change is observed in the G-peak position as well as the shape of the blister above 150°C up to 200°C. However, a wavy pattern appears in the Raman spectra at 200°C, which is up-shifted on the intensity axis with unaltered peak positions with respect to that of the MLG blister (Figure 2.8). We attribute this finding to thermal degradation of the PVA layer at the elevated temperature[275]. On cooling down to room temperature after the heat treatment, we captured optical and AFM images of the sub-micron blister, as shown in Figure 2.10. In order to investigate the shape and size of the blister further, the sample is heated again up to ∼ 150°C in the ambient atmosphere for a dwell time of ∼ 10 min with continuously monitoring the shape profile of the blister using optical microscopy. We did not observe any change in the shape & size of the blisters, however, a few wrinkles appeared in some thinner graphene flakes (see Figure 2.11) possibly due to thermal expansion mismatch between the graphene flakes and the PVA substrate[276]. It confirms the earlier statement that the blister takes a final shape at 150°C after the leakage of the water vapor or gas molecules after the softening of PVA and the formation of the tiny channels at the graphene/PVA interface (as graphene is almost impermeable to water vapor[277]). Detailed optical microscopy, time-lapse AFM topographic imaging, and temperature-dependent Raman spectroscopy allow us to consider the confinement of water inside the sub-micron blisters.

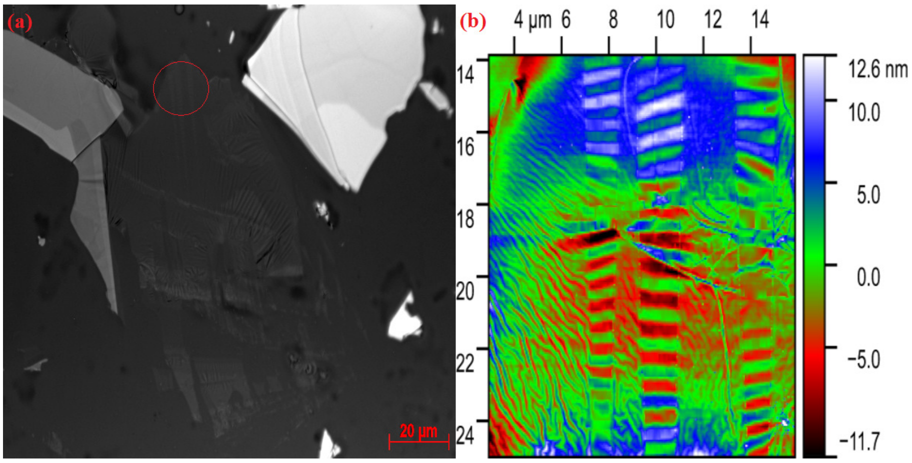

Figure 2.11: (a) Optical image, (b) AFM topographic image of the encircled area showing thermal-expansion mismatch induced graphene wrinkles on PVA-coated glass (Pyrex) substrate.

In order to estimate the mechanical properties of the PVA-supported multilayered 2D flakes (interfacial adhesion energy and confinement pressure), we have, further, analyzed the water-filled sub-micron blisters of the MLG flakes using a blister test model[1]. In a blister, the debonding strength (adhesion energy) of the 2D flakes depends upon the vdW interactions acting among the flakes, substrate and the trapped matter inside the blister[34]. At a given temperature, the adhesion energy and the pressure inside a blister are found to increase with the degree of conformation between the flakes and the substrate but decrease with the increasing number of layers in the 2D flakes[199]. In the case of our PVA-curing induced sub-micron blisters, the ratio of bubble height to the thickness of the 2D flakes ($\frac{h}{\tau}$) is $\lesssim 1.5$, therefore the nonlinear plate model is applicable[1]. A small deflection h at the center of the sub-micron bubble in comparison to its radius a results in a small value of the aspect-ratio ($h/a \ll 1$), which reflects the appreciable bending rigidity of the multilayered 2D flakes for their out-of-plane deformation to form the blisters[1,23,196]. However, the out-of-plane deformation in a multilayered 2D flake depends upon its overall bending rigidity "D", which is related to its 2D elastic stiffness (E_{2D}) and thickness (τ) of the 2D flakes by $D = \frac{E_{2D}\tau^2}{12(1-\nu^2)}$, where ν is the Poisson's ratio of the 2D flakes. For a thick 2D flake acting as an elastic plate, the overall effective bending rigidity can be expressed as $D_{eff} = \frac{N^3 E t^3}{12(1-\nu^2)} \sim N^3$, where E is the Young's modulus of the 2D flake consisting of N identical layers[23].

Further, the adhesion energy of 2D flakes can be estimated in two extreme interface limits: strong-shear limit (fully bonded interface) and weak-shear limit (frictionless interface)[2,23]. In our case of PVA curing-induced sub-micron blister formation, the possibility of sliding at the interface is reduced due to the simultaneous curing of PVA and deposition of the 2D flakes, which leads to the case of a strong-shear interface. However, a small but appreciable out-of-plane bending is possible in 2D flakes for the blister formation as a result of competition between the in-plane deformation of the flake and the interlayer slippage, as the out-of-plane bending favors the interlayer slippage, which cannot be ruled out completely in the layered materials.

We carried out quantitative mechanical analyses of the sub-micron blister using nonlinear plate model, where the elastic energy contributions associated with the in-plane stretching/compression (related to in-plane covalent (σ) bonds, out-of-plane bending (due to distortion of out-of-plane π bonds) and the surface tension of the confined water are considered in the analytical estimation of the interfacial adhesion energy (discussed in the next section). We considered water as an incompressible liquid inside the sub-micron blister with a constant volume $V = \frac{\pi}{3}a^2 h$. The effective adhesion energy per unit area (Γ) of the MLG-substrate interface can be estimated as, $\Gamma = \Delta\gamma + \gamma_w(\cos\theta_G + \cos\theta_s)$; where $\Delta\gamma$ is the change in the interfacial adhesion energy density due to the formation of the water-filled MLG blister, which is given by, $\Delta\gamma = \gamma_{Gs} - \gamma_{Gw} - \gamma_{sw}$; where γ_{Gs}, γ_{Gw} and γ_{sw} are the adhesion (vdW) energies per unit area for MLG-substrate, MLG-water, and substrate-water interfaces, respectively[34]; and γ_w is the surface tension of the confined water interacting with the 2D multilayer & the substrate (with θ_G & θ_s as the water contact angles with the 2D flake and the substrate, respectively)[2].

The optical and AFM topographic images have been used to find out the shape and size of the sub-micron blisters. The aspect ratio of the sub-micron blisters is found to be shape-dependent, but size (volume) independent for a blister of particular shape and flake thickness[34]. However, the size of the sub-micron blister varies with the thickness of the 2D flake. We employed the nonlinear plate model (taking the bending stiffness of the 2D flakes into account) for analyzing a circular sub-micron blister or bubble (approximately axisymmetric), where the deflection profile of the bubble is approximated to a spherical cap[23]. The deflection profile of the circular sub-micron blister, which satisfies the zero-slope boundary condition at the edge of the bubble for a pressurized elastic plate, is given as

$$w(r) = h\left(1 - \frac{r^2}{a^2}\right)^2 \tag{2.2}$$

which is fourth order in the radial distance r. The radius a and the central deflection h of the bubble are estimated by fitting the height profile of the spherical cap (Figure 2.5(c)) obtained from the atomic force microscopy (AFM) image in tapping mode. The height profile of the blisters is fitted to a fourth-order polynomial function of radial distance r as, $\mathrm{w(r)} = \mathrm{intercept} + \mathrm{B_1 r} + \mathrm{B_2 r^2} + \mathrm{B_3 r^3} + \mathrm{B_4 r^4}$; which gives central deflection or height h as intercept and radius a as $\left(-2\frac{\mathrm{intercept}}{\mathrm{B_2}}\right)^{\frac{1}{2}}$.

Analytical analysis of our non-linear elastic plate model for water-filled sub-micron blisters

For a water-filled sub-micron blister of height h on a multilayer graphene (MLG) flake of thickness τ, satisfying the condition $\frac{h}{\tau} \lesssim 1.5$, the Von Karman nonlinear elastic plate model can be used, considering the prominent effect of bending stiffness of the PVA-supported MLG flakes. The supporting layer of PVA provides a strong-shear interface to the MLG flakes, which prevents the sliding at the interface during the PVA-curing assisted blister formation. The edge of the bubble is assumed to be fully clamped onto the substrate. The deflection profile of the non-linear plate is assumed to be[1]:

$$w(r) = h\left(1 - \frac{r^2}{a^2}\right)^2 \tag{2.3}$$

where, r, h and, a are radial positions across the bubble, height, and radius of the bubble respectively; with $h \ll a$. This relation satisfies the zero slope boundary condition at the edge of the bubble. We consider the strong shear limit, for which the elastic plate outside the blister edge is not deformed. The liquid within the blister is assumed to be incompressible with a constant blister volume $V = \pi a^2 h/3$. The area of the bulged surface $A' = \pi a\left(\sqrt{a^2 + h^2}\right) \approx \pi a^2$ for $h/\mathrm{a} \to 0$. Further, the radial displacement is assumed to take the form,

$$u(r) = r(a - r)\left(\mathrm{c}_1 + \mathrm{c}_2 r + \mathrm{c}_3 r^2\right) \tag{2.4}$$

where, the three unknown parameters c_1, c_2 and c_3 are to be determined. The 4^{th} order (quartic) function form of the radial displacement is used for a better approximation than a cubic function[1,278].

The non-uniform strain distribution with radial and circumferential strain components $(\varepsilon_r, \varepsilon_\theta)$ is analyzed by considering the axial symmetry of the bubble in the model. Using Eqs. 2.3 and 2.4 the radial and circumferential strain components are obtained, as

$\varepsilon_r = \frac{du}{dr} + \frac{1}{2}\left(\frac{dw}{dr}\right)^2$

$$\varepsilon_r = (a-r)r(c_2+2c_3 r) + \frac{8h^2r^2\left(1-\frac{r^2}{a^2}\right)^2}{a^4} + (a-r)\left(c_1 + c_2 r + c_3 r^2\right) - r\left(c_1 + c_2 r + c_3 r^2\right) \tag{2.5}$$

$$\varepsilon_\theta = \frac{u}{r} = (a - r)\left(\mathrm{c}_1 + \mathrm{c}_2 r + \mathrm{c}_3 r^2\right) \tag{2.6}$$

At the edge $(r = a)$, the circumferential strain ε_θ is zero.

The total potential energy for the multilayer graphene bubble is $\Pi_{total} = \Pi_{stretching} + \Pi_{bending} + \Pi_{fluid-interaction}$. The elastic stretching energy per unit area of the elastic plate (MLG flake) is

$$U_{\mathrm{s}}(r) = \frac{E_{\mathrm{2D}}}{2\left(1 - \nu^2\right)}\left(\varepsilon_r^2 + 2\nu\varepsilon_r\varepsilon_\theta + \varepsilon_\theta^2\right) \tag{2.7}$$

The elastic bending energy per unit area is,

$$U_b(r) = \frac{D}{2}\left[\left(\frac{d^2w}{dr^2}\right)^2 + \frac{1}{r^2}\left(\frac{dw}{dr}\right)^2 + \frac{2\nu}{r}\frac{dw}{dr}\frac{d^2w}{dr^2}\right] \tag{2.8}$$

where D is the bending stiffness of the MLG flake (elastic plate) and ν is the Poisson's ratio of MLG[1,2].

The total potential energy for the liquid-filled multilayer graphene (MLG) bubble can be written as

$$\Pi\left(a, c_1, c_2, c_3\right) = 2\pi \int_0^a \left[U_s(r) + U_b(r)\right] r dr + \pi a^2 \Delta\gamma \tag{2.9}$$

where, $\Delta\gamma = \gamma_{Gc} + \gamma_{sc} - \gamma_{Gs}$, which is the change of interface energy for the formation of the liquid-filled blister in terms of the interfacial energy densities of MLG-content, substrate-content and MLG-substrate interfaces, respectively. The adhesion energy of the elastic plate (MLG) to the substrate (PVA) will be given by, $\Gamma = \Delta\gamma + \gamma_w(\cos\theta_G + \cos\theta_s)$, where, γ_w is the surface tension of liquid-water with θ_G and θ_s as the water contact-angles of the MLG and the substrate, respectively. Unlike gas-filled blisters, the height of the blister $h = \frac{3V}{\pi a^2}$ is not an independent variable in equation 2.9 due to the assumption of incompressible water with a constant volume[2]. For a fixed radius a and height h, the mechanical equilibrium determines the three parameters c_1, c_2 and c_3 by setting $\frac{\partial\Pi}{\partial c_1} = \frac{\partial\Pi}{\partial c_2} = \frac{\partial\Pi}{\partial c_3} = 0$, which yields

$$\mathrm{c_1} = \frac{\mathrm{h}^2(1585 - 723\nu)}{1386\mathrm{a}^3} \tag{2.10}$$

$$\mathrm{c_2} = -\frac{17\ \mathrm{h}^2(9 + 5\nu)}{198\mathrm{a}^4} \tag{2.11}$$

$$\mathrm{c_3} = \frac{32\ \mathrm{h}^2(-3 + 2\nu)}{99\mathrm{a}^5} \tag{2.12}$$

By putting the expressions for c_1, c_2 and c_3 in the equation 2.9, we obtain the free energy as a function of the bubble radius:

$$\Pi(a) = \left\{\frac{\mathrm{E_{2D}}(896585 + 529610\nu - 342831\nu^2)\mathrm{V}^4}{59290\mathrm{a}^{10}\pi^3\left(1 - \nu^2\right)} + \frac{96D\mathrm{V}^2}{\mathrm{a}^6\pi} + \pi a^2\Delta\gamma\right\}$$

Next, by setting $\left(\frac{\partial\Pi}{\partial a}\right)_V = 0$, and solving for $\Delta\gamma$, we get

$$\Gamma = \zeta E_{2D}\left(\frac{h}{a}\right)^4 + 32\frac{Dh^2}{a^4} + \gamma_w(\cos\theta_G + \cos\theta_s) \tag{2.13}$$

where, $\zeta = \frac{896585+529610\nu-342831\nu^2}{960498(1-\nu^2)}$ and, E_{2D} is the 2D elastic stiffness of the elastic plate. Note that the first term on the right-hand side of equation 2.13 is the contribution of in-plane stretching, the second term is the contribution of the finite bending stiffness, while the third term is the contribution from the fluid (liquid)-interactions (see Appendix A).

Using the nonlinear plate model[1,23,199,266,279] for our water-filled blisters considering strong shear limit at the interface of the MLG flakes (elastic plate) and the PVA film (substrate), the interfacial adhesion energy density Γ for the PVA-supported MLG flakes using the above equation 2.13 is estimated in the range of $58.47 - 219.96$ mJ/m^2.

The following parameters, related to the MLG blisters, have been used for the estimation of the interfacial adhesion energy: $E_{2D} = NEt$, where N (number of layers)$= 441 \rightarrow 800$, $Et = 340$ N/m [where E (in-plane elastic modulus of graphene) $= 1.00$ TPa, t (thickness of single layer graphene) $= 0.34$ nm][280], constant prefactor $\zeta = \frac{896585+529610\nu-342831\nu^2}{960498(1-\nu^2)}$, taking ν (Poisson's ratio of MLG) $= 0.16$[199,281], γ_w (surface tension of water) $= 72$ mN/m[282], and contact angles of $\theta_s = 51°$ & $\theta_G = 100°$ for water/PVA & water/MLG[283] interfaces, respectively.

Role of radial displacement function in the determination of the elastic strain energy for different models

We analyzed the relative change in the elastic deformation term of the total interfacial adhesion energy (${\Gamma_e}^{l/g}$; l: liquid-filled blister & g: gas-filled blister) for graphene blisters with the same aspect-ratio (h/a) and thickness (τ), using different models as[1,2,278,284]:

$$\Gamma_e = \Gamma_s + \alpha\Gamma_b$$

where Γ_e is the elastic deformation (stretching (s) + bending (b)) term of the total interfacial adhesion energy and α is the model selecting parameter which takes values 0 (for **Membrane model**) and 1 (for **Elastic plate model**).

(i) $\frac{{\Gamma_e}^l-{\Gamma_e}^g}{{\Gamma_e}^g} \times 100 \simeq -3.9\%$ (For the **membrane model**, where, ${\Gamma_e}^l$ corresponds to the cubic function approximation to the radial displacement[2] while ${\Gamma_e}^g$ corresponds to the quadratic function approximation[1].)

(ii) ${\Gamma_e}^l \rightarrow {\Gamma_e}^g$ (For the **membrane model**, where, ${\Gamma_e}^l$ and ${\Gamma_e}^g$ both correspond to the quadratic function approximation to the radial displacement.)

(iii) $\frac{{\Gamma_s}^l-{\Gamma_s}^g}{{\Gamma_s}^g} \times 100 \simeq -0.94\%$, and ${\Gamma_b}^l \rightarrow {\Gamma_b}^g$ (For the **nonlinear elastic plate model**, where, Γ^l corresponds to the quartic (4^{th} order) function approximation to the radial displacement (**our work**) while Γ^g corresponds to the cubic function approximation[1].)

(iv) $\Gamma_e{}^l \rightarrow \Gamma_e{}^g$ (For the **nonlinear elastic plate model**, where, $\Gamma_e{}^l$ and $\Gamma_e{}^g$ both correspond to the cubic function approximation to the radial displacement.)

For a better approximation of the adhesion energy, we employed the nonlinear elastic plate model with a quartic function in the radial displacement. However, it may be noted that by using the cubic function form of the radial displacement in the nonlinear elastic plate model, we obtained the same expression for the adhesion energy (excluding the fluid-interaction term) for the liquid-filled blister as that of the gas-filled blister[1]; which manifests that only the fluid-interaction term in the case of the liquid-filled blister plays a critical role in deducing the interfacial adhesion energy.

Table 2.1: Interfacial adhesion energy & confining pressure w.r.t. number of layers of the MLG flakes (which contain the PVA curing induced approximately axisymmetric circular sub-micron blisters).

h/τ	**h/a**	**N**	**Γ (in mJ/m^2)**	**p (in MPa)**
1.64	0.028	441	219.96	1.244
1.078	0.016	490	71.16	0.296
0.805	0.013	600	62.79	0.209
0.943	0.0123	800	58.47	0.176

In our case, the height of circular sub-micron blisters is $\gtrsim$ 100 nm, therefore the nonlinear plate model and membrane model for estimating the confining pressure would collapse with the Hencky's solution[1,199,259], which is the uppermost limit of the pressures calculated using both the models. According to Hencky's model, the confinement pressure and the geometry of the blister are related by[2,199,259]

$$p - p_0 = \Delta p = K(\nu)\frac{NEth^3}{a^4} \tag{2.14}$$

where $K(\nu) \simeq 3.09$[199] and $p_0 = 1$ atm. pressure $= 0.1013$ MPa. The maximum confining pressure (p) inside the liquid-filled sub-micron blisters is estimated in the range $\sim 0.176 - 1.244$ MPa. The pressure estimated inside the blister is greater than the pressure estimated before at a high temperature using temperature-dependent dynamics, which is consistent with our pressure analyses.

We analyzed the interfacial adhesion energy obtained for a few MLG sub-micron blisters (approximately circular) of different flake thicknesses. It is observed that the aspect ratio (h/a) of the sub-micron blisters decreases on increasing the thickness of the 2D flakes, possibly due to an increase in the blister delamination area (size or

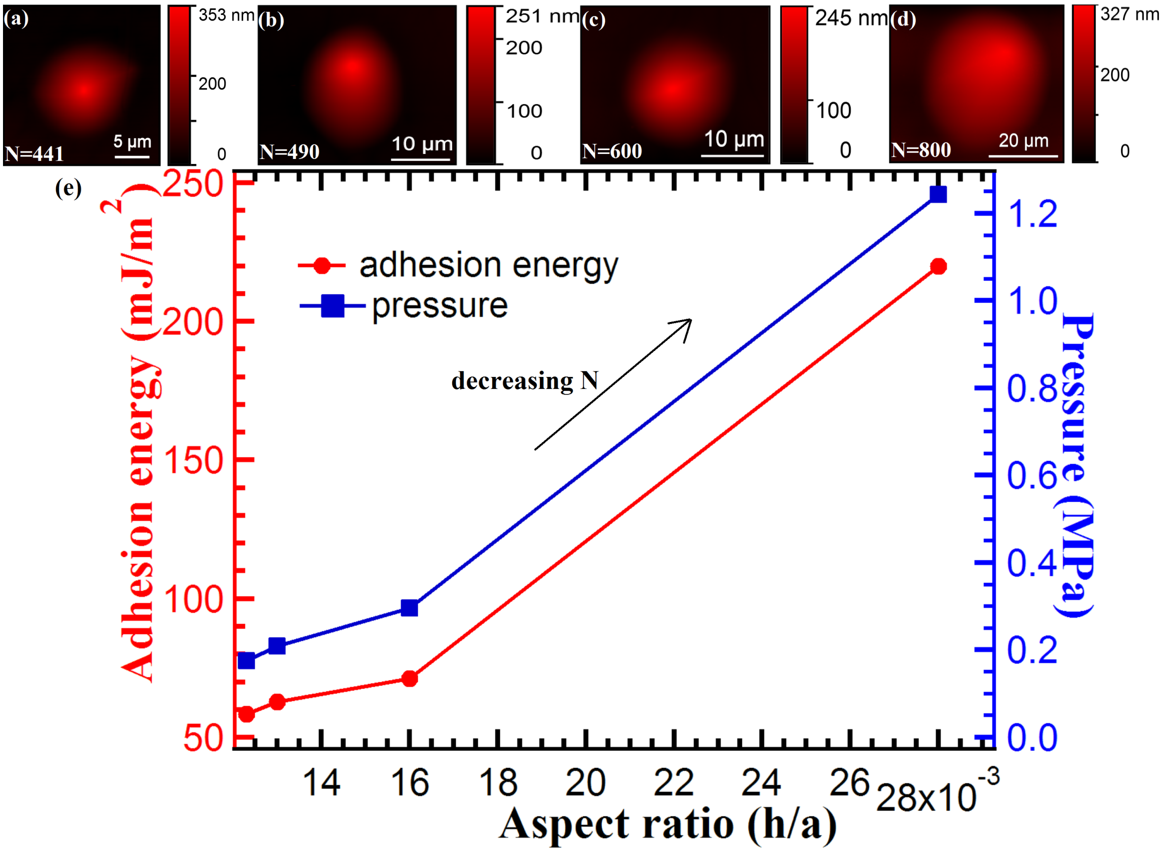

Figure 2.12: [(a)-(d)]AFM topographic images of the approximately circular sub-micron MLG blisters on flakes of different thicknesses (number of layers: N), (e) Interfacial adhesion energy & confining pressure as a function of aspect-ratio of the MLG blisters at room temperature.

radius) as a result of decrement in the interfacial adhesion or debonding energy of the 2D flakes (Figure 2.12). It shows that the non-linear elastic plate behavior is more prominent for thicker graphene flakes (see Table 2.1). It is worth mentioning that the evaluated interfacial adhesion energy might have been overestimated due to the simplified assumptions: (i) constant radius without any delamination other than the blister formation, and (ii) a small error in deducing the number of layers (thickness) of graphene flakes from the AFM topographic images due to the surface roughness (RMS $\sim$ 1 - 2 nm) of the PVA layer. For the single-layer graphene (SLG), the interfacial adhesion energy is expected to be higher because of its higher flexibility, which helps it conform more closely to a polymeric substrate than the multilayer flakes.

We also observed some liquid(water)-filled approximately axisymmetric sub-micron blisters located near the edges of the PVA-supported multilayer graphene flakes, which satisfy the condition for the membrane model, i.e., $\frac{h}{\tau} \gtrsim 2$ (Figure 2.13). We believe that the interlayer sliding is prominent near the edges, which enables the indepen-

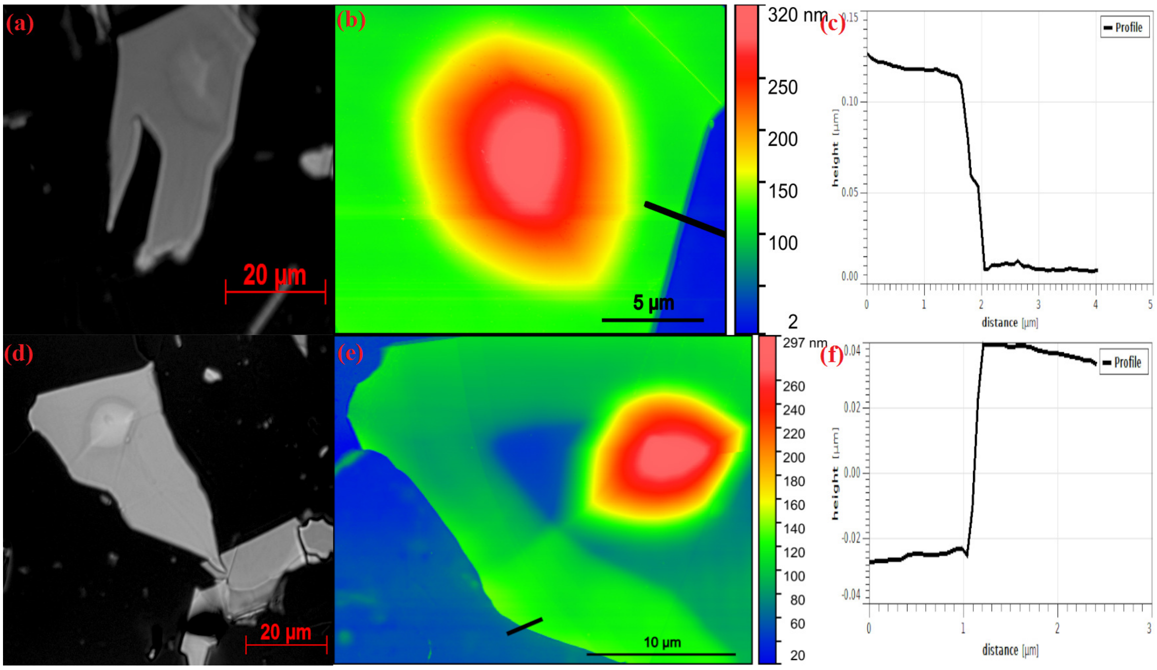

Figure 2.13: PVA-curing induced sub-micron blisters: (a) and (d) are optical images; (b) and (e) are AFM topographic images; (c) and (f) are AFM thickness profiles along the marked black lines in the AFM images.

dent bending of the layers due to the weak vdW interlayer interactions, making the effective thickness of the flake as that of the single layer. This results in the lesser effective bending stiffness of the 2D flakes, such that, the overall bending rigidity scales linearly with the number of layers, which corresponds to $D_{eff} = \frac{NEt^3}{12(1-\nu^2)} \sim N$, validating the membrane limit[23]. This implies that interlayer sliding is possible even for the thick-layered 2D flakes acting as elastic plates (with large bending rigidity) at the strong-shear interface.

2.4 Summary

In summary, the simultaneous PVA curing & 2D material deposition process helps in the formation of optically visible sub-micron MLG blisters, which is rare to achieve in ambient and ordinary deposition conditions. The mechanism and the robust procedure of the PVA curing assisted blistering ensures the possibility for the formation of such large sub-micron blisters of a 2D material on any flat & smooth substrate experimentally. The appreciable adhesion of the multilayer graphene flakes with the thin film of PVA enables them to hold a high pressure inside the blisters.

The detailed analyses of temperature-dependent optical microscopy, Raman spectroscopy, and AFM topographic imaging confirmed that the confined matter inside the sub-micron blisters is liquid (water). The presence of the water-filled sub-micron blisters significantly modulates the vibrational properties of the 2D flakes locally as a result of the modulated lattice structure. In this work, we put simple but strategic efforts into understanding the physics and chemistry behind the out-of-plane bending of the PVA-supported multilayered graphene flakes by analyzing the water-filled submicron blister system using the nonlinear elastic plate model in order to estimate the interfacial adhesion energy and the confined pressure. This study opens up new pathways for an alternative for local strain engineering of the 2D materials and exploiting the bubble physics towards practical applications. The technique can be explored for confining other liquids inside the blisters and their controlled temperature-dependent release.

Chapter 3

Elastic solid- and viscoelastic substrate-based instabilities in spontaneously formed multilayer Graphene blisters

3.1 Introduction

Graphene is a mechanically robust two-dimensional (2D) material in terms of its remarkably high bendability (flexibility), elasticity, and strain-bearing capacity, which is capable of forming blisters through the confinement of different kinds of matter such as liquid, gas, nanoparticles, etc. at the graphene/ substrate interface[24,34]. The blisters on the surface of a 2D material like graphene offer local strain-sites with altered physical properties, and also help in probing its adhesion mechanics, which show huge potentiality for fundamental research as well as practical applications in flexible & tunable electronics, optoelectronics, and nanophotonics[2,22,23,49,196,218,285–288]. Furthermore, the properties of the 2D material can be manipulated by engineering the size and the shape-profiles of the blisters[195]. Therefore, an exhaustive understanding of the underlying mechanism behind the onset of instabilities in the 2D material blisters is a prerequisite. The instabilities in the bulged elastic sheets over the rigid/ solid substrates have been elucidated by considering the interfacial slippage while mechanical force-indentation or pressurized bulge-tests[25,26,28,245,289]. Chopin *et al*[28] investigated the mechanically indented blisters of a thin plastic sheet, adhering to a rigid glass plate by means of a thin liquid layer, and found that a large central vertical displacement or the indentor height (greater than a critical value) with respect to the thickness of the sheet, pronounceably, generates the solid-based instabilities[28]. The blisters are typically circular for the small values of the ratio of blister-height to sheet-thickness, but on further increasing the vertical displacement of the indented plastic sheet, the delaminated front undulates along the adhering annular region due to the interfacial slippage, giving rise to a tent-like shape of the blister, and finally, the delaminated front behaves like an open curve to form trapezoidal, triangular or star-like shapes. The interfacial slippage causes complexity in the conventional blister-test models, which are generally used for deducing the interfacial adhesion energy (debonding strength) of the elastic 2D sheets over a given substrate[1,2,25,26]. The adhesion energy of a 2D flake depends upon the van der Waals (vdW) interactions acting among the flake, the substrate, and the trapped matter inside the axisymmetric blister[34,195,199]. However, the interplay between the vdW interactions and the elastic stresses in an axisymmetric blister at a slippery interface may result in the development of wrinkling instabilities[289]. Recently, Ares *et al*[36] showed that the diffusion of water molecules from the surroundings, between the top and bottom 2D layers of two distinct 2D materials (hBN/$\mathrm{MoS_2}$) in a bubble, enhances the radial tension in the top membrane and induces azimuthal stress i.e., 'hoop compression' in the bubble. This stress is compressive in nature outside the bubble, whose suppression results in the development of solid-based instabilities in the form of radially oriented wrinkles around the bubble. The periodic wrinkling patterns in the delaminated region of the membrane develop as a result of competition between its bending rigidity (which opposes the wrinkling or favors the large wavelength of the wrinkles) and the 2D flake-substrate vdW interactions (which support the wrinkling, and result in the small wavelength of wrinkles)[36]. Recently, the elastic-wetting phenomenon has also been exploited for elucidating the elastocapillary self-cleaning of twisted bilayer graphene interfaces by means of the coalescence of tiny bubbles into the bigger ones[35]. The conventional blister-test models assume the single phase of the confined matter inside the blisters for simplified explanation[1,2,34]. However, the phase-transition of the trapped matter has a crucial role in the formation and the stability of the blisters, which still remains unexplored[25,49,284]. Therefore, a more realistic & universal model is required to elucidate the involved mechanism behind the solid-based instabilities (e.g. tents, pyramids, etc.) in the 2D material blisters.

The investigations of adhesion and debonding mechanisms of the thin elastic sheets from the polymeric substrates have great significance in applications such as adhesives & coatings, biomedical implants, micro/nanoelectromechanical devices, etc.[36,290,291]. In the debonding of a rigid & stiff plate from a confined viscous fluid in the presence of a less viscous medium, the viscous instabilities arise at the interface of the more viscous fluid and less viscous fluid[292–295]. The debonding process may be achieved either by applying an out-of-plane mechanical delamination force on the upper-bounding plate[296,297] or by simply peeling off the plate starting from its one end (peeling-by-tension)[298,299] or by pressurized bulging of the plate through controlled injection of a less viscous fluid (gas) at the interface of more viscous fluid (liquid) & the upper-bounding plate (peeling-by-bending)[29,225]. The viscoelasticity of the underlying polymeric substrate and the elasticity of the upper-bounding plate play a key role in the formation of the complex Saffman-Taylor-like instabilities[226,227,294]. Nase *et al*[296] showed the crossover from the "viscoelastic" regime (formation of bulk fingering instabilities[300,301], where the fingering wavelength varies with the initial viscous film-thickness and the normal debonding speed) to an "elastic" regime (formation of the interfacial crack propagation[302–304], where the fingering wavelength varies only with the initial viscous film-thickness). The process of debonding of a flat & rigid plate from purely elastic adhesive solids like (poly)dimethylsiloxane (PDMS) polymer as a function of temperature causes dynamical changes in viscous fingering patterns, owing to the temperature-dependent degrees of cross-linking in the polymer[226,296,301]. Gong *et al*[297] showed the formation of bulk fingering instabilities and cavities on mechanical separation of the two rigid bounding plates confining a thin film of Polystyrene (PS) of low molecular weight at its glass-transition temperature. Housseiny *et al*[295] theoretically, investigated that the taper angle & the out-of-plane bending of the upper-bounding elastic plate over the gas-liquid interface play a critical role in the suppression of the viscous fingering instabilities, developed while the displacement of a viscous liquid by an injected gas in a radial Hele-Shaw cell. The classical "Saffman-Taylor instabilities" are found to vanish by replacing the rigid plate (high bending rigidity) with an elastic membrane (low bending rigidity) in a Hele-Shaw cell[29]. Despite extensive efforts in analyzing the viscous fingering instabilities from the conventional mechanical peeling and pressurized bulging techniques in the microscale systems[225,291,296,297,299], the involved mechanisms behind the instabilities in spontaneous blistering of the elastic membranes such as 2D materials over the polymeric surfaces, still remain unexplored. The lack of attention, paid to the spontaneous blistering of a 2D material over any viscoelastic substrate[305], led to the overlooked attempts in viscous fingering in the 2D material blisters. The thickness-dependent elasticity of a 2D material can be utilized to investigate the growth dynamics of the viscous fingering instabilities while it's blistering over a viscoelastic substrate, as the out-of-plane bending rigidity decreases from multilayer to monolayer of the 2D material[23,36,306].

The investigations on the adhesion mechanics & the spontaneous blistering of the 2D materials are only limited to the rigid & solid substrates[24,288,305,307–312], where the substrate-based instabilities remain absent. The spontaneous blistering of the MLG flakes over a poly(vinyl) alcohol (PVA) substrate has been recently observed through a polymer-curing assisted technique[49], but the elastic-solid based instabilities still remain unexplored in such a system. In this work, we strategically investigate the elastic-solid as well as viscoelastic-substrate-based instabilities in the spontaneous blistering of the MLG flakes over the PVA substrate upon manipulating the polymeric-layer content. In order to investigate the instabilities, we captured the interface as well as the surface morphologies of the sub-micron blisters using interference reflection microscopy (IRM) and atomic force microscopy (AFM), respectively. The interference patterns, observed across the MLG blisters through IRM, have been analyzed rigorously, which are found to be correlated with their height profiles. We propose a "blister-collapse model" to elucidate the mechanism behind the onset of solid-based instabilities on the basis of hoop compression. The interplay between the in-plane compression/ stretching stiffness and the out-of-plane bending stiffness of the 2D flakes while blistering determines the ratio of the blister-height to the flake-thickness, which are correlated with the solid as well as substrate-based instabilities in the blisters. We also investigated (i) the effect of tapering angle on the finger growth-dynamics, and (ii) the impact of temperature on the viscous fingering patterns under the spontaneously formed MLG blisters. Our investigations provide fundamental & practical insights into the adhesion and debonding mechanisms of the 2D materials for establishing a better understanding of the elastic stresses as well as the vdW interactions acting within the 2D material blisters.

3.2 Experimental methods

3.2.1 Ice-water adsorption assisted PVA-curing induced blistering of MLG flakes

Prior to the exfoliation experiments, borosilicate glass or Pyrex (Borofloat®) substrates (size: 1 cm × 1 cm) are thoroughly cleaned in trichloroethylene, acetone, and methanol, each for 10 min at their respective boiling temperatures and then rinsed in isopropyl-alcohol and DI water. Thereafter, the glass substrates are dried and cleaned further with oxygen plasma. A cleaned borosilicate glass substrate is spin-coated with a thin layer of 4% w/w PVA [Alfa Aesar™, 86-89% hydrolyzed, av. Mw ~ 10,000-20,000, having viscosity $\mu \simeq 4.5$ - 4.7 mPa.s (measured using Rheometer: Anton Paar MCR102), and surface tension $\sigma \simeq 38.1$ - 38.3 mN/m (measured using Force tensiometer: Attension Sigma-700 by Biolin Scientific at the room temperature)] at 1600 rpm for 60 s. The PVA-coated glass substrate is placed over a thermoelectric cooler plate at a temperature of ~5°C in a normal atmosphere with relative humidity of 30±2% for 10-20 s. As a consequence, the cold and tiny water droplets (mist) get adsorbed on the surface of the PVA-coated glass substrate. Thereafter, a Nitto tape decorated with MLG flakes is placed in conformal contact to the PVA-coated glass substrate, followed by a brief thermal treatment at ~120°C for 60 s on a hot plate. The Nitto tape is then peeled off slowly from one of the ends of the substrate, once the sample is rapidly cooled down to room temperature. It is to be noted that the RMS roughness of a flat MLG flake is ~ 0.5 nm, the RMS roughness of the spin-coated PVA polymeric film is ~ 1.5 nm, and the RMS roughness of Pyrex (borosilicate glass) is ~ 0.5 nm for selected areas of 1 μm × 1 μm each. It should also be noted that the PVA film is not cured just after the spin-coating and prior to the exfoliation step. The PVA polymer with the prescribed properties facilitates appreciable deposition-yield and sufficient MLG blister-density. The hydrophobic-to-hydrophilic interface provided by the MLG/PVA stack is found to be highly suited for the confinement of water molecules to form the blisters.

3.2.2 Characterizations

Optical identification of the blisters of high-quality single-crystalline graphene flakes, having elastic-solid or viscoelastic-substrate-based instabilities, has been carried out under an optical microscope through interference reflection microscopy. The Raman spectroscopic measurements have been carried out using a HORIBA LabRAM HR Evolution system on the identified MLG blisters in ambient atmospheric conditions. The output power of the laser light is kept low (to avoid local heating) at ~1 mW for the laser excitation wavelength of 532 nm using a 100× air objective lens (NA=0.8) in a confocal microscopy setup. The acquisition time is kept 10 s with a detector grating of 1800 lines mm^{-1}. The tapping mode atomic force microscopy (AFM) measurements in air have been performed with a standard silicon cantilever on a Bruker MultiMode-8 AFM setup. The AFM data visualization and analyses have been carried out using Gwyddion software.

3.3 Results and Discussion

3.3.1 Interference from a thin film of varying thickness (confined water inside a blister) due to reflected light

We consider the simplified assumptions that the blister is perfectly circular (axisymmetric) in shape, which is completely filled with water. As we did not observe a noticeable change in the shape of the blister even after a period of 80 days (see figure

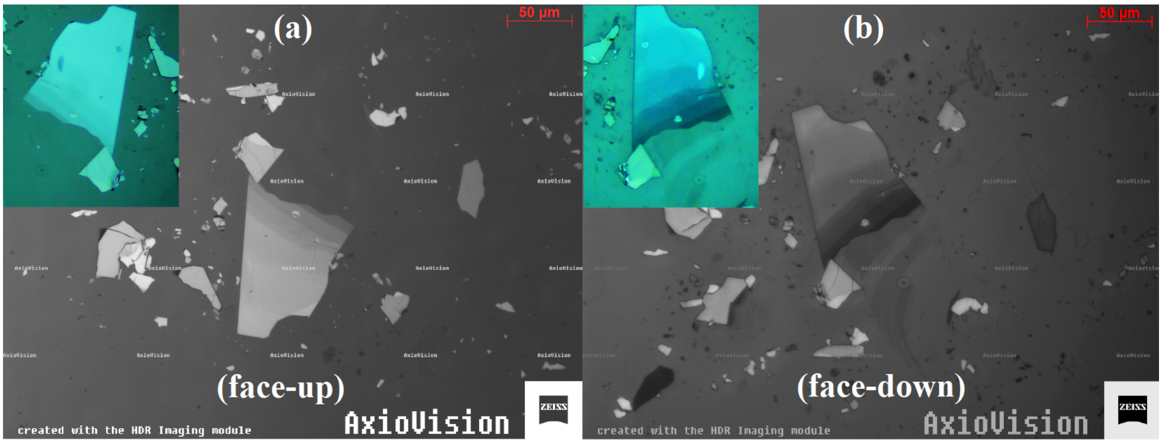
(a)
50 µm
(face-up)
created with the HDR Imaging module
AxioVision
(b)
50 µm
(face-down)
created with the HDR Imaging module
AxioVision

Figure 3.1: The high-resolution optical images, showing (a) face-up oriented graphene flakes, and (b) face-down oriented graphene flakes deposited over PVA-coated Pyrex substrate under monochromatic-light illumination (Inset: the optical images under white-light illumination). The optical contrast for the PVA-supported 2D flakes (in upside-down or face-down orientation) is sufficiently higher than that for the face-up orientation of the flakes, which significantly helps in the identification of single to few-layer flakes[47,48]. Further, the different kinds of shapes of MLG flakes can be easily characterized with the help of the interference patterns (rings or fringes), optically visible at the 'flake-PVA' interfaces.

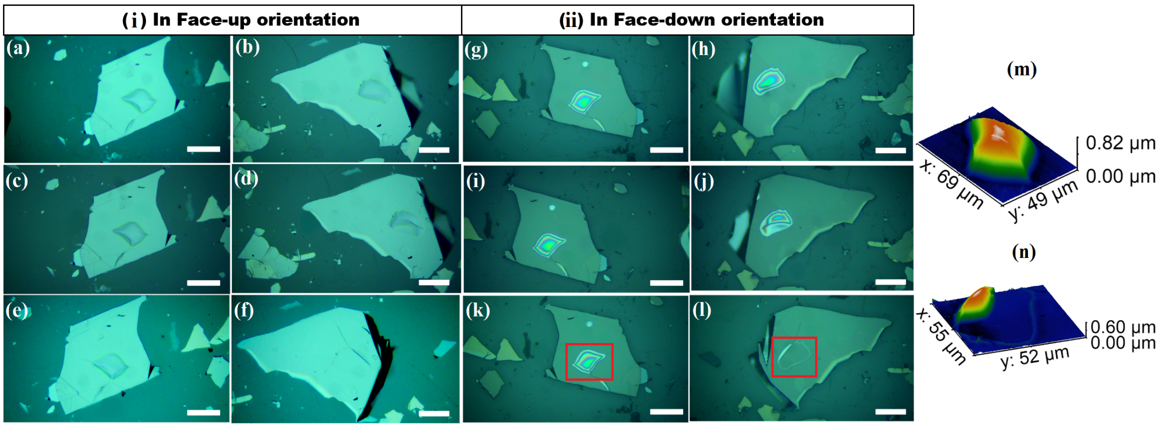
(i) In Face-up orientation
(ii) In Face-down orientation
(a)
(b)
(g)
(h)
(c)
(d)
(i)
(j)
(e)
(f)
(k)
(l)
(m)
0.82 µm
0.00 µm
x: 69 µm
y: 49 µm
(n)
0.60 µm
0.00 µm
x: 55 µm
y: 52 µm

Figure 3.2: The optical images, showing the time-lapse deflation of the MLG blisters, when optically visualized in [i:(a-f)] face-up orientation, and [ii:(g-l)] face-down orientation; the optical images (a,b,g,h) are captured at the beginning just after the deposition, (c,d,i,j) are captured after a time-lapse of ∼ 12 hours, and (e,f,k,l) are captured after a time-lapse of ∼ 24 hours with (m & n), depicting the corresponding AFM topographic 3D images of the blisters (shown by red squares in (k & l), respectively) (scale bar: 50 μm). The Newton's rings or interference patterns over a blister change as the confined matter releases with time. The time-lapse deflation of the blisters can be easily detected by analyzing the change in the interference patterns. Therefore, any bulk or surface events (e.g. deflation, folds, fingering etc.) can be visualized by just focusing the laser light beam at the interface of the MLG blister and the supporting layer of PVA.

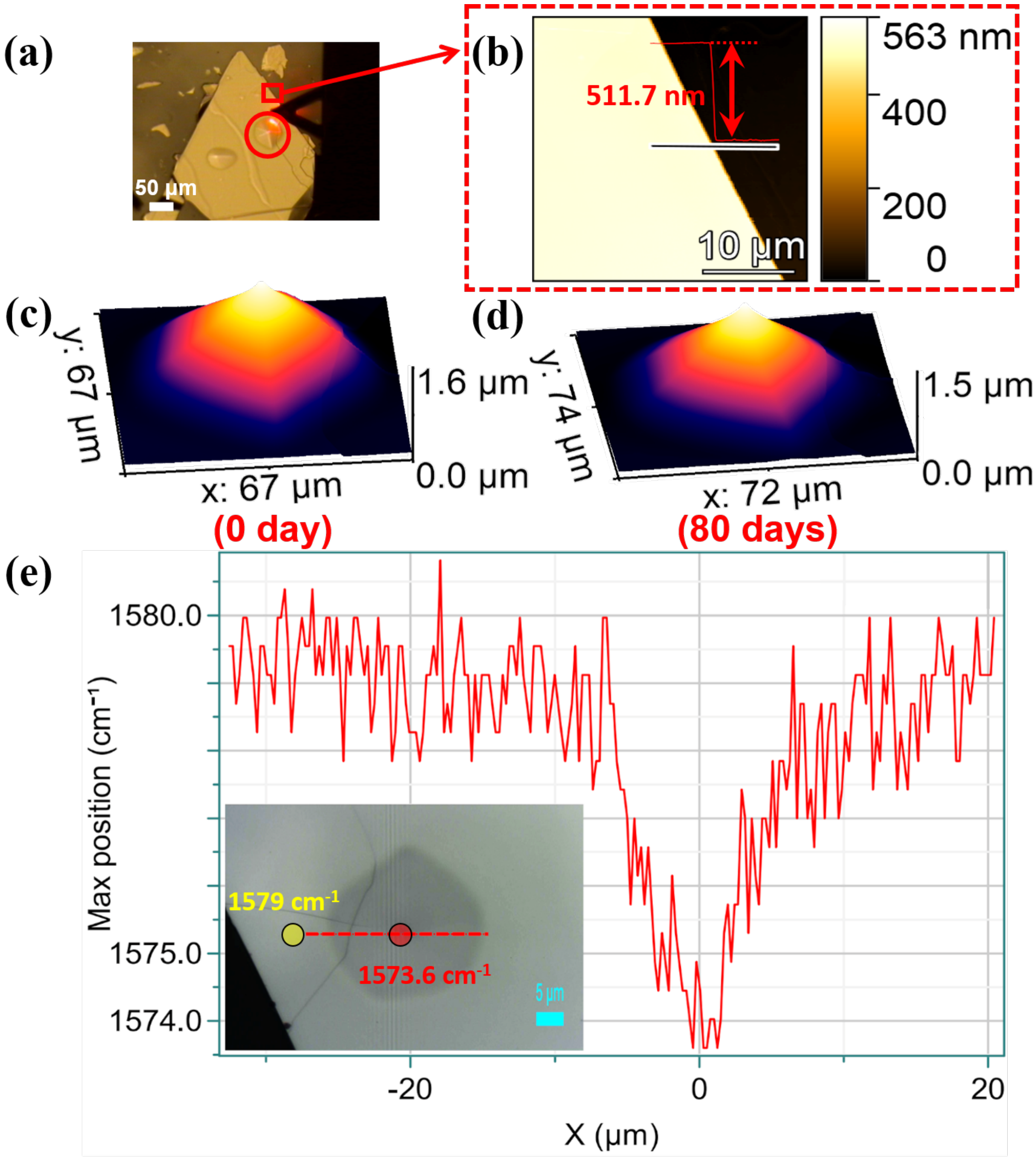

Figure 3.3: (a) Optical image, showing the MLG sub-micron blisters with located AFM-tip; (b) AFM topographic image captured at the edge of the MLG flake (shown by a red square in (a)) for deducing the thickness of the flake (measured from the PVA surface); [(c), (d)] AFM topographic 3D images, showing negligible deflation of the blister (encircled in red in (a)) even after a period of 80 days; and (e) Raman mapping of the G-peak position along a line (marked in red) across the blister, showing the accumulation of tensile strain at the center of the blister with a red-shifting of $\sim 5.4\text{cm}^{-1}$ with respect to the flat region of the MLG flake[49]. The deflation-free nature of the blisters, as depicted by their time-lapse AFM topographic images (captured with standard Silicon cantilever in tapping mode with consistent parameters) allow us to consider the confinement of water (liquid) inside the sub-micron blisters[2].

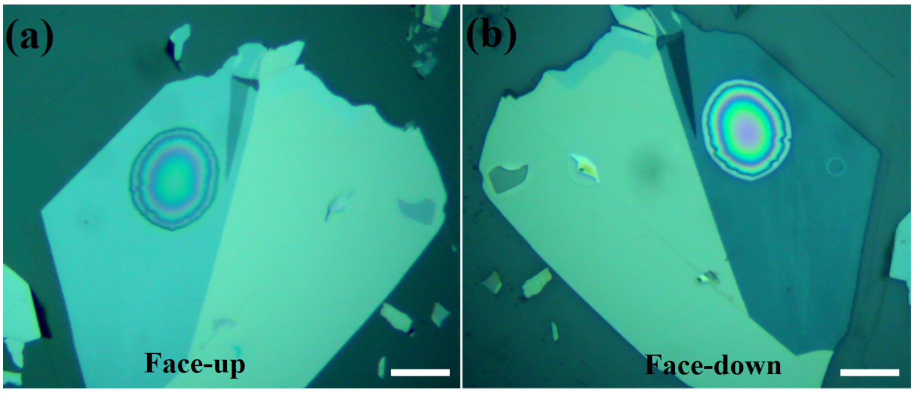

Figure 3.4: Optical images (with incident white light) of a few-layer graphene blister in (a) face-up and (b) face-down orientation (scale bar: 20 μm). The complementary Newton's rings in the cases (a) & (b) are formed by the light beams, reflected from the confined water inside the blister.

3.3), we consider the confinement of water (liquid) molecules inside the blister, for simplicity.

Optical path difference between interfering rays: 3 and 4 in the ray-diagram (see figure 3.5(a)),

$$\Delta = \mu_w(MN + NO) + \frac{\lambda}{2} - \mu_{air} PQ$$

where, μ_{air} = refractive index of air = 1, μ_w = refractive index of confined water, and λ = wavelength of incident light. (the additional path difference of $\frac{\lambda}{2}$ is due to a phase change of π on reflection of the ray: 4 from a rare (water)-to-dense (MLG) medium interface). In right triangle ΔPQR,

$$\cos(90^\circ - \mathrm{i}) = \frac{\mathrm{PQ}}{\mathrm{PR}}$$

since, $PR = MO = MS + SO = 2MS$

$$\tan(90^\circ - r) = \cot r = \frac{SN}{MS}$$

since, $SN = t_w, MS = \frac{PR}{2}$

$$PR = 2t_w \tan r$$

$$PQ = 2t_w \tan r \sin i$$

In right triangle ΔMSN,

$$MN = NO = \frac{t_w}{\cos r}$$

hence, we get,

$$\Delta = \frac{2\mu_w t_w}{\cos r} - 2t_w \tan r \sin i + \frac{\lambda}{2}$$

taking $r = 0$ for normal incidence of rays, we obtain

$$\Delta = 2\mu_w t_w + \frac{\lambda}{2}$$

We consider the case, where, the radius of curvature R, and the radius of Newton's ring ρ are sufficiently larger than the water-film thickness t_w. From figure (3.5(b)), using Pythagoras theorem in right triangle ΔOAB, we get

$$t_{air} = \frac{\rho^2}{2R} = t_w$$

.

Since, from the figure 3.5(b), we can write, $t_w + \tau_g = t_{air} + \tau_g$; where, t_w, t_{air}, and τ_g are the thicknesses of confined water-film, the air-film (in between the face-down blister and the glass slide), and the MLG flake, respectively. Therefore, it is clear that $t_{air} = t_w = h$ (height measured from AFM).

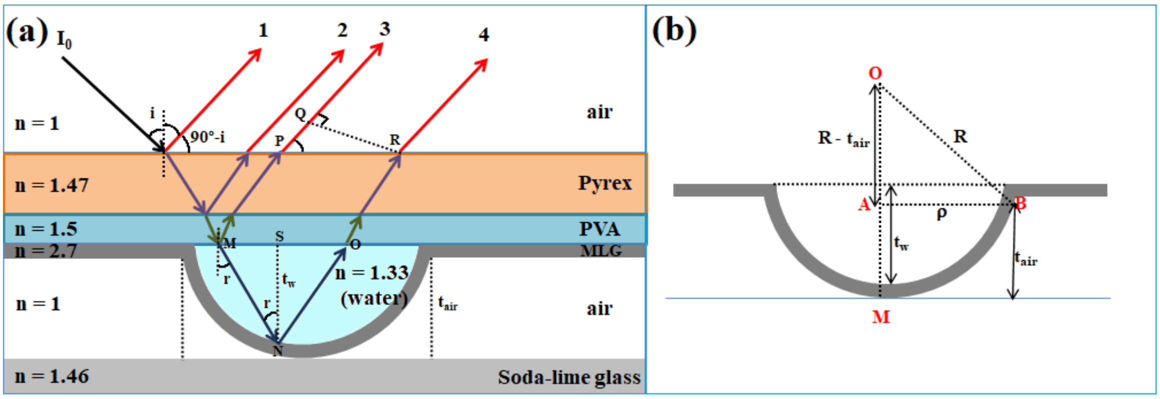

Figure 3.5: (a) Schematic of the Newton's ring model & optical ray-diagram for the interference from a tiny gap of varying height (blister) due to reflected light, and (b) schematic representation of the curved geometry.

If, the diameter of a Newton's ring $D = 2\rho$.

$$\Delta = \mu_w \frac{D^2}{4R} + \frac{\lambda}{2}$$

for a dark ring (destructive interference), $\Delta = (2n+1)\frac{\lambda}{2}$, where, $n = 0, 1, 2, ...$, while for a bright ring (constructive interference), $\Delta = n\lambda$, where, $n = 1, 2, ...$

Therefore, for n^{th} dark ring,

$$\mu_w \frac{{\rho_n}^2}{R} = 2\mu_w t_w = n\lambda \tag{3.1}$$

with $n = 0, 1, 2, ...$ This implies that the Newton's rings are unequally spaced, with a dark ring at the edge (i.e. at $t_w = 0 \Rightarrow n = 0$).

3.3.2 Significance of h/τ in blistering the MLG flakes

The MLG bubbles (circular blisters), showing significant bending stiffness, follow the non-linear elastic plate model (4^{th} order of radial distance r, i.e. $w(r) = h[1 - (\frac{r}{a})^2]^2$, for $h/\tau \lesssim 1.5$[1,23,49]). The change in the interfacial adhesion of the MLG flakes with the PVA substrate through blister-formation, can be expressed in terms of the interfacial energy densities of MLG-content, substrate-content and MLG-substrate interfaces, respectively, as $\Delta\gamma = \gamma_{Gc} + \gamma_{sc} - \gamma_{Gs}$. The net interfacial adhesion energy of the MLG flake (acting as a nonlinear elastic plate, having a significant bending stiffness $B \sim N^3$) over the PVA substrate is given by, $\Gamma = \Delta\gamma + \gamma_l(\cos\theta_G + \cos\theta_s)$, where γ_l is the surface tension of a liquid (water) with θ_G and θ_s are the contact-angles of the liquid with the MLG and the substrate (PVA), respectively, which gives rise to the following equation[49]:

$$\Gamma = \zeta E_{2\text{D}} \left(\frac{h}{a}\right)^4 + 32\frac{Bh^2}{a^4} + \gamma_w(\cos\theta_G + \cos\theta_s)$$

where $\zeta = \frac{896585+529610\nu-342831\nu^2}{960498(1-\nu^2)}$, ν is the Poisson's ratio, h/a is the aspect-ratio of the blister, and E_{2D} is the 2D elastic extensional (in-plane) stiffness of the MLG flake. We can rewrite the above equation as

$$\Gamma = \Gamma_{\text{stretching/compression}} + \Gamma_{\text{bending}} + \Gamma_{\text{fluid-interaction}}$$

where the ratio of interfacial adhesion energy contributions from in-plane stretching/compression stiffness (I^{st} term) and the out-of-plane bending stiffness (II^{nd} term) is directly proportional to $(h/\tau)^2$.

3.3.3 vdW interactions affect the aspect-ratio of the blisters

The force-balance in the direction normal to the elastic sheet yields coupling between the effective fluid-pressure (p) and the deflection (h) as follows (Föppl-von Kármán (FvK) equation) :

$$p = B\nabla^4 h - T\nabla^2 h \tag{3.2}$$

where the first term depicts the effect of bending stresses (B), and the second term depicts the effect of imposed tension (T) in the development of net pressure (P)[196,313]. The tension stresses dominate when the 2D in-plane elastic stiffness (E_{2D}) is much larger than the out-of-plane bending stiffness (B), this is mostly true for 'peeling-by-tension' experiments (similar to our viscous fingering results in the tension-dominated regime). Since, we observed $h/\tau \gtrsim 2$ for most of the MLG blisters, which implies the least effect of bending rigidity in the blistering of the MLG flakes, therefore the effective bending stiffness (B_{eff}) would scale as N (not N^3) due to considerable interlayer slippage resulting from weak interlayer vdW interactions. The FvK number (bendability) for the multilayered 2D materials $\mathcal{K} = \frac{E_{2D}a^2}{B_{\text{eff}}} \gg 1$, which resembles the tension-dominated regime.

We assume the case of slippery interface while formation of the blister through conventional PVA-curing induced blistering technique[49]. The deflection profile of an axisymmetric MLG blister (having $h/\tau \gtrsim 2$) in the membrane-limit is given by

$$w(r) = h\left(1 - \frac{r^2}{a^2}\right), \tag{3.3}$$

where $h \ll a$, and the area of the bulged surface is assumed to be $A' \approx \pi a^2$ for $h/\mathrm{a} \to 0$. The deflection profile allows the direct solution to the in-plane equilibrium of the membrane limit of Föppl-von Kármán (FvK) equations in terms of displacements

$$u(r) = \frac{3-\nu}{4}\frac{h^2}{a}\left(\frac{r}{a} - \left(\frac{r}{a}\right)^3\right) + u_s\frac{r}{a}, \tag{3.4}$$

where u is the in-plane displacement and ν is the Poisson's ratio, and u_s accounts for the in-plane interfacial sliding at the edge of the blister ($r = a$). The kinematics results in the radial and circumferential strain fields, such that

$$\epsilon_r = \frac{\mathrm{d}u}{\mathrm{d}r} + \frac{1}{2}\left(\frac{\mathrm{d}w}{\mathrm{d}r}\right)^2 \quad \text{and} \quad \epsilon_\theta = \frac{u}{r}. \tag{3.5}$$

For the slippery boundary conditions, the plane-stress classical Lame solution in the linear elastic regime can be adopted. The radial and circumferential stress components (in the generic far-field behavior) are as follows:

$$N_r = \frac{A}{r^2} + T_{\text{pre}} \quad \text{and} \quad N_\theta = -\frac{A}{r^2} + T_{\text{pre}}\ , \tag{3.6}$$

where $N_r = \sigma_r\tau$ and $N_\theta = \sigma_\theta\tau$; σ_r and σ_θ are radial and circumferential stresses, respectively; τ is the membrane thickness; A is a constant to be determined; T_{pre} ($= E_{\text{2D}}\varepsilon$)

is the mechanical pretension in the membrane, where $E_{2\mathrm{D}}$ is the in-plane elastic stiffness of the membrane and ε is the induced mechanical strain[314]. The radial stress and displacement have to be continuous at the edge of the blister. Using equation 3.3-3.6 and linear Hooke's law, we obtain

$$A = \frac{E_{2\mathrm{D}}h^2}{4} \quad \text{and} \quad u_s = \frac{(1-v)aT_{\mathrm{pre}}}{E_{2\mathrm{D}}} - \frac{(1+v)h^2}{4a}. \tag{3.7}$$

From the continuity of radial stress across the edge of the blister, we can have $N_r^+ = N_r^- = T = \frac{E_{2\mathrm{D}}h^2}{4a^2} + T_{\mathrm{pre}}$. Since, the total free energy as well as the aspect ratio (h/a) of the blister is determined solely by the competition between vdW and elastic strain energies of the 2D material system. The total potential energy for the MLG blister with a confined matter having a finite compressibility at a raised temperature can be given by,

$$\Pi = \mathrm{c}\,(T)\,h^2 + \pi a^2\Delta\gamma + E_{\mathrm{int}}(V) = \mathrm{c}\left(\frac{E_{2\mathrm{D}}h^4}{4a^2} + T_{\mathrm{pre}}h^2\right) + \pi a^2\Delta\gamma + E_{\mathrm{int}}(V) \tag{3.8}$$

where c is a constant prefactor to be determined (unlike the case of clamped boundary conditions, where it is a function of Poisson's ratio ν), $\Delta\gamma$ is the overall surface energy density, and $E_{\mathrm{int}}(V)$ is the free internal energy of the blister content of volume $V = \pi a^2 h/2$ and pressure $P = -\frac{\partial E_{\mathrm{int}}}{\partial V}$. Now, by minimizing the equation 3.8 with respect to h and a, we obtain

$$\frac{\partial\Pi}{\partial h} = 4ch^3\frac{E_{2\mathrm{D}}}{4a^2} + 2chT_{\mathrm{pre}} - \frac{\pi}{2}a^2P = 0 \quad \text{and} \quad \frac{\partial\Pi}{\partial a} = -2c\frac{E_{2\mathrm{D}}h^4}{4a^3} + 2\pi a\Delta\gamma - \pi ahP = 0. \tag{3.9}$$

By eliminating P in equation 3.9, we obtain

$$\left(\frac{h}{a}\right)^4 + \frac{8T_{\mathrm{pre}}}{5E_{2\mathrm{D}}}\left(\frac{h}{a}\right)^2 - \frac{4\pi\Delta\gamma}{5\mathrm{c}E_{2\mathrm{D}}} = 0. \tag{3.10}$$

The real solutions of equation 3.10 exist, only when $\Delta\gamma > 0$, for which the formation of the blisters is energetically favorable. We can non-dimensionalize the parameters T_{pre} and $\Delta\gamma$ as $\tilde{T}_{\mathrm{pre}} = \frac{T_{\mathrm{pre}}}{E_{2\mathrm{D}}}$ and $\Delta\tilde{\gamma} = \frac{\Delta\gamma}{E_{2\mathrm{D}}}$, such that $\tilde{T}_{\mathrm{pre}} \ll 1$ and $\Delta\tilde{\gamma} \ll 1$, since for graphene, $E_{2\mathrm{D}}$ ($\sim$ 340 N/m) is relatively very large. For the blistering of MLG flakes at the raised temperature over the slippery interface, T_{pre} is negligible. Therefore, the overall surface energy dominates over the pretension i.e. $\tilde{T}_{\mathrm{pre}} \ll \Delta\tilde{\gamma}$, we obtain

$$\left(\frac{h}{a}\right) = \left(\frac{4\pi\Delta\tilde{\gamma}}{5c}\right)^{\frac{1}{4}}. \tag{3.11}$$

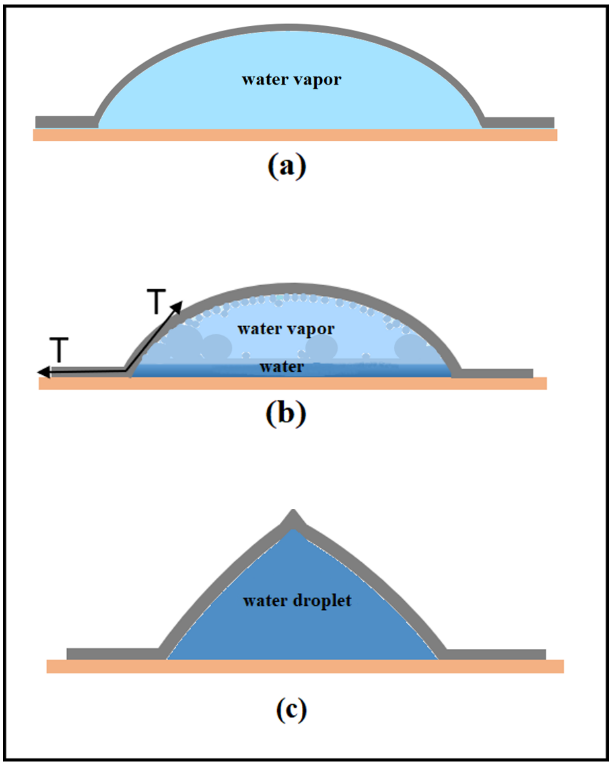

Figure 3.6: Schematic representation of the ‘blister-collapse model’: (a) water-vapor pressure driven blistering of MLG flake, (b) the tapered region of the MLG flake around the blister-edge collapses downwards due to phase-transition of water-vapor into water droplets and thereby, generating a pretension, which induces the hoop compression, (c) the suppression of hoop compression results into the development of elastic solid-based instabilities in the blister.

3.3.4 Effect of hoop compression

We considered the slippery boundary conditions for the MLG blisters formed at the raised temperature, where the initial radius of the blister does not remain constant. While cooling down the sample to room temperature, the condensation of moisture-vapor into water droplets occurs via drop-wise condensation, and simultaneously, it allows the tapered region of the MLG flake around the blister-edge to collapse downwards, thereby generating a radial pretension in the blister (see Figure 3.6). The pretension causes the development of pressure within the blister[28,34,196], given by $p \sim \frac{T_{\text{pre}}h}{a^2}$. The pretension induces a hoop (azimuthal) compression, which is suppressed with the onset of the solid-based instabilities in the blister.

For the compressive stress $T_{\mathrm{pre}} < 0$, and the total energy of the blister-system is given by (neglecting the contribution from the internal energy of the blister content),

$$E_{\mathrm{tot}} = \mathrm{c}\left(\frac{E_{\mathrm{2D}}h^4}{4a^2} - |T_{\mathrm{pre}}|h^2\right) + \pi a^2 \Delta\gamma. \tag{3.12}$$

By minimizing E_{tot} with respect to a at constant h, we find

$$\left(\frac{h}{a}\right)^4 = \frac{4\pi\Delta\tilde{\gamma}}{\mathrm{c}}. \tag{3.13}$$

Now, the total energy of the blister (under hoop compression) as a function of a, can be rewritten as

$$E_{\mathrm{tot}} = a^2\left(2\pi\Delta\gamma - \mathrm{c}|T_{\mathrm{pre}}|\sqrt{\frac{4\pi\Delta\gamma}{\mathrm{c}E_{\mathrm{2D}}}}\right). \tag{3.14}$$

For the blister to be unstable, the energy must be released by increasing the perturbations, i.e. $E_{\mathrm{tot}} \leq 0$. This results in the condition

$$|\tilde{T}_{\mathrm{pre}}| \geq \sqrt{\frac{\pi\Delta\tilde{\gamma}}{\mathrm{c}}}. \tag{3.15}$$

In this case, the blister is highly susceptible to solid-based instabilities. In terms of the compressive strain ε, the condition for the blister to be unstable is

$$|\varepsilon| \geq \sqrt{\frac{\pi\Delta\tilde{\gamma}}{\mathrm{c}}}. \tag{3.16}$$

On the other hand, the compressive stress required for the blister to be stable (i.e $E_{\mathrm{tot}} > 0$) is

$$|\tilde{T}_{\mathrm{pre}}| < \sqrt{\frac{\pi\Delta\tilde{\gamma}}{\mathrm{c}}}. \tag{3.17}$$

In terms of the compressive strain ε,

$$|\varepsilon| < \sqrt{\frac{\pi\Delta\tilde{\gamma}}{\mathrm{c}}}. \tag{3.18}$$

3.3.5 Partial elastic wetting analogy for the liquid-drop model

In order to find the constant prefactor c, we enforce the force balance at the contact line of the blister-system at equilibrium (considering the liquid-drop model for simplicity)[289],

$$\cos\beta_0 = \frac{N_r^+ + \gamma_{ms} - \gamma_{ls}}{N_r^- + \gamma_{lm}}. \tag{3.19}$$

Employing the small-angle approximation ($\beta_0 \approx \sin\beta_0 = \sqrt{1-\cos^2\beta_0}$) and for the radial tension (having continuity across the edge of the blister) to be much greater than any interfacial tension in the system, we can have $N_r^+ = N_r^- = T = \frac{E_{2\mathrm{D}}h^2}{4a^2} + T_{\mathrm{pre}} \gg \Delta\gamma$ (since for graphene, Young's modulus $E \sim 1$TPa), we obtain

$$\beta_0 = \sqrt{\frac{2\Delta\gamma}{T+\gamma_{lm}}} \approx \sqrt{\frac{2\Delta\gamma}{T}}, \tag{3.20}$$

where β_0 is the contact angle at the edge of the blister, $\Delta\gamma$ is the resultant energy density (i.e. energy per unit area) for the blister system. Since, $(1-\cos\beta_0)$ and the strain components scale as h^2/a^2[35], therefore the contact angle can be converted to the aspect-ratio of the blister. Using this, the equation 3.19 can be rewritten as

$$\left(\frac{h}{a}\right)^4 + 4\tilde{T}_{\mathrm{eff}}\left(\frac{h}{a}\right)^2 - 4\Delta\tilde{\gamma} = 0, \tag{3.21}$$

where $\Delta\tilde{\gamma} = \frac{\gamma_{lm}+\gamma_{ls}-\gamma_{ms}}{E_{2\mathrm{D}}}$ and $\tilde{T}_{\mathrm{eff}} = \frac{\gamma_{lm}+T_{\mathrm{pre}}}{E_{2\mathrm{D}}} = \tilde{\gamma}_{lm} + \tilde{T}_{\mathrm{pre}}$. Herein, the overall surface energy density (interfacial tension) $\Delta\gamma = \gamma_{lm} + \gamma_{ls} - \gamma_{ms}$, where γ_{lm}, γ_{ls} and γ_{ms} are the surface energy densities for the three interfaces: membrane-liquid, substrate-liquid and membrane-substrate interfaces, respectively.

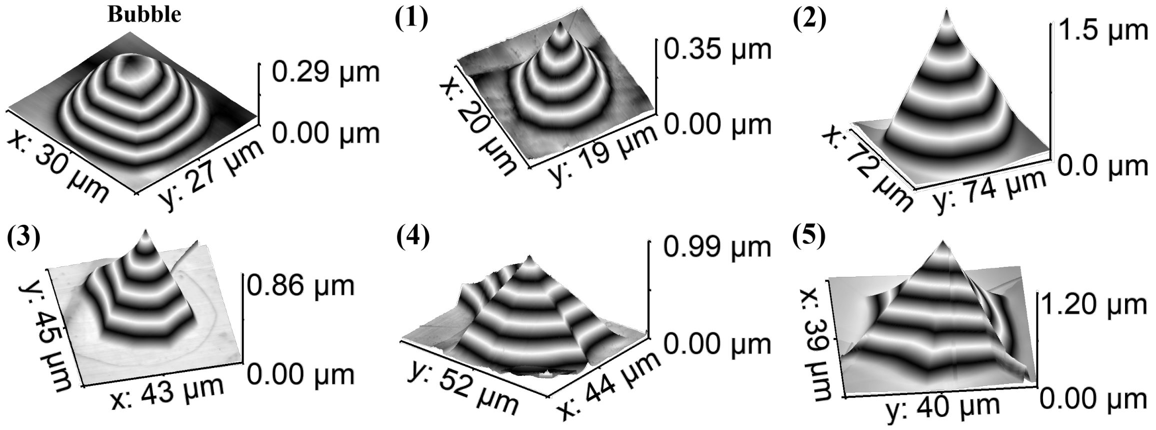

Figure 3.7: AFM topographic images of the tent-like MLG blisters (having a pointed tip at the center, where a maximum tensile strain accumulates). The AFM 3D profile of a circular blister (bubble) is presented for reference.

Since, the solutions exist in the case of $\Delta\tilde{\gamma} > 0$, which means that the formation of the blisters is energetically favorable only when $\Delta\tilde{\gamma} > 0$, where $\Delta\tilde{\gamma}$ is the change of interfacial energy densities for the formation of a blister. We can then find out the equilibrated aspect ratio on solving the above equation 3.21 as

$$\left(\frac{h}{a}\right)^2 = -2\tilde{T}_{\text{eff}} + 2\sqrt{\tilde{T}_{\text{eff}}^2 + \Delta\tilde{\gamma}}. \tag{3.22}$$

Now, we can analyze the equation 3.22 by considering different conditions:

(i) For sufficiently small strains i.e. $|\tilde{T}_{\text{eff}}| \to 0$: We obtain on further simplifying the equation 3.22

$$\left(\frac{h}{a}\right) = \sqrt{2}\,(\Delta\tilde{\gamma})^{1/4} - \frac{\tilde{T}_{\text{eff}}}{\sqrt{2}\,(\Delta\tilde{\gamma})^{1/4}}, \tag{3.23}$$

which implies that for $\tilde{T}_{\text{eff}} < 0$ (compressive strain), the aspect ratio (h/a) increases with respect to that in the absence of the strain[28,35].

(ii) Pretension dominates over the overall surface energy : Assuming $\tilde{\gamma}_{lm} \sim \Delta\tilde{\gamma} \ll \tilde{T}_{\text{pre}} \ll 1$ and by further simplifying the equation 3.22, we obtain

$$\left(\frac{h}{a}\right)_{\tilde{T}_{\text{pre}} \gg \Delta\tilde{\gamma}} = \left(\frac{\Delta\tilde{\gamma}}{\tilde{T}_{\text{eff}}}\right)^{1/2}. \tag{3.24}$$

Therefore, the aspect-ratio is expected to decline with the increasing pretension.

(iii) Overall surface energy dominates over the pretension : Assuming $\tilde{T}_{\text{pre}} \ll \tilde{\gamma}_{lm} \sim \Delta\tilde{\gamma} \ll 1$, then the equation 3.22 can be rewritten as

$$\left(\frac{h}{a}\right)_{\tilde{T}_{\text{pre}} \ll \Delta\tilde{\gamma}} = (4\Delta\tilde{\gamma})^{1/4}. \tag{3.25}$$

Therefore, the aspect-ratio is expected to rise with the increasing overall surface energy.

Now, on comparing the equation 3.11 viz. obtained from the concept of minimization of potential energy with the equation 3.25 viz. obtained from partial elastic-wetting analogy, both in the case when the overall surface energy dominates over the pretension, we obtain c = $\frac{\pi}{5}$. This results in the following expression for the total potential energy (E_{tot}) for the 2D material blister-system at equilibrium:

$$E_{\text{tot}} = \frac{\pi}{5}\left(\frac{E_{2\text{D}}h^4}{4a^2} + T_{\text{pre}}h^2\right) + \pi a^2 \Delta\gamma. \tag{3.26}$$

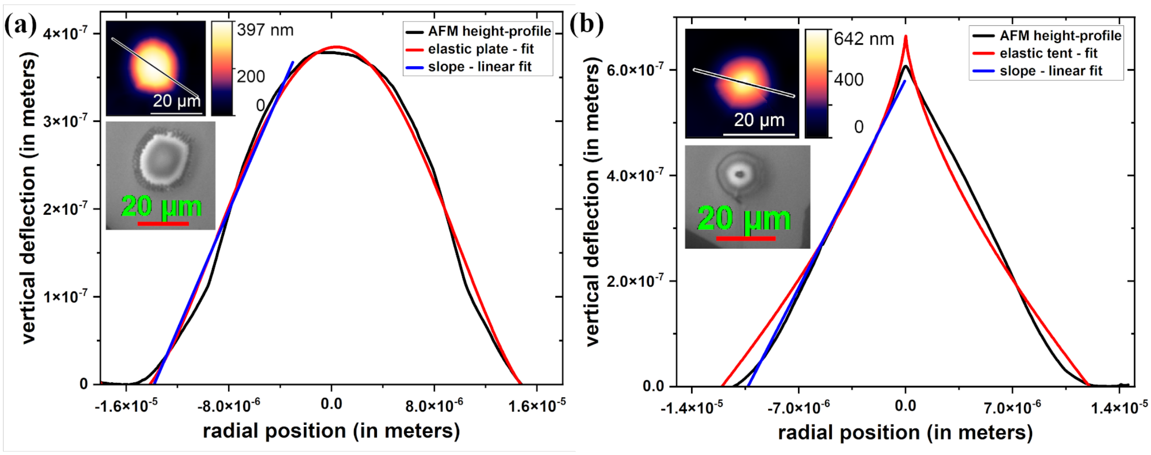

Figure 3.8: Graphical representation of the scheme employed for the determination of the height and the radius of the axisymmetric (circular) MLG blisters, following either the elastic-plate profile or the elastic-tent profile. The parameters are evaluated by fitting the shape of a blister with an appropriate profile. For determining the taper angle of a blister, the slope of the blister is fitted with a line profile. The radius a and the central deflection h of the blister is estimated by fitting the height profile of the spherical/ conical cap obtained from the atomic force microscopy (AFM) image in tapping mode. If the AFM height profile of a blister fits well with the fourth order polynomial function of radial distance r (elastic-plate profile) as, $\mathrm{w(r) = B_0 + B_1r + B_2r^2 + B_3r^3 + B_4r^4}$; then the characteristic parameters: central deflection or height h and the radius a of the blister are determined as $\mathrm{B_0}$ and $\left(-2\frac{\mathrm{B_0}}{\mathrm{B_2}}\right)^{\frac{1}{2}}$, respectively. But, if the AFM height profile of a blister fits well with the $\frac{2}{3}^{rd}$ power function of radial distance r (elastic-tent profile) as, $\mathrm{w(r) = A - Br^{2/3}}$; then the characteristic parameters: central deflection or height h and the radius a of the blister are determined as A and $\left(\frac{\mathrm{A}}{\mathrm{B}}\right)^{\frac{3}{2}}$, respectively.

3.3.6 Elastic solid- and viscoelastic substrate-based instabilities

The 2D flakes (hydrophobic in nature) have an appreciable debonding rigidity with a polymeric film of PVA solution (hydrophilic in nature) of low molecular weight & low concentration as a result of good interfacial adhesive interactions[88,291]. In the conventional PVA-curing induced spontaneous blistering approach[49], the water-vapor, arising from the vaporization of the water content in the PVA film (spin-coated at 1600 rpm for 60 s over a Pyrex substrate) while curing it at a raised temperature, gets trapped under the graphene flakes at the hydrophobic-to-hydrophilic interface, and consequently, the vapor-pressure develops to form the blisters with stable interface[309,315]. The shapes of blisters get stabilized once the trapped water-vapor condenses into the liquid phase on cooling down to room temperature[2,49,257,277]. Apart from the axisymmetric circular blisters, as obtained in our recent work[49], we also obtained pyramidal as well as tent-like MLG blisters. The optical interference reflection microscopy (see Figure 3.9(a))[47,316,317] of the PVA-supported graphene flakes facilitates an efficient optical identification (owing to enhanced optical contrast) of the monolayer to few-layer graphene flakes and the surface & interfacial events such as viscous fingering, deflation, blistering etc. using the interference patterns (see Figures 3.1 and 3.2). The fringes are formed due to the feeble interference of the light beams, reflected from the top and bottom of the confined water-droplet inside the blister (see Figure 3.5), since the optical reflection dominates over the optical transmission through MLG flakes[49,318]. The fringe patterns are found to vary with the shape and size of the blister, which can be correlated with its height profile[48].

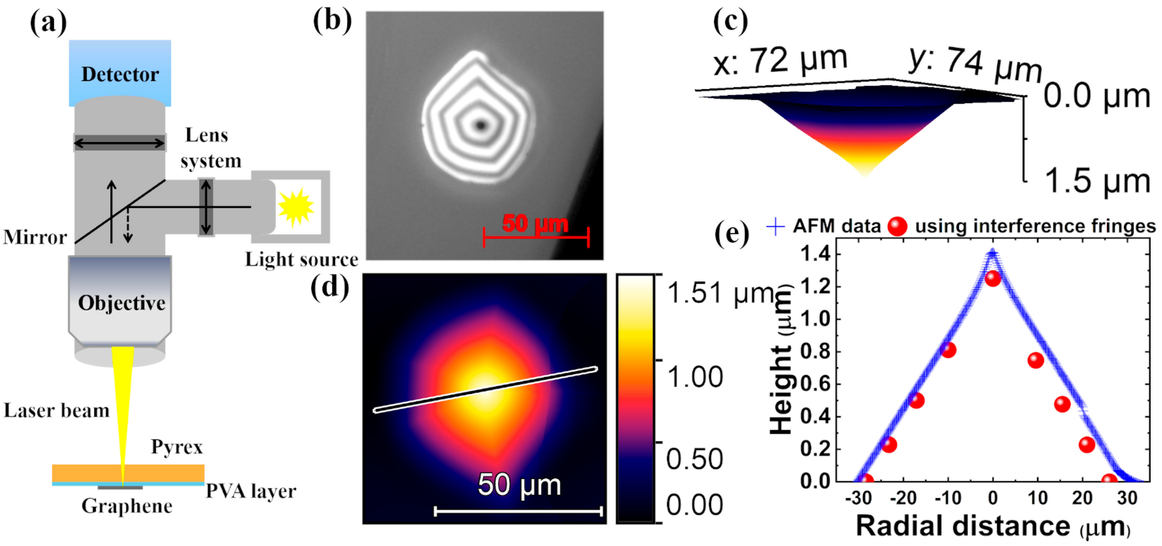

Figure 3.9: (a) The interference reflection microscopy (IRM) set-up, (b) optical image of interference fringes at the MLG blister interface, when illuminated with monochromatic light ($\lambda \sim 605$nm), (c) AFM topographic 2D image & (d) 3D image of the blister, placed in upside-down orientation to optically visualize the interface using the IRM set-up, and (e) comparison of the height profile obtained using optical analyses of the interference fringe pattern with the height profile of the blister measured using AFM, across a line marked in (d).

We observed fringes of equal as well as unequal spacing. It is well known that the fringes of equal width (δ) appear in the wedge-shaped faces (having an inclination angle $\theta = \sin^{-1}(\frac{\lambda}{2\mu_w\delta})$). We deduced the height profile h of a blister having equally-spaced fringes, using the formula $h = d\tan\theta$[48], where d is the horizontal distance of a point on the fringe pattern from the edge of the blister. It matches well with the height profile of the blister, measured using AFM (see Figure 3.9). It confirms that the blister with equally spaced fringes consists of wedge-shaped faces. For the analyses of the interference pattern of unequal fringe-widths, similar to Newton's rings[319], the height profile of the sub-micron blister can be deduced as, $h = \frac{n\lambda}{2\mu_w}$, where, $n = 0, 1, 2, ...$ for dark rings, μ_w is the refractive index of the confined water, and λ is the wavelength of the monochromatic light source, which should be of the order of the blister-height (see Section **3.3.1**). We believe that the PVA-supported MLG sub-micron circular blister (in upside-down orientation) with a finite radius of curvature causes the formation of concentric fringes of unequal widths like Newton's rings (NR) due to the variation of the depth of the confined water-droplet in accordance to the shape-profile of the blister.

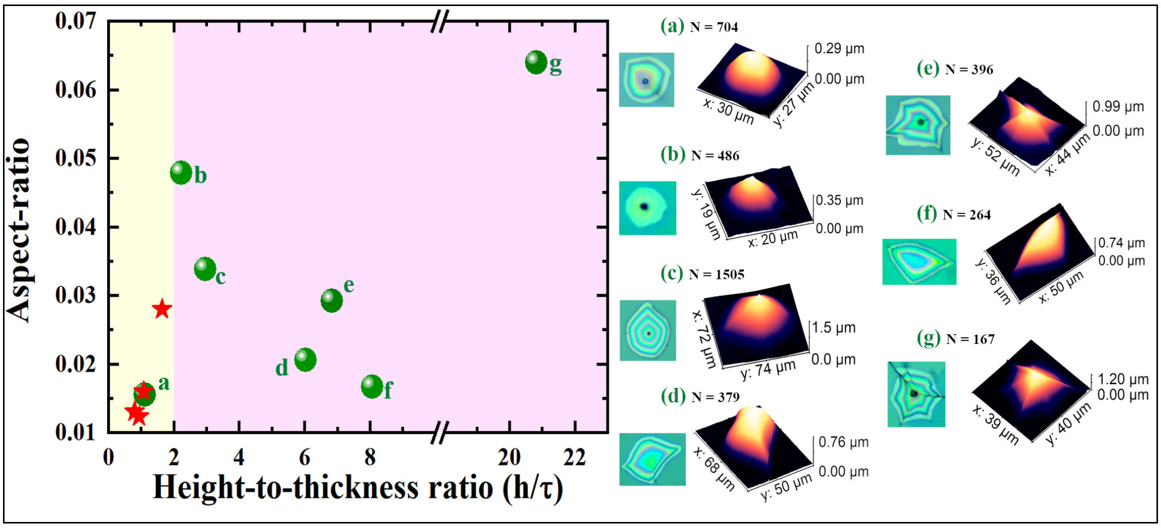

Figure 3.10: A graphical representation of the solid-based instabilities in the blisters: showing the variation in the shape-profiles of the MLG blisters (optical and AFM topographic images) with respect to their respective aspect-ratios (h/a for axisymmetric (circular) or h/L for asymmetric blisters) and the blister-height to flake-thickness ratios (h/τ). The side length L of the typical triangular pyramidal blister was experimentally determined as $L = \sqrt{\frac{4A}{\sqrt{3}}}$; the side length L of the typical trapezoidal blister was measured as $L = \sqrt{A}$; the side length L of the typical pentagonal pyramidal blister was measured as $L \simeq \sqrt{\frac{1.74V}{h}}$; and the side length L of the typical hexagonal pyramidal blister was measured as $L = \sqrt{\frac{2V}{\sqrt{3}h}}$, where V is the measured volume of the blister, A is the measured base-area of the blister, and h is the maximum vertical deflection for an asymmetric MLG blister[34]. However, for an axisymmetric (circular) blister, the characteristic parameters: height (h) and radius (a), are deduced by fitting the AFM height profile of the blister with an appropriate profile, e.g. elastic plate, tent, etc. Red stars represent the circular MLG blisters (following the elastic plate profile with a stable interface) from a recent work[49].

In our experiments, we observe different shapes of the MLG blisters such as tent-like, triangular, trapezoidal, pentagonal, hexagonal, star-like, etc. (see Figure 3.10), resulting from the elastic solid-based instabilities in the spontaneous blistering of the MLG flakes[49,273]. We investigated the shape-profile of the differently shaped MLG blisters for analyzing the instabilities. We observed that the shape-profile of the blisters varies with the ratio of blister-height to flake-thickness (i.e., h/τ). However, the aspect-ratio remains the same for a given shape-profile of the blisters with a constant elasticity of the bulged nanosheet[34]. Using the Föppl-von Kármán model for the deformation of thin elastic plates[1,49,184], we noted that the ratio of interfacial adhesion energy contributions from the in-plane stretching/ compression stiffness and the out-of-plane bending stiffness is directly proportional to $(h/\tau)^2$. Therefore, the relative dominance between the in-plane extensional stiffness and the out-of-plane bending stiffness in the blister-formation would effectively control the parameter h/τ. In our experiments, we noted the large values of h/τ even for the thick MLG flakes, which analytically indicates to result from the suppression of out-of-plane bending stresses by interlayer slippage. The interlayer sliding in the MLG flake (owing to weak vdW interlayer interactions) allows each layer to bend independently, resulting in the linear variation of overall bending rigidity with N (number of layers), as $B_{\text{eff}} = \frac{NEt^3}{12(1-\nu^2)} \sim N$ (where E is Young's modulus, $E_{2D}(= E\tau)$ is the 2D elastic stiffness, and ν is the Poisson's ratio of the MLG flake, t is the thickness of the monolayer graphene (0.34 nm), and $N = \frac{\tau}{t}$ is the number of layers in the MLG flake), in contrast to N^3 variation for perfectly glued multilayer[23,36,184,196]. The 'Föppl von Kármán (FvK) number' (bendability)[25] $\mathcal{K} = \frac{E_{2D}a^2}{B_{\text{eff}}} \gg 1$ for the multilayered 2D flakes with significant interlayer slippage resembles the dominance of elastic tension over the bending stresses, and allows us to apply the membrane-limit for the MLG blisters. We observed that the MLG blisters attain different shapes as a function of h/τ, being typically circular for the small values of h/τ, tent-like for the moderate values of h/τ, and trapezoidal, triangular, or star-like for the larger values of h/τ. Therefore, a circular blister tends to lose the axisymmetry with the increasing value of h/τ as a result of growing elastic instability in the blister[28]. Thus, the competitive interplay between the extensional and bending stresses while blistering of the multilayered 2D flakes is correlated with the extent of solid-based instability in the blisters[36]. The parameter h/τ governs the shape-profile of a blister and thereby gives rise to the shape-dependent aspect-ratio of the blister.

The MLG blisters form at the raised temperature of ~120°C and thereby, attain an equilibrium shape resulting from the vaporization of the water content (adsorbed/ absorbed) of the wet & uncured PVA film. Therefore, the interfacial slippery boundary conditions could be reasonably assumed for the formation of the MLG blisters over the PVA film (which is initially wet, and then gradually becomes viscoelastic as the temperature rises)[289]. However, in the absence of interfacial slippage, the analysis of any instability mechanism in blistering is unfeasible[25,28,289]. The total potential energy for the MLG blister with a confined matter having finite compressibility at the raised temperature would be given by,

$$\Pi = \mathrm{c}\left(\frac{E_{2\mathrm{D}}h^4}{4a^2} + T_{\mathrm{pre}}h^2\right) + \pi a^2\Delta\gamma + E_{\mathrm{int}}(V) \tag{3.27}$$

where c is a constant prefactor to be determined (unlike the case of clamped boundary conditions, where it is a function of Poisson's ratio ν[1,2]), $\Delta\gamma$ is the change of the interfacial energy densities for the blister-formation, $T_{\mathrm{pre}}(= E_{2\mathrm{D}}\varepsilon)$ is pretension, which induces a mechanical strain (ε), and $E_{\mathrm{int}}(V)$ is the free internal energy of the blister-content having volume V and pressure $P(= -\frac{\partial E_{\mathrm{int}}}{\partial V})$. The equilibrium shape of the MLG blister (having the volume $V = \frac{\pi}{2}a^2h$ in the membrane-model[1]) can be determined by minimizing the total energy with respect to h and a, and further, by eliminating the pressure P as following[34]: $\left(\frac{\pi}{2}a^2h\right)P = -h\frac{\partial E_{\mathrm{int}}}{\partial h} = -\frac{a}{2}\frac{\partial E_{\mathrm{int}}}{\partial a}$, we obtain

$$\left(\frac{h}{a}\right)^4 + \frac{8T_{\mathrm{pre}}}{5E_{2\mathrm{D}}}\left(\frac{h}{a}\right)^2 - \frac{4\pi\Delta\gamma}{5\mathrm{c}E_{2\mathrm{D}}} = 0. \tag{3.28}$$

The formation of the blister is energetically favorable, only when $\Delta\gamma > 0$. The parameters T_{pre} and $\Delta\gamma$ can be non-dimensionalized as $\tilde{T}_{\mathrm{pre}} = \frac{T_{\mathrm{pre}}}{E_{2\mathrm{D}}}$ and $\Delta\tilde{\gamma} = \frac{\Delta\gamma}{E_{2\mathrm{D}}}$, such that $\tilde{T}_{\mathrm{pre}} \ll 1$ and $\Delta\tilde{\gamma} \ll 1$, since for graphene, $E_{2\mathrm{D}}$ (∼340 N/m) is relatively very large. Solving for the aspect-ratio, we obtain from the equation 3.28:

$$\left(\frac{h}{a}\right)^2 = -\frac{4}{5}\tilde{T}_{\mathrm{pre}} + \sqrt{\frac{16}{25}\tilde{T}^2_{\mathrm{pre}} + \frac{4\pi}{5c}\Delta\tilde{\gamma}}. \tag{3.29}$$

Therefore, the interplay between the pretension (T_{pre}) and the overall surface energy ($\Delta\gamma$) with respect to the in-plane extensional stiffness ($E_{2\mathrm{D}}$) determines the aspect-ratio of the blisters. In our case, the blister attains the equilibrium shape in the presence of interfacial slippage, which allows us to consider the pretension $T_{\mathrm{pre}} = 0$, therefore only the surface energies play a deterministic role in deducing the aspect-ratio of the blister as

$$\left(\frac{h}{a}\right) = \left(\frac{4\pi\Delta\tilde{\gamma}}{5\mathrm{c}}\right)^{\frac{1}{4}}. \tag{3.30}$$

The MLG blister, with confined water-vapor, attains the equilibrium shape at the raised temperature, where the PVA film also gets cured. On cooling down the blister to room temperature, the water-vapor would condense into water droplets (dropwise

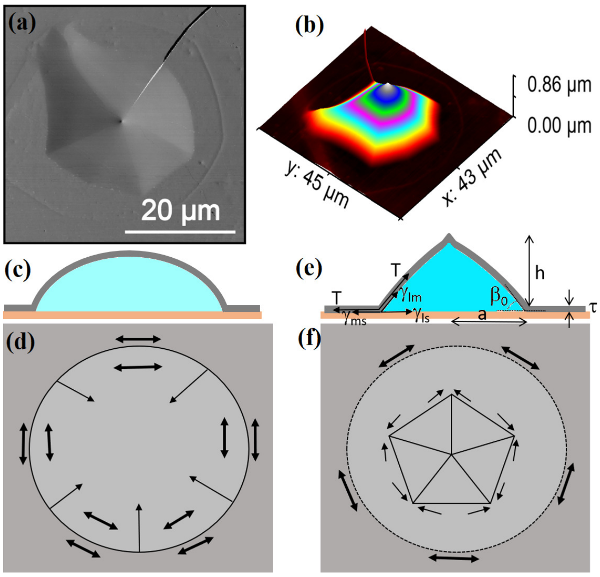

Figure 3.11: Schematic representation of the 'blister-collapse model', governing the solid-based instabilities in the blisters. The tapered region of the MLG flake around the blister-edge collapses downwards as the water-vapor condenses into the liquid phase. (a & b) AFM topographic phase and height profile of the MLG blister (top-view), (c & d) side and top schematic views of the MLG blister before collapse, and (e & f) side and top schematic views of the MLG blister after collapse. The single-headed arrows represent the elastic stresses or interfacial tensions acting at the perimeter of the blister, whereas the double-headed arrows represent the azimuthal (hoop) stress components, distributed across the blister.

condensation process[320]), which allows the tapered region around the blister-edge to collapse downwards, thereby generating a radial pretension in the MLG blister. The radial pretension would induce the 'hoop (azimuthal) compression', whose suppression is only possible through the development of solid-based instabilities in the blister (see Figure 3.11(e, f))[28,36,225,273,321]. When a circular blister collapses due to the phase-transition of the confined matter, it attains a final shape depending upon the parameter h/τ. We note that the parameter h/τ is different for different shapes of the blisters, as shown in Figure 3.10. Therefore, h/τ is a crucial parameter in determining the final shape of the blister. From equation 3.29, it can be seen that the aspect-ratio (h/a) of the blister increases in the presence of a compressive stress $T_{\text{pre}} < 0$[34]. It is equivalent to the development of a pressure inside the blister, given by $p \sim \frac{T_{\text{pre}} h}{a^2}$, which enhances the aspect-ratio of the blister[28,34,196]. Therefore, the compressive pretension ($T_{\text{pre}} < 0$) would play a crucial role in the development of the solid-based instabilities in the MLG blisters. Considering the 'blister-collapse model' (see Figure 3.11), the total potential energy of the blister-system can be given as

$$E_{\text{tot}} = \mathrm{c}\left(\frac{E_{2\text{D}}h^4}{4a^2} - |T_{\text{pre}}|h^2\right) + \pi a^2 \Delta\gamma. \tag{3.31}$$

The condition for the equilibrium state can be achieved by minimizing E_{tot} with respect to a at constant h, which gives $\left(\frac{h}{a}\right)^2 = \sqrt{\frac{4\pi\Delta\tilde{\gamma}}{\mathrm{c}}}$. For a blister to be unstable, energy must be released from the blister-system, which may result in the development of the instabilities, therefore $E_{\text{tot}} \leq 0$. This results in the condition $|\tilde{T}_{\text{pre}}| \geq \sqrt{\frac{\pi\Delta\tilde{\gamma}}{\mathrm{c}}}$, which would lead to solid-based instabilities in the blister. However, the compressive stress required for the blister to be stable (i.e. $E_{\text{tot}} > 0$) is $|\tilde{T}_{\text{pre}}| < \sqrt{\frac{\pi\Delta\tilde{\gamma}}{\mathrm{c}}}$. The development of non-uniform biaxial strain across the blister during collapse, in contrast to the uniform biaxial strain distribution across an initially circular blister, would lead to the generation of an asymmetric hoop compression[25,49]. If the hoop compression overcomes the interfacial adhesive interactions in the annular region outside the blister-edge, then it would give rise to different shapes of the blister (e.g. triangular, trapezoidal, pentagonal, star-like, etc.). Thus, our "blister-collapse model" elucidates the mechanism behind the development of tent or pyramidal-like elastic solid-based instabilities in the multilayered 2D material blisters[25], in contrast to the 2D monolayers, where the hoop compression results in the propagating undulations at the blister edge, owing to the stronger interfacial vdW interactions[36].

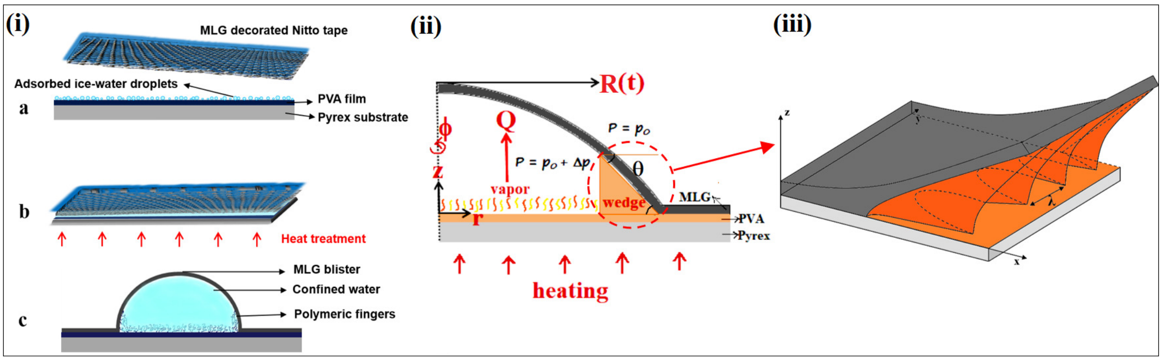

Figure 3.12: Schematic representation of the (i) formation process of viscous fingering instabilities, (ii) axisymmterically growing MLG blister with other involved parameters, and (iii) fingering pattern at the edge of the blister, having a typical finger wavelength λ.

Now, in order to find out the constant prefactor c, we employ the classical partial elastic-wetting analogy of the liquid-drop model for simplicity, by balancing the mechanical and interfacial tensions in the horizontal direction at the contact line of the blister-system[2,289,314], which gives

$$\cos\beta_0 = \frac{N_r^+ + \gamma_{ms} - \gamma_{ls}}{N_r^- + \gamma_{lm}}, \tag{3.32}$$

where β_0 is the contact angle at the edge of the blister, and γ_{lm}, γ_{ls} and γ_{ms} are surface energy densities for the three interfaces: liquid-membrane, liquid-substrate, and membrane-substrate interfaces, respectively. From the continuity of radial stress (N_r) across the edge of the blister, we can have $N_r^+ = N_r^- = T = \frac{E_{2\mathrm{D}}h^2}{4a^2} + T_{\mathrm{pre}}$. For the MLG blisters having $\frac{h}{a} \ll 1$, we can employ the small-angle approximation ($\beta_0 \approx \sin\beta_0 = \sqrt{1-\cos^2\beta_0}$), and for the radial tension to be much greater than any interfacial tension in the system, i.e. $T \gg \Delta\gamma$, where $\Delta\gamma = \gamma_{lm} + \gamma_{ls} - \gamma_{ms}$, we obtain

$$\beta_0 = \sqrt{\frac{2\Delta\gamma}{T + \gamma_{lm}}} \approx \sqrt{\frac{2\Delta\gamma}{T}}. \tag{3.33}$$

Thus, the interplay between the mechanical tension and the surface energies determines the contact angle of the confined liquid with the elastic membrane (MLG) and the PVA substrate. The contact angle decreases with an increase in the mechanical tension, therefore the spherical shape of the water-capped elastic membrane flattens with the increasing tension[314]. Since, $(1 - \cos\beta_0)$ and the strain components are found to scale as h^2/a^2 [25,28,35], therefore the equation 3.32 can be rewritten in terms of the aspect-ratio (h/a), i.e. similar to the expression obtained from the free-energy minimization (equation 3.28)(see Section **3.3.5**). The aspect-ratio of a blister is expected to rise with an increase in the overall surface energy with respect to the pretension[35,289], as $\left(\frac{h}{a}\right)_{\tilde{T}_{\mathrm{pre}} \ll \Delta\tilde{\gamma}} = (4\Delta\tilde{\gamma})^{1/4}$. Comparing this case with equation 3.30, we find the value of the constant prefactor c as $\pi/5$. Therefore, the condition, responsible for the onset of the solid-based instabilities in the liquid-filled blister, can be given by $|\tilde{T}_{\mathrm{pre}}| \geq \sqrt{5\Delta\tilde{\gamma}}$.

However, it remains a significant matter of interest to understand the mechanism behind the onset of substrate-based instabilities in blistering. For this, we explored the different synthesis & processing conditions and found that the 'ice-water adsorption assisted PVA-curing induced blistering' process gives rise to the development of viscoelastic-substrate based instabilities in the form of viscous fingering patterns under the MLG blisters. In this process, the PVA-coated Pyrex (glass) substrate is exposed to the mist at lower temperatures before placing the Nitto tape (decorated with MLG flakes) in its conformal contact, followed by a brief heat treatment of the stack (at ∼120°C for 60 s on a hot plate). The differently shaped viscous fingering patterns have been observed under the MLG blisters of different flake-thicknesses at room temperature through interference reflection microscopy (see Figure 3.12, 3.13 & 3.14). It can be inferred from our experimental observations that the viscous fingering patterns form as a result of the displacement of the viscoelastic PVA (more viscous) by the water-vapor (less viscous) at the raised temperature (above the glass-transition temperature T_g of PVA) during the water-vapor pressure driven blistering of the upper-bounding MLG flake. A recent work by Xie *et al*[322] reports the mechanism of the onset of wrinkling instability in the PEDOT:PSS polymeric film by its swelling on water-absorption, which is absolutely ruled out for our experimental findings.

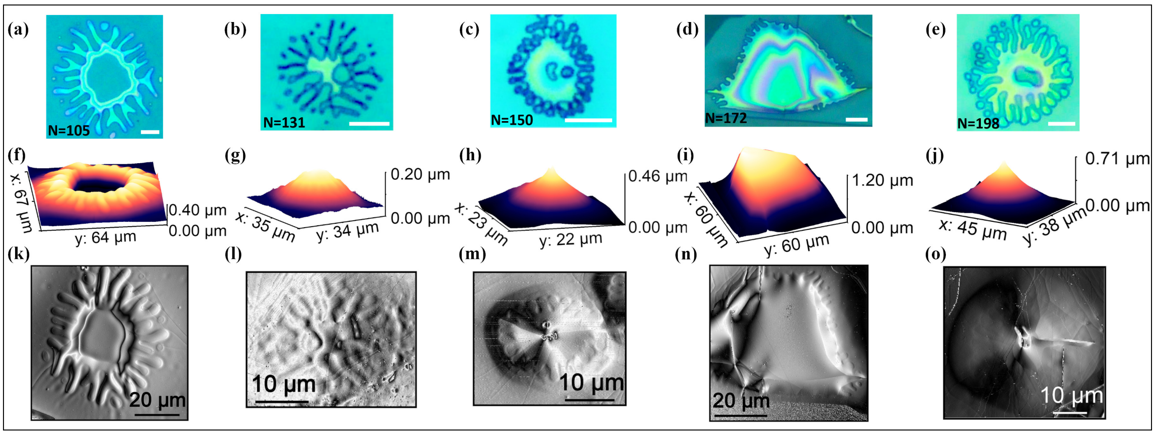

Figure 3.13: [a-e] Optical images of the viscous fingering patterns under the MLG blisters (number of layers (N) is increasing order from left-to-right), with [f-j] the AFM topographic 3D images and [k-o] amplitude images. The scale bar is 10 μm.

We employed the out-of-plane deformation model for the blistering of the MLG flakes in the framework of the 'Föppl von Kármán theory of thin elastic plates' and the 'simplified lubrication theory model' for the two-phase fluid-flow in order to analyze the viscous fingering[1,2,225,323]. The expansion of the blister occurs via displacement of viscoelastic PVA (occupying the space between the MLG flake and the Pyrex substrate) by the water-vapor flow, which concurrently helps in debonding of the MLG flake from the viscoelastic PVA film. The role of the strength of fluid-structure (water-vapor to MLG) vdW interactions is crucial in the onset of instabilities in blistering of the MLG flakes, which can be analyzed in terms of a non-dimensional parameter $\mathcal{J}$, i.e., the ratio of viscous stresses in the viscoelastic PVA (fluid-mechanical forces that tend to resist the shear deformation of the viscous medium) to the bending stiffness of the upper bounding MLG flake (elastic restoring forces that tend to resist the out-of-plane bending of the elastic membrane)[37,227], given as $\mathcal{J} = \frac{6\mu Q\mathcal{L}^3}{\pi b^3 B_{\mathrm{eff}}}$, where μ is the dynamic viscosity of the viscoelastic PVA film (at the raised temperature $T \gtrsim T_g$), Q is the volumetric flow rate of the water-vapor, $\mathcal{L}$ is the blister's overall horizontal length scale, b is the undeformed initial thickness of the PVA film, and B_{eff} is the effective bending stiffness of the upper bounding MLG flake. Since the volumetric flow rate (Q) is proportional to the volume of the blister ($V \sim \mathcal{L}^2 h$), therefore we can reframe the expression for the parameter $\mathcal{J}$ in terms of h/τ as

$$\mathcal{J} \propto \frac{\mu h \mathcal{L}^5}{B_{\mathrm{eff}}} \propto \mu \mathcal{L}^5 \left(\frac{h}{\tau}\right). \tag{3.34}$$

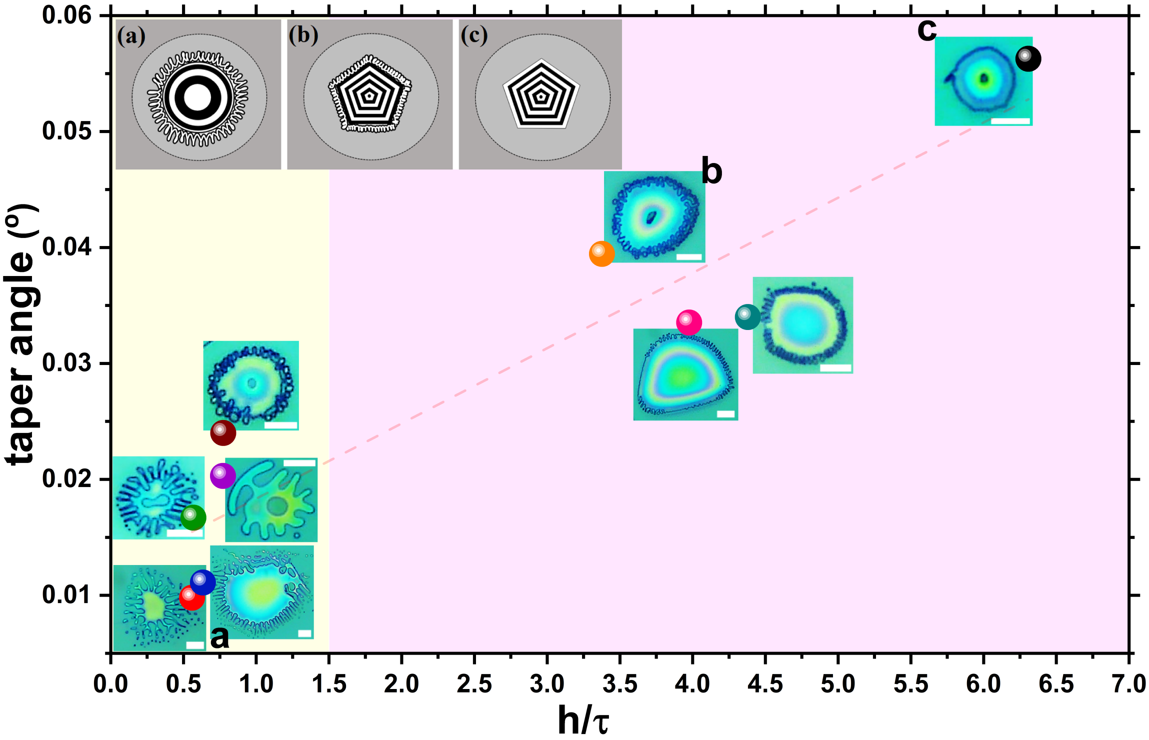

Figure 3.14: A graphical representation, depicting the tapering-controlled viscous fingering under sub-micron MLG blisters as a function of blister-height to flake-thickness ratio (h/τ). The number of layers in MLG flakes typically decreases with increasing h/τ. The scale bar is 10 μm. Inset shows the schematic representation of the transition from ‘peeling by bending’ regime to ‘peeling by tension’ regime.

The observations of the elastic solid-based instabilities and the viscous instabilities in the ‘conventional’[49,88] and ‘ice-water adsorption assisted PVA-curing induced blistering’ approaches, respectively, can be attributed to the variation in the strength of fluid-structure (water-vapor to MLG) interactions. The stronger fluid-structure interactions give rise to the higher values of the blister-height (h) for a constant thickness (or, bending stiffness) of the elastic membrane, and tend to suppress the viscous fingering instabilities. However, the compressive azimuthal stress (hoop compression) increases with an increase in the fluid-structure interactions $\mathcal{J}$, which enhances the susceptibility of the MLG blisters to elastic solid-based instabilities[37]. We noted that the elastic solid-based instabilities are more pronounced for the large-sized MLG

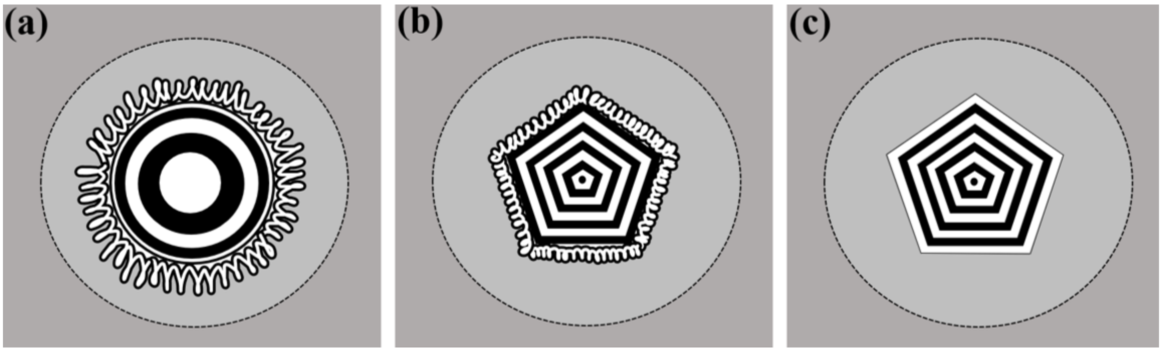

Figure 3.15: The interfacial viscous fingering instability is noticeably observed in the bending-dominated regime in spontaneous blistering of the MLG flakes over the viscoelastic PVA substrate (a), however, the tension-dominated regime is highly susceptible to the elastic solid-based instability (c). We also come across an intermediate transition between the two, where both types of instabilities occur concurrently (b). However, it is also possible that a circular blister with interfacial viscous fingering instability, being prone to the elastic-solid based instability, leads to the tent-like shape of the blister with modulated fingering pattern at the interface under phase-transition (resulting from dropwise condensation of the confined water-vapor on cooling) driven collapse of the blister, depicting the transition from a → b.

blisters, having large values of h/τ (see Figure 3.10), whereas the viscous fingering instabilities are more pronounced for comparatively small MLG blisters, having smaller values of h/τ (see Figure 3.14). The elastic solid-based instabilities in the large-sized MLG blisters (larger $\mathcal{L}$), having large h/τ ratio, would correspond to the case of large $\mathfrak{I}$ (depicting the strong fluid-structure interactions). This possibly, results from the larger viscous stresses in the viscoelastic PVA in comparison to the bending stresses in the MLG flakes, making the interface stable, i.e., free from the viscous instabilities. Conversely, the viscous fingering instabilities (in ice-water adsorption assisted PVA-curing induced blistering) occur in the small-sized MLG blisters (smaller $\mathcal{L}$), having a smaller h/τ ratio. The smaller horizontal length scales of the MLG blisters and the reduced effect of the viscous stresses, via decrement in the dynamic viscosity of PVA due to dilution of the PVA film by absorbed water at the raised temperature, in comparison to the bending stresses in the upper-bounding MLG flake while blistering, would result in the smaller values of $\mathfrak{I}$ (depicting the weaker fluid-structure interactions) (see Figure 3.14).

A particular shape of the viscous fingering pattern is attained as a result of competition between the viscous stresses and the bending stresses. The viscous instabilities result from the two-phase displacement flow while blistering (where the water-vapor displaces the viscoelastic PVA), whereas the elastic solid-based instabilities arise due to the suppression of the hoop compression (induced by the radial tension, developed

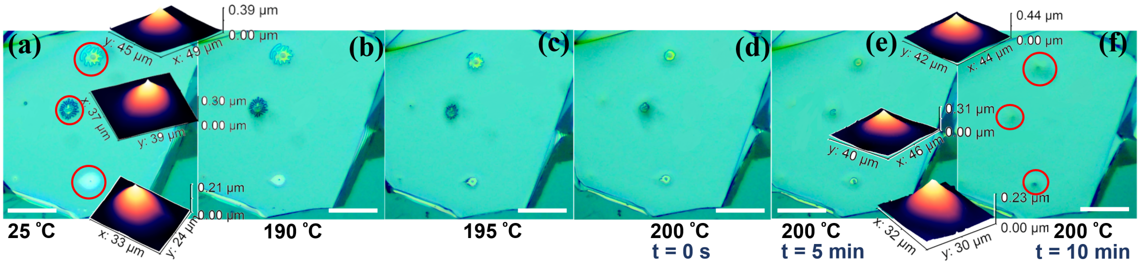

Figure 3.16: Heating assisted reshaping of the MLG blisters for corroboration of the interfacial nature of the viscous fingering. The optical images (captured continuously with rising temperature) and the AFM topographic 3D images (captured at room temperature) of the MLG sub-micron blisters having viscous fingering instabilities at the interface, during heat-treatment up to ∼200°C in upside-down or face-down orientation (scale bar: 50 μm). The interfacial nature of the viscous fingering instabilities have been confirmed by analyzing the temperature-dependent dynamics of the fingering patterns under the MLG blisters. The rapid & unstable axisymmetric in-plane propagation of the more viscous PVA (viscoelastic in nature) in the less viscous medium of water-vapor (gaseous in nature) results into the development of interfacial viscous fingering patterns.

while the blister collapses due to phase-transition of the confined water-vapor). The suppression of the hoop compression not only develops the solid-based instabilities in the bulged MLG flakes but also modulates the shape of the viscous fingering patterns, formed while blistering the MLG flakes. In our experiments, we did not observe the viscous fingering instabilities in sufficiently thin graphene flakes (few-layer, N $\ll$ 100), possibly due to the strong interfacial adhesive interactions. The blistering of the thin elastic MLG flakes is possible, once the adhesive forces are overcome by the fluid-structure interactions. For the blisters of thin elastic MLG flakes ($N \simeq 100$), the viscous fingering instabilities (mostly in the bulk) arise concurrently with the solid-based instabilities (see Figure 3.13). However, for the blisters of thicker & stiffer MLG flakes, the viscous fingering instabilities are mostly interfacial and decoupled from the solid-based instabilities (see Figure 3.14(a)). We noted that the axial symmetry of the thicker MLG blisters is mostly maintained even after the development of the viscous fingering instabilities. Since the viscous fingering instabilities are obtained as a result of dominant water-vapor to PVA interactions over the water-vapor to MLG flake interactions, the viscous fingering instability seems to have negligible impact on the water-vapor driven transverse deflection of the thick MLG flakes (Figure 3.14). The observations can be correlated to the extreme limits of $\mathcal{I}$, i.e.: $\mathcal{I} \rightarrow 0$ corresponds to the case of the onset of viscous fingering instabilities, where the bending stresses dominate over the viscous stresses, whereas $\mathcal{I} \rightarrow \infty$ corresponds to the case of the onset of elastic solid-based instabilities, where the viscous stresses dominate over the bending stresses. In our experiments, we also come across an intermediate transition of the two extreme limits, where coupling between both kinds of instabilities is observed, possibly due to comparable viscous & bending stresses (see the transition: a → b → c, in Figure 3.14).

Figure 3.6 depicts the variation in the shape of viscous fingering patterns under the thicker MLG blisters with respect to the ratio of blister-height to flake-thickness (i.e., h/τ) and the taper angle (θ). We found that the height profiles of the sub-micron blisters ($w(r)$), mostly follow the tent model ($\frac{2}{3}^{rd}$ power of radial distance r, i.e., $w(r) = h[1-(\frac{r}{a})^{\frac{2}{3}}]$[196]), independent of the ratio h/τ[1]. The tents form due to suppression of the hoop compression (induced due to radial tension while collapse of the blisters)[26]. In order to investigate the nature of viscous fingering instabilities (whether interfacial or bulk), as presented in Figure 3.14, we employed the thermal treatment of the blisters, capping the fingering patterns. We analyzed the temperature-dependent dynamics and the shape of the polymeric fingers at the MLG/PVA interface while heating the PVA-supported MLG blisters in upside-down (face-down) orientation up to ∼200°C. We observed reshaping of the polymeric fingering patterns as the temperature reaches close to the melting point of the PVA (∼200°C)[275]. It is to be noted that the reshaping of the fingering patterns starts from their edges, positioned at the periphery of the blisters, which implies that the instabilities are present at the interface not within the bulk[324] (see Figure 3.16). Therefore, it corroborates our hypothesis that the water-vapor (less viscous fluid) displaces the viscoelastic PVA (more viscous fluid) along the interface while blistering of the MLG flakes at the raised temperature, which leads to the development of the complex viscous fingering patterns at the interface. We also found that the viscous fingering patterns vanish completely on heating the sample at 200°C for approx. 10 min (owing to the high thermal conductivity of the MLG flake[325]). Therefore, the heat treatment of the blister-system (having viscous fingering instabilities) in an upside-down orientation, effectively helps in eliminating the interfacial viscous fingering pattern from the blister via the replacement of the confined matter by the melted polymer fluid (which therefore, causes the interference pattern across the blister to disappear).

The relation between the viscous forces and capillary forces is governed by the capillary number[27,295], $Ca = \frac{\mu U}{\sigma}$, where μ is the dynamic viscosity of the viscoelastic PVA, U is the instantaneous radial velocity of the circular interface, and σ is the surface tension at the vapor-to-PVA interface. The length and width of the polymeric fingers depend on the taper angle (θ) (which can be approximated by the aspect-ratio (h/a) of the blister, see Figure 3.17) as well as on the capillary number (Ca)[225,226,326].

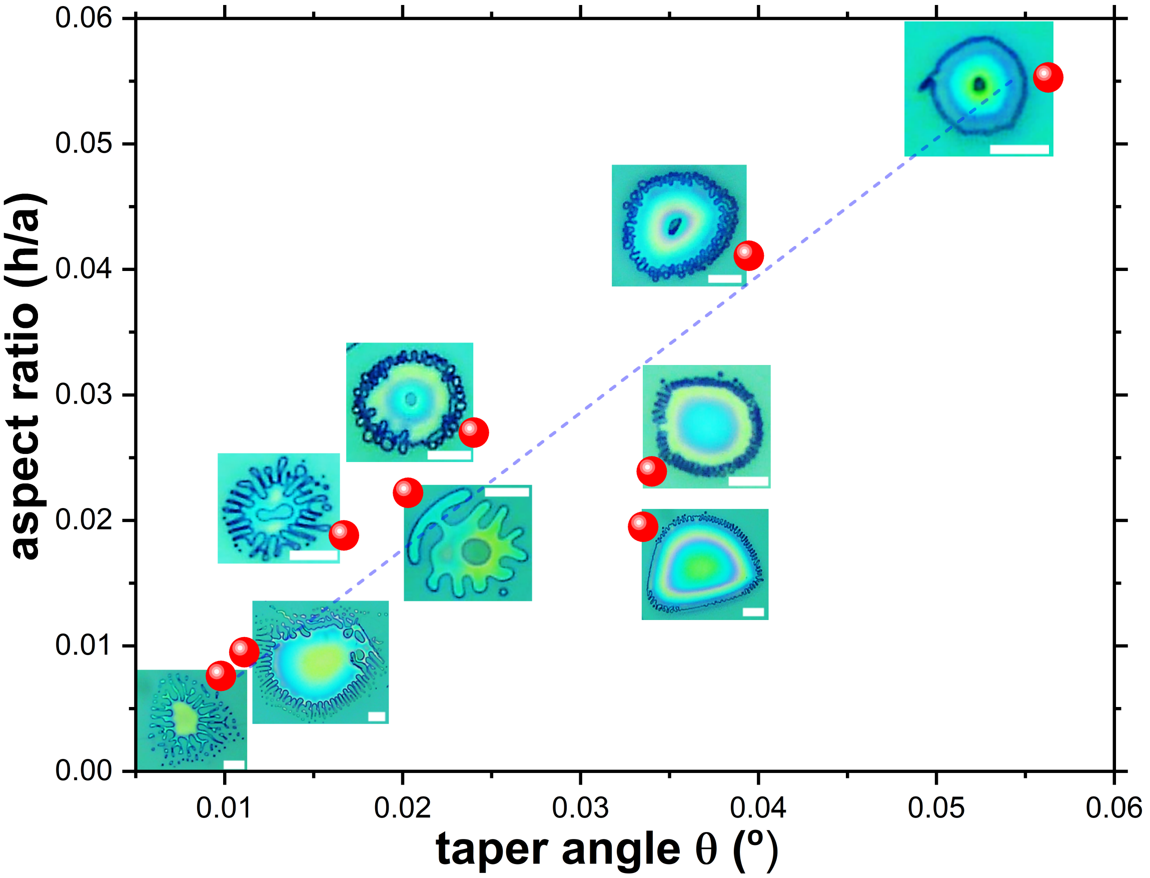

Figure 3.17: Aspect-ratio of the MLG blisters (having viscous fingering instabilities) as a function of the taper angle. As the taper angle is increased the fingering pattern tries to concentrate at the edges only and thereby tends to stabilize the interface. This depicts the tapering controlled viscous fingering instabilities under the 2D material blisters (scale bar: 10 μm).

We observed that the fingers become shorter and stubby with increasing θ as well as h/τ (see Figure 3.14). Therefore, the wavelength (width) as well as the length of the polymeric fingers is inversely proportional to the taper angle. We noted that for the blisters, having lower values of h/τ (larger bending stresses), the fingering patterns depict the 'peeling by bending' regime, where the significant bending stresses allow the radial-growth of the blisters, but with small vertical deflection, resulting from the radial propagation of the water-vapor through in-plane displacement of the viscoelastic PVA, in contrast to the 'peeling by tension' regime (larger h/τ), where the water-vapor to MLG (fluid-structure) interactions dominate over the water-vapor to PVA (fluid-substrate) interactions, resulting from the planar propagation of the confined water-vapor. Our results indicate the transition of interfacial viscous fingering patterns from 'peeling by bending' regime to 'peeling by tension' regime[225,226,298].

The wavelength of the polymeric fingers follows the expression, derived by Saffman and Taylor[226,327], i.e. $\lambda = \pi b\sqrt{\frac{\sigma}{\Delta\mu U}}$, where $\Delta\mu$ is the viscosity-difference between the two fluids. A simultaneous increase in θ and h/τ, tends to stabilize the interface against the interfacial viscous instabilities. The stabilization of the interface, can be attributed to the enhanced and dominant contribution of the viscous forces over the restoring capillary forces[326]. For the smaller values of θ, the polymeric fingers grow to much larger lengths, having appreciable mutual interactions to develop the tip-splitting instabilities (Figure 3.14)[225,328]. The larger wavelength of polymeric fingers under the MLG blisters having lower h/τ, would have resulted from the smaller radial velocity of the circular interface and the reduced viscosity of PVA at the raised temperature. Therefore, the smaller values of h/τ & θ in the blistering of the MLG flake are more susceptible to the onset of the interfacial viscous fingering instabilities, where the out-of-plane bending stiffness of the MLG flake dominates over the viscous stresses, as the water-vapor interacts more with the viscoelastic PVA substrate while blistering.

Therefore, the hoop-compression drives the solid-based instabilities (in the form of tent-like or pyramidal blisters) as well as substrate-based instabilities (in the form of viscous fingering patterns) in the spontaneous blistering of the multilayered 2D flakes over polymeric substrate, in contrast to the blistering of a single or few-layer 2D nanosheet (having lower bending rigidity) over a 2D crystal, where the hoop-compression drives only the wrinkling instabilities around the perimeter of the bulged nanosheet[36].

3.4 Summary

In conclusion, we observed both the elastic-solid and viscoelastic-substrate-based instabilities through polymer-curing-assisted spontaneous blistering of MLG flakes over a polymeric PVA substrate upon manipulating the polymeric-layer content in the same experiment. The interchangeable dominance of the pretension & the overall surface energy as well as the viscous stresses in viscoelastic PVA & the bending stresses in MLG flakes play a crucial role in the development of the solid as well as fluid (viscoelastic) mechanical instabilities in the blister-system. According to our "blister-collapse model", the hoop compression develops while the collapse of the blister, as a result of phase-transition of the confined water-vapor into the liquid phase, which plays a crucial role in the development of instabilities apart from the interfacial slippage while blistering. The growth-dynamics of the viscous fingering patterns have been correlated with the end-results of the blistering, such as the inclination (taper) angle and the parameter h/τ of the MLG blisters, owing to the thickness-dependent elasticity of the MLG flakes. Our results provide a fundamental perspective of the elastic-solid as well as viscoelastic-substrate-based instabilities in the polymer-supported 2D material blisters at the sub-micron level by exploiting the involved adhesion mechanics. This study highlights the role of the vdW interactions acting within the blister, elastic properties of the 2D material, viscoelastic properties of the polymeric substrate, and the physical properties of the confined matter in the onset of the instabilities in the spontaneously formed 2D material blister-system. This work opens new pathways for controlling as well as manipulating the instabilities in the 2D material blister-systems. Furthermore, the tent-like blisters might be harnessed for micro-/nanoelectromechanical sensors as well as single-photon emitters.

Chapter 4

Dynamical evolution of viscous fingering instability underneath spontaneously formed blisters of MoS_2 crystal

4.1 Introduction

In recent years, the bending of 2D materials during the blister formation has been a subject of extensive focus due to their exceptional elasticity and the weak van der Waals (vdW) interlayer interactions[23,61,230,258]. The 2D material blisters offer local strain sites with altered physical properties[62,176,177,329,330]. Knowing the physics and chemistry underlying the intended[266,285,331] or spontaneous formation[230,290,332,333] of blisters is extremely important for the utilization or removal of 2D material blisters[34,312]. It has also been demonstrated that the blisters of direct band gap semiconductors (e.g. transition metal dichalcogenides- TMDCs) act as 'single photon emitters'[334–337]. In addition, the blisters show remarkable photo-detection capability as the excitons have a longer lifetime against recombination due to the funneling effect[64]. A blister test can be used to determine the intrinsic mechanical properties of a 2D material as well as its interfacial adhesion strength with a given substrate[65,288,338].

The blistering of 2D materials over rigid solid substrates has been extensively investigated[266,305]. However, a lack of attention has been paid to the 2D material blister formation over the soft polymeric substrates, possibly due to their considerable roughness and deformability. It's interesting to note that a hydrophilic polymer PVA acts as a potential substrate for mechanically exfoliated 2D materials, offering a larger deposition yield and monolayer area[88,339]. It has been observed that the 2D material blister formation over the PVA substrate may lead to an unconventional phenomenon, i.e., 'viscous fingering'[230]. This type of viscous fingering matches well with the Saffman-Taylor-like instability[226] in which the length-scale of the polymeric fingers depends on the viscous and surface tension forces, elastic properties of the material and the thickness of the confined viscoelastic film. On the contrary, the length-scale of surface undulations in the confined viscoelastic film developed due to the peeling of elastic/plastic sheets from the adhesive surface does not depend on the geometrical and material properties except the thickness of the film[299,302,340–342].

The Saffman-Taylor-like instability, observed while debonding of a stiff plate from a viscous medium due to the displacement of a more viscous fluid by an injected less viscous fluid, gets suppressed when replacing the stiff plate with an elastic membrane[27,29,294]. However, researchers have been unable to demonstrate a dynamic evolution of the viscous fingering patterns using a single material. Recently, M. Pandey *et al*[230] showed for the first time that the graphene multilayer, having thickness-dependent elasticity, can show the evolution of viscous fingering patterns in a cold mist adsorption-assisted PVA-curing-induced blistering process. The adsorbed ice-water droplets over the PVA substrate locally manipulate the viscosity of the polymeric substrate surface, which alters its adhesive properties and thereby makes the polymeric surface more deformable. The water vapor displaces the viscoelastic PVA at the raised temperature, and results in the formation of viscous fingering patterns underneath the 2D material blisters. The phase-transition of the confined matter inside a graphene blister induces hoop compression, whose suppression results in the formation of wrinkles around the perimeter of the blister or the tent at the center of the blister. The wrinkling is more prominent for blisters of thin 2D flakes (single to few layers) whereas the tent formation is more pronounced for thick 2D multilayers[230]. Such kinds of elastic solid-based instabilities in the 2D material blisters arise as a result of (i) phase-transition of the confined matter[36,195,230,307], and (ii) interfacial sliding or contact failure[25,28,289]. The hoop compression not only causes elastic solid-based instabilities but also has an impact on the viscoelastic substrate-based instabilities. M. Pandey *et al*[230] showed how the tent-like instability interacts with the viscous fingering instability underneath a multilayer graphene blister. It follows that it is quite possible for the viscous fingering instability at the interface to interact with the wrinkling instability developed around the perimeter of a blister of a relatively thin 2D elastic nanosheet. Such an investigation based on the 2D material blisters is currently lacking in the literature. However, through theoretical modeling, D. Pihler-Puzovic *et al* have demonstrated this interaction between the two types of instabilities in an elastic-walled circular Hele-Shaw cell[37].

The onset of elastic solid or viscoelastic substrate-based instabilities and their mutual interaction depend on the strength of fluid-structure interactions, which is measured by the fluid-structure interaction parameter $\mathcal{I}$, i.e., the ratio of viscous stresses in the viscous fluid to the bending stiffness of the upper-bounding elastic membrane[37,225]. In the cold mist adsorption-assisted PVA-curing-induced blistering of graphene multilayers, the water-vapor displaces the viscoelastic PVA in the in-plane direction inhomogeneously and simultaneously bends the elastic membrane in the out-of-plane direction, thereby forming the viscous fingering patterns underneath the blisters[230]. At lower values of $\mathcal{I}$, where the viscoelastic substrate exhibits smaller resistance to deformation than the upper-bounding elastic sheet, the viscous fingering instability predominates over the elastic solid-based instability. Chopin *et al*[28] demonstrated that the parameter h/τ (ratio of blister's height to flake thickness) regulates the shape profile of the blisters of a plastic sheet confining a liquid. M. Pandey *et al*[230] showed that the parameter h/τ not only regulates the solid-based instability or the shape profile of a multilayered 2D material blister but also the viscous fingering instability underneath the blisters over a viscoelastic substrate. For a single or few-layered 2D material blister, the solid-based instability occurs in the form of periodic wrinkles around the perimeter of the blister[36]. Therefore, it is essential to comprehend the involved mechanism and the factors controlling the interaction between wrinkling and viscous fingering in the blisters. In the present work, we performed the polymer-curing-induced blistering of MoS_2 multilayers in different synthesis and processing conditions to investigate the stability of the blisters and the interface based on the outcome of the blistering process. We utilize the 2D material blister-test model in the framework of 'Föppl von Kármán theory of thin elastic plates' and the two-phase fluid flow model in the framework of 'simplified lubrication theory' to elucidate the role of the interfacial velocity of viscoelastic polymer while blistering and the interfacial adhesion strength of the 2D flakes with the substrate in the evolution of viscous fingering patterns underneath the blisters. We also provide intriguing insights into a scenario, where the viscous fingering instability couples with the wrinkling instability in the MoS_2 blisters. We show that the presence of a solid- or substrate-based instability results in an anomaly in the modeling, where the parameter h/τ of the blisters attains unconventionally high values.

Graphical abstract

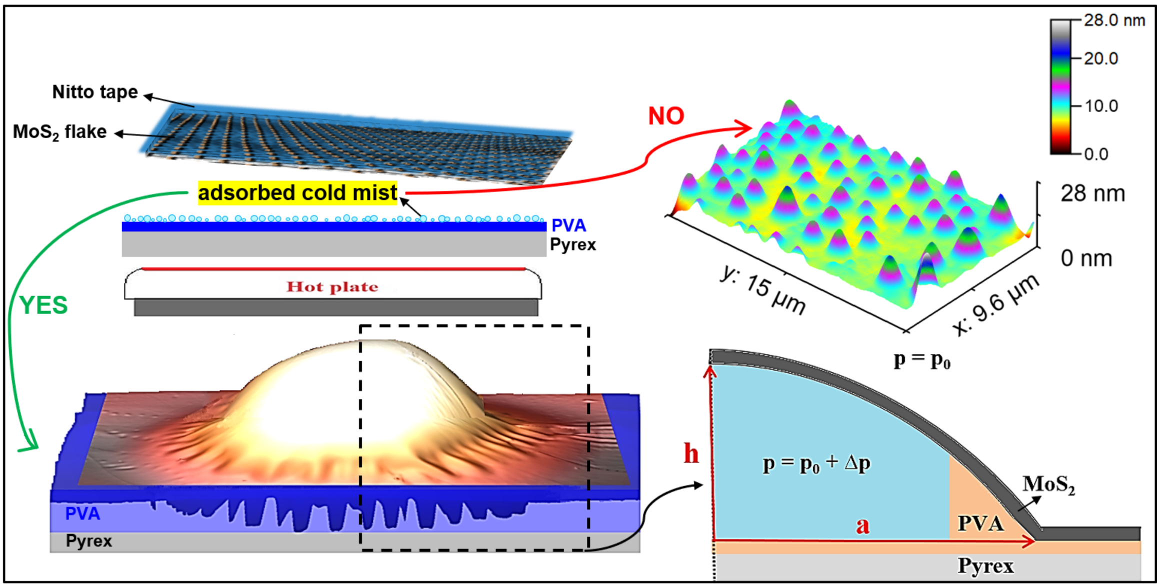

Schematic representation of PVA-curing-induced blistering of MoS_2 multilayer with and without the adsorption of tiny ice-water droplets (mist) over the PVA-coated Pyrex substrate prior to the mechanical exfoliation step.

4.2 Experimental methods

4.2.1 PVA-curing-induced blistering of MoS_2 multilayers in different synthesis and processing conditions

The blisters of micromechanically exfoliated MoS_2 multilayers are formed by a PVA-curing-induced blistering process both with and without the adsorption of tiny ice-water droplets (mist) over the PVA-coated Pyrex substrate prior to the mechanical exfoliation step. The steps in detail can be seen elsewhere[230].

4.2.2 Characterizations

The identification of MoS_2 blisters is carried out using interference reflection microscopy (IRM). The Raman and PL spectra have been acquired from the identified blisters using a HORIBA LabRAM HR Evolution system in ambient atmospheric conditions. The laser light output power is kept low (to prevent local heating) at ~ 1 mW for the laser excitation wavelength of 532 nm using a 100× air objective lens (NA = 0.8) and a detector grating of 600 lines/mm in a confocal microscopy setup. The tapping-mode AFM measurements have been performed with a standard silicon cantilever using a Bruker MultiMode-8 AFM setup. The AFM data visualization and analysis have been carried out using the Gwyddion and WSxM software packages.

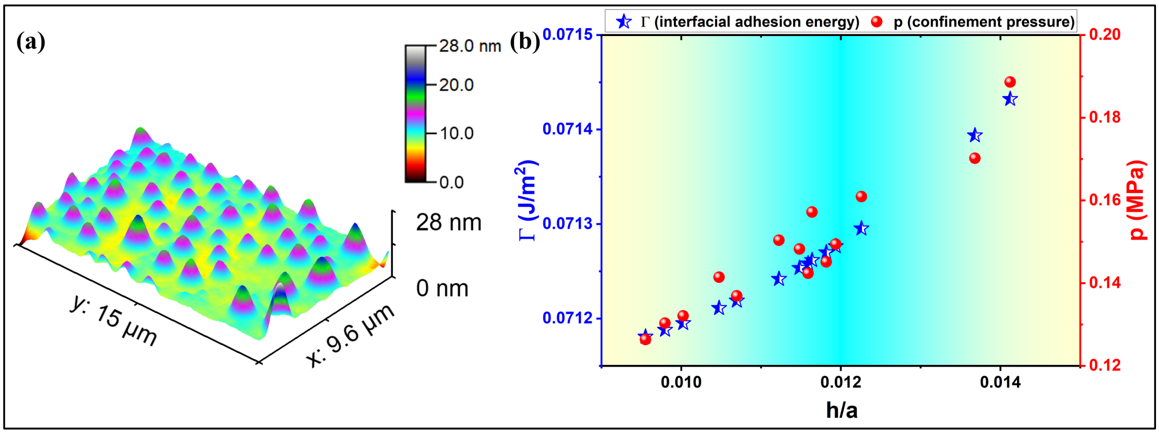

Figure 4.1: (a) Nanoblisters of multilayer MoS$_2$, having the number of layers N = 39, formed spontaneously through conventional PVA-curing-induced blistering process. (b) The interfacial adhesion energy and the net confinement pressure as a function of the blister aspect ratio for 14 different nano-blisters across the flake.

4.3 Results and Discussion

We analyzed our previous experimental findings on the PVA-curing-induced blistering of MLG flakes[62,230] and observed that the conventional PVA-curing-induced blistering process results in 2D material blisters of lower h/τ with a stable and regular interface whereas the cold mist adsorption-assisted blistering process results in the blisters of larger h/τ with a complex interface. We further, investigated the PVA-curing-induced blistering of MoS$_2$ flakes under the different synthesis and processing conditions to find the crucial parameter that is directly connected to the synthesis and processing conditions used in the experiment, whether it be the conventional or cold mist adsorption-assisted blistering process. M. Pandey *et al*[62] found that multilayered graphene blisters, formed spontaneously through the conventional PVA-curing-induced blistering process, follow the elastic plate model, which satisfies the condition $h/\tau \lesssim 1.5$, owing to significant bending rigidity of the multilayered flakes having minimal interlayer slippage. We find this observation also valid for multilayered MoS$_2$ blisters formed through the same blistering process. But interestingly, when the PVA-coated Pyrex substrate is exposed briefly to a humid atmosphere at a lower temperature prior to the simultaneous curing and exfoliation step, the blisters of MoS$_2$ multilayers form spontaneously with an exceptionally high h/τ ratio[230]. The existing literature suggests that the parameter h/τ is larger (> 2) for the blisters following the membrane profile[1]. This hypothesis seems to be oversimplified because even if the condition $h/\tau \lesssim 1.5$ is no longer true, the blisters follow the nonlinear elastic plate profile, i.e.,

$$w(r) = h\left(1 - \frac{r^2}{a^2}\right)^2 \tag{4.1}$$

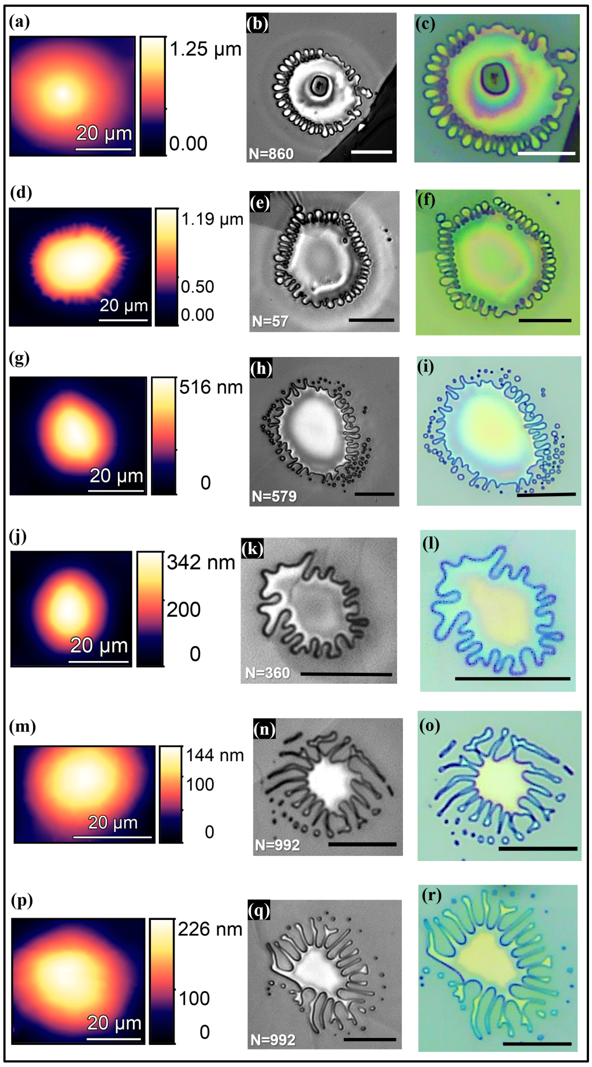
(a)
1.25 μm
0.00
20 μm
(b)
N=860
(c)
(d)
1.19 μm
0.50
0.00
20 μm
(e)
N=57
(f)
(g)
516 nm
0
20 μm
(h)
N=579
(i)
(j)
342 nm
200
0
20 μm
(k)
N=360
(l)
(m)
144 nm
100
0
20 μm
(n)
N=992
(o)
(p)
226 nm
100
0
20 μm
(q)
N=992
(r)

Figure 4.2: Blisters of MoS_2 multilayers having viscous fingering instability underneath. The scale bar is 20 μm.

which is a fourth-order function of the radial distance r. The height profile of the blisters is fitted to a fourth-order polynomial function of radial distance r as, $\mathrm{w(r)} = \mathrm{intercept} + \mathrm{B_1 r} + \mathrm{B_2 r^2} + \mathrm{B_3 r^3} + \mathrm{B_4 r^4}$; which gives central deflection or height h as intercept and radius a as $\left(-2\frac{\mathrm{intercept}}{\mathrm{B_2}}\right)^{\frac{1}{2}}$. We attribute the larger h/τ to the interlayer sliding due to weak vdW forces in between the layers of a multilayered 2D material. Therefore, we can reasonably assume that each layer bends independently while blistering such that the out-of-plane bending rigidity effectively scales linearly with the number of layers, i.e., $B_{\text{eff}} \sim N$ (not N^3)[23,343]. However, the level of interlayer sliding is more prominent (i) during the collapse of the blister due to the phase-transition of the confined matter, which gives rise to the tent-like shape of the blister, and also (ii) during the ice-water adsorption-assisted PVA-curing-induced blistering due to the ultralubricated interface resulted from the wetting[230]. The interfacial adhesion energy density (Γ) of the PVA-supported MoS_2 flakes consisting of N layers can be estimated using the equation[62]:

$$\Gamma = \zeta E_{2D} \left(\frac{h}{a}\right)^4 + 32\frac{B_{\text{eff}} h^2}{a^4} + \gamma_w(\cos\theta_m + \cos\theta_s), \tag{4.2}$$

where $E_{2D} = E\tau$ is the 2D elastic stiffness of the 2D flake, $\tau = Nt$ is the thickness of the 2D flake, N is the number of layers, t is the thickness of the monolayer, E is the in-plane elastic modulus of the 2D material, $B_{\text{eff}} = \frac{NEt^3}{12(1-\nu^2)}$ is the effective bending stiffness, $\zeta = \frac{896585+529610\nu-342831\nu^2}{960498(1-\nu^2)}$ is the constant prefactor, ν is Poisson's ratio, γ_w is the surface tension of water $= 72$ mN/m, θ_m is the water contact angle with the 2D flake, and θ_s is the water contact angle with the substrate. For MoS_2 blisters over the PVA substrate, we use the following parameters[62,65,344,345]: $E = 270$ GPa, $t = 0.65$ nm, $\nu = 0.29$, $\theta_m = 69°$, $\theta_s = 51°$.

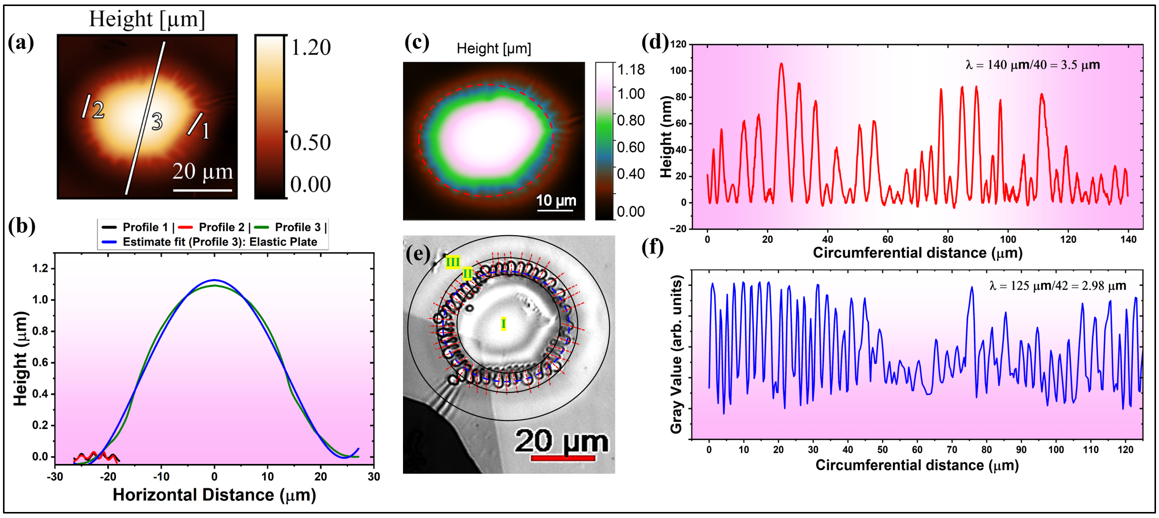

Figure 4.3: (a) AFM topographic 2D map of the blister with coupled instability; (b) AFM height profiles along the lines marked in (a). (c, d) AFM topographic 2D height image and the line profile across the periphery of the blister shown by a red dotted circle, respectively, and (e, f) optical image captured at the interface of the blister using interference reflection microscopy, depicting three zones of the blister, and the gray value plot profile across the periphery of the blister shown by a blue dotted circle, respectively.

Hencky's model gives a relation between the confinement pressure (Δp) and the topography of the blister[1], as

$$\Delta p = p - p_0 = K(\nu)\frac{NEt}{a}\left(\frac{h}{a}\right)^3, \tag{4.3}$$

where $p_0 = 1$ atm. pressure $= 101325$ Pa, p is the net pressure inside the blister, and $K(\nu)$ is a constant prefactor; $K(\nu = 0.16) = 3.09$ for graphene, and $K(\nu = 0.29) = 3.54$ for MoS_2[65,199,344]. On employing the elastic plate model with modified bending stiffness term for the MoS_2 blisters formed through the conventional PVA-curing-induced blistering process, the interfacial adhesion energy (Γ) of the MoS_2 multilayer (see Figure 4.1) is estimated as ~ 71.3 mJ/m^2, and the net pressure inside the nanoblisters is ~ 0.15 MPa.

By employing the PVA-curing-induced blistering process after exposing the PVA surface to cold mist, we observed that the ratio of blister height to flake thickness (h/τ) dramatically increases, apart from observing the viscous fingering instability at the interface (see Figure 4.2). It is clear from our observations that the elastic plate model that is applicable for $h/\tau \lesssim 1.5$ is violated in spontaneously formed blisters having at least one kind of instability, either the elastic solid-based instability (tenting or wrinkling), resulting from the phase transition of the confined matter, or the viscoelastic substrate-based instability (viscous fingering)[36,230]. To understand the underlying mechanisms, we employ the 2D material blistering model in the framework of the 'Föppl von Kármán theory of thin elastic plates' and the 'simplified lubrication theory model' for the two-phase fluid flow in an elastic-walled circular Hele-Shaw cell[225,230]. The degree of instability in blistering is governed by the fluid-structure interaction parameter (dimensionless), i.e.,

$$\mathcal{I} = \frac{\gamma}{B_{\text{eff}}}, \tag{4.4}$$

where γ is the viscous stiffness in the viscous fluid and B_{eff} is the bending stiffness of the upper-bounding elastic membrane. The parameter $\mathcal{I}$ has an impact on the growth dynamics of viscous fingering patterns underneath the 2D material blisters. The parameter $\mathcal{I}$ has two extreme limits: (i) $\mathcal{I} \to 0$, which depicts the case where the viscoelastic substrate is easily deformable in comparison to the upper-bounding elastic membrane; this condition is responsible for the onset of viscous fingering instability; and (ii) $\mathcal{I} \to \infty$, which depicts the case where the upper-bounding elastic membrane is easily deformable in comparison to the viscoelastic substrate; this condition is responsible for the onset of solid-based instability. For a constant viscosity of the viscoelastic substrate, the parameter $\mathcal{J}$ depends on the blister's length scale $\mathcal{L}$ and the parameter h/τ at a unit time interval[230]. The fluid-structure interaction parameter $\mathcal{J}$ is related to the pressure for flux-driven flow P, as

$$\mathcal{J} = \frac{P\mathcal{L}^3}{B_{\text{eff}}} \propto \mu\mathcal{L}^5\frac{h}{\tau}. \tag{4.5}$$

Assuming the flux-driven pressure to be of the order of the confinement pressure inside the 2D material blister, i.e., $P \sim \Delta p$. This yields an effective fluid-interaction parameter, as

$$\mathcal{J}^* = \frac{\Delta p\mathcal{L}^3}{B_{\text{eff}}}. \tag{4.6}$$

Assuming, $\mathcal{L} \sim 2a$, and using equation 4.3, we obtain

$$\mathcal{J}^* \propto \left(\frac{h}{t}\right)^2\left(\frac{h}{a}\right). \tag{4.7}$$

This approximation is valid for the case when the interlayer sliding is prominent due to weak vdW interactions, which is possible for an ultralubricated (frictionless) interface. Each layer of the multilayered flake attains the same bulging height h as that of the flake itself because each layer of the 2D material bends independently. Therefore, the effective thickness of the multilayered flake would be equal to the thickness of the single layer[36].

We also observed the concurrence of wrinkling at the perimeter of blisters of thinner MoS_2 flakes ($N \lesssim 100$) and the viscous fingering at the interfaces (see Figure 4.3). The 2D material blisters form at the raised temperature of ∼ 100°C due to the trapping of water vapor resulting from the evaporation of water content (absorbed/adsorbed) of the PVA. The blister is of a circular shape at the raised temperature due to symmetrically distributed pressure across the blister walls, which collapses at the edge due to condensation of water vapor (gas) into the liquid phase as it is cooled down to room temperature[230]. We observe three regions in a blister, as shown in Figure 4.3(e), viz. (i) region I: the spherical or tent-like tip of the blister, (ii) region II: viscous fingering patterns at the periphery of the blister, and (iii) region III: the nearly deflated region of the initially circular blister due to phase transition-induced collapse. The tip height of the blister is almost 25 times larger than the average height of the wrinkles at the periphery of the blister (see Figure 4.3(b). On removing the bulged upper-bounding flake using a Nitto tape, the polymeric fingers formed at the periphery of a 2D material blister can be visualized (see Figure 4.4(e-h)). It is clear from the topographic images 4.4(g, h)) that the viscoelastic polymer PVA

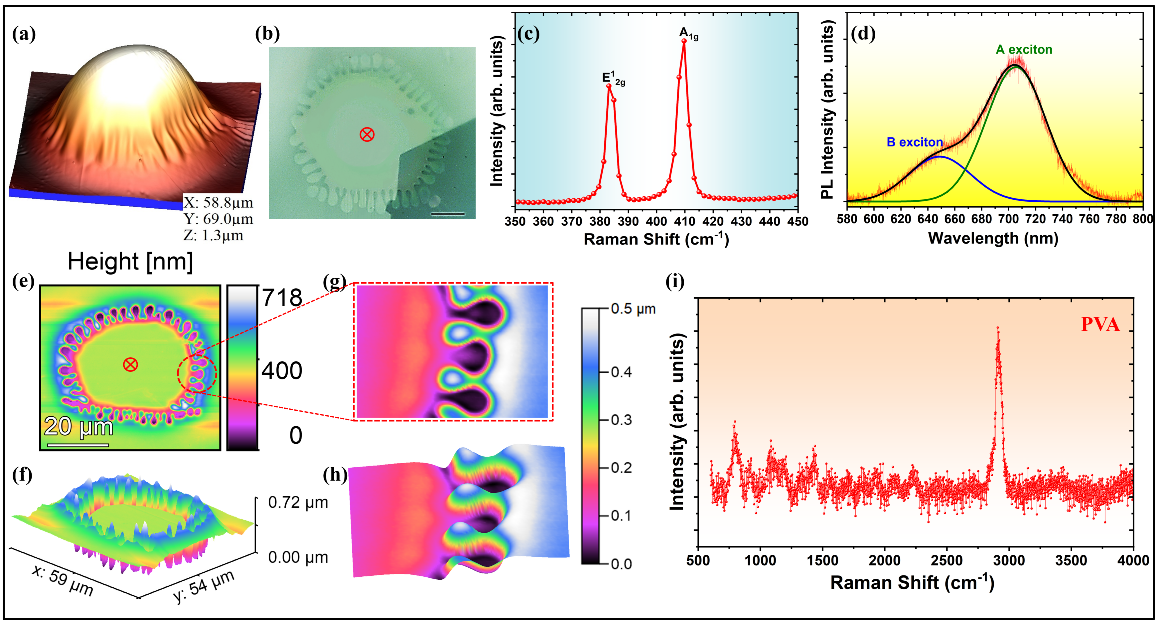

Figure 4.4: Multilayer MoS_2 blister with coupled instability: (a) AFM topographic 3D image, (b) optical image (scale bar: 10 μm), (c, d) Raman and PL spectra acquired at a point (red-colored, as shown in (b)) located at the center of the blister, respectively, (e, f) AFM topographic 2D and 3D image of the viscous fingering pattern on the PVA surface, (g, h) top-view and side-view of the polymeric fingers, respectively, and (i) Raman spectrum acquired at the center of the pattern, indicating no degradation of the polymer.

is radially displaced by the water vapor at the raised temperature. The polymeric fingers are captured by the wrinkles only at the edge of the blister, which depicts the interfacial nature of viscous fingering. The heat treatment (at ∼ 200°C) of a PVA-supported blister in upside-down orientation can also reveal the type of viscous instability whether interfacial or bulk[230]. Due to the good thermal conductivity of the 2D material, the polymeric fingers at the periphery of the blister deform prior to the central region of the blister, depicting the interfacial nature of the viscous fingering. The blisters showing negligible deflation rate due to confinement of liquid water (see Figure 4.5) facilitate the local strain engineering of the MoS_2 flake (see Figure 4.6).

Interestingly, we found that the wrinkle wavelength is nearly equal to the finger wavelength (see Figure 4.3(d, f)). Therefore, the parameters governing the wrinkling in the thin MoS_2 blister are directly related to the parameters for the onset of viscous fingering. Finding a critical criterion for such a situation to occur would indeed be worthwhile. According to the ‘local wavelength law’, the wrinkle wavelength is given by[36]

$$\lambda_w = 2\pi \left(\frac{B_{\text{eff}}}{\mathcal{K}_{\text{eff}}}\right)^{1/4}, \tag{4.8}$$

where $\mathcal{K}_{\text{eff}}$ is the 'effective stiffness', i.e., the spring constant per a unit area of a compliant substrate, having units of $\frac{[\text{Energy}]}{[\text{Length}]^4}$. The wavelength of the polymeric fingers, derived by Saffman and Taylor, is given by[37,225]

$$\lambda_f = \pi b \sqrt{\frac{\sigma}{\Delta\mu U}}, \tag{4.9}$$

where U is the instantaneous radial velocity of the circular interface, σ is the surface tension at the water vapor to viscoelastic PVA interface, b is the undeformed initial thickness of the PVA film, and $\Delta\mu = \mu - \mu_0$ is the viscosity difference between viscoelastic PVA and water vapor. Since the PVA is more viscous ($\mu \sim 0.03$ Poise) than the water vapor ($\mu_0 \sim 0.00013$ Poise), the viscosity difference $\Delta\mu \approx \mu$.

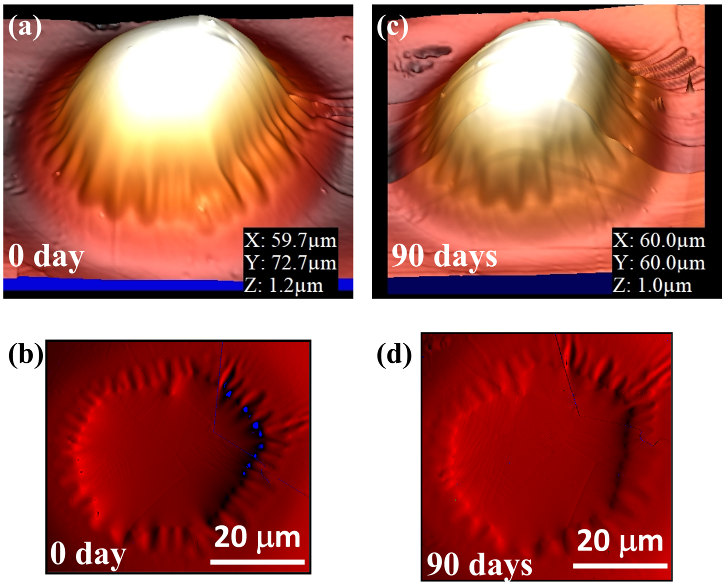

Figure 4.5: (a, c) The AFM 3D height images, and (b, d) the 2D amplitude images of a blister with coupled instability. The onset of wrinkling instability around the perimeter of a bubble of thin 2D flake is attributed to the phase transition of the confined water vapor during the cooling process[36]. The negligible time-lapse deflation of the polymer-curing-induced blisters at the ambient atmosphere indicates the liquid phase of the confined matter[2]. The blisters can sustain more than a period of 90 days. No new wrinkles were observed after the time-lapse, however, a few of the wrinkles vanish due to deflation.

On setting $\lambda_w \approx \lambda_f$, we obtain

$$U \approx \frac{\sigma b^2}{4\mu}\left(\frac{\mathcal{K}_{\text{eff}}}{B_{\text{eff}}}\right)^{1/2}, \tag{4.10}$$

where $\mathcal{K}_{\text{eff}} \approx \frac{\gamma}{\mathcal{L}^4}$ manifests the energetic cost required to deform the viscoelastic substrate, which should be of the order of the debonding (or, adhesion) strength of upper-bounding membrane for the viscous fingering instability to occur concurrently while blistering[36]. However, in the case of blistering of a 2D elastic membrane over a 2D layered vdW crystal as a substrate, $\mathcal{K}_{\text{eff}} \approx \frac{\Gamma}{d^2}$, i.e., the ratio of interfacial adhesion energy density to the power 2 of the interlayer spacing in the 2D crystal. Near the glass-transition temperature of the PVA substrate, the surface tension (σ) and viscosity (μ) measurements of 4% w/w PVA solution (prepared in water) yield $\sigma \sim 38$ mN/m, and $\mu \sim 3$ mPa.s, respectively. The thickness of the PVA film (b) is measured to be ~ 100 nm. The interfacial velocity U can be rewritten as

$$U \approx \frac{\sigma b^2}{4\mu\mathcal{L}^2}(\mathcal{J})^{1/2}, \quad \text{where} \quad \mathcal{J} = \frac{\gamma}{B_{\text{eff}}} = \left(\frac{6\mu Q}{\pi b^3}\right)\frac{\mathcal{L}^3}{B_{\text{eff}}}. \tag{4.11}$$

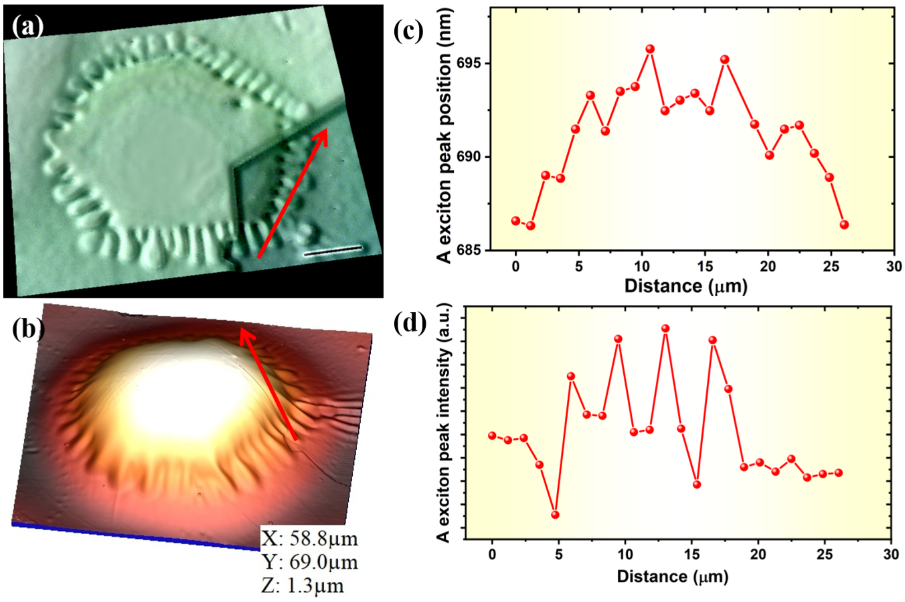

Figure 4.6: (a) Surface plot of the optical image; (b) AFM topographic 3D image of the blister; the arrow indicates the direction of the line map of the PL spectrum; (c, d) the line maps for the position and the PL intensity of the A-exciton peak, respectively. The optical band gap evolves across the curvature of the blister. The fluctuating line profile is because of the presence of wrinkles along the periphery of the blister.

For the volumetric flow rate $Q = \frac{\mathrm{d}V}{\mathrm{d}t} \sim \frac{\mathrm{d}(\mathcal{L}^2 h)}{\mathrm{d}t} = \mathcal{L}^2\dot{h}$, and for a given system with fixed elastic and viscoelastic parameters, we obtain for all time:

$$U = \dot{R} \sim C \left(\frac{\dot{h}}{\tau} \right)^{1/2}, \tag{4.12}$$

where C is a constant prefactor. The equation 4.12 implies that a resonance between the in-plane velocity of the radially propagating viscoelastic fluid and the out-of-plane debonding velocity of the upper-bounding membrane leads to a condition where both the viscous fingering and the wrinkling instability in a blister interact with each other and occur concurrently. For the flux-driven pressure to be of the order of the confinement pressure, i.e., $P = \left(\frac{6\mu Q}{\pi b^3}\right) \sim \Delta p$, $\mathcal{J} \to \mathcal{J}^* \Rightarrow U \to U^*$. It is to be noted that the atmospheric pressure outside the blister (i.e., p_0) remains constant, which has not been taken into account in the model to avoid complexities. This hypothesis effectively helped us in relating the growth dynamics of the viscous fingering patterns with the interfacial adhesion energy (Γ) and the interfacial in-plane velocity (U^*) of the viscoelastic PVA being displaced by the water vapor while blistering (see Figure 4.7). We observed that both the parameters (Γ and U^*) simultaneously affect the growth dynamics of the fingering patterns.

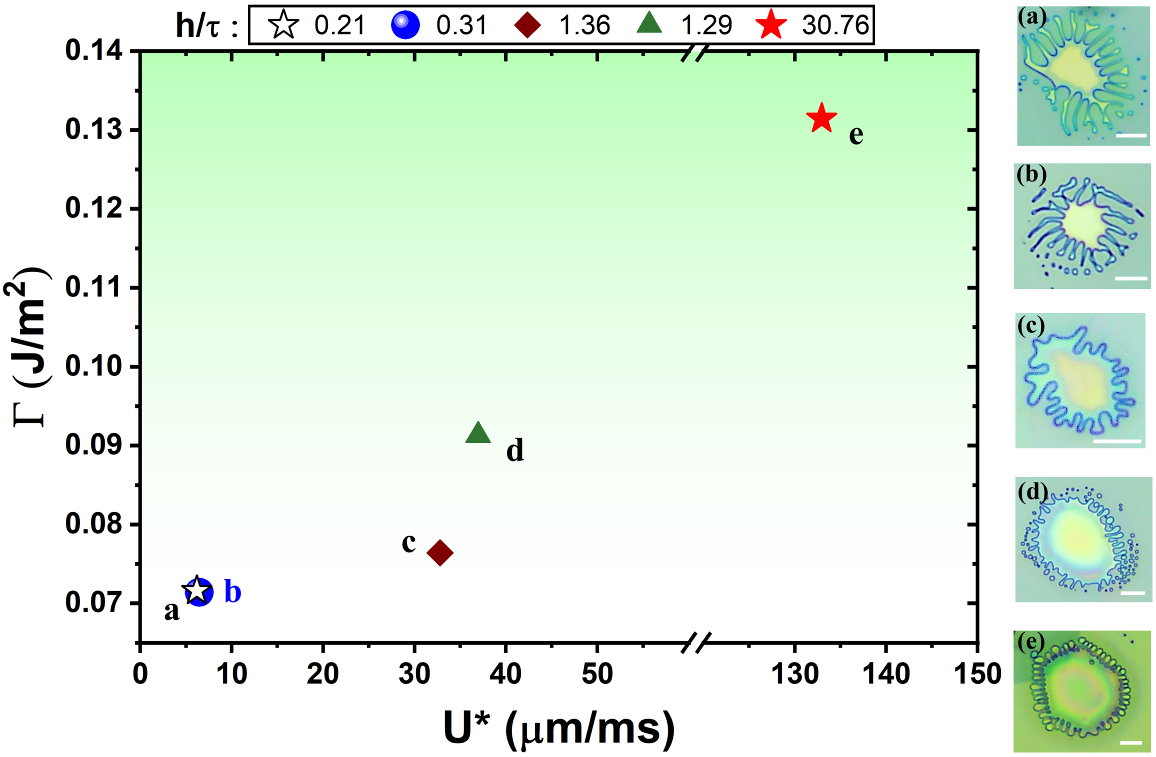

Figure 4.7: Graphical representation of circular blisters showing the dynamical evolution of interfacial viscous fingering instability with respect to the effective interfacial radial velocity (U^*) and the interfacial adhesion energy (Γ). The scale bar is 10 μm.

The 2D material blisters with stable interfaces form spontaneously in the conventional PVA-curing-induced blistering process, where the stability of the interface is due to the higher viscosity and stronger viscous stresses of the PVA surface. The viscoelastic PVA remains typically static while PVA-curing-induced blistering at the ambient condition (see Figure 4.1), however, under the cold-mist adsorption-assisted PVA-curing-induced blistering, the viscoelastic PVA radially propagates with an appreciable in-plane velocity and makes the interface unstable (see Figure 4.7). The weaker the interfacial adhesion of the multilayered MoS_2 flakes, the larger the polymeric finger length due to the smaller interfacial velocity of the viscoelastic PVA. The ice-water droplets locally reduce the viscosity of the PVA and make it quite deformable at the raised temperatures ($\sim$ 100°C). The adsorbed water content or wetting results in the formation of blisters with exceptionally large values of the parameter h/τ, which indicates significant interlayer sliding during the blistering of the 2D multilayered flake. It should be noted that the blisters with a large $h/\tau >> 1.5$, still follow the elastic plate profile. This observation suggests that the parameter h/τ is significantly influenced by the interlayer slippage as well as the interfacial adhesion strength.

4.4 Summary

In summary, the synthesis and processing conditions, in addition to the interfacial debonding strength of the MoS_2 multilayers, the confinement pressure inside the blisters, and the phase of the confined matter have crucial roles to play in the stability and dynamics of the blister system. The elastic properties of the 2D material, the viscoelastic properties of the polymeric substrate, and the physical properties of the confined fluid affect the blistering of the 2D multilayers. The adsorption of ice-water droplets on the hydrophilic PVA surface favors the interlayer sliding while blistering of the 2D multilayers at the raised temperature, which results in the exceptionally high values of the parameter h/τ, violating the non-linear elastic plate model. In the cold mist adsorption-assisted blistering of a 2D multilayer, the lower the interfacial radial velocity of the viscoelastic PVA, the larger the finger length. When the criterion of the resonance between the interfacial (in-plane) velocity of the polymer and the out-of-plane bending velocity of the 2D material is met, the solid-based wrinkling instability occurs concurrently with the viscous fingering instability. The mechanical insights of the blisters could potentially provide information about regulating the viscoelastic substrate-based instabilities in the blistering of the 2D layered vdW materials. The developed understanding might facilitate the next-generation applications of 2D materials and their blisters in flexible electronics, biomedical implants, single-photon detection, micro-/nanoelectromechanical sensing, etc.

Chapter 5

Pinning of graphene for conformal wrinkling over a soft corrugated substrate via snap-through transition

5.1 Introduction

The thinnest two-dimensional (2D) material, graphene shows remarkable mechanical strength as it can withstand a mechanical strain up to $\sim$ 20% before rapture[3,64]. The ultra-high flexibility and stretchability of the 2D materials make them mechanically reliable and promising materials for wearable electronics[84–86]. In addition, the 2D materials show remarkably strain-sensitive electronic, optical, and vibrational properties, which make them worthy for nanoscale strain engineering[80,81,109,110]. The Nitto tape-based micromechanical exfoliation method produces 2D flakes of the highest quality amongst the other known deposition or growth techniques[88]. However, the direct transfer of single-crystalline graphene flakes (hydrophobic in nature) from the Nitto tape onto a pristine PDMS substrate faces incomplete as well as random transfer, which produces low deposition yield with several delamination regions and wrinkles[115,116,346]. This transfer process is probabilistic, non-deterministic, and unselective and demands the wettability of the PDMS substrate, which is hydrophobic by nature in its pristine state. For better wettability, its surface-functionalization is carried out through oxygen-plasma treatment before transfer[117]. However, it has been observed that the oxygen-plasma treatment time has a substantial effect on the surface roughness of the PDMS substrate.

The surface roughness of the underlying substrate, the number of layers in the 2D nanosheet, and the interfacial adhesion play crucial roles in the conformation or delamination of the 2D nanosheet[347–350]. Through the theoretical framework of continuum mechanics, it is found that a conformally adhered 2D nanosheet over a corrugated substrate has higher debonding strength than that over a smooth and flat one[351]. The nanosheet must remain static and conformed during a mechanical straining process for an efficient and larger strain transfer. The conformity of the nanosheet is found to vary with the amplitude and wavelength of the substrate's surface corrugation. In the literature, several ways have been proposed to strengthen the interfacial adhesion between the 2D flakes and the substrates, such as (i) by polymeric encapsulation of the 2D flakes[352,353], (ii) by increasing the substrate's surface wettability[117], (iii) by anchoring the flake with metallic clamps at the edges[109], etc. These methods have their individual pros and cons. Despite extensive efforts in achieving good interfacial adhesion of 2D nanosheets, a lack of attention has been paid to the substrate's surface roughness manipulation through surface-engineering methods, possibly due to the fact that the substrate's surface roughness negatively impacts the interfacial adhesion of the 2D nanosheets. The adhesion characteristics of a 2D nanosheet over a substrate are investigated by analyzing the topographical features of the delaminated regions (blisters, folds, buckle delaminations, wrinkles, etc.)[2,62,115,230,354,355]. The wrinkled/buckled nano-/microstructures of 2D materials over polymeric substrates are commonly observed in thermal-mismatch-induced straining[356,357] and polymer-based transfer processes[14,105,120,121,358,359]. In addition, a significant Young's modulus mismatch between a 2D material and an elastomeric substrate results in the formation of the wrinkles of the 2D material through a conventional prestretch-release process[19,33,39,46,224,355,360–362]. However, the interfacial contact failure or sliding results in the formation of buckling-induced delaminations, folds, or fractures[50,350]. The physical properties of the wrinkled/buckled 2D nanosheet alter in accordance with the local deformation of the lattice structure[222]. It has been observed that the probability of the onset of the buckling-induced delamination of the 2D nanosheet reduces severely by O_2-plasma treatment of the PDMS surface[223]. The plasma treatment forms a stiff skin layer at the top of the PDMS surface but may also induce unwanted surface cracks[118]. Therefore, it is highly challenging to obtain the conformal adhesion of the 2D elastic nanosheets over hydrophobic elastomeric substrates such as PDMS.

Recently, Teng Cui *et al*[350] reported that the interfacial fatigue propagation at the graphene-polymer interface causes mechanical folding instabilities in the graphene membrane under loading-unloading cycles. The ultralow bending stiffness of the 2D materials makes them susceptible to out-of-plane buckling delamination over the stretchable substrates at small compressions due to elastic modulus mismatch. However, there is a spontaneous transition from buckle delamination to fold due to interfacial slippage at higher compression above 10%[50]. The folding instability must be suppressed in order to achieve good conformal adhesion of a 2D elastic nanosheet over a flexible substrate. The conformal and stretchable nano-/microstructures of 2D materials on flexible substrates have outstanding implications in healthcare monitoring systems, artificial electronic skins, and wearable strain/pressure sensing applications[363–365]. Current studies have been especially focussing on maximizing the structural compliance of the implanted devices[363]. The conventional electronic skins based on metal matrix have lower stability, poor compatibility with human skin, and low strain-sensing capability because of their low sensitivity and poor stretchability[366]. Graphene, on the other hand, is a very robust material for conformal artificial electronic skins due to its exceptional sensitivity, stretchability, durability, and biocompatibility. In addition, the high transparency, thermal stability, flexibility, and biocompatibility of PDMS assure the mechanical reliability of the device[367]. The PDMS (Sylgard 184) exhibits stable mechanical properties with negligible elastic hysteresis under a cyclic loading-unloading process. In addition, it immediately regains the steady state independent of the deformation rate, making it a promising substrate for wearable sensors[368]. The conformal wrinkles of single or even few-layered 2D materials over polymeric substrates allow tuning of the out-of-plane interlayer coupling in the 2D layered vdW materials to result in tunable mechanical properties[46,223], and also show remarkably enhanced mechanical, electrical, and thermal properties[363,369–373]. Despite devoted theoretical footing for the wrinkling of the 2D elastic membranes, the quest for a scalable experimental approach for creating conformal wrinkles over the corrugated soft substrates without forming folds or buckle delaminations still continues[374–376].

The conventional prestretch-release process at higher prestrain values ($\gtrsim 5\%$) results in the formation of folds or buckle delaminations in the 2D elastic nanosheets such as graphene, MoS_2, etc. over a smooth PDMS substrate[50,350,377]. The substrate roughness, interfacial adhesion, and elastic moduli mismatch affect the surface traction of the 2D material under compression, which determines the effective shear stress at the interface that causes buckling instability to develop. In this work, we showcase the utilization of the prestretch-release process for the pinning of the graphene membrane over periodic depressions on a PDMS substrate. We found that this technique effectively suppresses the mechanical folding instabilities in the 2D elastic nanosheets. The membrane is pinned via ‘snap-through transitions’. A ‘snap-through transition’ occurs to change the morphology of an elastic 2D nanosheet from a flat state to a near conformal state over a corrugated substrate[378]. Similarly, a morphological switch (transition) of a buckle delamination from one stable configuration to another under the application of strain is called 'snap-through buckling instability'[333,379–384]. The elastic membranes are susceptible to snap-through instability in the presence of external strain[40,385–387]. It has been observed that the stress-transfer efficiency for graphene over a smooth & flat PDMS substrate under uniaxial stretching is as low as $\sim 3\%$[81,388] because of its weak interfacial adhesion with the PDMS substrate (~ 0.007 J/m^2)[389]. However, by exploiting the membrane pinning method, the stress-transfer efficiency can be severely enhanced. Herein, we utilized the differently rippled PDMS substrates to investigate the role of substrate roughness in the adhesion mechanics of the graphene membrane under a stress loading-unloading cycle. The ripples on the PDMS substrates are formed through low-energy ion beam (IB) irradiation at different angles of incidence[390–393]. The ripple patterns on the PDMS surface undergo morphological evolution through ion beam irradiation not only under the varying angles of incidence[391] but also under the varying ion energy[390,394] as well as the PDMS annealing temperature[395]. Our work offers fundamental as well as practical insights into the membrane pinning mechanism for conformal wrinkling over a corrugated soft substrate under the prestretch-release process at the nanoscale. This technique can be exploited to obtain hierarchical graphene architectures[46]. The regulation of the graphene configuration over the engineered surfaces opens up new pathways for conformal and tunable electronics[215,382,393].

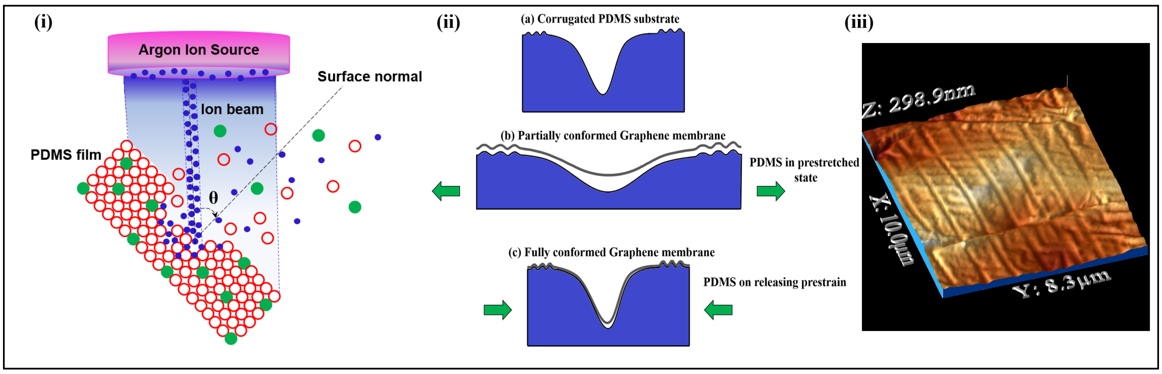
(i)
Argon Ion Source
Surface normal
Ion beam
PDMS film
θ
(ii)
(a) Corrugated PDMS substrate
(b) Partially conformed Graphene membrane
PDMS in prestretched state
(c) Fully conformed Graphene membrane
PDMS on releasing prestrain
(iii)
Z: 298.9nm
X: 10.0μm
Y: 8.3μm

Graphical abstract depicting the conformal wrinkling of graphene over a soft corrugated substrate through pinning via snap-through transitions.

5.2 Experimental methods

5.2.1 Fabrication of PDMS substrates

First, the silicone elastomer base and silicone elastomer curing agent of the Dow Corning SYLGARD-184 kit (Sigma Aldrich) taken in a 10:1 ratio by mass, are properly mixed in a petri-dish for 10 min to make a homogeneous solution. The solution is kept inside a vacuum desiccator for 5 min to pop out the bubbles formed in the PDMS solution during the stirring. The mixture is then spin-coated at 200 rpm for 90 s on a 4-inch borosilicate glass wafer to ensure better flattening of the polymer surface. The spin-coated PDMS is cured in a convection oven at 100°C for 1 h after letting it settle down for 10 min. The PDMS film is peeled from the wafer once it cools down to room temperature. The PDMS sheet ($\sim 250\ \mu$m thick) is cut into smaller sheets of dimensions 1 cm × 1 cm to use as flexible substrates for further investigation.

5.2.2 Ion-beam bombardment assisted rippling of PDMS substrates

Low energy (500 eV) argon ion beams, extracted from a Kaufman-type broad-beam ion source, are incident on a pristine flat/smooth PDMS substrate. All experiments are conducted in an ultra-high vacuum (UHV) chamber of base pressure 8×10^{-8} mbar and working pressure of 1×10^{-4} mbar. To avoid the impurity, special care has been taken using the load lock system attached to the UHV chamber. The ion flux is set to 2.87×10^{15} ions/cm^2/s, the ion fluence is set to 8.62×10^{17} ions/cm^2, and the angle of incidence of the ion beam with respect to a normal to the PDMS substrate's surface is set to 0°, 30°, and 60°, sequentially, each for a bombardment period of 5 min. We obtain the surface nanoripples of different corrugation profiles. The pristine PDMS substrate surface has a root mean square (RMS) roughness of ~ 5 nm. Ion beam (IB) irradiation, however, causes the RMS roughness to dramatically increase up to ~ 30 nm.

5.2.3 Sample fabrication and PVA-assisted wet transfer process

PVA-assisted exfoliation (PAE) technique is used to deposit graphene flakes onto a PVA-coated borosilicate glass (Pyrex) substrate[62,88], wherein the deposition of the high-quality single-crystalline graphene flakes from a Nitto tape decorated with graphitic flakes in conformal contact with the substrate takes place while curing the PVA film. The graphene/PVA/Pyrex stack, in upside-down orientation, is aligned &

placed in conformal contact with a smooth or rippled "**p**restretched-(poly)dimethylsiloxane" (**p**-PDMS) substrate (uniaxially stretched by 40% of its length using a two-point stretching tool). The PVA film is dissolved with continuously but gradually falling DI water droplets over it for ∼ 6 h at room temperature, which thereby leaves behind the graphene flakes on the p-PDMS substrate. No water intercalation between the graphene flakes and the PDMS substrate (as both are hydrophobic by nature) helps the water-soluble layer of PVA to get dissolved properly, and a clean & complete transfer of the graphene flakes is obtained with their unaltered relative positions. The graphene/p-PDMS stack, held with the straining stage, is then dried overnight under reduced pressure for better adhesion. Thereafter, the uniaxially prestretched PDMS substrate is released controllably, which generates periodic wrinkles or buckle delaminations of the graphene flakes on the PDMS substrate (see Figure 5.1).

5.2.4 Characterizations

Optical identification of the graphene flakes has been carried out under a high-resolution optical microscope. The Raman spectroscopic measurements have been carried out using a HORIBA LabRAM HR Evolution system on the identified 2D flakes in ambient atmospheric conditions. The output power of the laser light is kept low (to avoid local heating) at ∼ 1 mW for the laser excitation wavelength of 633 nm using a 100× air objective lens (NA=0.8) with a detector grating of 600 lines mm^{-1} in a confocal microscopy setup. The laser spot size is of the order of 1 μm. For the Raman mapping, the acquisition time is set to 1 s for single accumulation with a step size of 160 nm. The atomic force microscopy (AFM)-based topographical measurements have been performed with a standard silicon cantilever (in tapping mode) on a Bruker MultiMode-8 AFM setup. The AFM data visualizations and analyses have been carried out using the Gwyddion and WSxM software packages. The field emission scanning electron microscopy (FESEM) images of the samples (after gold coating) were captured with JEOL JSM-7610F Plus setup for morphological characterization.

5.3 Results and Discussion

The conventional prestretch-release process (as depicted in Figure 5.1) has been extensively utilized for controlled buckling of the 2D elastic nanosheets[19,39,360]. The micromechanically exfoliated single or few-layer graphene (SLG/FLG) flakes (hydrophobic in nature) are deposited onto prestretched (by 40% of its original length) PDMS substrate having a flat or rippled surface (see Figure 5.2) by employing the 'PVA-assisted wet transfer process'. Due to the large elastic modulus mismatch between the graphene membrane and the PDMS substrate ($10^6 : 1$), periodic wrinkles (confor-

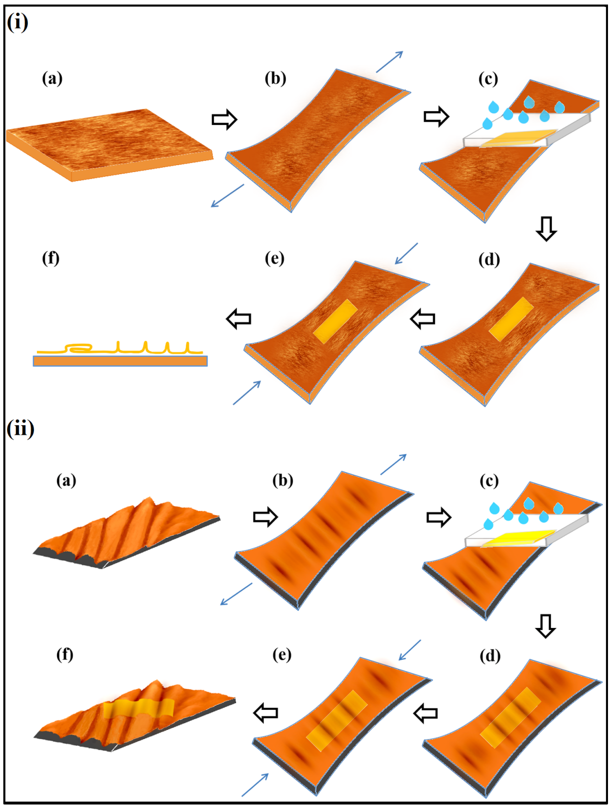

Figure 5.1: Schematics showing (i) the buckling-induced folds and delaminations of a 2D elastic membrane over a flat & smooth surface of PDMS, and (ii) the conformal wrinkling of a 2D elastic membrane over a corrugated surface of PDMS, resulting from the conventional prestretch-release process.

mal deformation of the membrane and the substrate) or buckle delaminations develop over the substrate upon release of the prestrain.

The interfacial behavior in the context of the substrate's roughness and slipperiness has an impact on the buckling topography of a 2D elastic nanosheet, in addition to the elastic properties of the 2D material, thickness of the nanosheet, and the amount of compressive stress[50,350,396] (see Figures 5.3 and 5.4). Now, in order to analyze the role of substrate surface corrugation in the adhesion mechanics of the graphene flakes under the prestretch-release process, we utilize the PDMS substrates rippled or patterned through IB irradiation. The low-energy (500 eV) argon ion beams, incident on the pristine PDMS substrate at different incident angles, produce surface ripples of different corrugation profiles as a result of the stress-driven instabilities. For the IB irradiation at the angles of incidence of 0° and 60° to the normal to the PDMS surface, we obtained serpentine-shaped ripples (see Figure 5.2(b & d, respectively)), but interestingly, at an angle of incidence of around 30° a nearly periodic trench (depression) pattern in addition to the ripples is obtained on the PDMS surface (see Figure

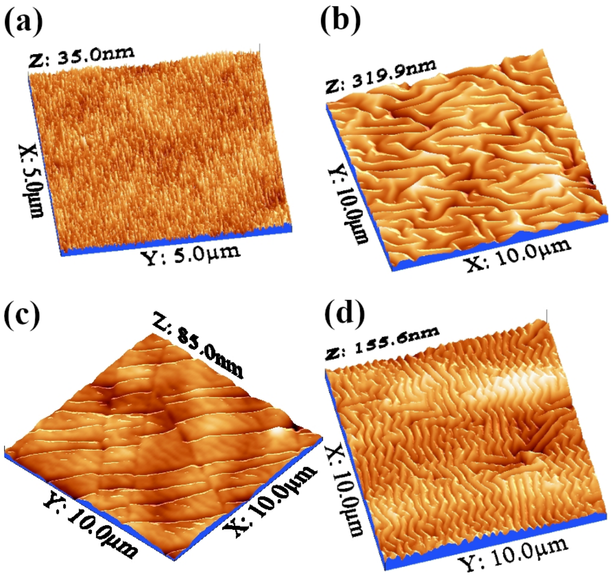
(a)
Z: 35.0nm
X: 5.0µm
Y: 5.0µm
(b)
Z: 319.9nm
Y: 10.0µm
X: 10.0µm
(c)
Z: 85.0nm
Y: 10.0µm
X: 10.0µm
(d)
Z: 155.6nm
X: 10.0µm
Y: 10.0µm

Figure 5.2: AFM topographic 3D images of (a) the flat & smooth surface of a pristine PDMS substrate and (b, c, and d) rippled PDMS surfaces obtained through IB irradiation at angles of incidence of 0°, 30°, and 60°, respectively, with respect to a normal to the PDMS substrate's surface.

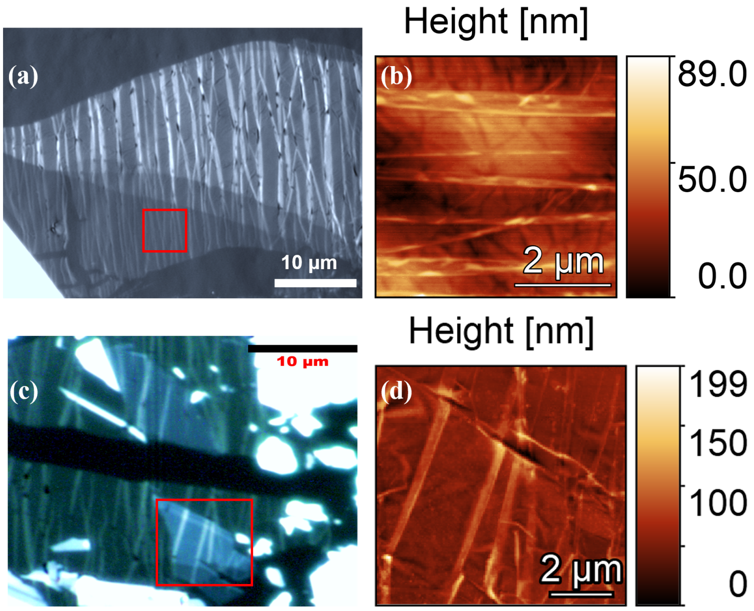
Height [nm]
(a)
10 µm
(b)
2 µm
89.0
50.0
0.0
Height [nm]
(c)
10 µm
(d)
2 µm
199
150
100
0

Figure 5.3: (a, b) Optical and corresponding AFM height image of a fewlayer graphene flake having folds (standing and fallen) over a smooth PDMS substrate, (c, d) Optical and corresponding AFM height image of a hetero-fewlayer MoS_2/graphene flake having folds (standing and fallen) over a smooth PDMS substrate. The folds are optically visible and appear as white belts. The applied prestrain level is ∼40%.

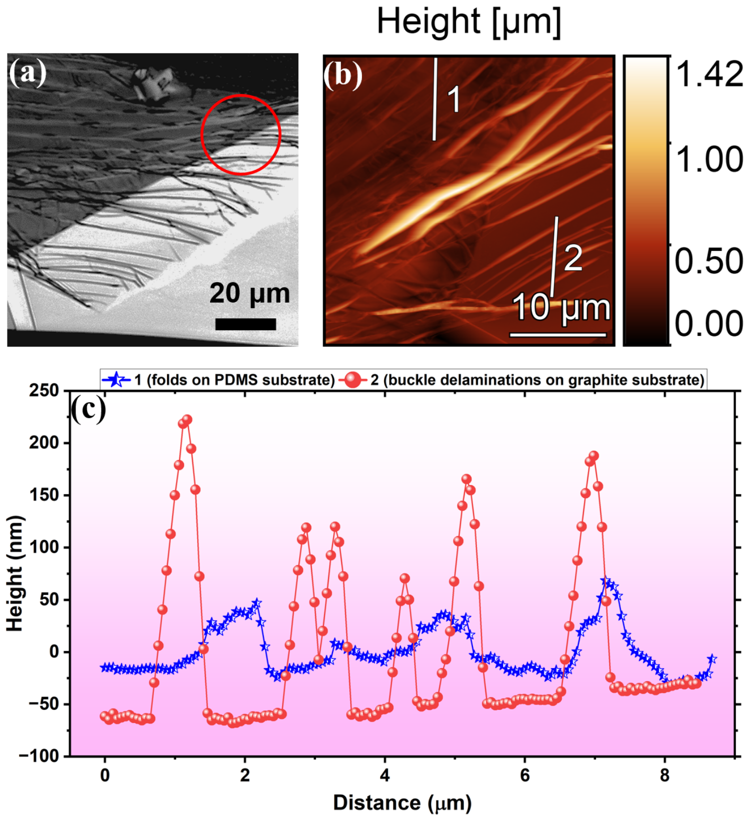

Figure 5.4: (a, b) Optical and corresponding AFM height image of a mechanically exfoliated fewlayer graphene flake over a smooth PDMS substrate that is partially suspended to the graphite substrate. The prestretch-release process results in the formation of folds and buckle delaminations; (c) AFM line profiles across the lines marked in (b), where the line profiles 1 and 2, respectively correspond to the folds and buckle delaminations of fewlayer graphene flake over smooth PDMS and graphite substrate, respectively. This infers that the degree of mechanical folding instability depends on the substrate roughness and interfacial adhesion, in addition to the elastic properties of the 2D material, the thickness of the 2D nanosheet, and the amount of compressive stress, as reported by Jaehyung Yu *et al*[50]. The more slippery the interface, the larger will be the height of the folds.

5.2 (c)). The competition between the bending energy of the homogeneous silica-like stiff skin layer (formed due to ion beam irradiation) and the stretching energy of the soft supporting layer of PDMS plays a crucial role in determining the ripple parameters or the corrugation profile[391]. The ion beam collision-induced local heating effect increases the local degree of crosslinking in the PDMS, which varies with the angle of incidence of the ion beam. As the degree of crosslinking increases, the number of polymeric chains in the PDMS decreases. Consequently, its stiffness (toughness) increases and the free volume in the polymer decreases locally, which restricts the local movement of the reactive ions. The thermal effect-driven restriction in the movement of the ions would reduce their penetration depth into the PDMS substrate[395]. The penetrating energetic ions collide with the PDMS structure and thereby, erode the molecules out of the structure. After the reorganization of the atoms on the surface, thinner silica-like skin layers form in the PDMS substrate, which results in the formation of ripples of smaller corrugation wavelengths. Therefore, a competitive interplay between the sputtering-induced self-diffusion and thermally activated self-diffusion processes determines the growth dynamics of the surface instability in the form of ripples[397].

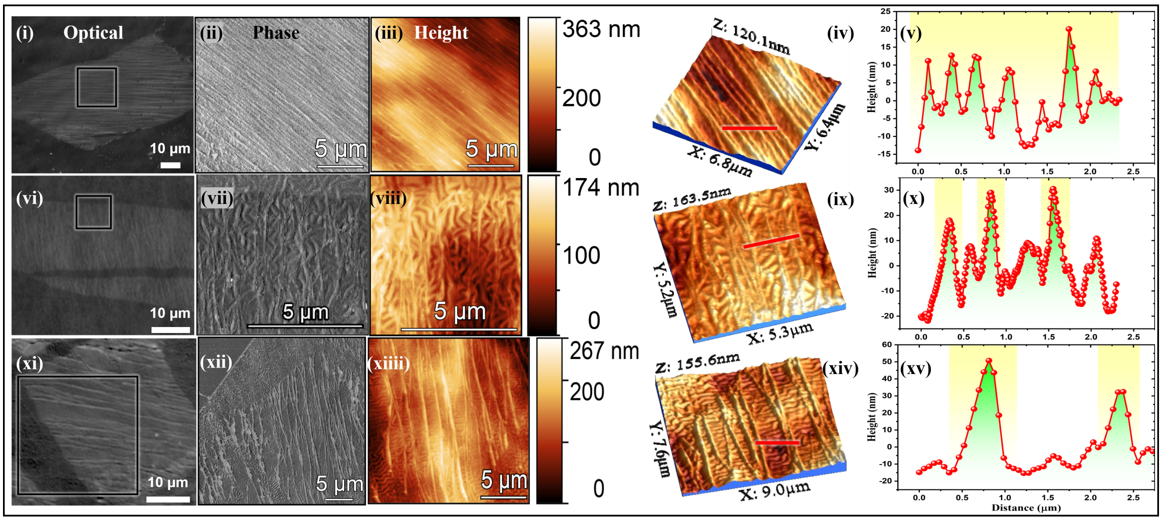
(i) Optical
10 μm
(ii) Phase
5 μm
(iii) Height
5 μm
363 nm
200
0
(iv)
Z: 120.1nm
X: 6.8μm
Y: 6.4μm
(v)
Height (nm)
(vi)
10 μm
(vii)
5 μm
(viii)
5 μm
174 nm
100
0
(ix)
Z: 163.5nm
X: 5.3μm
Y: 5.2μm
(x)
Height (nm)
(xi)
10 μm
(xii)
5 μm
(xiii)
5 μm
267 nm
200
0
(xiv)
Z: 155.6nm
X: 9.0μm
Y: 7.6μm
(xv)
Height (nm)
Distance (μm)
0.0
0.5
1.0
1.5
2.0
2.5

Figure 5.5: Optical, AFM phase, 2D & 3D height images, and corresponding line profiles across the lines marked in red (respectively, from left to right in a row) of the graphene flakes (single to few layers) over the smooth (i-v), and rippled PDMS surfaces obtained through IB irradiation at the angles of incidence of 0° (vi-x), and 60° (xi-xv). The optically visible white belts across the graphene flakes depict the buckling-induced folds. The shaded portions in graphs represent the graphene folds distinguishing it from the PDMS surface corrugations.

We observed folds of SLG/FLG flakes not only over the smooth PDMS substrate but also over the randomly oriented serpentine ripples on the PDMS substrates (obtained from argon ion beam incident angles: 0° and 60°) in the uniaxial prestrain-release process with a prestrain level of 40% (see Figure 5.5). The compressive stress resulting from the uniaxial loading-unloading cycle leads to local activation of the buckle delamination regions alongside the existing wrinkles, which spontaneously collapse to form the folds[350]. The collapsed folds appear as white belts through high-resolution optical microscopy and FESEM imaging[50] (see Figure 5.6). The wrinkle-to-fold transition occurs due to interfacial sliding in a stress-release process for a significant prestrain level[350]. The prestretch-release process not only induces the

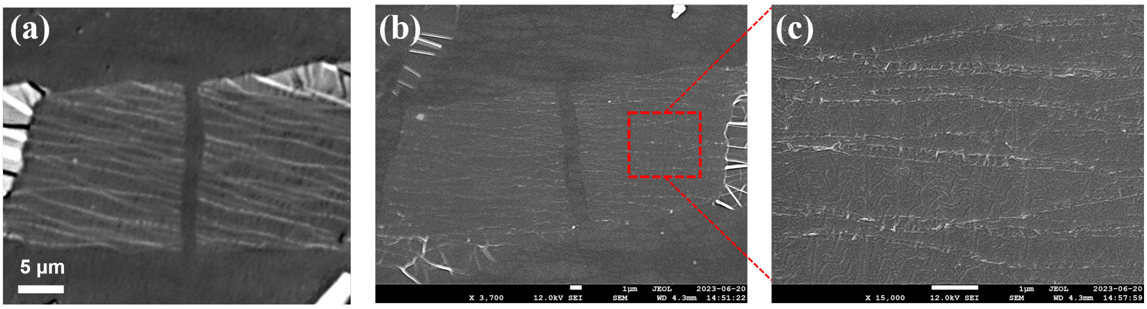
(a)
5 μm
(b)
1μm JEOL 2023-06-20
X 3,700 12.0kV SEI SEM WD 4.3mm 14:51:22
(c)
1μm JEOL 2023-06-20
X 15,000 12.0kV SEI SEM WD 4.3mm 14:57:59

Figure 5.6: (a) Optical image of graphene folds over an ion-beam irradiated PDMS surface having serpentine ripples, (b) the corresponding FESEM image, and (c) the zoomed-in FESEM image depicting the folds of graphene over the rippled PDMS substrate.

buckling zone but also propagates the buckle wave-fronts dynamically from the edges toward the internal region, and the wrinkle-to-fold transition occurs in the buckling zone. The ultra-low bending stiffness and high self-adhesion of the single to few-layer graphene flakes give rise to the formation of the hair-pin-shaped folds, however, the buckle delaminations are more pronounced for the multilayered flakes[50]. We noticed that as the roughness of the PDMS surface increases the density of the graphene folds decreases with the increasing width of the folds due to rising friction under compression (see Figure 5.5). The roughness of the substrate influences the interplay of interfacial slippage and delamination under compression. As the compressive stress reaches a threshold value (σ_{thr}) at a point, the delamination of the membrane occurs spontaneously, depending upon the interfacial adhesion energy (Γ) of the 2D elastic membrane and the substrate, such that[50]

$$\sigma_{\text{thr}} = \sqrt{2E_{\text{2D}}\Gamma}. \tag{5.1}$$

Hence, it is possible to suppress the mechanical folding instabilities in 2D elastic nanosheets under compression by altering the interfacial adhesion by means of manipulating the substrate's surface roughness. It is therefore compelling to search for an appropriate surface feature that can offer a conformal as well as durable adherence to the graphene membrane without causing any folding instability. Interestingly, we observed conformal wrinkles of graphene flakes (which are free from folds) over periodically trenched PDMS surfaces obtained with IB irradiation at an incident angle of around 30° (see Figures 5.7(b), 5.8(c), 5.9, and 5.10). However, the randomly oriented ripples of PDMS are inefficient to suppress the mechanical folding instability in a 2D elastic nanosheet at a larger compression level during the release of prestrain. We note that almost equally & parallelly spaced unidirectional depressions

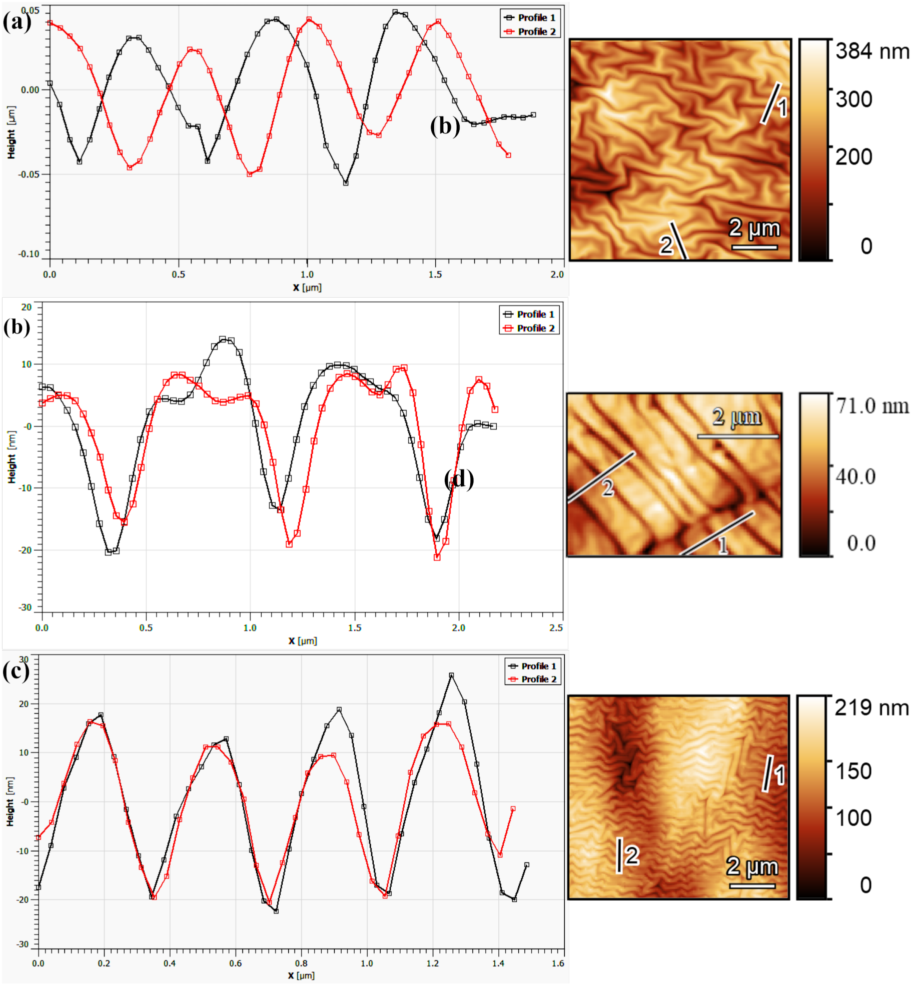

Figure 5.7: The topographic line profiles, across the lines marked in the corresponding AFM images (at the right), across the corrugations over the rippled (at 0° (a), 30° (b), and 60° (c)) PDMS surfaces.

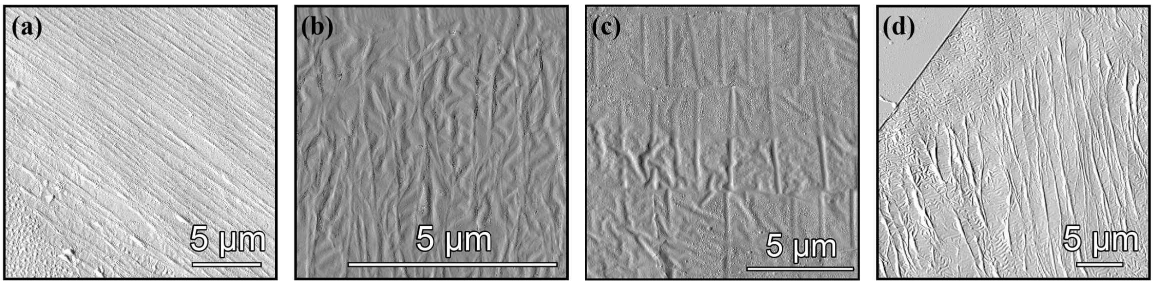

Figure 5.8: AFM-based amplitude images of the single to few-layer graphene flakes over the PDMS substrates((a) flat, and (b-d) patterned at different angles of incidence: (b) 0°, (c) 30°, & (d) 60°). The folds are inevitably observed (as shown in a, b, and d) in the prestretch-release process except for the trenched PDMS substrate (as shown in (c)).

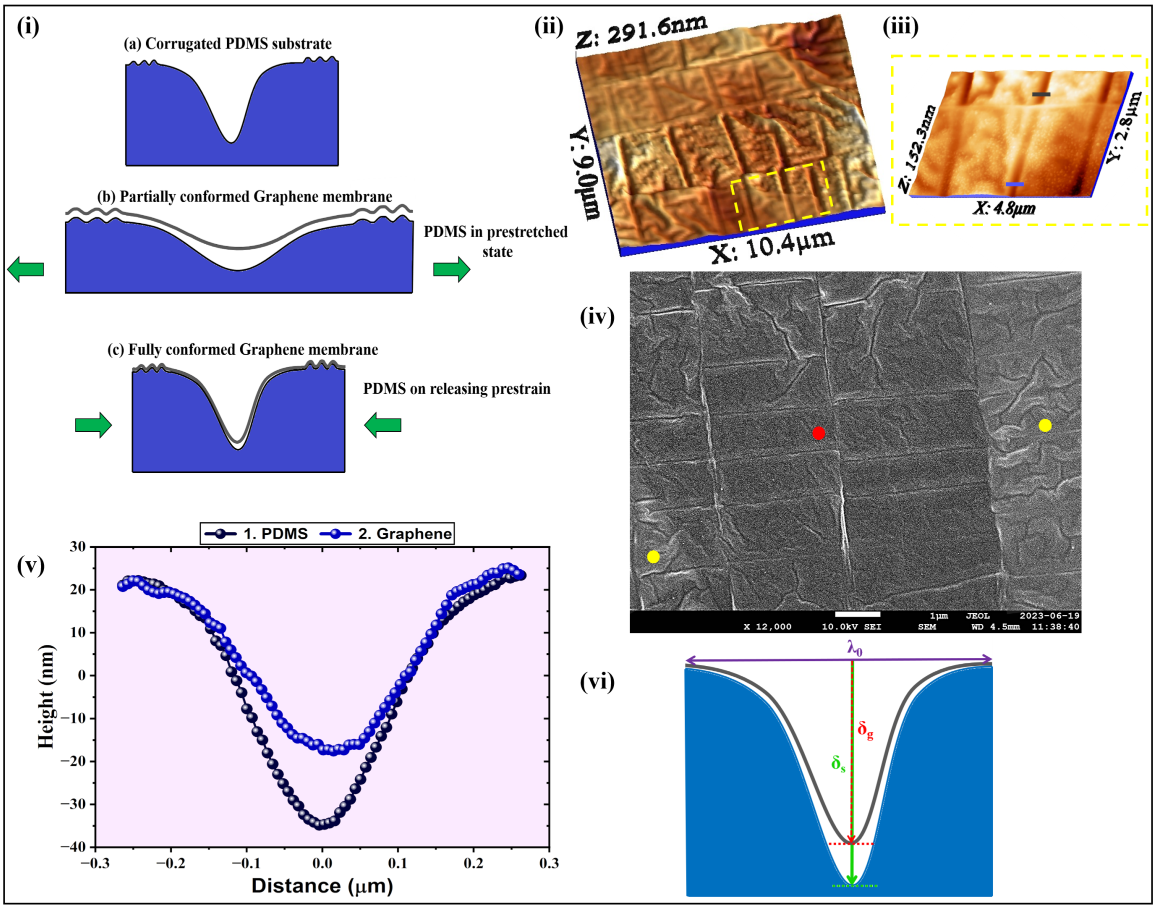

Figure 5.9: (i) Pinning of graphene membrane over the corrugated PDMS substrate via snap-through transition under the prestretch-release process. (ii) AFM topographic 3D image of the wrinkled graphene over a corrugated PDMS substrate having trenches, obtained through IB irradiation at an angle of incidence of 30°. (iii) Zoomed-in AFM topographic 3D image of the wrinkled graphene over trenches. (iv) FESEM image of the wrinkled graphene on the corrugated PDMS substrate (the red point indicates the wrinkled graphene region, and the yellow point indicates the corrugated PDMS region). (v) Topographic pinned configuration of the graphene membrane over a periodic depression. The line profiles correspond to the lines marked in black (for PDMS trench) and blue (for graphene wrinkle) in figure (iii). (vi) A schematic representation of the pinned configuration.

(trenches), having a maximum wavelength of $\sim 0.5\,\mu$m and a maximum depth of $\sim 50\,$nm, on the ion-irradiated surface of the PDMS, help in the conformal wrinkling of SLG/FLG flakes under the prestretch-release process. The degree of conformation of a membrane having single to few atomic layers of carbon atoms (SLG/FLG flake) increases with an increase in the corrugation wavelength of a rippled substrate[351]. It has been observed that single-layer graphene conforms more closely to a corrugated substrate having a larger curvature[398,399]. Therefore, a larger corrugation wavelength of the depressions on the PDMS substrate would prevent the atomically thin 2D flakes from forming folds under the prestretch-release process. This indicates that a better conformation of the graphene flakes is expected over a ‘corrugated PDMS substrate in a prestretched state’ in comparison to its normal state. When uniaxial tensile stress is applied in a direction normal to the axis of the periodic depressions in the plane of the trenched PDMS surface prior to the deposition of graphene, the depressions become shallower & broader (see Figure 5.9(i)-b). The shallower depressions allow the graphene membrane to conform more closely, which thereby helps in its conformal wrinkling under compression while the prestrain is released (see Figure 5.9). The graphene membrane does not conform close enough to the trenches over the PDMS surface directly, but under extension, the trenches broaden enough to make the membrane snap-through due to interfacial slippage. When the prestretched PDMS substrate is released, the pinning of the membrane over the periodic trenches takes place. As a result, the membrane adheres to the trenches conformally. As a consequence, the graphene membrane conformally adheres to the protrusions in the neighborhood of the trenches on the PDMS substrate without forming folds or buckle delaminations.

It should be noted that the thickness of the soft PDMS substrate is sufficiently large in comparison to that of the graphene membrane, which is consistent with the thin-film buckling theory[350,400]. The critical compressive stress for the onset of the wrinkling is given by, $\sigma_c = \frac{\tilde{E}_g}{4}\left(\frac{3\tilde{E}_s}{\tilde{E}_g}\right)^{2/3}$, where E_s and E_g are Young’s modulus of the PDMS substrate and the graphene membrane, respectively, and $\tilde{E} = \frac{E}{1-\nu^2}$, where ν is the Poisson’s ratio[396]. The wrinkling is favored for $\sigma > \sigma_c$. The release of the prestrain leads to the development of purely sinusoidal wrinkles of the graphene flake of thickness τ with a wrinkle amplitude $\delta_0 = \tau\sqrt{\frac{\sigma}{\sigma_c} - 1}$, and a wrinkle wavelength $\lambda_0 = 2\pi\tau\left(\frac{\tilde{E}_\mathrm{g}}{3\tilde{E}_\mathrm{s}}\right)^{1/3} = \frac{\pi\tau}{\sqrt{\varepsilon}}$, where $\varepsilon = \sigma_c/\tilde{E}_g$, is the elastic modulus mismatch strain. Under the prestretch-release process with a significant prestrain level of 40%, the wrinkle-to-buckle delamination transition would have begun at the lower values of compression, but at the later stages of the compression, the buckle comes into closure proximity due to vdW interactions and snaps into the form of a fold on the slippery interface[40,350].

The out-of-plane bending energy, in-plane strain (stretch/compression) energy, pinning (adhesion) energy of the graphene membrane, and surface roughness of the corrugated substrate play crucial roles in determining the equilibrium configuration profile (pinned or depinned) of the membrane over the corrugated soft substrate. As the Föpple von Kármán (FvK) number (bendability) of the layered 2D materials is

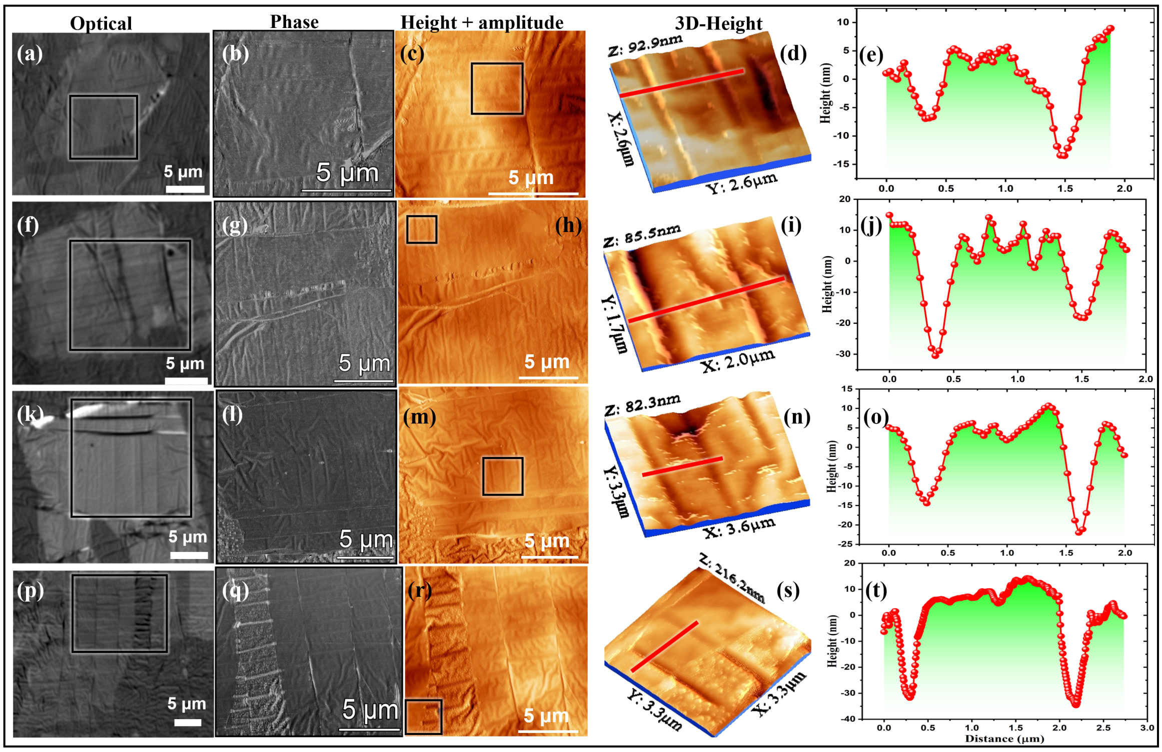

Figure 5.10: Optical, AFM phase, superimposed height & amplitude, zoomed-in 3D height images, and corresponding line profiles, across the lines marked in red, (respectively, from left to right in a row) of the wrinkled graphene (SLG (a, p) & FLG (f, k)) flakes over the trenched PDMS substrates obtained through IB irradiation at an angle of incidence of 30°. Note that the mechanical folding instabilities are suppressed effectively.

very large, i.e. $\kappa = \frac{E_{2\text{D}}a^2}{B_{\text{eff}}} \gg 1$, where $B_{\text{eff}} = \frac{E\tau^3}{12(1-\nu^2)} \approx \frac{NEt^3}{12(1-\nu^2)}$ is the effective out-of-plane bending stiffness (as each layer of a layered 2D material bends independently[23,401]), and $E_{2\text{D}} = E\tau$ is the in-plane (2D) elastic strain stiffness of the graphene membrane of thickness $\tau = Nt$, having the number of layers N, Young's modulus E, the Poisson's ratio ν, and the thickness of each layer of graphene t. The in-plane elastic strain energy dominates over the out-of-plane bending energy. The length scale parameter in the continuum model[402], i.e. $l = \sqrt{\frac{B_{\text{eff}}}{E_{2\text{D}}}}$, determines a crossover from the bending rigidity-dominated regime ($\delta_g < l$) to the in-plane strain-dominated regime ($\delta_g > l$), where δ_g is the corrugation amplitude of the graphene membrane. For the standard elastic parameters of single-layer graphene, $l \approx 0.1\,\text{nm}$, which implies that the elastic in-plane strain-dominated regime is more favorable for graphene. This regime favors the pinned configuration of graphene over the trenched PDMS substrate, which is attained via its snap-through transition over the shallower depressions[402].

At the snap-through condition, the pinning or interfacial adhesion energy of the graphene membrane becomes equal to its elastic strain energy over the trenched PDMS substrate, and the morphological transition occurs from the less conformal (or flat) state to the more conformal state, as depicted in Figure 5.9(i)-b. The elastic modulus mismatch-induced out-of-plane buckling or folding under in-plane compression is suppressed due to pinning of the graphene membrane over the trenches (depressions) on the rippled PDMS substrate via snap-through instability[380] (see Figure 5.10). For the corrugated graphene membrane having corrugation amplitude δ_g and corrugation wavelength λ_0 over a trenched PDMS substrate, the out-of-plane bending energy is given by $E_b \approx B_{\mathrm{eff}}\frac{\delta_g^2}{\lambda_0^2}$, and the in-plane elastic stretching energy is $E_s \approx E_{\mathrm{2D}}\frac{\delta_g^4}{\lambda_0^2}$[351,402]. The interfacial adhesion (pinning) energy density of the graphene membrane is $\Gamma_0 \approx E_{\mathrm{pin}}/\lambda_0^2$. The competitive interplay between the aspect ratio $\left(\frac{\delta_g}{\lambda_0}\right)$ and the elasticity of the corrugated membrane determines the configuration (pinned or depinned) of the membrane over the corrugated substrate. In the regime ($\delta_g > l$), where the elastic in-plane strains are dominant and also responsible for the depinning of the membrane[402], the membrane favors the pinned configuration in the limit $\frac{E_{\mathrm{pin}}}{E_s} > 1$, which results in (simplified approximation)

$$\frac{\delta_g}{\lambda_0} < \left(\frac{\Gamma_0}{E_{\mathrm{2D}}}\right)^{\frac{1}{4}}. \tag{5.2}$$

This infers that the shallower depression favors the pinning of the membrane under the prestretch-release process (see Figure 5.9(i)-b)[402]. The pinned configuration is always a local minimum of the total energy of the system. As a simplified assumption, a conformally adhered graphene membrane on a sinusoidally corrugated PDMS surface, having a corrugation wavelength of λ_0 and corrugation amplitude δ_{s}, attains a corrugation amplitude of δ_{g} due to vdW interactions (as shown in Figure 5.9(vi)). For fully conformal wrinkles, the corrugation amplitude of graphene equals to that of the substrate, i.e. $\delta_{\mathrm{g}} \approx \delta_{\mathrm{s}}$. From the minimization of the total free energy of the system (by following the approach by Aitken and Huang[351]), the interfacial adhesion energy density (Γ_0) of the membrane, having an equilibrium separation h_0 from the substrate's surface in the pinned state, turns out to be[351,376,378] (see Appendix B)

$$\frac{\Gamma_0}{E_{\mathrm{2D}}} \approx \frac{1}{24}\left(\frac{2\pi\delta_g}{\lambda_0}\right)^4. \tag{5.3}$$

For the pinned graphene membrane over the trenched PDMS substrate in our experiment, the above equation 1.4 yields the interfacial adhesion energy of the order of 2.2 J/m^2. The adhesion strength is almost 5 times larger than that reported for monolayer graphene on a smooth silicon oxide substrate[199]. The ultrastrong adhe-

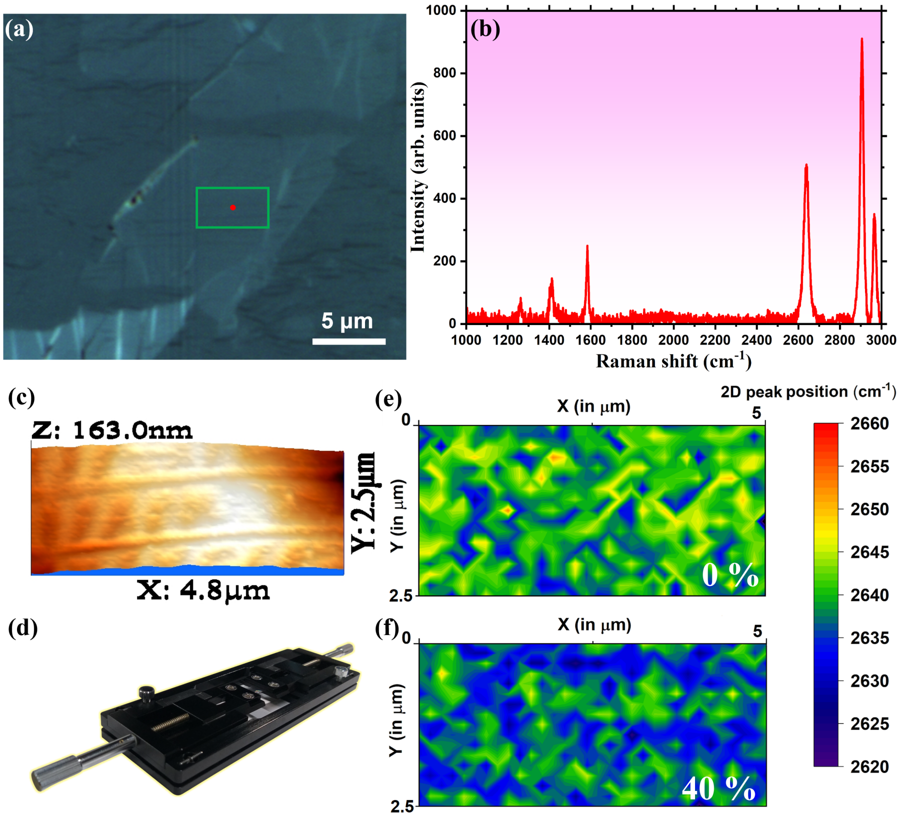

Figure 5.11: (a) Optical image of wrinkled single-layer graphene over a trenched PDMS substrate, and (b) the corresponding Raman spectrum taken at a point. (c) AFM 3D height image of the wrinkled graphene flake, (d) a two-point uniaxial straining tool; (e, f) Raman maps of 2D peak position for the area indicated by the green square in figure (a) under the applied tensile strain-level of (e) 0%, and (f) 40%, respectively.

sion of the graphene membrane over the soft corrugated substrate results from the pinning effect. An increase in the corrugation wavelength while prestretching the trenched PDMS substrate favors the snap-through transition of the membrane from flat morphology to a conformal state, which gives rise to the pinning effect while releasing the prestrain. Though the degree of interfacial adhesion improves via the optimized substrate's surface engineering through the prestretch-release process, in order to release any residual strain and to attain a fully conformal state of the graphene wrinkles over the rippled PDMS surface with periodic depressions, repeated stress loading-unloading cycles could be performed[81,403]. We analyzed the strain distribution across the wrinkled single-layer graphene under the varying applied tensile strain in the clamped PDMS substrate using a two-point bending/stretching tool (as shown in Figure 5.11) with in-situ μ-Raman mapping. The characteristic 2D peak is typically found to red-shift up to a tensile strain level of 40% applied uniaxially across the adhered graphene flake. Since the laser spot size ($\sim 1\ \mu$m) is not consistent with the corrugation wavelength or width ($\lesssim 0.5\ \mu$m) of the wrinkles, the acquired Raman signals mainly manifest the strain distribution across the flat regions of the wrinkled flake. As an estimate, the flat regions of wrinkled graphene experience a uniaxial tensile strain of $\sim 0.2\%$[39,404] at an applied tensile strain level of 40% (see Figure 5.11(f)). On stretching the trenched PDMS substrate uniaxially, the corrugation amplitude (depth) of the depressions on the substrate's surface would reduce to match the corrugation amplitude of the graphene membrane, which would further strengthen the interfacial bonding. The stronger conformation of graphene would reduce the probability of the graphene wrinkles to alter their orientation during loading-unloading cycles[405]. Such a wrinkled architecture obtained via the pinning of graphene over the trenched PDMS substrate could be beneficial for conformal and tunable electronics.

5.4 Summary

In summary, the corrugation profile of the polymeric substrate plays a crucial role in the buckling of the 2D elastic nanosheet under the prestretch-release process. The mechanical folding instabilities in the graphene membrane over a flat & smooth flexible substrate are inevitably observed at higher compressions in the prestretch-release process due to a significant elastic modulus mismatch. On the contrary, the snap-through transition of the graphene membrane across the shallower & nearly periodic depressions (trenches) on a prestretched PDMS substrate helps in the conformal wrinkling of the membrane on releasing the prestrain. Hence, we present a technique to manipulate the corrugation profile of a trenched soft substrate using the prestretch-release procedure to suppress the mechanical folding instabilities and thereby achieve conformal adherence of the graphene membrane through the pinning mechanism. This work opens up new pathways for achieving the substrate-regulated morphologies of the 2D elastic nanosheets. The conformal wrinkling of the 2D nanosheets may be harnessed for designing functional nanoelectromechanical conformal devices.

Chapter 6

Conclusions and Outlook

6.1 Conclusions

- The adhesive and mechanical behavior of 2D materials over diverse solid or soft substrates can be derived through the formation of different nano/microstructures of 2D materials like blisters, wrinkles, buckles, etc.

- Polymer-curing-assisted blistering (PCAB) technique is an efficient technique to form the bubbles of 2D flakes over a polymeric substrate.

- The elastic solid and substrate-based instabilities in the naturally occurring 2D material blisters arise respectively due to phase-transition of the confined matter with temperature, and viscous fingering while blistering of 2D flake, respectively.

- The confinement pressure inside a blister is directly related to the fluid-structure interactions, which impact the interfacial velocity of a more viscous fluid (polymer) being displaced by a less viscous fluid (water vapor) while blistering of a 2D elastic sheet.

- The pinning of 2D elastic nanosheets over periodic trenches via snap through transitions under prestretch-release process suppresses the mechanical folding instabilities under larger compressions.

6.2 Scope and Outlook

The adhesion-driven mechanical instabilities in the blistering and buckling of 2D materials have significant implications in fundamental research and straintronic applications. The elastocapillarity and adhesive interactions responsible for the onset of

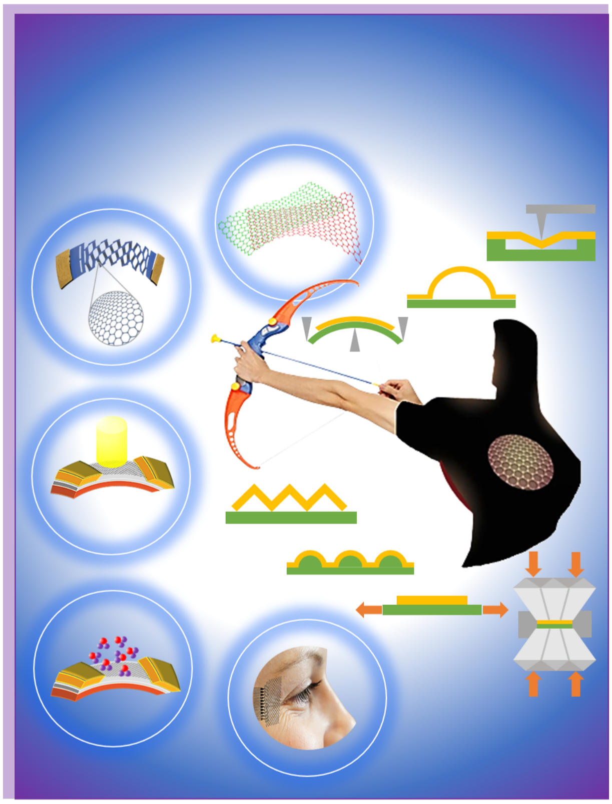

Figure 6.1: Schematic depicting the scope of the blistering and buckling of 2D elastic nanoshhets.

the elastic solid- or the viscoelastic substrate-based instabilities are not yet completely understood. Therefore, still some more dedicated efforts are highly sought for. It would be really interesting if one can visualize the dynamics of viscous fingering patterns with in-situ formation of 2D material blister since this event occurs in a very small time period. A more detailed investigation of coupled instabilities in the 2D material blisters over a viscoelastic substrate may contribute in the growth of this multidisciplinary field. The controlled formation of nano/microstrcutures (bubbles/tents/wrinkles/buckles/folds) of 2D materials by utilizing various straining techniques (Figure 6.1) has shown an upsurge of interest for meticulous straintronic applications, such as single photon detection, nano/microelectromechanical sensors, flexible gas sensors, photodetectors, strain sensors, etc.

Appendix A

Review of previous analytical blister-test models

A.1 Analysis of previous analytical models for liquid-filled blisters

A.1.1 Membrane model[1] for liquid-filled blisters with quadratic form of radial displacement

The membrane theory ignores the bending stiffness of the film, giving rise to relatively simple solutions. Here, the boundary condition at the edge of the bubble is relaxed, which results in a kink (infinite curvature) at the edge. For an elastic thin film to be treated as a membrane, the ratio of the height of the bubble to the thickness of the membrane $\frac{h}{\tau} \gtrsim 2$.

Considering an axisymmetric bubble with radius a and central deflection h, with a deflection profile,

$$w(r) = h\left(1 - \frac{r^2}{a^2}\right)$$

We assume the area of the bulged surface $A' \approx \pi a^2$ for $h/\mathrm{a} \to 0$. In addition, for the deformation to be kinematically admissible, a radial displacement is assumed as

$$u(r) = u_0 \frac{r}{a}\left(1 - \frac{r}{a}\right)$$

where, u_0 is an unknown parameter. Taking the strong shear limit of the interface, which restricts the deformation of the membrane outside the blister edge, the free energy for the blister can be obtained as a function of two kinematic parameters:

$$\Pi\left(a, u_0\right) = 2\pi \int_0^a U_s(r) r dr + \pi a^2 \Delta\gamma,$$

where, U_s is the elastic stretching energy; $\Delta\gamma = \gamma_{mc} + \gamma_{sc} - \gamma_{ms} = \Gamma - \gamma_l \left(\cos\theta_s + \cos\theta_m\right)$, is the change of interface energy for the formation of a liquid-filled blister in terms of the interfacial energy densities of membrane-content, substrate-content and membrane-substrate interfaces, respectively; γ_l is the surface tension of the liquid with θ_m and θ_s as the liquid contact-angles of the membrane and the substrate, respectively. The bubble height $h = 2V/\pi a^2$ is taken as a constant for the incompressible liquid with a constant volume.

For a fixed radius, the mechanical equilibrium requires that

$$\left(\frac{\partial \Pi}{\partial u_0}\right)_a = 0$$

which gives $u_0 \rightarrow -\frac{2h^2(-3+v)}{5a}$. Putting u_0 into the expression of the free energy, we get:

$$\Pi(a) = \frac{16 E_{2D}(23 + 18\nu - 3\nu^2) V^4}{75 a^{10} \pi^3 \left(1 - \nu^2\right)} + \pi a^2 \Delta\gamma$$

The total free energy consists of the elastic strain energy and the fluid-interaction term. The competition between the two terms minimizes the free energy to give an equilibrium blister radius, as

$$\left(\frac{\partial \Pi}{\partial a}\right)_V = 0$$

using the above equilibrium condition, the adhesion energy of the membrane to the substrate can be obtained, as

$$\Gamma = \frac{5 E_{\mathrm{2D}} h^4}{8 \phi a^4} + \gamma_l \left(\cos\theta_s + \cos\theta_m\right)$$

where, $\phi(\nu) = \frac{75\left(1-\nu^2\right)}{8(23+18\nu-3\nu^2)}$ and E_{2D} is the 2D elastic stiffness of the membrane.

A.1.2 Membrane model by Sanchez *et al.*[2], for liquid-filled nanoblisters with cubic form of radial displacement

The interfacial adhesion energy (Γ) of a membrane, satisfying the condition $\frac{h}{\tau} \gtrsim 2$, has the contributions from the stretching of the membrane, bending of the membrane and the interactions of the fluid with the membrane & the substrate.

$$\Gamma = \Gamma_{stretching} + \Gamma_{bending} + \Gamma_{fluid-interaction}$$

In the membrane model[1], the bending term is omitted due to consideration of negligible bending rigidity (i.e. $\Gamma_{bending} \to 0$). The phase of the fluid (**liquid(l) or gas(g)**) confined inside the blisters decides the kind of modeling to be applied for deducing its mechanical response[2]. In the membrane model for a liquid-filled blister, the volume of the blister is taken as constant and the fluid-interaction term is included for estimating the interfacial adhesion energy due to the finite surface tension of the incompressible liquid. On the other hand, the membrane model for a gas-filled blister[1] follows the ideal-gas law, where the central deflection (h) is taken as a variable, the fluid-interaction term is neglected and the total potential energy for the graphene bubble is balanced by the interfacial adhesion energy for a fixed number of gas molecules inside the bubble.

Assuming the edge of the blister to be fully clamped onto the substrate due to strong shear interactions that resist slippage along the interface. There are two limiting cases: blisters with fully clamped edges (strong shear limit) and with frictionless sliding interfaces (weak shear limit). On following a simple membrane analysis for strong shear limit, where the deflection profile of the liquid-filled blister on a membrane is assumed to be:

$$w(r) = h\left(1 - \frac{r^2}{a^2}\right)$$

where, $h \ll a$, and the area of the bulged surface is assumed to be $A' \approx \pi a^2$ for $h/\mathrm{a} \to 0$. To calculate the elastic strain energy of the membrane, a cubic form of the radial displacement is assumed viz. kinematically admissible:

$$u(r) = u_0 \frac{r}{a}\left(1 - \frac{r^2}{a^2}\right) + u_s \frac{r}{a},$$

where u_0 is an unknown parameter and u_s accounts for the in-plane interfacial sliding at the edge of the bubble ($r = a$). For the strong shear limit, $u_s = 0$. The cubic function form of the radial displacement is used for a better approximation than a quadratic function used in the previous section. For a liquid-filled blister, the liquid within the blister is assumed to be incompressible so that the volume of the blister, $V = \pi a^2 h/2$, remains constant.

Using the equilibrium condition, the interfacial adhesion energy can be obtained, as

$$\Gamma = \frac{E_{2\mathrm{D}} h^4}{\phi a^4} + \gamma_l \left(\cos\theta_m + \cos\theta_s\right)$$

where, the dimensionless coefficient $\phi = \frac{24(1-\nu)}{5(7-\nu)}$ for the strong shear limit, E_{2D} is the 2D elastic stiffness of the membrane, γ_l is the surface tension of the liquid with θ_m and θ_s as the liquid contact angles of the membrane and the substrate, respectively. For graphene ($\nu = 0.16$) in the strong shear limit, $\phi = 0.6$.

A.1.3 Nonlinear elastic plate model[1] for liquid-filled blisters with cubic form of radial displacement

In the Von Karman nonlinear elastic plate theory ($\frac{h}{\tau} \lesssim 1.5$), the edge of the bubble is assumed to be clamped with zero slope. The bending stiffness of the thin film is taken into account. The volume of the bubble with radius a and central deflection h is $\mathrm{V} = \frac{\pi}{3}a^2h$, for the deflection profile,

$$w(r) = h\left(1 - \frac{r^2}{a^2}\right)^2$$

which satisfies the zero-slope boundary condition at the edge of the bubble. The area of the bulged surface $A' \approx \pi a^2$ for $h/\mathrm{a} \to 0$. In addition, the radial displacement is assumed to take the form

$$u(r) = r(a - r)\left(\mathrm{c}_1 + \mathrm{c}_2 r\right)$$

where, c_1 and c_2 are two unknown parameters. Taking the strong shear limit of the interface, which restricts the deformation of the elastic plate outside the blister edge. The free energy for the blister can be obtained as a function of two kinematic parameters:

$$\Pi\left(a, c_1, c_2\right) = 2\pi \int_0^a [U_s(r) + U_b(r)] r dr + \pi a^2 \Delta\gamma,$$

where, U_s and U_b are the elastic stretching and bending energy, respectively. $\Delta\gamma = \Gamma - \gamma_l\left(\cos\theta_s + \cos\theta_p\right)$ is the change of interface energy for the formation of a liquid-filled blister, where, γ_l is the surface tension of the liquid with θ_p and θ_s as the liquid contact-angles of the elastic plate and the substrate, respectively. The bubble height $h = 3V/\pi a^2$ is taken as a constant for the incompressible liquid with a constant volume.

For a fixed radius a and height h, the mechanical equilibrium determines the two parameters c_1 and c_2 by setting $\frac{\partial \Pi}{\partial \mathrm{c}_1} = \frac{\partial \Pi}{\partial \mathrm{c}_2} = 0$, which yields

$$\mathrm{c}_1 = \frac{(179 - 89\nu)\mathrm{V}^2}{14\mathrm{a}^7\pi^2}$$

$$\mathrm{c}_2 = \frac{3\left(-79+13\nu\right)\mathrm{V}^2}{14\mathrm{a}^8\pi^2}$$

By putting the expressions for c_1 and c_2, we obtain the total free energy as a function of the bubble radius:

$$\Pi(a) = \left\{ \frac{E_{2D}(7505+4250\nu-2791\nu^2)V^4}{490a^{10}\pi^3\left(1-\nu^2\right)} + \frac{96DV^2}{a^6\pi} \right\} + \pi a^2 \Delta\gamma$$

Next, by setting $\left(\frac{\partial\Pi}{\partial a}\right)_V = 0$, and solving for $\Delta\gamma$, we get

$$\Gamma = \frac{80\eta E_{\mathrm{2D}} h^4}{3a^4} + \frac{32Dh^2}{a^4} + \gamma_l\left(\cos\theta_s + \cos\theta_p\right)$$

where $\eta = \frac{7505+4250\nu-2791\nu^2}{211680(1-\nu^2)}$, E_{2D} is the 2D elastic stiffness of the elastic plate, D is the bending stiffness of the elastic plate.

Appendix B

Adhesion mechanical model for conformal wrinkles of graphene on a corrugated soft substrate

B.1 Corrugation of graphene membrane induced by sinusoidal ripples on PDMS substrate

We consider the case of conformally adhered wrinkles of graphene over the sinusoidally corrugated PDMS substrate to avoid the complexities in the system[351,376,378].

The separation between the membrane and the corrugated substrate is assumed to be $h(x) = h_\mathrm{m} + (\delta_\mathrm{g} - \delta_\mathrm{s})\sin(2\pi x/\lambda_0)$. For a given corrugation wavelength of the substrate λ_0 and corrugation amplitude of the substrate δ_s, the corrugation amplitude of the membrane δ_g and the mean separation h_m can be determined by minimizing the total free energy of the system.

The total free energy of the system is given by the sum of the vdW interaction energy and the elastic strain energy, as

$$\tilde{U}_\mathrm{total}\ (h_\mathrm{m}, \delta_\mathrm{g}) = \tilde{U}_\mathrm{vdW}\,(h_\mathrm{m}, \delta_\mathrm{g}) + \tilde{U}_\mathrm{g}\,(\delta_\mathrm{g})\,. \tag{B.1}$$

The vdW interaction energy per unit area can be approximated as

$$\tilde{U}_\mathrm{vdW}\,(h_\mathrm{m}, \delta_\mathrm{g}) \approx U_\mathrm{vdW}\,(h_\mathrm{m}) + U_1\,(h_\mathrm{m}) \left[\left(\frac{\delta_\mathrm{g}}{h_0}\right)^2 + \left(\frac{\delta_\mathrm{s}}{h_0}\right)^2\right], \tag{B.2}$$

where

$$U_{\mathrm{vdW}}(h) = -\Gamma_0 \left[\frac{3}{2} \left(\frac{h_0}{h} \right)^3 - \frac{1}{2} \left(\frac{h_0}{h} \right)^9 \right],$$

and

$$U_1(h) = \frac{9\Gamma_0}{2} \left[- \left(\frac{h_0}{h} \right)^5 + \frac{5}{2} \left(\frac{h_0}{h} \right)^{11} \right],$$

where h is the separation between the membrane and the surface, h_0 is the equilibrium separation in the pinned state, and Γ_0 is the interfacial adhesion (pinning) energy per unit area, i.e. $\Gamma_0 = E_{\mathrm{pin}}/L^2$. The interfacial vdW interaction pronounceably acts between the substrate and the bottom layer of the layered 2D material. The interactions with the other layers, being further apart and shielded by the bottom layer, are much weaker and thus ignored in our model.

The total elastic strain energy of the membrane is the sum of the elastic modulus-mismatch strain energy, the bending energy, and the stretching energy. To the leading orders of the corrugation amplitude δ_g, the elastic strain energy density of the membrane is given by[351]

$$\tilde{U}_g\left(\delta_g\right) \approx \frac{E_{2\mathrm{D}}\varepsilon}{4} \left(\frac{2\pi}{\lambda_0} \right)^2 \delta_g^2 + \frac{B_{\mathrm{eff}}}{4} \left(\frac{2\pi}{\lambda_0} \right)^4 \delta_g^2 + \frac{3E_{2\mathrm{D}}}{64} \left(\frac{2\pi}{\lambda_0} \right)^4 \delta_g^4 \tag{B.3}$$

where ε is the mismatch strain, $B_{\mathrm{eff}} = \frac{E\tau^3}{12(1-\nu^2)} \approx \frac{NEt^3}{12(1-\nu^2)}$ is the effective bending stiffness (as each layer of a layered 2D material bends independently), and $E_{2\mathrm{D}} = E\tau$ is the in-plane (2D) elastic stiffness of the graphene membrane of thickness $\tau = Nt$, having the number of layers N, Young's modulus E, the Poisson's ratio ν, and the thickness of each layer of graphene t.

For the equilibrium state, by setting $\partial\tilde{U}_{\mathrm{total}}/\partial\delta_{\mathrm{g}} = 0$, we obtain

$$\frac{9\Gamma_0}{2{h_0}^2} \left[\left(\frac{h_0}{h_{\mathrm{m}}} \right)^5 - \frac{5}{2} \left(\frac{h_0}{h_{\mathrm{m}}} \right)^{11} \right] = \frac{E_{2\mathrm{D}}\varepsilon}{4} \left(\frac{2\pi}{\lambda_0} \right)^2 + \frac{B_{\mathrm{eff}}}{4} \left(\frac{2\pi}{\lambda_0} \right)^4 + \frac{3E_{2\mathrm{D}}}{32} \left(\frac{2\pi}{\lambda_0} \right)^4 \delta_g^2, \tag{B.4}$$

and by setting $\partial\tilde{U}_{\mathrm{total}}/\partial h_{\mathrm{m}} = 0$, and for the case of pinning, we assume $h_0 \ll h_m$; we obtain

$$\left(\frac{h_{\mathrm{m}}}{h_0} \right)^5 \sim \left[\left(\frac{\delta_{\mathrm{g}}}{h_0} \right)^2 + \left(\frac{\delta_{\mathrm{s}}}{h_0} \right)^2 \right]. \tag{B.5}$$

For fully conformal wrinkling of the graphene membrane, the in-plane elastic stretching energy dominates over the bending energy[402], and $\delta_{\mathrm{g}} \approx \delta_{\mathrm{s}}$. The existing experimental investigations suggest that the condition $h_0 \ll \delta_{\mathrm{g}}$ is valid in our experiments as well. On substituting equation B.5 into equation B.4, we finally obtain

$$\frac{\Gamma_0}{E_{\mathrm{2D}}} \sim \frac{\varepsilon}{9}\left(\frac{2\pi\delta_g}{\lambda_0}\right)^2 + \frac{1}{24}\left(\frac{2\pi\delta_g}{\lambda_0}\right)^4. \tag{B.6}$$

The first term can be neglected as the critical strain (ε) for the onset of wrinkling of the graphene membrane over the PDMS substrate is negligible. The wrinkling of 2D elastic nanosheets is energetically more favorable than buckle delamination because of their ultralow bending stiffness[350]. Equation B.6 indicates that the compressive elastic modulus-mismatch strain ($\varepsilon < 0$) would lower the interfacial adhesion between the flake and the substrate.

Bibliography

[1] Kaimin Yue, Wei Gao, Rui Huang, and Kenneth M. Liechti. Analytical methods for the mechanics of graphene bubbles. *Journal of Applied Physics*, 112(8): 083512, 2012. doi: 10.1063/1.4759146. URL `https://doi.org/10.1063/1.4759146`.

[2] Daniel A. Sanchez, Zhaohe Dai, Peng Wang, Arturo Cantu-Chavez, Christopher J. Brennan, Rui Huang, and Nanshu Lu. Mechanics of spontaneously formed nanoblisters trapped by transferred 2d crystals. *Proceedings of the National Academy of Sciences*, 115(31):7884–7889, 2018. ISSN 0027-8424. doi: 10.1073/pnas.1801551115. URL `https://www.pnas.org/content/115/31/7884`.

[3] A. K. Geim and K. S. Novoselov. The rise of graphene. *Nature Materials*, 6 (3):183–191, Mar 2007. ISSN 1476-4660. doi: 10.1038/nmat1849. URL `https://doi.org/10.1038/nmat1849`.

[4] R. R. Nair, P. Blake, A. N. Grigorenko, K. S. Novoselov, T. J. Booth, T. Stauber, N. M. R. Peres, and A. K. Geim. Fine structure constant defines visual transparency of graphene. *Science*, 320(5881):1308–1308, 2008. doi: 10.1126/science.1156965. URL `https://www.science.org/doi/abs/10.1126/science.1156965`.

[5] Da Zhan, Jiaxu Yan, Linfei Lai, Zhenhua Ni, Lei Liu, and Zexiang Shen. Engineering the electronic structure of graphene. *Advanced Materials*, 24 (30):4055–4069, 2012. doi: https://doi.org/10.1002/adma.201200011. URL `https://onlinelibrary.wiley.com/doi/abs/10.1002/adma.201200011`.

[6] Francesco Bonaccorso, Antonio Lombardo, Tawfique Hasan, Zhipei Sun, Luigi Colombo, and Andrea C. Ferrari. Production and processing of graphene and 2d crystals. *Materials Today*, 15(12):564–589, 2012. ISSN 1369-7021. doi: https://doi.org/10.1016/S1369-7021(13)70014-2. URL `https://www.sciencedirect.com/science/article/pii/S1369702113700142`.

[7] Xisai Zhang, Yang Li, Wenqian Mu, Wenqi Bai, Xiaoxue Sun, Mingyu Zhao, Zhijie Zhang, Fukai Shan, and Zhenyu Yang. Advanced tape-exfoliated method for preparing large-area 2d monolayers: a review. *2D Materials*, 8(3):032002, may 2021. doi: 10.1088/2053-1583/ac016f. URL `https://dx.doi.org/10.1088/2053-1583/ac016f`.

[8] Min Yi and Zhigang Shen. A review on mechanical exfoliation for the scalable production of graphene. *J. Mater. Chem. A*, 3:11700–11715, 2015. doi: 10.1039/C5TA00252D. URL `http://dx.doi.org/10.1039/C5TA00252D`.

[9] Fang Liu. Mechanical exfoliation of large area 2d materials from vdw crystals. *Progress in Surface Science*, 96(2):100626, 2021. ISSN 0079-6816. doi: https://doi.org/10.1016/j.progsurf.2021.100626. URL `https://www.sciencedirect.com/science/article/pii/S0079681621000149`.

[10] Yuan Huang, Eli Sutter, Norman N. Shi, Jiabao Zheng, Tianzhong Yang, Dirk Englund, Hong-Jun Gao, and Peter Sutter. Reliable exfoliation of large-area high-quality flakes of graphene and other two-dimensional materials. *ACS Nano*, 9(11):10612–10620, 2015. doi: 10.1021/acsnano.5b04258. URL `https://doi.org/10.1021/acsnano.5b04258`. PMID: 26336975.

[11] Zhujun Huang, Abdullah Alharbi, William Mayer, Edoardo Cuniberto, Takashi Taniguchi, Kenji Watanabe, Javad Shabani, and Davood Shahrjerdi. Versatile construction of van der waals heterostructures using a dual-function polymeric film. *Nature Communications*, 11(1):3029, Jun 2020. ISSN 2041-1723. doi: 10.1038/s41467-020-16817-1. URL `https://doi.org/10.1038/s41467-020-16817-1`.

[12] Matěj Velický, Gavin E. Donnelly, William R. Hendren, Stephen McFarland, Declan Scullion, William J. I. DeBenedetti, Gabriela Calinao Correa, Yimo Han, Andrew J. Wain, Melissa A. Hines, David A. Muller, Kostya S. Novoselov, Héctor D. Abruña, Robert M. Bowman, Elton J. G. Santos, and Fumin Huang. Mechanism of gold-assisted exfoliation of centimeter-sized transition-metal dichalcogenide monolayers. *ACS Nano*, 12(10):10463–10472, 2018. doi: 10.1021/acsnano.8b06101. URL `https://doi.org/10.1021/acsnano.8b06101`. PMID: 30265515.

[13] Zhesheng Chen. *Novel two dimensional material devices : from fabrication to photo-detection*. Theses, Université Pierre et Marie Curie - Paris VI, September 2015. URL `https://theses.hal.science/tel-01336408`.

[14] Riccardo Frisenda, Efrén Navarro-Moratalla, Patricia Gant, David Pérez De Lara, Pablo Jarillo-Herrero, Roman V. Gorbachev, and Andres Castellanos-Gomez. Recent progress in the assembly of nanodevices and van der waals heterostructures by deterministic placement of 2d materials. *Chem. Soc. Rev.*, 47: 53–68, 2018. doi: 10.1039/C7CS00556C. URL `http://dx.doi.org/10.1039/C7CS00556C`.

[15] Jiafu Wang, Min Yang, Li Yang, Yun Zhang, Jing Yuan, Qian Liu, Xiaohua Hou, and Ling Fu. A confocal endoscope for cellular imaging. *Engineering*, 1(3):351–360, 2015. ISSN 2095-8099. doi: https://doi.org/10.15302/J-ENG-2015081. URL `https://www.sciencedirect.com/science/article/pii/S2095809916300121`.

[16] Andrew Yacoot and Ludger Koenders. Aspects of scanning force microscope probes and their effects on dimensional measurement. *Journal of Physics D: Applied Physics*, 41(10):103001, apr 2008. doi: 10.1088/0022-3727/41/10/103001. URL `https://dx.doi.org/10.1088/0022-3727/41/10/103001`.

[17] B.J. Inkson. 2 - scanning electron microscopy (sem) and transmission electron microscopy (tem) for materials characterization. In Gerhard Hübschen, Iris Altpeter, Ralf Tschuncky, and Hans-Georg Herrmann, editors, *Materials Characterization Using Nondestructive Evaluation (NDE) Methods*, pages 17–43. Woodhead Publishing, 2016. ISBN 978-0-08-100040-3. doi: https://doi.org/10.1016/B978-0-08-100040-3.00002-X. URL `https://www.sciencedirect.com/science/article/pii/B978008100040300002X`.

[18] Isaac , Luis A Jauregui, Wonjun Park, Helin Cao, and Yong P Chen. Raman spectroscopy of graphene and related materials. *New developments in photon and materials research*, 1, 2013.

[19] Andres Castellanos-Gomez, Rafael Roldán, Emmanuele Cappelluti, Michele Buscema, Francisco Guinea, Herre S. J. van der Zant, and Gary A. Steele. Local strain engineering in atomically thin mos2. *Nano Letters*, 13(11):5361–5366, 2013. doi: 10.1021/nl402875m. URL `https://doi.org/10.1021/nl402875m`. PMID: 24083520.

[20] Guillaume Froehlicher. *Optical spectroscopy of two-dimensional materials : graphene, transition metal dichalcogenides and van der Waals heterostructures*. Theses, Université de Strasbourg, December 2016. URL `https://tel.archives-ouvertes.fr/tel-01546048`.

[21] Mukesh Pandey, Cheeranjiv Pandey, Rajeev Ahuja, and Rakesh Kumar. Straining techniques for strain engineering of 2d materials towards flexible straintronic applications. *Nano Energy*, 109:108278, 2023. ISSN 2211-2855. doi: https://doi.org/10.1016/j.nanoen.2023.108278. URL `https://www.sciencedirect.com/science/article/pii/S2211285523001143`.

[22] Yuan Huang, Xiao Wang, Xu Zhang, Xianjue Chen, Baowen Li, Bin Wang, Ming Huang, Chongyang Zhu, Xuewei Zhang, Wolfgang S. Bacsa, Feng Ding, and Rodney S. Ruoff. Raman spectral band oscillations in large graphene bubbles. *Phys. Rev. Lett.*, 120:186104, May 2018. doi: 10.1103/PhysRevLett.120.186104. URL `https://link.aps.org/doi/10.1103/PhysRevLett.120.186104`.

[23] Guorui Wang, Zhaohe Dai, Junkai Xiao, ShiZhe Feng, Chuanxin Weng, Luqi Liu, Zhiping Xu, Rui Huang, and Zhong Zhang. Bending of multilayer van der waals materials. *Phys. Rev. Lett.*, 123:116101, Sep 2019. doi: 10.1103/PhysRevLett.123.116101. URL `https://link.aps.org/doi/10.1103/PhysRevLett.123.116101`.

[24] Daniel A. Sanchez, Zhaohe Dai, and Nanshu Lu. 2d material bubbles: Fabrication, characterization, and applications. *Trends in Chemistry*, 3(3): 204–217, 2021. ISSN 2589-5974. doi: https://doi.org/10.1016/j.trechm.2020.12.011. URL `https://www.sciencedirect.com/science/article/pii/S2589597420303221`.

[25] Zhaohe Dai and Nanshu Lu. Poking and bulging of suspended thin sheets: Slippage, instabilities, and metrology. *Journal of the Mechanics and Physics of Solids*, 149:104320, 2021. ISSN 0022-5096. doi: https://doi.org/10.1016/j.jmps.2021.104320. URL `https://www.sciencedirect.com/science/article/pii/S0022509621000272`.

[26] Zhaohe Dai, Daniel A. Sanchez, Christopher J. Brennan, and Nanshu Lu. Radial buckle delamination around 2d material tents. *Journal of the Mechanics and Physics of Solids*, 137:103843, 2020. ISSN 0022-5096. doi: https://doi.org/10.1016/j.jmps.2019.103843. URL `https://www.sciencedirect.com/science/article/pii/S0022509619304338`.

[27] John R. Lister, Gunnar G. Peng, and Jerome A. Neufeld. Viscous control of peeling an elastic sheet by bending and pulling. *Phys. Rev. Lett.*, 111:154501, Oct 2013. doi: 10.1103/PhysRevLett.111.154501. URL `https://link.aps.org/doi/10.1103/PhysRevLett.111.154501`.

[28] Julien Chopin, Dominic Vella, and Arezki Boudaoud. The liquid blister test. *Proceedings of the Royal Society A: Mathematical, Physical and Engineering Sciences*, 464(2099):2887–2906, 2008. doi: 10.1098/rspa.2008.0095. URL https://royalsocietypublishing.org/doi/abs/10.1098/rspa.2008.0095.

[29] D. Pihler-Puzović, P. Illien, M. Heil, and A. Juel. Suppression of complex fingerlike patterns at the interface between air and a viscous fluid by elastic membranes. *Phys. Rev. Lett.*, 108:074502, Feb 2012. doi: 10.1103/PhysRevLett.108.074502. URL https://link.aps.org/doi/10.1103/PhysRevLett.108.074502.

[30] Draga Pihler-Puzović, Gunnar G. Peng, John R. Lister, Matthias Heil, and Anne Juel. Viscous fingering in a radial elastic-walled hele-shaw cell. *Journal of Fluid Mechanics*, 849:163–191, 2018. doi: 10.1017/jfm.2018.404. URL https://www.cambridge.org/core/journals/journal-of-fluid-mechanics/article/viscous-fingering-in-a-radial-elasticwalled-heleshaw-cell/799D5046C4F15585FC28721ED26C8E2F?utm_campaign=shareaholic&utm_medium=copy_link&utm_source=bookmark.

[31] Hongbo Zeng, Jun Huang, Yu Tian, Lin Li, Matthew V. Tirrell, and Jacob N. Israelachvili. Adhesion and detachment mechanisms between polymer and solid substrate surfaces: Using polystyrene–mica as a model system. *Macromolecules*, 49(14):5223–5231, 2016. doi: 10.1021/acs.macromol.6b00949. URL https://doi.org/10.1021/acs.macromol.6b00949.

[32] Animangsu Ghatak, Manoj K. Chaudhury, Vijay Shenoy, and Ashutosh Sharma. Meniscus instability in a thin elastic film. *Phys. Rev. Lett.*, 85:4329–4332, Nov 2000. doi: 10.1103/PhysRevLett.85.4329. URL https://link.aps.org/doi/10.1103/PhysRevLett.85.4329.

[33] E. Cerda and L. Mahadevan. Geometry and physics of wrinkling. *Phys. Rev. Lett.*, 90:074302, Feb 2003. doi: 10.1103/PhysRevLett.90.074302. URL https://link.aps.org/doi/10.1103/PhysRevLett.90.074302.

[34] E. Khestanova, F. Guinea, L. Fumagalli, A. K. Geim, and I. V. Grigorieva. Universal shape and pressure inside bubbles appearing in van der waals heterostructures. *Nature Communications*, 7(1):12587, Aug 2016. ISSN 2041-1723. doi: 10.1038/ncomms12587. URL https://doi.org/10.1038/ncomms12587.

[35] Yuan Hou, Zhaohe Dai, Shuai Zhang, Shizhe Feng, Guorui Wang, Luqi Liu, Zhiping Xu, Qunyang Li, and Zhong Zhang. Elastocapillary cleaning of twisted bilayer graphene interfaces. *Nature Communications*, 12(1):5069, Aug 2021. ISSN 2041-1723. doi: 10.1038/s41467-021-25302-2. URL `https://doi.org/10.1038/s41467-021-25302-2`.

[36] Pablo Ares, Yi Bo Wang, Colin R. Woods, James Dougherty, Laura Fumagalli, Francisco Guinea, Benny Davidovitch, and Kostya S. Novoselov. Van der waals interaction affects wrinkle formation in two-dimensional materials. *Proceedings of the National Academy of Sciences*, 118(14):e2025870118, 2021. doi: 10.1073/pnas.2025870118. URL `https://www.pnas.org/doi/abs/10.1073/pnas.2025870118`.

[37] D. Pihler-Puzović, A. Juel, and M. Heil. The interaction between viscous fingering and wrinkling in elastic-walled hele-shaw cells. *Physics of Fluids*, 26(2): 022102, 2014. doi: 10.1063/1.4864188. URL `https://doi.org/10.1063/1.4864188`.

[38] Dongjoon Rhee, Jeffrey T. Paci, Shikai Deng, Won-Kyu Lee, George C. Schatz, and Teri W. Odom. Soft skin layers enable area-specific, multiscale graphene wrinkles with switchable orientations. *ACS Nano*, 14(1):166–174, 2020. doi: 10.1021/acsnano.9b06325. URL `https://doi.org/10.1021/acsnano.9b06325`. PMID: 31675210.

[39] Ping Xu, Junmo Kang, Jonghwan Suhr, Joseph P. Smith, Karl S. Booksh, Bingqing Wei, Jianyong Yu, Faxue Li, Joon-Hyung Byun, Youngseok Oh, and Tsu-Wei Chou. Spatial strain variation of graphene films for stretchable electrodes. *Carbon*, 93, 2015. URL `https://www.sciencedirect.com/science/article/pii/S0008622315005035`.

[40] Ch. Androulidakis, E. N. Koukaras, M. G. Pastore Carbone, M. Hadjinicolaou, and C. Galiotis. Wrinkling formation in simply-supported graphenes under tension and compression loadings. *Nanoscale*, 9:18180–18188, 2017. doi: 10.1039/C7NR06463B. URL `http://dx.doi.org/10.1039/C7NR06463B`.

[41] Yongjie Guo, Senjiang Yu, Chenxi Lu, Liang Hu, Weitao Su, and Lingwei Li. Interfacial degradation and pattern evolution of exfoliated graphene by cyclic mechanical loading. *Advanced Materials Interfaces*, 10(11):2201531, 2023. doi: https://doi.org/10.1002/admi.202201531. URL `https://onlinelibrary.wiley.com/doi/abs/10.1002/admi.202201531`.

[42] Maria Giovanna Pastore Carbone, Anastasios C. Manikas, Ioanna Souli, Christos Pavlou, and Costas Galiotis. Mosaic pattern formation in exfoliated graphene by mechanical deformation. *Nature Communications*, 10(1):1572, Apr 2019. ISSN 2041-1723. doi: 10.1038/s41467-019-09489-z. URL https://doi.org/10.1038/s41467-019-09489-z.

[43] Jaehyung Yu, SunPhil Kim, Elif Ertekin, and Arend M. van der Zande. Material-dependent evolution of mechanical folding instabilities in two-dimensional atomic membranes. *ACS Applied Materials & Interfaces*, 12(9): 10801–10808, 2020. doi: 10.1021/acsami.9b20909. URL https://doi.org/10.1021/acsami.9b20909. PMID: 32036649.

[44] Scott Scharfenberg, D. Z. Rocklin, Cesar Chialvo, Richard L. Weaver, Paul M. Goldbart, and Nadya Mason. Probing the mechanical properties of graphene using a corrugated elastic substrate. *Applied Physics Letters*, 98(9):091908, 03 2011. ISSN 0003-6951. doi: 10.1063/1.3553228. URL https://doi.org/10.1063/1.3553228.

[45] Scott Scharfenberg, Nikhita Mansukhani, Cesar Chialvo, Richard L. Weaver, and Nadya Mason. Observation of a snap-through instability in graphene. *Applied Physics Letters*, 100(2):021910, 01 2012. ISSN 0003-6951. doi: 10.1063/1.3676059. URL https://doi.org/10.1063/1.3676059.

[46] Won-Kyu Lee, Junmo Kang, Kan-Sheng Chen, Clifford J. Engel, Woo-Bin Jung, Dongjoon Rhee, Mark C. Hersam, and Teri W. Odom. Multiscale, hierarchical patterning of graphene by conformal wrinkling. *Nano Letters*, 16(11):7121–7127, 2016. doi: 10.1021/acs.nanolett.6b03415. URL https://doi.org/10.1021/acs.nanolett.6b03415. PMID: 27726404.

[47] M. Dorn, P. Lange, A. Chekushin, N. Severin, and J. P. Rabe. High contrast optical detection of single graphenes on optically transparent substrates. *Journal of Applied Physics*, 108(10):106101, 2010. doi: 10.1063/1.3496619. URL https://doi.org/10.1063/1.3496619.

[48] Peng Wang, Si Xiao, Xiaohong Li, Bosai Lyu, Yingbao Huang, Shubo Cheng, Han Huang, Jun He, and Yongli Gao. Investigation of the dynamic bending properties of mos2 thin films by interference colours. *Scientific Reports*, 5(1): 18441, Dec 2015. ISSN 2045-2322. doi: 10.1038/srep18441. URL https://doi.org/10.1038/srep18441.

[49] Mukesh Pandey and Rakesh Kumar. Polymer curing assisted formation of optically visible sub-micron blisters of multilayer graphene for local strain engineering. *Journal of Physics: Condensed Matter*, 34(24):245401, apr 2022. doi: 10.1088/1361-648x/ac61b4. URL https://doi.org/10.1088/1361-648x/ac61b4.

[50] Jaehyung Yu, SunPhil Kim, Elif Ertekin, and Arend M. van der Zande. Material-dependent evolution of mechanical folding instabilities in two-dimensional atomic membranes. *ACS Applied Materials & Interfaces*, 12(9): 10801–10808, 2020. doi: 10.1021/acsami.9b20909. URL https://doi.org/10.1021/acsami.9b20909. PMID: 32036649.

[51] K. S. Novoselov, A. K. Geim, S. V. Morozov, D. Jiang, Y. Zhang, S. V. Dubonos, I. V. Grigorieva, and A. A. Firsov. Electric field effect in atomically thin carbon films. *Science*, 306(5696):666–669, 2004. doi: 10.1126/science.1102896. URL https://www.science.org/doi/abs/10.1126/science.1102896.

[52] A K Geim. Graphene prehistory. *Physica Scripta*, 2012(T146):014003, jan 2012. doi: 10.1088/0031-8949/2012/T146/014003. URL https://dx.doi.org/10.1088/0031-8949/2012/T146/014003.

[53] Benjamin Collins Brodie. Xiii. on the atomic weight of graphite. *Philosophical Transactions of the Royal Society of London*, 149:249–259, 1859. doi: 10.1098/rstl.1859.0013. URL https://royalsocietypublishing.org/doi/abs/10.1098/rstl.1859.0013.

[54] P. R. Wallace. The band theory of graphite. *Phys. Rev.*, 71:622–634, May 1947. doi: 10.1103/PhysRev.71.622. URL https://link.aps.org/doi/10.1103/PhysRev.71.622.

[55] G. Ruess and F. Vogt. Highly lamellar carbon from graphite oxyhydroxide. *Monatshefte für Chemie und verwandte Teile anderer Wissenschaften*, 78(3): 222–242, May 1948. ISSN 1434-4475. doi: 10.1007/BF01141527. URL https://doi.org/10.1007/BF01141527.

[56] H. P. Boehm, A. Clauss, G. O. Fischer, and U. Hofmann. Das adsorptionsverhalten sehr dünner kohlenstoff-folien. *Zeitschrift für anorganische und allgemeine Chemie*, 316(3-4):119–127, 1962. doi: https://doi.org/10.1002/zaac.19623160303. URL https://onlinelibrary.wiley.com/doi/abs/10.1002/zaac.19623160303.

[57] H.P. Boehm, R. Setton, and E. Stumpp. Nomenclature and terminology of graphite intercalation compounds. *Carbon*, 24(2):241–245, 1986. ISSN 0008-6223. doi: https://doi.org/10.1016/0008-6223(86)90126-0. URL https://www.sciencedirect.com/science/article/pii/0008622386901260.

[58] K. S. Novoselov, D. Jiang, F. Schedin, T. J. Booth, V. V. Khotkevich, S. V. Morozov, and A. K. Geim. Two-dimensional atomic crystals. *Proceedings of the National Academy of Sciences*, 102(30):10451–10453, 2005. doi: 10.1073/pnas.0502848102. URL https://www.pnas.org/doi/abs/10.1073/pnas.0502848102.

[59] Sajedeh Manzeli, Dmitry Ovchinnikov, Diego Pasquier, Oleg V. Yazyev, and Andras Kis. 2d transition metal dichalcogenides. *Nature Reviews Materials*, 2 (8):17033, Jun 2017. ISSN 2058-8437. doi: 10.1038/natrevmats.2017.33. URL https://doi.org/10.1038/natrevmats.2017.33.

[60] K. S. Novoselov, A. K. Geim, S. V. Morozov, D. Jiang, M. I. Katsnelson, I. V. Grigorieva, S. V. Dubonos, and A. A. Firsov. Two-dimensional gas of massless dirac fermions in graphene. *Nature*, 438(7065):197–200, Nov 2005. ISSN 1476-4687. doi: 10.1038/nature04233. URL https://doi.org/10.1038/nature04233.

[61] Daniel A. Sanchez, Zhaohe Dai, and Nanshu Lu. 2d material bubbles: Fabrication, characterization, and applications. *Trends in Chemistry*, 3(3): 204–217, 2021. ISSN 2589-5974. doi: https://doi.org/10.1016/j.trechm.2020.12.011. URL https://www.sciencedirect.com/science/article/pii/S2589597420303221.

[62] Mukesh Pandey and Rakesh Kumar. Polymer curing assisted formation of optically visible sub-micron blisters of multilayer graphene for local strain engineering. *Journal of Physics: Condensed Matter*, 34(24):245401, apr 2022. doi: 10.1088/1361-648x/ac61b4. URL https://doi.org/10.1088/1361-648x/ac61b4.

[63] Mukesh Pandey, Rajeev Ahuja, and Rakesh Kumar. Hoop compression driven instabilities in spontaneously formed multilayer graphene blisters over a polymeric substrate. *Nanotechnology*, 2022. URL http://iopscience.iop.org/article/10.1088/1361-6528/acaf33.

[64] Mukesh Pandey, B.K. Parida, M. Ranjan, Rajeev Ahuja, and Rakesh Kumar. Pinning of graphene for conformal wrinkling over a soft corrugated substrate through prestretch-release process. *Applied Surface Science Advances*, 16:100433, 2023. ISSN 2666-5239. doi: https://doi.org/10.1016/j.apsadv.2023.100433. URL `https://www.sciencedirect.com/science/article/pii/S2666523923000685`.

[65] Metehan Calis, David Lloyd, Narasimha Boddeti, and J. Scott Bunch. Adhesion of 2d mos2 to graphite and metal substrates measured by a blister test. *Nano Letters*, 23(7):2607–2614, 2023. doi: 10.1021/acs.nanolett.2c04886. URL `https://doi.org/10.1021/acs.nanolett.2c04886`. PMID: 37011413.

[66] Jorge Torres, Yisi Zhu, Pei Liu, Seong Chu Lim, and Minhee Yun. Adhesion energies of 2d graphene and mos2 to silicon and metal substrates. *physica status solidi (a)*, 215(1):1700512, 2018. doi: https://doi.org/10.1002/pssa.201700512. URL `https://onlinelibrary.wiley.com/doi/abs/10.1002/pssa.201700512`.

[67] Abhay Shukla, Rakesh Kumar, Javed Mazher, and Adrian Balan. Graphene made easy: High quality, large-area samples. *Solid State Communications*, 149(17):718–721, 2009. ISSN 0038-1098. doi: https://doi.org/10.1016/j.ssc.2009.02.007. URL `https://www.sciencedirect.com/science/article/pii/S0038109809000829`.

[68] Adrian Balan, Rakesh Kumar, Mohamed Boukhicha, Olivier Beyssac, Jean-Claude Bouillard, Dario Taverna, William Sacks, Massimiliano Marangolo, Emanuelle Lacaze, Roger Gohler, Walter Escoffier, Jean-Marie Poumirol, and Abhay Shukla. Anodic bonded graphene. *Journal of Physics D: Applied Physics*, 43(37):374013, sep 2010. doi: 10.1088/0022-3727/43/37/374013. URL `https://dx.doi.org/10.1088/0022-3727/43/37/374013`.

[69] Andrea Paradisi, Johan Biscaras, and Abhay Shukla. Space charge induced electrostatic doping of two-dimensional materials: Graphene as a case study. *Applied Physics Letters*, 107(14):143103, 10 2015. ISSN 0003-6951. doi: 10.1063/1.4932572. URL `https://doi.org/10.1063/1.4932572`.

[70] Karim Gacem, Mohamed Boukhicha, Zhesheng Chen, and Abhay Shukla. High quality 2d crystals made by anodic bonding: a general technique for layered materials. *Nanotechnology*, 23(50):505709, nov 2012. doi: 10.1088/0957-4484/23/50/505709. URL `https://dx.doi.org/10.1088/0957-4484/23/50/505709`.

[71] Zhesheng Chen, Karim Gacem, Mohamed Boukhicha, Johan Biscaras, and Abhay Shukla. Anodic bonded 2d semiconductors: from synthesis to device fabrication. *Nanotechnology*, 24(41):415708, sep 2013. doi: 10.1088/0957-4484/24/41/415708. URL `https://dx.doi.org/10.1088/0957-4484/24/41/415708`.

[72] Thomas Moldt, Axel Eckmann, Philipp Klar, Sergey V. Morozov, Alexander A. Zhukov, Kostya S. Novoselov, and Cinzia Casiraghi. High-yield production and transfer of graphene flakes obtained by anodic bonding. *ACS Nano*, 5(10):7700–7706, 2011. doi: 10.1021/nn202293f. URL `https://doi.org/10.1021/nn202293f`. PMID: 21899357.

[73] Zheling Li, Robert J. Young, Claudia Backes, Wen Zhao, Xun Zhang, Alexander A. Zhukov, Evan Tillotson, Aidan P. Conlan, Feng Ding, Sarah J. Haigh, Kostya S. Novoselov, and Jonathan N. Coleman. Mechanisms of liquid-phase exfoliation for the production of graphene. *ACS Nano*, 14(9):10976–10985, 2020. doi: 10.1021/acsnano.0c03916. URL `https://doi.org/10.1021/acsnano.0c03916`. PMID: 32598132.

[74] Yenny Hernandez, Mustafa Lotya, David Rickard, Shane D. Bergin, and Jonathan N. Coleman. Measurement of multicomponent solubility parameters for graphene facilitates solvent discovery. *Langmuir*, 26(5):3208–3213, 2010. doi: 10.1021/la903188a. URL `https://doi.org/10.1021/la903188a`. PMID: 19883090.

[75] Xu Cui, Chenzhen Zhang, Rui Hao, and Yanglong Hou. Liquid-phase exfoliation, functionalization and applications of graphene. *Nanoscale*, 3:2118–2126, 2011. doi: 10.1039/C1NR10127G. URL `http://dx.doi.org/10.1039/C1NR10127G`.

[76] G Nandamuri, S Roumimov, and R Solanki. Chemical vapor deposition of graphene films. *Nanotechnology*, 21(14):145604, mar 2010. doi: 10.1088/0957-4484/21/14/145604. URL `https://dx.doi.org/10.1088/0957-4484/21/14/145604`.

[77] Phaedon Avouris and Christos Dimitrakopoulos. Graphene: synthesis and applications. *Materials Today*, 15(3):86–97, 2012. ISSN 1369-7021. doi: https://doi.org/10.1016/S1369-7021(12)70044-5. URL `https://www.sciencedirect.com/science/article/pii/S1369702112700445`.

[78] Taisuke Ohta, Farid El Gabaly, Aaron Bostwick, Jessica L McChesney, Konstantin V Emtsev, Andreas K Schmid, Thomas Seyller, Karsten Horn, and Eli Rotenberg. Morphology of graphene thin film growth on sic(0001). *New Journal of Physics*, 10(2):023034, feb 2008. doi: 10.1088/1367-2630/10/2/023034. URL https://dx.doi.org/10.1088/1367-2630/10/2/023034.

[79] Konstantin V. Emtsev, Aaron Bostwick, Karsten Horn, Johannes Jobst, Gary L. Kellogg, Lothar Ley, Jessica L. McChesney, Taisuke Ohta, Sergey A. Reshanov, Jonas Röhrl, Eli Rotenberg, Andreas K. Schmid, Daniel Waldmann, Heiko B. Weber, and Thomas Seyller. Towards wafer-size graphene layers by atmospheric pressure graphitization of silicon carbide. *Nature Materials*, 8(3):203–207, Mar 2009. ISSN 1476-4660. doi: 10.1038/nmat2382. URL https://doi.org/10.1038/nmat2382.

[80] Deji Akinwande, Nicholas Petrone, and James Hone. Two-dimensional flexible nanoelectronics. *Nature Communications*, 5(1):5678, Dec 2014. ISSN 2041-1723. doi: 10.1038/ncomms6678. URL https://doi.org/10.1038/ncomms6678.

[81] Tao Jiang, Rui Huang, and Yong Zhu. Interfacial sliding and buckling of monolayer graphene on a stretchable substrate. *Advanced Functional Materials*, 24(3):396–402, 2014. doi: https://doi.org/10.1002/adfm.201301999. URL https://onlinelibrary.wiley.com/doi/abs/10.1002/adfm.201301999.

[82] Chen Si, Zhimei Sun, and Feng Liu. Strain engineering of graphene: a review. *Nanoscale*, 8:3207–3217, 2016. doi: 10.1039/C5NR07755A. URL http://dx.doi.org/10.1039/C5NR07755A.

[83] Daniel E. Sheehy and Jörg Schmalian. Optical transparency of graphene as determined by the fine-structure constant. *Phys. Rev. B*, 80:193411, Nov 2009. doi: 10.1103/PhysRevB.80.193411. URL https://link.aps.org/doi/10.1103/PhysRevB.80.193411.

[84] Li Gao. Flexible device applications of 2d semiconductors. *Small*, 13(35):1603994, 2017. doi: https://doi.org/10.1002/smll.201603994. URL https://onlinelibrary.wiley.com/doi/abs/10.1002/smll.201603994.

[85] Jong-Hyun Ahn and Byung Hee Hong. for displays that bend. *Nature Nanotechnology*, 9(10):737–738, Oct 2014. ISSN 1748-3395. doi: 10.1038/nnano.2014.226. URL https://doi.org/10.1038/nnano.2014.226.

[86] Nikhil Patil, Aparna Gupta, Manu Jaiswal, and Soumya Dutta. Chemical-free transfer of patterned reduced graphene oxide thin films for large area flexible electronics and nanoelectromechanical systems. *Nanotechnology*, 31(49):495301, sep 2020. doi: 10.1088/1361-6528/abb26b. URL `https://doi.org/10.1088/1361-6528/abb26b`.

[87] Viet Phuong Pham. Direct growth of graphene on flexible substrates toward flexible electronics: A promising perspective. In Simas Rackauskas, editor, *Flexible Electronics*, chapter 4. IntechOpen, Rijeka, 2018. doi: 10.5772/intechopen.73171. URL `https://doi.org/10.5772/intechopen.73171`.

[88] Yuan Huang, Yu-Hao Pan, Rong Yang, Li-Hong Bao, Lei Meng, Hai-Lan Luo, Yong-Qing Cai, Guo-Dong Liu, Wen-Juan Zhao, Zhang Zhou, Liang-Mei Wu, Zhi-Li Zhu, Ming Huang, Li-Wei Liu, Lei Liu, Peng Cheng, Ke-Hui Wu, Shi-Bing Tian, Chang-Zhi Gu, You-Guo Shi, Yan-Feng Guo, Zhi Gang Cheng, Jiang-Ping Hu, Lin Zhao, Guan-Hua Yang, Eli Sutter, Peter Sutter, Ye-Liang Wang, Wei Ji, Xing-Jiang Zhou, and Hong-Jun Gao. Universal mechanical exfoliation of large-area 2d crystals. *Nature Communications*, 11(1):2453, May 2020. ISSN 2041-1723. doi: 10.1038/s41467-020-16266-w. URL `https://doi.org/10.1038/s41467-020-16266-w`.

[89] Riccardo Frisenda, Yue Niu, Patricia Gant, Manuel Muñoz, and Andres Castellanos-Gomez. Naturally occurring van der waals materials. *npj 2D Materials and Applications*, 4(1):38, Oct 2020. ISSN 2397-7132. doi: 10.1038/s41699-020-00172-2. URL `https://doi.org/10.1038/s41699-020-00172-2`.

[90] Alfonso Reina, Hyungbin Son, Liying Jiao, Ben Fan, Mildred S. Dresselhaus, ZhongFan Liu, and Jing Kong. Transferring and identification of single- and few-layer graphene on arbitrary substrates. *The Journal of Physical Chemistry C*, 112(46):17741–17744, 2008. doi: 10.1021/jp807380s. URL `https://doi.org/10.1021/jp807380s`.

[91] Ana Laura Elías, Néstor Perea-López, Andrés Castro-Beltrán, Ayse Berkdemir, Ruitao Lv, Simin Feng, Aaron D. Long, Takuya Hayashi, Yoong Ahm Kim, Morinobu Endo, Humberto R. Gutiérrez, Nihar R. Pradhan, Luis Balicas, Thomas E. Mallouk, Florentino López-Urías, Humberto Terrones, and Mauricio Terrones. Controlled synthesis and transfer of large-area ws2 sheets: From single layer to few layers. *ACS Nano*, 7(6):5235–5242, 2013. doi: 10.1021/nn400971k. URL `https://doi.org/10.1021/nn400971k`. PMID: 23647141.

[92] Joshua D Wood, Gregory P Doidge, Enrique A Carrion, Justin C Koepke, Joshua A Kaitz, Isha Datye, Ashkan Behnam, Jayan Hewaparakrama, Basil Aruin, Yaofeng Chen, Hefei Dong, Richard T Haasch, Joseph W Lyding, and Eric Pop. Annealing free, clean graphene transfer using alternative polymer scaffolds. *Nanotechnology*, 26(5):055302, jan 2015. doi: 10.1088/0957-4484/26/5/055302. URL `https://doi.org/10.1088/0957-4484/26/5/055302`.

[93] Donglin Ma, Jianping Shi, Qingqing Ji, Ke Chen, Jianbo Yin, Yuanwei Lin, Yu Zhang, Mengxi Liu, Qingliang Feng, Xiuju Song, Xuefeng Guo, Jin Zhang, Yanfeng Zhang, and Zhongfan Liu. A universal etching-free transfer of mos2 films for applications in photodetectors. *Nano Research*, 8(11):3662–3672, Nov 2015. ISSN 1998-0000. doi: 10.1007/s12274-015-0866-z. URL `https://doi.org/10.1007/s12274-015-0866-z`.

[94] Sandeep Gorantla, Alicja Bachmatiuk, Jeonghyun Hwang, Hussain A. Alsalman, Joon Young Kwak, Thomas Seyller, Jürgen Eckert, Michael G. Spencer, and Mark H. Rümmeli. A universal transfer route for graphene. *Nanoscale*, 6: 889–896, 2014. doi: 10.1039/C3NR04739C. URL `http://dx.doi.org/10.1039/C3NR04739C`.

[95] Li Tao, Hao Li, Yun Gao, Zefeng Chen, Lei Wang, Ya Deng, Jian Zhang, and Jian-Bin Xu. Deterministic and etching-free transfer of large-scale 2d layered materials for constructing interlayer coupled van der waals heterostructures. *Advanced Materials Technologies*, 3(5):1700282, 2018. doi: https://doi.org/10.1002/admt.201700282. URL `https://onlinelibrary.wiley.com/doi/abs/10.1002/admt.201700282`.

[96] Grégory F. Schneider, Victor E. Calado, Henny Zandbergen, Lieven M. K. Vandersypen, and Cees Dekker. Wedging transfer of nanostructures. *Nano Letters*, 10(5):1912–1916, 2010. doi: 10.1021/nl1008037. URL `https://doi.org/10.1021/nl1008037`. PMID: 20402493.

[97] Francesco Bonaccorso, Antonio Lombardo, Tawfique Hasan, Zhipei Sun, Luigi Colombo, and Andrea C. Ferrari. Production and processing of graphene and 2d crystals. *Materials Today*, 15(12):564–589, 2012. ISSN 1369-7021. doi: https://doi.org/10.1016/S1369-7021(13)70014-2. URL `https://www.sciencedirect.com/science/article/pii/S1369702113700142`.

[98] Fu Zhang, Chad Erb, Lauren Runkle, Xiaotian Zhang, and Nasim Alem. Etchant-free transfer of 2d nanostructures. *Nanotechnology*, 29(2):025602,

dec 2017. doi: 10.1088/1361-6528/aa9c21. URL https://doi.org/10.1088/1361-6528/aa9c21.

[99] Madan Sharma, Aditya Singh, and Rajendra Singh. Monolayer mos2 transferred on arbitrary substrates for potential use in flexible electronics. *ACS Applied Nano Materials*, 3(5):4445–4453, 2020. doi: 10.1021/acsanm.0c00551. URL https://doi.org/10.1021/acsanm.0c00551.

[100] Huynh Van Ngoc, Yongteng Qian, Suk Kil Han, and Dae Joon Kang. -etching-free transfer of wafer-scale chemical vapor deposition two-dimensional atomic crystal by a water soluble polyvinyl alcohol polymer method. *Scientific Reports*, 6(1):33096, Sep 2016. ISSN 2045-2322. doi: 10.1038/srep33096. URL https://doi.org/10.1038/srep33096.

[101] Caoyuan Cai, Feixiang Jia, Alei Li, Fan Huang, Zhihao Xu, Longzhen Qiu, Yiqing Chen, Guangtao Fei, and Min Wang. Crackless transfer of large-area graphene films for superior-performance transparent electrodes. *Carbon*, 98:457–462, 2016. ISSN 0008-6223. doi: https://doi.org/10.1016/j.carbon.2015.11.041. URL https://www.sciencedirect.com/science/article/pii/S0008622315304504.

[102] William Regan, Nasim Alem, Benjamín Alemán, Baisong Geng, Çağlar Girit, Lorenzo Maserati, Feng Wang, Michael Crommie, and A. Zettl. A direct transfer of layer-area graphene. *Applied Physics Letters*, 96(11):113102, 2010. doi: 10.1063/1.3337091. URL https://doi.org/10.1063/1.3337091.

[103] Witchawate Hiranyawasit, Krirktakul Punpattanakul, Alongkorn Pimpin, Houngkyung Kim, Seokwoo Jeon, and Werayut Srituravanich. A novel method for transferring graphene onto pdms. *Applied Surface Science*, 358:70–74, 2015. ISSN 0169-4332. doi: https://doi.org/10.1016/j.apsusc.2015.08.218. URL https://www.sciencedirect.com/science/article/pii/S0169433215020425. Graphene and C3N4-based Photocatalysts.

[104] Sang Jin Kim, Teajun Choi, Bora Lee, Sunwoo Lee, Kyoungjun Choi, Jong Bo Park, Je Min Yoo, Yong Seok Choi, Jaechul Ryu, Philip Kim, James Hone, and Byung Hee Hong. Ultraclean patterned transfer of single-layer graphene by recyclable pressure sensitive adhesive films. *Nano Letters*, 15(5):3236–3240, 2015. doi: 10.1021/acs.nanolett.5b00440. PMID: 25844634.

[105] V. E. Calado, G. F. Schneider, A. M. M. G. Theulings, C. Dekker, and L. M. K. Vandersypen. Formation and control of wrinkles in graphene by the wedging transfer method. *Applied Physics Letters*, 101(10):103116, 2012. doi: 10.1063/1.4751982. URL https://doi.org/10.1063/1.4751982.

[106] Nicksay Villa, Juan D. Zapata, and Daniel Ramirez. Paraffin wax assisted chemical vapor deposited graphene transfer method. *Thin Solid Films*, 721:138556, 2021. ISSN 0040-6090. doi: https://doi.org/10.1016/j.tsf.2021.138556. URL https://www.sciencedirect.com/science/article/pii/S0040609021000390.

[107] Aleksandar Matković, Uroš Ralević, Manisha Chhikara, Milka M. Jakovljević, Djordje Jovanović, Gvido Bratina, and Radoš Gajić. Influence of transfer residue on the optical properties of chemical vapor deposited graphene investigated through spectroscopic ellipsometry. *Journal of Applied Physics*, 114(9):093505, 2013. doi: 10.1063/1.4819967. URL https://doi.org/10.1063/1.4819967.

[108] Mi Jang, Tran Quang Trung, Jin-Heak Jung, Bo-Yeong Kim, and Nae-Eung Lee. Improved performance and stability of field-effect transistors with polymeric residue-free graphene channel transferred by gold layer. *Phys. Chem. Chem. Phys.*, 16:4098–4105, 2014. doi: 10.1039/C3CP53900H. URL http://dx.doi.org/10.1039/C3CP53900H.

[109] Hiram J. Conley, Bin Wang, Jed I. Ziegler, Richard F. Haglund, Sokrates T. Pantelides, and Kirill I. Bolotin. Bandgap engineering of strained monolayer and bilayer mos2. *Nano Letters*, 13(8):3626–3630, 2013. doi: 10.1021/nl4014748. URL https://doi.org/10.1021/nl4014748. PMID: 23819588.

[110] Shikai Deng, Anirudha V. Sumant, and Vikas Berry. Strain engineering in two-dimensional nanomaterials beyond graphene. *Nano Today*, 22: 14 – 35, 2018. ISSN 1748-0132. doi: https://doi.org/10.1016/j.nantod.2018.07.001. URL http://www.sciencedirect.com/science/article/pii/S1748013217306345.

[111] Youngkun Ahn, Hyein Kim, Young-Hwan Kim, Yeonjin Yi, and Seong-Il Kim. Procedure of removing polymer residues and its influences on electronic and structural characteristics of graphene. *Applied Physics Letters*, 102(9):091602, 2013. doi: 10.1063/1.4794900. URL https://doi.org/10.1063/1.4794900.

[112] Wonsuk Jung, Donghwan Kim, Mingu Lee, Soohyun Kim, Jae-Hyun Kim, and Chang-Soo Han. Ultraconformal contact transfer of monolayer graphene on metal to various substrates. *Advanced Materials*, 26(37):6394–6400, 2014. doi: https://doi.org/10.1002/adma.201400773. URL `https://onlinelibrary.wiley.com/doi/abs/10.1002/adma.201400773`.

[113] Zhiying Chen, Yanhui Zhang, Xiaoming Ge, Yanping Sui, Yijian Liang, Shike Hu, Jing Li, and Guanghui Yu. Thermal-assisted direct transfer of graphene onto flexible substrates. *Materials Letters*, 229:252–255, 2018. ISSN 0167-577X. doi: https://doi.org/10.1016/j.matlet.2018.06.124. URL `https://www.sciencedirect.com/science/article/pii/S0167577X18310292`.

[114] Chih-Sheng Chen and Chien-Kuo Hsieh. An easy, low-cost method to transfer large-scale graphene onto polyethylene terephthalate as a transparent conductive flexible substrate. *Thin Solid Films*, 570:595–598, 2014. ISSN 0040-6090. doi: https://doi.org/10.1016/j.tsf.2014.03.092. URL `https://www.sciencedirect.com/science/article/pii/S0040609014004842`. TACT 2013 International Thin Films Conference.

[115] Christopher J. Brennan, Jessica Nguyen, Edward T. Yu, and Nanshu Lu. Interface adhesion between 2d materials and elastomers measured by buckle delaminations. *Advanced Materials Interfaces*, 2(16):1500176, 2015. doi: https://doi.org/10.1002/admi.201500176. URL `https://onlinelibrary.wiley.com/doi/abs/10.1002/admi.201500176`.

[116] Buddhika Jayasena and Shreyes N. Melkote. An investigation of pdms stamp assisted mechanical exfoliation of large area graphene. *Procedia Manufacturing*, 1:840–853, 2015. ISSN 2351-9789. doi: https://doi.org/10.1016/j.promfg.2015.09.073. URL `https://www.sciencedirect.com/science/article/pii/S2351978915010732`. 43rd North American Manufacturing Research Conference, NAMRC 43, 8-12 June 2015, UNC Charlotte, North Carolina, United States.

[117] F. Du, H. L. Duan, C. Y. Xiong, and J. X. Wang. Substrate wettability requirement for the direct transfer of graphene. *Applied Physics Letters*, 107(14):143109, 2015. doi: 10.1063/1.4932655. URL `https://doi.org/10.1063/1.4932655`.

[118] Mehrnaz Amerian, Mahshid Amerian, Mahyar Sameti, and Ehsan Seyedjafari. Improvement of pdms surface biocompatibility is limited by the duration of

oxygen plasma treatment. *Journal of Biomedical Materials Research Part A*, 107 (12):2806–2813, 2019. doi: https://doi.org/10.1002/jbm.a.36783. URL `https://onlinelibrary.wiley.com/doi/abs/10.1002/jbm.a.36783`.

[119] Achint Jain, Palash Bharadwaj, Sebastian Heeg, Markus Parzefall, Takashi Taniguchi, Kenji Watanabe, and Lukas Novotny. Minimizing residues and strain in 2d materials transferred from PDMS. *Nanotechnology*, 29(26):265203, may 2018. doi: 10.1088/1361-6528/aabd90. URL `https://doi.org/10.1088/1361-6528/aabd90`.

[120] Filippo Pizzocchero, Lene Gammelgaard, Bjarke S. Jessen, José M. Caridad, Lei Wang, James Hone, Peter Bøggild, and Timothy J. Booth. The hot pick-up technique for batch assembly of van der waals heterostructures. *Nature Communications*, 7(1):11894, Jun 2016. ISSN 2041-1723. doi: 10.1038/ncomms11894. URL `https://doi.org/10.1038/ncomms11894`.

[121] Andres Castellanos-Gomez, Michele Buscema, Rianda Molenaar, Vibhor Singh, Laurens Janssen, Herre S J van der Zant, and Gary A Steele. Deterministic transfer of two-dimensional materials by all-dry viscoelastic stamping. *2D Materials*, 1(1):011002, apr 2014. doi: 10.1088/2053-1583/1/1/011002. URL `https://doi.org/10.1088/2053-1583/1/1/011002`.

[122] Xiao-Li Li, Wen-Peng Han, Jiang-Bin Wu, Xiao-Fen Qiao, Jun Zhang, and Ping-Heng Tan. Layer-number dependent optical properties of 2d materials and their application for thickness determination. *Advanced Functional Materials*, 27(19): 1604468, 2017. doi: https://doi.org/10.1002/adfm.201604468. URL `https://onlinelibrary.wiley.com/doi/abs/10.1002/adfm.201604468`.

[123] M M Benameur, B Radisavljevic, J S Héron, S Sahoo, H Berger, and A Kis. Visibility of dichalcogenide nanolayers. *Nanotechnology*, 22(12):125706, feb 2011. doi: 10.1088/0957-4484/22/12/125706. URL `https://dx.doi.org/10.1088/0957-4484/22/12/125706`.

[124] P. Blake, E. W. Hill, A. H. Castro Neto, K. S. Novoselov, D. Jiang, R. Yang, T. J. Booth, and A. K. Geim. Making graphene visible. *Applied Physics Letters*, 91(6):063124, 08 2007. ISSN 0003-6951. doi: 10.1063/1.2768624. URL `https://doi.org/10.1063/1.2768624`.

[125] Hang Zhang, Junxiang Huang, Yongwei Wang, Rui Liu, Xiulan Huai, Jingjing Jiang, and Chantelle Anfuso. Atomic force microscopy for two-dimensional

materials: A tutorial review. *Optics Communications*, 406:3–17, 2018. ISSN 0030-4018. doi: https://doi.org/10.1016/j.optcom.2017.05.015. URL https://www.sciencedirect.com/science/article/pii/S0030401817303887. Optoelectronics and Photonics Based on Two-dimensional Materials.

[126] A. Adetayo and D. Runsewe. Synthesis and fabrication of graphene and graphene oxide: A review. *Open Journal of Composite Materials*, 9:207–229, 2019. doi: https://doi.org/10.4236/ojcm.2019.92012. URL https://www.scirp.org/html/10-1810295_92162.htm.

[127] Jaemyung Kim, Franklin Kim, and Jiaxing Huang. Seeing graphene-based sheets. *Materials Today*, 13(3):28–38, 2010. ISSN 1369-7021. doi: https://doi.org/10.1016/S1369-7021(10)70031-6. URL https://www.sciencedirect.com/science/article/pii/S1369702110700316.

[128] Peter Larkin. Chapter 2 - basic principles. In Peter Larkin, editor, *Infrared and Raman Spectroscopy*, pages 7–25. Elsevier, Oxford, 2011. ISBN 978-0-12-386984-5. doi: https://doi.org/10.1016/B978-0-12-386984-5.10002-3. URL https://www.sciencedirect.com/science/article/pii/B9780123869845100023.

[129] S. Prati, E. Joseph, G. Sciutto, and R. Mazzeo. New advances in the application of ftir microscopy and spectroscopy for the characterization of artistic materials. *Accounts of Chemical Research*, 43(6):792–801, 2010. doi: 10.1021/ar900274f. URL https://doi.org/10.1021/ar900274f. PMID: 20476733.

[130] K. S. Novoselov, A. Mishchenko, A. Carvalho, and A. H. Castro Neto. 2d materials and van der waals heterostructures. *Science*, 353(6298):aac9439, 2016. doi: 10.1126/science.aac9439. URL https://www.science.org/doi/abs/10.1126/science.aac9439.

[131] K S Novoselov and A H Castro Neto. Two-dimensional crystals-based heterostructures: materials with tailored properties. *Physica Scripta*, T146:014006, jan 2012. doi: 10.1088/0031-8949/2012/t146/014006. URL https://doi.org/10.1088/0031-8949/2012/t146/014006.

[132] Zhaohe Dai, Luqi Liu, and Zhong Zhang. Strain engineering of 2d materials: Issues and opportunities at the interface. *Advanced Materials*, 31(45):1805417, 2019. doi: https://doi.org/10.1002/adma.201805417. URL https://onlinelibrary.wiley.com/doi/abs/10.1002/adma.201805417.

[133] Mukesh Pandey and Rakesh Kumar. Polymer curing assisted formation of optically visible sub-micron blisters of multilayer graphene for local strain engineering. *Journal of Physics: Condensed Matter*, 34(24):245401, apr 2022. doi: 10.1088/1361-648x/ac61b4. URL https://doi.org/10.1088/1361-648x/ac61b4.

[134] Shikai Deng, Anirudha V. Sumant, and Vikas Berry. Strain engineering in two-dimensional nanomaterials beyond graphene. *Nano Today*, 22:14–35, 2018. ISSN 1748-0132. doi: https://doi.org/10.1016/j.nantod.2018.07.001. URL https://www.sciencedirect.com/science/article/pii/S1748013217306345.

[135] Onur Çakıroğlu, Joshua O. Island, Yong Xie, Riccardo Frisenda, and Andres Castellanos-Gomez. An automated system for strain engineering and straintronics of 2d materials. *Advanced Materials Technologies*, 8(1):2201091, 2023. doi: https://doi.org/10.1002/admt.202201091. URL https://onlinelibrary.wiley.com/doi/abs/10.1002/admt.202201091.

[136] A. C. Ferrari, J. C. Meyer, V. Scardaci, C. Casiraghi, M. Lazzeri, F. Mauri, S. Piscanec, D. Jiang, K. S. Novoselov, S. Roth, and A. K. Geim. Raman spectrum of graphene and graphene layers. *Phys. Rev. Lett.*, 97:187401, Oct 2006. doi: 10.1103/PhysRevLett.97.187401. URL https://link.aps.org/doi/10.1103/PhysRevLett.97.187401.

[137] Jenő Sólyom. *Optical Properties of Solids*, pages 411–447. Springer Berlin Heidelberg, Berlin, Heidelberg, 2009. ISBN 978-3-540-85316-9. doi: 10.1007/978-3-540-85316-9_10. URL https://doi.org/10.1007/978-3-540-85316-9_10.

[138] Weibin Zhang, Fanghua Cheng, Junwei Huang, Hongtao Yuan, and Quan Wang. Investigation of uniaxial strain in twisted few-layer mos2. *Physics Letters A*, 418:127709, 2021. ISSN 0375-9601. doi: https://doi.org/10.1016/j.physleta.2021.127709. URL https://www.sciencedirect.com/science/article/pii/S0375960121005739.

[139] Ya ping Miao, Fei Ma, Yu hong Huang, and Ke wei Xu. Strain effects on electronic states and lattice vibration of monolayer mos2. *Physica E: Low-dimensional Systems and Nanostructures*, 71:1–6, 2015. ISSN 1386-9477. doi: https://doi.org/10.1016/j.physe.2015.03.015. URL https://www.sciencedirect.com/science/article/pii/S1386947715001149.

[140] Sheng Yu, Hao D. Xiong, Kwesi Eshun, Hui Yuan, and Qiliang Li. Phase transition, effective mass and carrier mobility of mos2 monolayer under tensile strain. *Applied Surface Science*, 325:27–32, 2015. ISSN 0169-4332. doi: https://doi.org/10.1016/j.apsusc.2014.11.079. URL https://www.sciencedirect.com/science/article/pii/S0169433214025604.

[141] S. Horzum, H. Sahin, S. Cahangirov, P. Cudazzo, A. Rubio, T. Serin, and F. M. Peeters. Phonon softening and direct to indirect band gap crossover in strained single-layer mose$_2$. *Phys. Rev. B*, 87:125415, Mar 2013. doi: 10.1103/PhysRevB.87.125415. URL https://link.aps.org/doi/10.1103/PhysRevB.87.125415.

[142] Priya Johari and Vivek B. Shenoy. Tuning the electronic properties of semiconducting transition metal dichalcogenides by applying mechanical strains. *ACS Nano*, 6(6):5449–5456, 2012. doi: 10.1021/nn301320r. URL https://doi.org/10.1021/nn301320r. PMID: 22591011.

[143] Joshua O. Island, Agnieszka Kuc, Erik H. Diependaal, Rudolf Bratschitsch, Herre S. J. van der Zant, Thomas Heine, and Andres Castellanos-Gomez. Precise and reversible band gap tuning in single-layer mose2 by uniaxial strain. *Nanoscale*, 8:2589–2593, 2016. doi: 10.1039/C5NR08219F. URL http://dx.doi.org/10.1039/C5NR08219F.

[144] Iris Niehues, Anna Blob, Torsten Stiehm, Steffen Michaelis de Vasconcellos, and Rudolf Bratschitsch. Interlayer excitons in bilayer mos2 under uniaxial tensile strain. *Nanoscale*, 11:12788–12792, 2019. doi: 10.1039/C9NR03332G. URL http://dx.doi.org/10.1039/C9NR03332G.

[145] Yajing Sun, Dong Wang, and Zhigang Shuai. Indirect-to-direct band gap crossover in few-layer transition metal dichalcogenides: A theoretical prediction. *The Journal of Physical Chemistry C*, 120(38):21866–21870, 2016. doi: 10.1021/acs.jpcc.6b08748. URL https://doi.org/10.1021/acs.jpcc.6b08748.

[146] Sujay B. Desai, Gyungseon Seol, Jeong Seuk Kang, Hui Fang, Corsin Battaglia, Rehan Kapadia, Joel W. Ager, Jing Guo, and Ali Javey. Strain-induced indirect to direct bandgap transition in multilayer wse2. *Nano Letters*, 14(8):4592–4597, 2014. doi: 10.1021/nl501638a. URL https://doi.org/10.1021/nl501638a. PMID: 24988370.

[147] Yuan Huang, Eli Sutter, Norman N. Shi, Jiabao Zheng, Tianzhong Yang, Dirk Englund, Hong-Jun Gao, and Peter Sutter. Reliable exfoliation of large-area

high-quality flakes of graphene and other two-dimensional materials. *ACS Nano*, 9(11):10612–10620, 2015. doi: 10.1021/acsnano.5b04258. PMID: 26336975.

[148] Jason W. Christopher, Mounika Vutukuru, David Lloyd, J. Scott Bunch, Bennett B. Goldberg, David J. Bishop, and Anna K. Swan. Monolayer mos$_2$ strained to 1.3% with a microelectromechanical system. *Journal of Microelectromechanical Systems*, 28(2):254–263, 2019. doi: 10.1109/JMEMS.2018.2877983.

[149] Y. C. Cheng, Z. Y. Zhu, G. S. Huang, and U. Schwingenschlögl. Grüneisen parameter of the g mode of strained monolayer graphene. *Phys. Rev. B*, 83: 115449, Mar 2011. doi: 10.1103/PhysRevB.83.115449. URL `https://link.aps.org/doi/10.1103/PhysRevB.83.115449`.

[150] Nathanael P. Kazmierczak, Madeline Van Winkle, Colin Ophus, Karen C. Bustillo, Stephen Carr, Hamish G. Brown, Jim Ciston, Takashi Taniguchi, Kenji Watanabe, and D. Kwabena Bediako. Strain fields in twisted bilayer graphene. *Nature Materials*, 20(7):956–963, Jul 2021. ISSN 1476-4660. doi: 10.1038/s41563-021-00973-w. URL `https://doi.org/10.1038/s41563-021-00973-w`.

[151] Ying Han, Libo Gao, Jingzhuo Zhou, Yuan Hou, Yanwen Jia, Ke Cao, Ke Duan, and Yang Lu. Deep elastic strain engineering of 2d materials and their twisted bilayers. *ACS Applied Materials & Interfaces*, 14(7):8655–8663, 2022. doi: 10.1021/acsami.1c23431. URL `https://doi.org/10.1021/acsami.1c23431`. PMID: 35147415.

[152] Sameer Kumar Mallik, Sandhyarani Sahoo, Mousam Charan Sahu, Anjan Kumar Jena, Gopal K. Pradhan, and Satyaprakash Sahoo. Polarized moiré phonon and strain-coupled phonon renormalization in twisted bilayer mos2. *The Journal of Physical Chemistry C*, 126(37):15788–15794, 2022. doi: 10.1021/acs.jpcc.2c04201. URL `https://doi.org/10.1021/acs.jpcc.2c04201`.

[153] Tommaso Cea, Niels R. Walet, and Francisco Guinea. Electronic band structure and pinning of fermi energy to van hove singularities in twisted bilayer graphene: A self-consistent approach. *Phys. Rev. B*, 100:205113, Nov 2019. doi: 10.1103/PhysRevB.100.205113. URL `https://link.aps.org/doi/10.1103/PhysRevB.100.205113`.

[154] Yuan Hou, Shuai Zhang, Qunyang Li, Luqi Liu, Xiaoping Wu, and Zhong Zhang. Evaluation local strain of twisted bilayer graphene via moiré pattern. *Optics and Lasers in Engineering*, 152:106946, 2022. ISSN 0143-8166. doi: https://

doi.org/10.1016/j.optlaseng.2022.106946. URL https://www.sciencedirect.com/science/article/pii/S014381662200001X.

[155] Wei Yan, Lan Meng, Mengxi Liu, Jia-Bin Qiao, Zhao-Dong Chu, Rui-Fen Dou, Zhongfan Liu, Jia-Cai Nie, Donald G. Naugle, and Lin He. Angle-dependent van hove singularities and their breakdown in twisted graphene bilayers. *Phys. Rev. B*, 90:115402, Sep 2014. doi: 10.1103/PhysRevB.90.115402. URL https://link.aps.org/doi/10.1103/PhysRevB.90.115402.

[156] Yuan Cao, Valla Fatemi, Shiang Fang, Kenji Watanabe, Takashi Taniguchi, Efthimios Kaxiras, and Pablo Jarillo-Herrero. Unconventional superconductivity in magic-angle graphene superlattices. *Nature*, 556(7699):43–50, Apr 2018. ISSN 1476-4687. doi: 10.1038/nature26160. URL https://doi.org/10.1038/nature26160.

[157] Matthew Yankowitz, Shaowen Chen, Hryhoriy Polshyn, Yuxuan Zhang, K. Watanabe, T. Taniguchi, David Graf, Andrea F. Young, and Cory R. Dean. Tuning superconductivity in twisted bilayer graphene. *Science*, 363(6431):1059–1064, 2019. doi: 10.1126/science.aav1910. URL https://www.science.org/doi/abs/10.1126/science.aav1910.

[158] Loïc Huder, Alexandre Artaud, Toai Le Quang, Guy Trambly de Laissardière, Aloysius G. M. Jansen, Gérard Lapertot, Claude Chapelier, and Vincent T. Renard. Electronic spectrum of twisted graphene layers under heterostrain. *Phys. Rev. Lett.*, 120:156405, Apr 2018. doi: 10.1103/PhysRevLett.120.156405. URL https://link.aps.org/doi/10.1103/PhysRevLett.120.156405.

[159] Zhen Bi, Noah F. Q. Yuan, and Liang Fu. Designing flat bands by strain. *Phys. Rev. B*, 100:035448, Jul 2019. doi: 10.1103/PhysRevB.100.035448. URL https://link.aps.org/doi/10.1103/PhysRevB.100.035448.

[160] Zhen-Bing Dai, Yan He, and Zhiqiang Li. Effects of heterostrain and lattice relaxation on the optical conductivity of twisted bilayer graphene. *Phys. Rev. B*, 104:045403, Jul 2021. doi: 10.1103/PhysRevB.104.045403. URL https://link.aps.org/doi/10.1103/PhysRevB.104.045403.

[161] Jia-Bin Qiao, Long-Jing Yin, and Lin He. Twisted graphene bilayer around the first magic angle engineered by heterostrain. *Phys. Rev. B*, 98:235402, Dec 2018. doi: 10.1103/PhysRevB.98.235402. URL https://link.aps.org/doi/10.1103/PhysRevB.98.235402.

[162] Marwa Mannaï and Sonia Haddad. Twistronics versus straintronics in twisted bilayers of graphene and transition metal dichalcogenides. *Phys. Rev. B*, 103: L201112, May 2021. doi: 10.1103/PhysRevB.103.L201112. URL `https://link.aps.org/doi/10.1103/PhysRevB.103.L201112`.

[163] Emmanuel Okogbue, Sang Sub Han, Tae-Jun Ko, Hee-Suk Chung, Jinwoo Ma, Mashiyat Sumaiya Shawkat, Jung Han Kim, Jong Hun Kim, Eunji Ji, Kyu Hwan Oh, Lei Zhai, Gwan-Hyoung Lee, and Yeonwoong Jung. Multifunctional two-dimensional ptse2-layer kirigami conductors with 2000% stretchability and metallic-to-semiconducting tunability. *Nano Letters*, 19(11):7598–7607, 2019. doi: 10.1021/acs.nanolett.9b01726. URL `https://doi.org/10.1021/acs.nanolett.9b01726`. PMID: 31244238.

[164] Wei Zheng, Weicheng Huang, Feng Gao, Huihui Yang, Mingjin Dai, Guangbo Liu, Bin Yang, Jia Zhang, Yong Qing Fu, Xiaoshuang Chen, Yunfeng Qiu, Dechang Jia, Yu Zhou, and PingAn Hu. Kirigami-inspired highly stretchable nanoscale devices using multidimensional deformation of monolayer mos2. *Chemistry of Materials*, 30(17):6063–6070, 2018. doi: 10.1021/acs.chemmater.8b02464. URL `https://doi.org/10.1021/acs.chemmater.8b02464`.

[165] David Lloyd, Xinghui Liu, Jason W. Christopher, Lauren Cantley, Anubhav Wadehra, Brian L. Kim, Bennett B. Goldberg, Anna K. Swan, and J. Scott Bunch. Band gap engineering with ultralarge biaxial strains in suspended monolayer mos2. *Nano Letters*, 16(9):5836–5841, 2016. doi: 10.1021/acs.nanolett.6b02615. URL `https://doi.org/10.1021/acs.nanolett.6b02615`. PMID: 27509768.

[166] Jakob Zabel, Rahul R. Nair, Anna Ott, Thanasis Georgiou, Andre K. Geim, Kostya S. Novoselov, and Cinzia Casiraghi. Raman spectroscopy of graphene and bilayer under biaxial strain: Bubbles and balloons. *Nano Letters*, 12(2): 617–621, 2012. doi: 10.1021/nl203359n. URL `https://doi.org/10.1021/nl203359n`. PMID: 22149458.

[167] Yuyoung Shin, Marcelo Lozada-Hidalgo, Jose L. Sambricio, Irina V. Grigorieva, Andre K. Geim, and Cinzia Casiraghi. Raman spectroscopy of highly pressurized graphene membranes. *Applied Physics Letters*, 108(22):221907, 2016. doi: 10.1063/1.4952972. URL `https://doi.org/10.1063/1.4952972`.

[168] Ch. Androulidakis, E. N. Koukaras, M. Poss, K. Papagelis, C. Galiotis, and S. Tawfick. Strained hexagonal boron nitride: Phonon shift and grüneisen pa-

rameter. *Phys. Rev. B*, 97:241414, Jun 2018. doi: 10.1103/PhysRevB.97.241414. URL https://link.aps.org/doi/10.1103/PhysRevB.97.241414.

[169] Dominik Metten, Fran çois Federspiel, Michelangelo Romeo, and Stéphane Berciaud. All-optical blister test of suspended graphene using micro-raman spectroscopy. *Phys. Rev. Applied*, 2:054008, Nov 2014. doi: 10.1103/PhysRevApplied.2.054008. URL https://link.aps.org/doi/10.1103/PhysRevApplied.2.054008.

[170] Jae-Ung Lee, Duhee Yoon, and Hyeonsik Cheong. Estimation of young's modulus of graphene by raman spectroscopy. *Nano Letters*, 12(9):4444–4448, 2012. doi: 10.1021/nl301073q. URL https://doi.org/10.1021/nl301073q. PMID: 22866776.

[171] Riccardo Frisenda, Matthias Drüppel, Robert Schmidt, Steffen Michaelis de Vasconcellos, David Perez de Lara, Rudolf Bratschitsch, Michael Rohlfing, and Andres Castellanos-Gomez. Biaxial strain tuning of the optical properties of single-layer transition metal dichalcogenides. *npj 2D Materials and Applications*, 1(1):10, May 2017. ISSN 2397-7132. doi: 10.1038/s41699-017-0013-7. URL https://doi.org/10.1038/s41699-017-0013-7.

[172] Felix Carrascoso, Der-Yuh Lin, Riccardo Frisenda, and Andres Castellanos-Gomez. Biaxial strain tuning of interlayer excitons in bilayer MoS2. *Journal of Physics: Materials*, 3(1):015003, oct 2019. doi: 10.1088/2515-7639/ab4432. URL https://doi.org/10.1088/2515-7639/ab4432.

[173] Shenyang Huang, Guowei Zhang, Fengren Fan, Chaoyu Song, Fanjie Wang, Qiaoxia Xing, Chong Wang, Hua Wu, and Hugen Yan. Strain-tunable van der waals interactions in few-layer black phosphorus. *Nature Communications*, 10 (1):2447, Jun 2019. ISSN 2041-1723. doi: 10.1038/s41467-019-10483-8. URL https://doi.org/10.1038/s41467-019-10483-8.

[174] Wei Pan, Jianliang Xiao, Junwei Zhu, Chenxi Yu, Gang Zhang, Zhenhua Ni, K. Watanabe, T. Taniguchi, Yi Shi, and Xinran Wang. Biaxial compressive strain engineering in graphene/boron nitride heterostructures. *Scientific Reports*, 2(1):893, Nov 2012. ISSN 2045-2322. doi: 10.1038/srep00893. URL https://doi.org/10.1038/srep00893.

[175] Tao Jiang, Zuyuan Wang, Xiulin Ruan, and Yong Zhu. Equi-biaxial compressive strain in graphene: Grüneisen parameter and buckling ridges. *2D Materials*, 6

(1):015026, dec 2018. doi: 10.1088/2053-1583/aaf20a. URL https://doi.org/10.1088/2053-1583/aaf20a.

[176] Yang Guo, Bin Li, Yuan Huang, Shuo Du, Chi Sun, Hailan Luo, Baoli Liu, Xingjiang Zhou, Jinlong Yang, Junjie Li, and Changzhi Gu. Direct bandgap engineering with local biaxial strain in few-layer mos2 bubbles. *Nano Research*, 13(8):2072–2078, Aug 2020. ISSN 1998-0000. doi: 10.1007/s12274-020-2809-6. URL https://doi.org/10.1007/s12274-020-2809-6.

[177] Hailan Luo, Xuanyi Li, Yanchong Zhao, Rong Yang, Lihong Bao, Yufeng Hao, Yu-nan Gao, Norman N. Shi, Yang Guo, Guodong Liu, Lin Zhao, Qingyan Wang, Zhongshan Zhang, Guangyu Zhang, Jiatao Sun, Yuan Huang, Hongjun Gao, and Xingjiang Zhou. Simultaneous generation of direct- and indirect-gap photoluminescence in multilayer mos$_2$ bubbles. *Phys. Rev. Materials*, 4:074006, Jul 2020. doi: 10.1103/PhysRevMaterials.4.074006. URL https://link.aps.org/doi/10.1103/PhysRevMaterials.4.074006.

[178] Isabella Gasparutti, Seung Hyun Song, Michael Neumann, Xu Wei, Kenji Watanabe, Takashi Taniguchi, and Young Hee Lee. How clean is clean? recipes for van der waals heterostructure cleanliness assessment. *ACS Applied Materials & Interfaces*, 12(6):7701–7709, 2020. doi: 10.1021/acsami.9b18821. URL https://doi.org/10.1021/acsami.9b18821. PMID: 31944093.

[179] Peng Yin and Ming Ma. Efficient and robust fabrication of microscale graphene drums. *ACS Applied Nano Materials*, 1(12):6596–6602, 2018. doi: 10.1021/acsanm.8b01347. URL https://doi.org/10.1021/acsanm.8b01347.

[180] Khadisha M. Zahra, Conor Byrne, Adriana Alieva, Cinzia Casiraghi, and Alex S. Walton. Intercalation, decomposition, entrapment – a new route to graphene nanobubbles. *Phys. Chem. Chem. Phys.*, 22:7606–7615, 2020. doi: 10.1039/D0CP00592D. URL http://dx.doi.org/10.1039/D0CP00592D.

[181] Li He, Huishan Wang, Lingxiu Chen, Xiujun Wang, Hong Xie, Chengxin Jiang, Chen Li, Kenan Elibol, Jannik Meyer, Kenji Watanabe, Takashi Taniguchi, Zhangting Wu, Wenhui Wang, Zhenhua Ni, Xiangshui Miao, Chi Zhang, Daoli Zhang, Haomin Wang, and Xiaoming Xie. Isolating hydrogen in hexagonal boron nitride bubbles by a plasma treatment. *Nature Communications*, 10(1):2815, Jun 2019. ISSN 2041-1723. doi: 10.1038/s41467-019-10660-9. URL https://doi.org/10.1038/s41467-019-10660-9.

[182] E. Stolyarova, D. Stolyarov, K. Bolotin, S. Ryu, L. Liu, K. T. Rim, M. Klima, M. Hybertsen, I. Pogorelsky, I. Pavlishin, K. Kusche, J. Hone, P. Kim, H. L. Stormer, V. Yakimenko, and G. Flynn. Observation of graphene bubbles and effective mass transport under graphene films. *Nano Letters*, 9(1):332–337, 2009. doi: 10.1021/nl803087x. URL https://doi.org/10.1021/nl803087x. PMID: 19105652.

[183] Charlotte Herbig, E. Harriet Åhlgren, Ulrike A. Schröder, Antonio J. Martínez-Galera, Mohammad A. Arman, Jani Kotakoski, Jan Knudsen, Arkady V. Krasheninnikov, and Thomas Michely. Xe irradiation of graphene on ir(111): From trapping to blistering. *Phys. Rev. B*, 92:085429, Aug 2015. doi: 10.1103/PhysRevB.92.085429. URL https://link.aps.org/doi/10.1103/PhysRevB.92.085429.

[184] Cinzia Di Giorgio, Elena Blundo, Giorgio Pettinari, Marco Felici, Yuerui Lu, Anna Maria Cucolo, Antonio Polimeni, and Fabrizio Bobba. Nanoscale measurements of elastic properties and hydrostatic pressure in h2-bulged mos2 membranes. *Advanced Materials Interfaces*, 7(23):2001024, 2020. doi: https://doi.org/10.1002/admi.202001024. URL https://onlinelibrary.wiley.com/doi/abs/10.1002/admi.202001024.

[185] Elena Blundo, Cinzia Di Giorgio, Giorgio Pettinari, Tanju Yildirim, Marco Felici, Yuerui Lu, Fabrizio Bobba, and Antonio Polimeni. Engineered creation of periodic giant, nonuniform strains in mos2 monolayers. *Advanced Materials Interfaces*, 7(17):2000621, 2020. doi: https://doi.org/10.1002/admi.202000621. URL https://onlinelibrary.wiley.com/doi/abs/10.1002/admi.202000621.

[186] E. Blundo, M. Felici, T. Yildirim, G. Pettinari, D. Tedeschi, A. Miriametro, B. Liu, W. Ma, Y. Lu, and A. Polimeni. Evidence of the direct-to-indirect band gap transition in strained two-dimensional ws_2, mos_2, and wse_2. *Phys. Rev. Res.*, 2:012024, Jan 2020. doi: 10.1103/PhysRevResearch.2.012024. URL https://link.aps.org/doi/10.1103/PhysRevResearch.2.012024.

[187] Pengfei Jia, Wenjing Chen, Jiabin Qiao, Miao Zhang, Xiaohu Zheng, Zhongying Xue, Rongda Liang, Chuanshan Tian, Lin He, Zengfeng Di, and Xi Wang. Programmable graphene nanobubbles with three-fold symmetric pseudo-magnetic fields. *Nature Communications*, 10(1):3127, Jul 2019. ISSN

2041-1723. doi: 10.1038/s41467-019-11038-7. URL `https://doi.org/10.1038/s41467-019-11038-7`.

[188] Xin Zhang, Haojie Zhang, Shiwei Cao, Ning Zhang, Bo Jin, Zewen Zong, Zhan Li, and Ximeng Chen. Construction of position-controllable graphene bubbles in liquid nitrogen with assistance of low-power laser. *ACS Applied Materials & Interfaces*, 12(50):56260–56268, 2020. doi: 10.1021/acsami.0c14857. URL `https://doi.org/10.1021/acsami.0c14857`. PMID: 33270436.

[189] Jong Hak Lee, Jun You Tan, Chee-Tat Toh, Steven P. Koenig, V. E. Fedorov, Antonio H. Castro Neto, and Barbaros Özyilmaz. Nanometer thick elastic graphene engine. *Nano Letters*, 14(5):2677–2680, 2014. doi: 10.1021/nl500568d. URL `https://doi.org/10.1021/nl500568d`. PMID: 24773247.

[190] Hongjie An, Beng Hau Tan, James Guo Sheng Moo, Sheng Liu, Martin Pumera, and Claus-Dieter Ohl. Graphene nanobubbles produced by water splitting. *Nano Letters*, 17(5):2833–2838, 2017. doi: 10.1021/acs.nanolett.6b05183. URL `https://doi.org/10.1021/acs.nanolett.6b05183`. PMID: 28394607.

[191] M Temmen, O Ochedowski, M Schleberger, M Reichling, and T R J Bollmann. Hydration layers trapped between graphene and a hydrophilic substrate. *New Journal of Physics*, 16(5):053039, may 2014. doi: 10.1088/1367-2630/16/5/053039. URL `https://doi.org/10.1088/1367-2630/16/5/053039`.

[192] P. Bampoulis. Temperature induced dynamics of water confined between graphene and mos2. *The Journal of Chemical Physics*, 154(13):134705, 2021. doi: 10.1063/5.0044123. URL `https://doi.org/10.1063/5.0044123`.

[193] Narasimha G. Boddeti, Xinghui Liu, Rong Long, Jianliang Xiao, J. Scott Bunch, and Martin L. Dunn. Graphene blisters with switchable shapes controlled by pressure and adhesion. *Nano Letters*, 13(12):6216–6221, 2013. doi: 10.1021/nl4036324. URL `https://doi.org/10.1021/nl4036324`. PMID: 24224793.

[194] Guorui Wang, Zhaohe Dai, Yanlei Wang, PingHeng Tan, Luqi Liu, Zhiping Xu, Yueguang Wei, Rui Huang, and Zhong Zhang. Measuring interlayer shear stress in bilayer graphene. *Phys. Rev. Lett.*, 119:036101, Jul 2017. doi: 10.1103/PhysRevLett.119.036101. URL `https://link.aps.org/doi/10.1103/PhysRevLett.119.036101`.

[195] H. Ghorbanfekr-Kalashami, K. S. Vasu, R. R. Nair, François M. Peeters, and M. Neek-Amal. Dependence of the shape of graphene nanobubbles on trapped

substance. *Nature Communications*, 8(1):15844, Jun 2017. ISSN 2041-1723. doi: 10.1038/ncomms15844. URL https://doi.org/10.1038/ncomms15844.

[196] Zhaohe Dai, Yuan Hou, Daniel A. Sanchez, Guorui Wang, Christopher J. Brennan, Zhong Zhang, Luqi Liu, and Nanshu Lu. Interface-governed deformation of nanobubbles and nanotents formed by two-dimensional materials. *Phys. Rev. Lett.*, 121:266101, Dec 2018. doi: 10.1103/PhysRevLett.121.266101. URL https://link.aps.org/doi/10.1103/PhysRevLett.121.266101.

[197] J.S. Bunch and M.L. Dunn. Adhesion mechanics of graphene membranes. *Solid State Communications*, 152(15):1359–1364, 2012. ISSN 0038-1098. doi: https://doi.org/10.1016/j.ssc.2012.04.029. URL https://www.sciencedirect.com/science/article/pii/S0038109812002359. Exploring Graphene, Recent Research Advances.

[198] Zong Zong, Chia-Ling Chen, Mehmet R. Dokmeci, and Kai-tak Wan. Direct measurement of graphene adhesion on silicon surface by intercalation of nanoparticles. *Journal of Applied Physics*, 107(2):026104, 2010. doi: 10.1063/1.3294960. URL https://doi.org/10.1063/1.3294960.

[199] Steven P. Koenig, Narasimha G. Boddeti, Martin L. Dunn, and J. Scott Bunch. Ultrastrong adhesion of graphene membranes. *Nature Nanotechnology*, 6(9): 543–546, Sep 2011. ISSN 1748-3395. doi: 10.1038/nnano.2011.123. URL https://doi.org/10.1038/nnano.2011.123.

[200] Taeshik Yoon, Woo Cheol Shin, Taek Yong Kim, Jeong Hun Mun, Taek-Soo Kim, and Byung Jin Cho. Direct measurement of adhesion energy of monolayer graphene as-grown on copper and its application to renewable transfer process. *Nano Letters*, 12(3):1448–1452, 2012. doi: 10.1021/nl204123h. URL https://doi.org/10.1021/nl204123h. PMID: 22335825.

[201] Jubok Lee, Seok Joon Yun, Changwon Seo, Kiwon Cho, Tae Soo Kim, Gwang Hwi An, Kibum Kang, Hyun Seok Lee, and Jeongyong Kim. Switchable, tunable, and directable exciton funneling in periodically wrinkled ws2. *Nano Letters*, 21(1):43–50, 2021. doi: 10.1021/acs.nanolett.0c02619. URL https://doi.org/10.1021/acs.nanolett.0c02619. PMID: 33052049.

[202] Shuliang Ren, Qinghai Tan, and Jun Zhang. Review on the quantum emitters in two-dimensional materials. *Journal of Semiconductors*, 40(7):071903, jul

2019. doi: 10.1088/1674-4926/40/7/071903. URL https://doi.org/10.1088/1674-4926/40/7/071903.

[203] Kenan Elibol, Bernhard C. Bayer, Stefan Hummel, Jani Kotakoski, Giacomo Argentero, and Jannik C. Meyer. Visualising the strain distribution in suspended two-dimensional materials under local deformation. *Scientific Reports*, 6(1):28485, Jun 2016. ISSN 2045-2322. doi: 10.1038/srep28485. URL https://doi.org/10.1038/srep28485.

[204] Simone Bertolazzi, Jacopo Brivio, and Andras Kis. Stretching and breaking of ultrathin mos2. *ACS Nano*, 5(12):9703–9709, 2011. doi: 10.1021/nn203879f. URL https://doi.org/10.1021/nn203879f. PMID: 22087740.

[205] Andres Castellanos-Gomez, Menno Poot, Gary A. Steele, Herre S. J. van der Zant, Nicolás Agraït, and Gabino Rubio-Bollinger. Elastic properties of freely suspended mos2 nanosheets. *Advanced Materials*, 24(6):772–775, 2012. doi: https://doi.org/10.1002/adma.201103965. URL https://onlinelibrary.wiley.com/doi/abs/10.1002/adma.201103965.

[206] Jin Tao, Wanfu Shen, Sen Wu, Lu Liu, Zhihong Feng, Chao Wang, Chunguang Hu, Pei Yao, Hao Zhang, Wei Pang, Xuexin Duan, Jing Liu, Chongwu Zhou, and Daihua Zhang. Mechanical and electrical anisotropy of few-layer black phosphorus. *ACS Nano*, 9(11):11362–11370, 2015. doi: 10.1021/acsnano.5b05151. URL https://doi.org/10.1021/acsnano.5b05151. PMID: 26422521.

[207] Aleksey Falin, Qiran Cai, Elton J.G. Santos, Declan Scullion, Dong Qian, Rui Zhang, Zhi Yang, Shaoming Huang, Kenji Watanabe, Takashi Taniguchi, Matthew R. Barnett, Ying Chen, Rodney S. Ruoff, and Lu Hua Li. Mechanical properties of atomically thin boron nitride and the role of interlayer interactions. *Nature Communications*, 8(1):15815, Jun 2017. ISSN 2041-1723. doi: 10.1038/ncomms15815. URL https://doi.org/10.1038/ncomms15815.

[208] Yufei Sun, Jinbo Pan, Zetao Zhang, Kenan Zhang, Jing Liang, Weijun Wang, Zhiquan Yuan, Yukun Hao, Bolun Wang, Jingwei Wang, Yang Wu, Jingying Zheng, Liying Jiao, Shuyun Zhou, Kaihui Liu, Chun Cheng, Wenhui Duan, Yong Xu, Qimin Yan, and Kai Liu. Elastic properties and fracture behaviors of biaxially deformed, polymorphic mote2. *Nano Letters*, 19(2):761–769, 2019. doi: 10.1021/acs.nanolett.8b03833. URL https://doi.org/10.1021/acs.nanolett.8b03833.

[209] Sajedeh Manzeli, Adrien Allain, Amirhossein Ghadimi, and Andras Kis. Piezoresistivity and strain-induced band gap tuning in atomically thin mos2. *Nano Letters*, 15(8):5330–5335, 2015. doi: 10.1021/acs.nanolett.5b01689. URL https://doi.org/10.1021/acs.nanolett.5b01689. PMID: 26191965.

[210] Hyowon Moon, Gabriele Grosso, Chitraleema Chakraborty, Cheng Peng, Takashi Taniguchi, Kenji Watanabe, and Dirk Englund. Dynamic exciton funneling by local strain control in a monolayer semiconductor. *Nano Letters*, 20(9):6791–6797, 2020. doi: 10.1021/acs.nanolett.0c02757. URL https://doi.org/10.1021/acs.nanolett.0c02757. PMID: 32790415.

[211] Matthew R. Rosenberger, Chandriker Kavir Dass, Hsun-Jen Chuang, Saujan V. Sivaram, Kathleen M. McCreary, Joshua R. Hendrickson, and Berend T. Jonker. Quantum calligraphy: Writing single-photon emitters in a two-dimensional materials platform. *ACS Nano*, 13(1):904–912, 2019. doi: 10.1021/acsnano.8b08730. URL https://doi.org/10.1021/acsnano.8b08730.

[212] Péter Nemes-Incze, Gergő Kukucska, János Koltai, Jenő Kürti, Chanyong Hwang, Levente Tapasztó, and László P. Biró. Preparing local strain patterns in graphene by atomic force microscope based indentation. *Scientific Reports*, 7(1):3035, Jun 2017. ISSN 2045-2322. doi: 10.1038/s41598-017-03332-5. URL https://doi.org/10.1038/s41598-017-03332-5.

[213] Xia Liu, Amit Kumar Sachan, Samuel Tobias Howell, Ana Conde-Rubio, Armin W. Knoll, Giovanni Boero, Renato Zenobi, and Jürgen Brugger. Thermomechanical nanostraining of two-dimensional materials. *Nano Letters*, 20(11):8250–8257, 2020. doi: 10.1021/acs.nanolett.0c03358. URL https://doi.org/10.1021/acs.nanolett.0c03358. PMID: 33030906.

[214] Julien Chaste, Amine Missaoui, Si Huang, Hugo Henck, Zeineb Ben Aziza, Laurence Ferlazzo, Carl Naylor, Adrian Balan, Alan T. Charlie Johnson, Rémy Braive, and Abdelkarim Ouerghi. Intrinsic properties of suspended mos2 on sio2/si pillar arrays for nanomechanics and optics. *ACS Nano*, 12(4):3235–3242, 2018. doi: 10.1021/acsnano.7b07689. URL https://doi.org/10.1021/acsnano.7b07689. PMID: 29553713.

[215] Jong-Kwon Lee, Shiro Yamazaki, Hoyeol Yun, Jinwoo Park, Gary P. Kennedy, Gyu-Tae Kim, Oswald Pietzsch, Roland Wiesendanger, SangWook Lee, Suklyun Hong, Urszula Dettlaff-Weglikowska, and Siegmar Roth. Modification of

electrical properties of graphene by substrate-induced nanomodulation. *Nano Letters*, 13(8):3494–3500, 2013. doi: 10.1021/nl400827p. URL https://doi.org/10.1021/nl400827p. PMID: 23848516.

[216] Hong Li, Alex W. Contryman, Xiaofeng Qian, Sina Moeini Ardakani, Yongji Gong, Xingli Wang, Jeffrey M. Weisse, Chi Hwan Lee, Jiheng Zhao, Pulickel M. Ajayan, Ju Li, Hari C. Manoharan, and Xiaolin Zheng. Optoelectronic crystal of artificial atoms in strain-textured molybdenum disulphide. *Nature Communications*, 6(1):7381, Jun 2015. ISSN 2041-1723. doi: 10.1038/ncomms8381. URL https://doi.org/10.1038/ncomms8381.

[217] Shikai Deng, Songwei Che, Rousan Debbarma, and Vikas Berry. Strain in a single wrinkle on an mos2 flake for in-plane realignment of band structure for enhanced photo-response. *Nanoscale*, 11:504–511, 2019. doi: 10.1039/C8NR05884A. URL http://dx.doi.org/10.1039/C8NR05884A.

[218] Artur Branny, Santosh Kumar, Raphaël Proux, and Brian D. Gerardot. Deterministic strain-induced arrays of quantum emitters in a two-dimensional semiconductor. *Nature Communications*, 8(1):15053, May 2017. ISSN 2041-1723. doi: 10.1038/ncomms15053. URL https://doi.org/10.1038/ncomms15053.

[219] Ahmed Raza Khan, Teng Lu, Wendi Ma, Yuerui Lu, and Yun Liu. Tunable optoelectronic properties of ws2 by local strain engineering and folding. *Advanced Electronic Materials*, 6(4):1901381, 2020. doi: https://doi.org/10.1002/aelm.201901381. URL https://onlinelibrary.wiley.com/doi/abs/10.1002/aelm.201901381.

[220] Qinghua Zhao, Riccardo Frisenda, Tao Wang, and Andres Castellanos-Gomez. Inse: a two-dimensional semiconductor with superior flexibility. *Nanoscale*, 11:9845–9850, 2019. doi: 10.1039/C9NR02172H. URL http://dx.doi.org/10.1039/C9NR02172H.

[221] Jorge Quereda, Pablo San-Jose, Vincenzo Parente, Luis Vaquero-Garzon, Aday J. Molina-Mendoza, Nicolás Agraït, Gabino Rubio-Bollinger, Francisco Guinea, Rafael Roldán, and Andres Castellanos-Gomez. Strong modulation of optical properties in black phosphorus through strain-engineered rippling. *Nano Letters*, 16(5):2931–2937, 2016. doi: 10.1021/acs.nanolett.5b04670. URL https://doi.org/10.1021/acs.nanolett.5b04670. PMID: 27042865.

[222] Shengxue Yang, Cong Wang, Hasan Sahin, Hui Chen, Yan Li, Shu-Shen Li, Aslihan Suslu, Francois M. Peeters, Qian Liu, Jingbo Li, and Sefaattin Tongay. Tuning the optical, magnetic, and electrical properties of rese2 by nanoscale strain engineering. *Nano Letters*, 15(3):1660–1666, 2015. doi: 10.1021/nl504276u. URL `https://doi.org/10.1021/nl504276u`. PMID: 25642738.

[223] Chullhee Cho, Joeson Wong, Amir Taqieddin, Souvik Biswas, Narayana R. Aluru, SungWoo Nam, and Harry A. Atwater. Highly strain-tunable interlayer excitons in mos2/wse2 heterobilayers. *Nano Letters*, 21(9):3956–3964, 2021. doi: 10.1021/acs.nanolett.1c00724. URL `https://doi.org/10.1021/acs.nanolett.1c00724`. PMID: 33914542.

[224] Shikai Deng, Dongjoon Rhee, Won-Kyu Lee, Songwei Che, Bijentimala Keisham, Vikas Berry, and Teri W. Odom. Graphene wrinkles enable spatially defined chemistry. *Nano Letters*, 19(8):5640–5646, 2019. doi: 10.1021/acs.nanolett.9b02178. URL `https://doi.org/10.1021/acs.nanolett.9b02178`. PMID: 31268720.

[225] Anne Juel, Draga Pihler-Puzović, and Matthias Heil. Instabilities in blistering. *Annual Review of Fluid Mechanics*, 50(1):691–714, 2018. doi: 10.1146/annurev-fluid-122316-045106. URL `https://doi.org/10.1146/annurev-fluid-122316-045106`.

[226] Philip Geoffrey Saffman and Geoffrey Ingram Taylor. The penetration of a fluid into a porous medium or hele-shaw cell containing a more viscous liquid. *Proceedings of the Royal Society of London. Series A. Mathematical and Physical Sciences*, 245(1242):312–329, 1958. doi: 10.1098/rspa.1958.0085. URL `https://royalsocietypublishing.org/doi/abs/10.1098/rspa.1958.0085`.

[227] Draga Pihler-Puzović, Raphaël Périllat, Matthew Russell, Anne Juel, and Matthias Heil. Modelling the suppression of viscous fingering in elastic-walled hele-shaw cells. *Journal of Fluid Mechanics*, 731:162–183, 2013. doi: 10.1017/jfm.2013.375.

[228] Eduardo O. Dias and José A. Miranda. Taper-induced control of viscous fingering in variable-gap hele-shaw flows. *Phys. Rev. E*, 87:053015, May 2013. doi: 10.1103/PhysRevE.87.053015. URL `https://link.aps.org/doi/10.1103/PhysRevE.87.053015`.

[229] Mukesh Pandey, Rajeev Ahuja, and Rakesh Kumar. Viscous fingering instabilities in spontaneously formed blisters of mos2 multilayers. *Nanoscale Adv.*, pages –, 2023. doi: 10.1039/D3NA00563A. URL `http://dx.doi.org/10.1039/D3NA00563A`.

[230] Mukesh Pandey, Rajeev Ahuja, and Rakesh Kumar. Hoop compression driven instabilities in spontaneously formed multilayer graphene blisters over a polymeric substrate. *Nanotechnology*, 34(17):175301, feb 2023. doi: 10.1088/1361-6528/acaf33. URL `https://dx.doi.org/10.1088/1361-6528/acaf33`.

[231] Teng Cui, Kevin Yip, Aly Hassan, Guorui Wang, Xingjian Liu, Yu Sun, and Tobin Filleter. Graphene fatigue through van der waals interactions. *Science Advances*, 6(42):eabb1335, 2020. doi: 10.1126/sciadv.abb1335. URL `https://www.science.org/doi/abs/10.1126/sciadv.abb1335`.

[232] Md Akibul Islam, Boran Kumral, Guorui Wang, Teng Cui, Yaoping Hou, Peng Pan, Xinyu Liu, and Tobin Filleter. Fatigue behavior of polymer encapsulated graphene to mitigate interfacial fatigue damage. *Advanced Engineering Materials*, n/a(n/a):2300336. doi: https://doi.org/10.1002/adem.202300336. URL `https://onlinelibrary.wiley.com/doi/abs/10.1002/adem.202300336`.

[233] Yanlong Wang, Chunxiao Cong, Weihuang Yang, Jingzhi Shang, Namphung Peimyoo, Yu Chen, Junyong Kang, Jianpu Wang, Wei Huang, and Ting Yu. Strain-induced direct–indirect bandgap transition and phonon modulation in monolayer ws2. *Nano Research*, 2015.

[234] Gyan Michael, Gongwei Hu, Dongqi Zheng, and Yan Zhang. Piezo-phototronic solar cell based on 2d monochalcogenides materials. *Journal of Physics D: Applied Physics*, 52(20):204001, mar 2019. doi: 10.1088/1361-6463/ab0ac4. URL `https://doi.org/10.1088/1361-6463/ab0ac4`.

[235] Rafael Roldán, Andrés Castellanos-Gomez, Emmanuele Cappelluti, and Francisco Guinea. Strain engineering in semiconducting two-dimensional crystals. *Journal of Physics: Condensed Matter*, 27(31):313201, jul 2015. doi: 10.1088/0953-8984/27/31/313201. URL `https://dx.doi.org/10.1088/0953-8984/27/31/313201`.

[236] Haoshen Ye, Haohao Sheng, Dongmei Bai, Junting Zhang, and Jianli Wang. Strain and electric field tuned electronic properties of bas/mose2 van der waals heterostructures for alternative electrodes and photovoltaic cell in

photocatalysis. *Physica E: Low-dimensional Systems and Nanostructures*, 120:114055, 2020. ISSN 1386-9477. doi: https://doi.org/10.1016/j.physe.2020.114055. URL https://www.sciencedirect.com/science/article/pii/S1386947719318892.

[237] Pan Xiong, Fan Zhang, Xiuyun Zhang, Shijian Wang, Hao Liu, Bing Sun, Jinqiang Zhang, Yi Sun, Renzhi Ma, Yoshio Bando, Cuifeng Zhou, Zongwen Liu, Takayoshi Sasaki, and Guoxiu Wang. Strain engineering of two-dimensional multilayered heterostructures for beyond-lithium-based rechargeable batteries. *Nature Communications*, 11(1):3297, Jul 2020. ISSN 2041-1723. doi: 10.1038/s41467-020-17014-w. URL https://doi.org/10.1038/s41467-020-17014-w.

[238] Zhiwei Peng, Xiaolin Chen, Yulong Fan, David J. Srolovitz, and Dangyuan Lei. Strain engineering of 2d semiconductors and graphene: from strain fields to band-structure tuning and photonic applications. *Light: Science & Applications*, 9(1):190, Nov 2020. ISSN 2047-7538. doi: 10.1038/s41377-020-00421-5. URL https://doi.org/10.1038/s41377-020-00421-5.

[239] Tuan V. Vu, Hien D. Tong, Truong Khang Nguyen, Chuong V. Nguyen, A.A. Lavrentyev, O.Y. Khyzhun, B.V. Gabrelian, Hai L. Luong, Khang D. Pham, Phuc Toan Dang, and Dat D. Vo. Enhancement of monolayer snse light absorption by strain engineering: A dft calculation. *Chemical Physics*, 521:5–13, 2019. ISSN 0301-0104. doi: https://doi.org/10.1016/j.chemphys.2019.01.017. URL https://www.sciencedirect.com/science/article/pii/S0301010418312308.

[240] Ji Feng, Xiaofeng Qian, Cheng-Wei Huang, and Ju Li. Strain-engineered artificial atom as a broad-spectrum solar energy funnel. *Nature Photonics*, 6(12):866–872, Dec 2012. ISSN 1749-4893. doi: 10.1038/nphoton.2012.285. URL https://doi.org/10.1038/nphoton.2012.285.

[241] Jin Myung Kim, Md Farhadul Haque, Ezekiel Y. Hsieh, Shahriar Muhammad Nahid, Ishrat Zarin, Kwang-Yong Jeong, Jae-Pil So, Hong-Gyu Park, and SungWoo Nam. Strain engineering of low-dimensional materials for emerging quantum phenomena and functionalities. *Advanced Materials*, 35(27):2107362, 2023. doi: https://doi.org/10.1002/adma.202107362. URL https://onlinelibrary.wiley.com/doi/abs/10.1002/adma.202107362.

[242] F. Bonaccorso, Z. Sun, T. Hasan, and A. C. Ferrari. Graphene photonics and optoelectronics. *Nature Photonics*, 4(9):611–622, Sep 2010. ISSN 1749-4893.

doi: 10.1038/nphoton.2010.186. URL https://doi.org/10.1038/nphoton.2010.186.

[243] Chen Si, Zhimei Sun, and Feng Liu. Strain engineering of graphene: a review. *Nanoscale*, 8:3207–3217, 2016. doi: 10.1039/C5NR07755A. URL http://dx.doi.org/10.1039/C5NR07755A.

[244] F. Guinea, M. I. Katsnelson, and A. K. Geim. Energy gaps and a zero-field quantum hall effect in graphene by strain engineering. *Nature Physics*, 6(1): 30–33, Jan 2010. ISSN 1745-2481. doi: 10.1038/nphys1420. URL https://doi.org/10.1038/nphys1420.

[245] Tao Jiang, Rui Huang, and Yong Zhu. Interfacial sliding and buckling of monolayer graphene on a stretchable substrate. *Advanced Functional Materials*, 24(3):396–402, 2014. doi: https://doi.org/10.1002/adfm.201301999. URL https://onlinelibrary.wiley.com/doi/abs/10.1002/adfm.201301999.

[246] Keliang He, Charles Poole, Kin Fai Mak, and Jie Shan. Experimental demonstration of continuous electronic structure tuning via strain in atomically thin mos2. *Nano Letters*, 13(6):2931–2936, 2013. doi: 10.1021/nl4013166. URL https://doi.org/10.1021/nl4013166. PMID: 23675872.

[247] Xin He, Hai Li, Zhiyong Zhu, Zhenyu Dai, Yang Yang, Peng Yang, Qiang Zhang, Peng Li, Udo Schwingenschlogl, and Xixiang Zhang. Strain engineering in monolayer ws2, mos2, and the ws2/mos2 heterostructure. *Applied Physics Letters*, 109(17):173105, 2016. doi: 10.1063/1.4966218. URL https://doi.org/10.1063/1.4966218.

[248] A. M. Dadgar, D. Scullion, K. Kang, D. Esposito, E. H. Yang, I. P. Herman, M. A. Pimenta, E.-J. G. Santos, and A. N. Pasupathy. Strain engineering and raman spectroscopy of monolayer transition metal dichalcogenides. *Chemistry of Materials*, 30(15):5148–5155, 2018. doi: 10.1021/acs.chemmater.8b01672. URL https://doi.org/10.1021/acs.chemmater.8b01672.

[249] Gerd Plechinger, Andres Castellanos-Gomez, Michele Buscema, Herre S J van der Zant, Gary A Steele, Agnieszka Kuc, Thomas Heine, Christian Schüller, and Tobias Korn. Control of biaxial strain in single-layer molybdenite using local thermal expansion of the substrate. *2D Materials*, 2(1):015006, mar 2015. doi: 10.1088/2053-1583/2/1/015006. URL https://doi.org/10.1088/2053-1583/2/1/015006.

[250] Rui Yang, Jaesung Lee, Souvik Ghosh, Hao Tang, R. Mohan Sankaran, Christian A. Zorman, and Philip X.-L. Feng. Tuning optical signatures of single- and few-layer mos2 by blown-bubble bulge straining up to fracture. *Nano Letters*, 17(8):4568–4575, 2017. doi: 10.1021/acs.nanolett.7b00730. URL https://doi.org/10.1021/acs.nanolett.7b00730. PMID: 28628325.

[251] Xisai Zhang, Yang Li, Wenqian Mu, Wenqi Bai, Xiaoxue Sun, Mingyu Zhao, Zhijie Zhang, Fukai Shan, and Zhenyu Yang. Advanced tape-exfoliated method for preparing large-area 2d monolayers: a review. *2D Materials*, 8(3):032002, may 2021. doi: 10.1088/2053-1583/ac016f. URL https://doi.org/10.1088/2053-1583/ac016f.

[252] Hong ping Zhang, Liangzhi Kou, Yan Jiao, Aijun Du, Youhong Tang, and Yuxiang Ni. Strain engineering of selective chemical adsorption on monolayer black phosphorous. *Applied Surface Science*, 503:144033, 2020. ISSN 0169-4332. doi: https://doi.org/10.1016/j.apsusc.2019.144033. URL https://www.sciencedirect.com/science/article/pii/S0169433219328491.

[253] T. Georgiou, L. Britnell, P. Blake, R. V. Gorbachev, A. Gholinia, A. K. Geim, C. Casiraghi, and K. S. Novoselov. Graphene bubbles with controllable curvature. *Applied Physics Letters*, 99(9):093103, 2011. doi: 10.1063/1.3631632. URL https://doi.org/10.1063/1.3631632.

[254] Pantelis Bampoulis, Vincent J. Teernstra, Detlef Lohse, Harold J. W. Zandvliet, and Bene Poelsema. Hydrophobic ice confined between graphene and mos2. *The Journal of Physical Chemistry C*, 120(47):27079–27084, 2016. doi: 10.1021/acs.jpcc.6b09812. URL https://doi.org/10.1021/acs.jpcc.6b09812.

[255] S. J. Haigh, A. Gholinia, R. Jalil, S. Romani, L. Britnell, D. C. Elias, K. S. Novoselov, L. A. Ponomarenko, A. K. Geim, and R. Gorbachev. Cross-sectional imaging of individual layers and buried interfaces of graphene-based heterostructures and superlattices. *Nature Materials*, 11(9):764–767, Sep 2012. ISSN 1476-4660. doi: 10.1038/nmat3386. URL https://doi.org/10.1038/nmat3386.

[256] Ke Xu, Peigen Cao, and James R. Heath. Graphene visualizes the first water adlayers on mica at ambient conditions. *Science*, 329(5996):1188–1191, 2010. ISSN 0036-8075. doi: 10.1126/science.1192907. URL https://science.sciencemag.org/content/329/5996/1188.

[257] Lee W. Drahushuk, Luda Wang, Steven P. Koenig, J. Scott Bunch, and Michael S. Strano. Analysis of time-varying, stochastic gas transport through graphene membranes. *ACS Nano*, 10(1):786–795, 2016. doi: 10.1021/acsnano.5b05870. URL https://doi.org/10.1021/acsnano.5b05870. PMID: 26720748.

[258] Cinzia Di Giorgio, Elena Blundo, Giorgio Pettinari, Marco Felici, Antonio Polimeni, and Fabrizio Bobba. Exceptional elasticity of microscale constrained mos2 domes. *ACS Applied Materials & Interfaces*, 13(40):48228–48238, 2021. doi: 10.1021/acsami.1c13293. URL https://doi.org/10.1021/acsami.1c13293. PMID: 34592817.

[259] Beng Hau Tan, Jun Zhang, Jing Jin, Chin Hong Ooi, Yi He, Renwu Zhou, Kostya Ostrikov, Nam-Trung Nguyen, and Hongjie An. Direct measurement of the contents, thickness, and internal pressure of molybdenum disulfide nanoblisters. *Nano Letters*, 20(5):3478–3484, 2020. doi: 10.1021/acs.nanolett.0c00398. URL https://doi.org/10.1021/acs.nanolett.0c00398. PMID: 32271023.

[260] Joseph D. Wood, Christopher M. Harvey, and Simon Wang. Adhesion toughness of multilayer graphene films. *Nature Communications*, 8(1):1952, Dec 2017. ISSN 2041-1723. doi: 10.1038/s41467-017-02115-w. URL https://doi.org/10.1038/s41467-017-02115-w.

[261] Yonas Tsegaye Megra and Ji Won Suk. Adhesion properties of 2d materials. *Journal of Physics D: Applied Physics*, 52(36):364002, jul 2019. doi: 10.1088/1361-6463/ab27ad. URL https://doi.org/10.1088/1361-6463/ab27ad.

[262] Deji Akinwande, Christopher J. Brennan, J. Scott Bunch, Philip Egberts, Jonathan R. Felts, Huajian Gao, Rui Huang, Joon-Seok Kim, Teng Li, Yao Li, Kenneth M. Liechti, Nanshu Lu, Harold S. Park, Evan J. Reed, Peng Wang, Boris I. Yakobson, Teng Zhang, Yong-Wei Zhang, Yao Zhou, and Yong Zhu. A review on mechanics and mechanical properties of 2d materials—graphene and beyond. *Extreme Mechanics Letters*, 13:42–77, 2017. ISSN 2352-4316. doi: https://doi.org/10.1016/j.eml.2017.01.008. URL https://www.sciencedirect.com/science/article/pii/S235243161630236X.

[263] Nicolas Leconte, Hakseong Kim, Ho-Jong Kim, Dong Han Ha, Kenji Watanabe, Takashi Taniguchi, Jeil Jung, and Suyong Jung. Graphene bubbles and their role in graphene quantum transport. *Nanoscale*, 9:6041–6047, 2017. doi: 10.1039/C7NR00339K. URL http://dx.doi.org/10.1039/C7NR00339K.

[264] Anastasia V. Tyurnina, Denis A. Bandurin, Ekaterina Khestanova, Vasyl G. Kravets, Maciej Koperski, Francisco Guinea, Alexander N. Grigorenko, Andre K. Geim, and Irina V. Grigorieva. Strained bubbles in van der waals heterostructures as local emitters of photoluminescence with adjustable wavelength. *ACS Photonics*, 6(2):516–524, 2019. doi: 10.1021/acsphotonics.8b01497. URL https://doi.org/10.1021/acsphotonics.8b01497.

[265] N. Levy, S. A. Burke, K. L. Meaker, M. Panlasigui, A. Zettl, F. Guinea, A. H. Castro Neto, and M. F. Crommie. Strain-induced pseudo–magnetic fields greater than 300 tesla in graphene nanobubbles. *Science*, 329(5991): 544–547, 2010. ISSN 0036-8075. doi: 10.1126/science.1191700. URL https://science.sciencemag.org/content/329/5991/544.

[266] Elena Blundo, Tanju Yildirim, Giorgio Pettinari, and Antonio Polimeni. Experimental adhesion energy in van der waals crystals and heterostructures from atomically thin bubbles. *Phys. Rev. Lett.*, 127:046101, Jul 2021. doi: 10.1103/PhysRevLett.127.046101. URL https://link.aps.org/doi/10.1103/PhysRevLett.127.046101.

[267] Andrea C. Ferrari. Raman spectroscopy of graphene and graphite: Disorder, electron–phonon coupling, doping and nonadiabatic effects. *Solid State Communications*, 143(1):47–57, 2007. ISSN 0038-1098. doi: https://doi.org/10.1016/j.ssc.2007.03.052. URL https://www.sciencedirect.com/science/article/pii/S0038109807002967. Exploring graphene.

[268] Un Gi Lee, Woo-Byoung Kim, Do Hyung Han, and Hyun Soo Chung. A modified equation for thickness of the film fabricated by spin coating. *Symmetry*, 11(9), 2019. ISSN 2073-8994. doi: 10.3390/sym11091183. URL https://www.mdpi.com/2073-8994/11/9/1183.

[269] Wei Pan, Jianliang Xiao, Junwei Zhu, Chenxi Yu, Gang Zhang, Zhenhua Ni, K. Watanabe, T. Taniguchi, Yi Shi, and Xinran Wang. Biaxial compressive strain engineering in graphene/boron nitride heterostructures. *Scientific Reports*, 2(1):893, Nov 2012. ISSN 2045-2322. doi: 10.1038/srep00893. URL https://doi.org/10.1038/srep00893.

[270] M. Hanfland, H. Beister, and K. Syassen. Graphite under pressure: Equation of state and first-order raman modes. *Phys. Rev. B*, 39:12598–12603, Jun 1989. doi: 10.1103/PhysRevB.39.12598. URL https://link.aps.org/doi/10.1103/PhysRevB.39.12598.

[271] Elena del Corro, Alberto Otero de la Roza, Mercedes Taravillo, and Valentín G. Baonza. Raman modes and grüneisen parameters of graphite under compressive biaxial stress. *Carbon*, 50(12):4600–4606, 2012. ISSN 0008-6223. doi: https://doi.org/10.1016/j.carbon.2012.05.046. URL https://www.sciencedirect.com/science/article/pii/S0008622312004769.

[272] P. Z. Sun, Q. Yang, W. J. Kuang, Y. V. Stebunov, W. Q. Xiong, J. Yu, R. R. Nair, M. I. Katsnelson, S. J. Yuan, I. V. Grigorieva, M. Lozada-Hidalgo, F. C. Wang, and A. K. Geim. Limits on gas impermeability of graphene. *Nature*, 579 (7798):229–232, Mar 2020. ISSN 1476-4687. doi: 10.1038/s41586-020-2070-x. URL https://doi.org/10.1038/s41586-020-2070-x.

[273] Kuan Zhang and Marino Arroyo. Coexistence of wrinkles and blisters in supported graphene. *Extreme Mechanics Letters*, 14:23–30, 2017. ISSN 2352-4316. doi: https://doi.org/10.1016/j.eml.2016.11.006. URL https://www.sciencedirect.com/science/article/pii/S2352431616301845. Mechanics and Mechanical Behavior of 2D Materials – Graphene and Beyond.

[274] F.M. White. *Fluid Mechanics*. McGraw-Hill series in mechanical engineering. WCB/McGraw-Hill, 1998. ISBN 9780072281927. URL https://books.google.co.in/books?id=MXidPwAACAAJ.

[275] I. Yu. Prosanov and A. A. Matvienko. Study of pva thermal destruction by means of ir and raman spectroscopy. *Physics of the Solid State*, 52(10):2203–2206, Oct 2010. ISSN 1090-6460. doi: 10.1134/S1063783410100318. URL https://doi.org/10.1134/S1063783410100318.

[276] Geun Ho Ahn, Matin Amani, Haider Rasool, Der-Hsien Lien, James P. Mastandrea, Joel W. Ager III, Madan Dubey, Daryl C. Chrzan, Andrew M. Minor, and Ali Javey. -engineered growth of two-dimensional materials. *Nature Communications*, 8(1):608, Sep 2017. ISSN 2041-1723. doi: 10.1038/s41467-017-00516-5. URL https://doi.org/10.1038/s41467-017-00516-5.

[277] Vikas Berry. Impermeability of graphene and its applications. *Carbon*, 62:1–10, 2013. ISSN 0008-6223. doi: https://doi.org/10.1016/j.carbon.2013.05.052. URL https://www.sciencedirect.com/science/article/pii/S0008622313004880.

[278] Yin Zhang. Large deflection of clamped circular plate and accuracy of its approximate analytical solutions. *Science China Physics, Mechanics & Astronomy*, 59

(2):624602, Jan 2016. ISSN 1869-1927. doi: 10.1007/s11433-015-5751-y. URL https://doi.org/10.1007/s11433-015-5751-y.

[279] Peng Wang, Wei Gao, Zhiyi Cao, Kenneth M. Liechti, and Rui Huang. Numerical Analysis of Circular Graphene Bubbles. *Journal of Applied Mechanics*, 80(4), 05 2013. ISSN 0021-8936. doi: 10.1115/1.4024169. URL https://doi.org/10.1115/1.4024169. 040905.

[280] Changgu Lee, Xiaoding Wei, Jeffrey W. Kysar, and James Hone. Measurement of the elastic properties and intrinsic strength of monolayer graphene. *Science*, 321(5887):385–388, 2008. doi: 10.1126/science.1157996. URL https://www.science.org/doi/abs/10.1126/science.1157996.

[281] Kai Liu and Junqiao Wu. Mechanical properties of two-dimensional materials and heterostructures. *Journal of Materials Research*, 31(7):832–844, Apr 2016. ISSN 2044-5326. doi: 10.1557/jmr.2015.324. URL https://doi.org/10.1557/jmr.2015.324.

[282] Chih-Jen Shih, Michael S. Strano, and Daniel Blankschtein. Wetting translucency of graphene. *Nature Materials*, 12(10):866–869, Oct 2013. ISSN 1476-4660. doi: 10.1038/nmat3760. URL https://doi.org/10.1038/nmat3760.

[283] Fereshte Taherian, Valentina Marcon, Nico F. A. van der Vegt, and Frédéric Leroy. What is the contact angle of water on graphene? *Langmuir*, 29(5):1457–1465, 2013. doi: 10.1021/la304645w. URL https://doi.org/10.1021/la304645w. PMID: 23320893.

[284] Kuan Zhang and Marino Arroyo. Coexistence of wrinkles and blisters in supported graphene. *Extreme Mechanics Letters*, 14:23–30, 2017. ISSN 2352-4316. doi: https://doi.org/10.1016/j.eml.2016.11.006. URL https://www.sciencedirect.com/science/article/pii/S2352431616301845. Mechanics and Mechanical Behavior of 2D Materials – Graphene and Beyond.

[285] Davide Tedeschi, Elena Blundo, Marco Felici, Giorgio Pettinari, Boqing Liu, Tanju Yildrim, Elisa Petroni, Chris Zhang, Yi Zhu, Simona Sennato, Yuerui Lu, and Antonio Polimeni. Controlled micro/nanodome formation in proton-irradiated bulk transition-metal dichalcogenides. *Advanced Materials*, 31(44):1903795, 2019. doi: https://doi.org/10.1002/adma.201903795. URL https://onlinelibrary.wiley.com/doi/abs/10.1002/adma.201903795.

[286] L. D. Varma Sangani, Supriya Mandal, Sanat Ghosh, Kenji Watanabe, Takashi Taniguchi, and Mandar M. Deshmukh. Dynamics of interfacial bubble controls adhesion mechanics in van der waals heterostructure. *Nano Letters*, 22(9):3612–3619, 2022. doi: 10.1021/acs.nanolett.1c04341. URL `https://doi.org/10.1021/acs.nanolett.1c04341`. PMID: 35389226.

[287] Yaping Qi, Mohammad A. Sadi, Dan Hu, Ming Zheng, Zhenping Wu, Yucheng Jiang, and Yong P. Chen. Recent progress in strain engineering on van der waals 2d materials: Tunable electrical, electrochemical, magnetic and optical properties. *Advanced Materials*, n/a(n/a):2205714. doi: https://doi.org/10.1002/adma.202205714. URL `https://onlinelibrary.wiley.com/doi/abs/10.1002/adma.202205714`.

[288] Cinzia Di Giorgio, Elena Blundo, Giorgio Pettinari, Marco Felici, Fabrizio Bobba, and Antonio Polimeni. Mechanical, elastic, and adhesive properties of two-dimensional materials: From straining techniques to state-of-the-art local probe measurements. *Advanced Materials Interfaces*, 9(13):2102220, 2022. doi: https://doi.org/10.1002/admi.202102220. URL `https://onlinelibrary.wiley.com/doi/abs/10.1002/admi.202102220`.

[289] Yifan Rao, Shutao Qiao, Zhaohe Dai, and Nanshu Lu. Elastic wetting: Substrate-supported droplets confined by soft elastic membranes. *Journal of the Mechanics and Physics of Solids*, 151:104399, 2021. ISSN 0022-5096. doi: https://doi.org/10.1016/j.jmps.2021.104399. URL `https://www.sciencedirect.com/science/article/pii/S0022509621000831`.

[290] T. Georgiou, L. Britnell, P. Blake, R. V. Gorbachev, A. Gholinia, A. K. Geim, C. Casiraghi, and K. S. Novoselov. Graphene bubbles with controllable curvature. *Applied Physics Letters*, 99(9):093103, 2011. doi: 10.1063/1.3631632. URL `https://doi.org/10.1063/1.3631632`.

[291] Hongbo Zeng, Jun Huang, Yu Tian, Lin Li, Matthew V. Tirrell, and Jacob N. Israelachvili. Adhesion and detachment mechanisms between polymer and solid substrate surfaces: Using polystyrene–mica as a model system. *Macromolecules*, 49(14):5223–5231, 2016. doi: 10.1021/acs.macromol.6b00949. URL `https://doi.org/10.1021/acs.macromol.6b00949`.

[292] J.W. Hutchinson, M.D. Thouless, and E.G. Liniger. Growth and configurational stability of circular, buckling-driven film delaminations. *Acta Metallurgica et Materialia*, 40(2):295–308, 1992. ISSN 0956-7151. doi: https://doi.

org/10.1016/0956-7151(92)90304-W. URL https://www.sciencedirect.com/science/article/pii/095671519290304W.

[293] O. E. Jensen, M. K. Horsburgh, D. Halpern, and D. P. Gaver. The steady propagation of a bubble in a flexible-walled channel: Asymptotic and computational models. *Physics of Fluids*, 14(2):443–457, 2002. doi: 10.1063/1.1432694. URL https://doi.org/10.1063/1.1432694.

[294] Talal T. Al-Housseiny and Howard A. Stone. Controlling viscous fingering in tapered hele-shaw cells. *Physics of Fluids*, 25(9):092102, 2013. doi: 10.1063/1.4819317. URL https://doi.org/10.1063/1.4819317.

[295] Talal T. Al-Housseiny, Ivan C. Christov, and Howard A. Stone. Two-phase fluid displacement and interfacial instabilities under elastic membranes. *Phys. Rev. Lett.*, 111:034502, Jul 2013. doi: 10.1103/PhysRevLett.111.034502. URL https://link.aps.org/doi/10.1103/PhysRevLett.111.034502.

[296] Julia Nase, Anke Lindner, and Costantino Creton. Pattern formation during deformation of a confined viscoelastic layer: From a viscous liquid to a soft elastic solid. *Phys. Rev. Lett.*, 101:074503, Aug 2008. doi: 10.1103/PhysRevLett.101.074503. URL https://link.aps.org/doi/10.1103/PhysRevLett.101.074503.

[297] Lu Gong, Li Xiang, Jiawen Zhang, Jingsi Chen, and Hongbo Zeng. Fundamentals and advances in the adhesion of polymer surfaces and thin films. *Langmuir*, 35(48):15914–15936, 2019. doi: 10.1021/acs.langmuir.9b02123. URL https://doi.org/10.1021/acs.langmuir.9b02123. PMID: 31436435.

[298] A. D. McEwan and G. I. Taylor. The peeling of a flexible strip attached by a viscous adhesive. *Journal of Fluid Mechanics*, 26(1):1–15, 1966. doi: 10.1017/S0022112066001058.

[299] Thomas Vilmin, Falko Ziebert, and Elie Raphaël. Simple view on fingering instability of debonding soft elastic adhesives. *Langmuir*, 26(5):3257–3260, 2010. doi: 10.1021/la903013z. URL https://doi.org/10.1021/la903013z. PMID: 19807118.

[300] B. Saintyves, O. Dauchot, and E. Bouchaud. Bulk elastic fingering instability in hele-shaw cells. *Phys. Rev. Lett.*, 111:047801, Jul 2013. doi: 10.1103/PhysRevLett.111.047801. URL https://link.aps.org/doi/10.1103/PhysRevLett.111.047801.

[301] Kenneth R. Shull, Cynthia M. Flanigan, and Alfred J. Crosby. Fingering instabilities of confined elastic layers in tension. *Phys. Rev. Lett.*, 84:3057–3060, Apr 2000. doi: 10.1103/PhysRevLett.84.3057. URL https://link.aps.org/doi/10.1103/PhysRevLett.84.3057.

[302] Animangsu Ghatak and Manoj K. Chaudhury. Adhesion-induced instability patterns in thin confined elastic film. *Langmuir*, 19(7):2621–2631, 2003. doi: 10.1021/la026932t. URL https://doi.org/10.1021/la026932t.

[303] M Adda-Bedia and L Mahadevan. Crack-front instability in a confined elastic film. *Proceedings of the Royal Society A: Mathematical, Physical and Engineering Sciences*, 462(2075):3233–3251, 2006. doi: 10.1098/rspa.2006.1708. URL https://royalsocietypublishing.org/doi/abs/10.1098/rspa.2006.1708.

[304] Vandita Sharma, Sada Nand, Satyajit Pramanik, Ching-Yao Chen, and Manoranjan Mishra. Control of radial miscible viscous fingering. *Journal of Fluid Mechanics*, 884:A16, 2020. doi: 10.1017/jfm.2019.932.

[305] Zhaohe Dai, Yifan Rao, and Nanshu Lu. Two-dimensional crystals on adhesive substrates subjected to uniform transverse pressure. *International Journal of Solids and Structures*, page 111829, 2022. ISSN 0020-7683. doi: https://doi.org/10.1016/j.ijsolstr.2022.111829. URL https://www.sciencedirect.com/science/article/pii/S0020768322003079.

[306] Georgia Tsoukleri, John Parthenios, Konstantinos Papagelis, Rashid Jalil, Andrea C. Ferrari, Andre K. Geim, Kostya S. Novoselov, and Costas Galiotis. Subjecting a graphene monolayer to tension and compression. *Small*, 5(21):2397–2402, 2009. doi: https://doi.org/10.1002/smll.200900802. URL https://onlinelibrary.wiley.com/doi/abs/10.1002/smll.200900802.

[307] K. S. Vasu, E. Prestat, J. Abraham, J. Dix, R. J. Kashtiban, J. Beheshtian, J. Sloan, P. Carbone, M. Neek-Amal, S. J. Haigh, A. K. Geim, and R. R. Nair. Van der waals pressure and its effect on trapped interlayer molecules. *Nature Communications*, 7(1):12168, Jul 2016. ISSN 2041-1723. doi: 10.1038/ncomms12168. URL https://doi.org/10.1038/ncomms12168.

[308] Elena Blundo, Alessandro Surrente, Davide Spirito, Giorgio Pettinari, Tanju Yildirim, Carlos Alvarado Chavarin, Leonetta Baldassarre, Marco Felici, and Antonio Polimeni. Vibrational properties in highly strained hexagonal boron nitride bubbles. *Nano Letters*, 22(4):1525–1533, 2022. doi: 10.1021/acs.nanolett.

1c04197. URL https://doi.org/10.1021/acs.nanolett.1c04197. PMID: 35107287.

[309] Wenxiang Wang, Xiaojie Ma, Zhaohe Dai, Shuai Zhang, Yuan Hou, Guorui Wang, Qunyang Li, Zhong Zhang, Yueguang Wei, and Luqi Liu. Mechanical behavior of blisters spontaneously formed by multilayer 2d materials. *Advanced Materials Interfaces*, 9(12):2101939, 2022. doi: https://doi.org/10.1002/admi.202101939. URL https://onlinelibrary.wiley.com/doi/abs/10.1002/admi.202101939.

[310] Mingyuan Xu, Deliang Zhang, Yin Wang, Yuge Zhang, Qiang Li, and Mingdong Dong. Nanoscale friction of strained molybdenum disulfide induced by nanoblisters. *Applied Physics Letters*, 120(15):151601, 2022. doi: 10.1063/5.0087756. URL https://doi.org/10.1063/5.0087756.

[311] Timur Aslyamov, Khadisha M. Zahra, Petr Zhilyaev, and Alex S. Walton. Universal shape of graphene nanobubbles on metallic substrate. *Phys. Chem. Chem. Phys.*, 24:6935–6940, 2022. doi: 10.1039/D1CP05902E. URL http://dx.doi.org/10.1039/D1CP05902E.

[312] Zhujun Huang, Edoardo Cuniberto, Suji Park, Kim Kisslinger, Qin Wu, Takashi Taniguchi, Kenji Watanabe, Kevin G. Yager, and Davood Shahrjerdi. Mechanisms of interface cleaning in heterostructures made from polymer-contaminated graphene. *Small*, 18(20):2201248, 2022. doi: https://doi.org/10.1002/smll.202201248. URL https://onlinelibrary.wiley.com/doi/abs/10.1002/smll.202201248.

[313] Gunnar G. Peng and John R. Lister. Viscous flow under an elastic sheet. *Journal of Fluid Mechanics*, 905:A30, 2020. doi: 10.1017/jfm.2020.745.

[314] Rafael D. Schulman and Kari Dalnoki-Veress. Droplets capped with an elastic film can be round, elliptical, or nearly square. *Phys. Rev. Lett.*, 121:248004, Dec 2018. doi: 10.1103/PhysRevLett.121.248004. URL https://link.aps.org/doi/10.1103/PhysRevLett.121.248004.

[315] Sukhyun Hong, Minsuk Park, Soonhyung Kwon, Jehyun Oh, Sungmin Bong, Balu Krishnakumar, and Sang-Yong Ju. Formation of graphene nanostructures using laser induced vaporization of entrapped water. *Carbon*, 183:84–92, 2021. ISSN 0008-6223. doi: https://doi.org/10.1016/j.carbon.

2021.06.071. URL https://www.sciencedirect.com/science/article/pii/S0008622321006588.

[316] David M. Goggin, Hanyu Zhang, Elisa M. Miller, and Joseph R. Samaniuk. Interference provides clarity: Direct observation of 2d materials at fluid–fluid interfaces. *ACS Nano*, 14(1):777–790, 2020. doi: 10.1021/acsnano.9b07776. URL https://doi.org/10.1021/acsnano.9b07776. PMID: 31820924.

[317] Najme S. Taghavi, Patricia Gant, Peng Huang, Iris Niehues, Robert Schmidt, Steffen Michaelis de Vasconcellos, Rudolf Bratschitsch, Mar García-Hernández, Riccardo Frisenda, and Andres Castellanos-Gomez. Thickness determination of mos2, mose2, ws2 and wse2 on transparent stamps used for deterministic transfer of 2d materials. *Nano Research*, 12(7):1691–1695, Jul 2019. ISSN 1998-0000. doi: 10.1007/s12274-019-2424-6. URL https://doi.org/10.1007/s12274-019-2424-6.

[318] K. Sasaki and K. Hitachi. Universal layer number in graphite. *Communications Physics*, 3(1):90, May 2020. ISSN 2399-3650. doi: 10.1038/s42005-020-0354-y. URL https://doi.org/10.1038/s42005-020-0354-y.

[319] Han Lin, Scott Fraser, Minghui Hong, Manish Chhowalla, Dan Li, and Baohua Jia. Near-perfect microlenses based on graphene microbubbles. *Advanced Photonics*, 2(5):1 – 6, 2020. doi: 10.1117/1.AP.2.5.055001. URL https://doi.org/10.1117/1.AP.2.5.055001.

[320] Rongfu Wen, Xuehu Ma, Yung-Cheng Lee, and Ronggui Yang. Liquid-vapor phase-change heat transfer on functionalized nanowired surfaces and beyond. *Joule*, 2(11):2307–2347, 2018. ISSN 2542-4351. doi: https://doi.org/10.1016/j.joule.2018.08.014. URL https://www.sciencedirect.com/science/article/pii/S2542435118303994.

[321] Xianheng Guan, Anantha P. Sarma, Eshwar Hamesh, Junyu Yang, Nhung Nguyen, Enrique Cerda, Luka Pocivavsek, and Sachin Velankar. Compression-induced buckling of thin films bonded to viscous substrates: Uniform wrinkles vs localized ridges. *International Journal of Solids and Structures*, page 111843, 2022. ISSN 0020-7683. doi: https://doi.org/10.1016/j.ijsolstr.2022.111843. URL https://www.sciencedirect.com/science/article/pii/S0020768322003171.

[322] Kaili Xie, Alizée Glasser, Shekhar Shinde, Zaicheng Zhang, Jean-Michel Rampnoux, Abdelhamid Maali, Eric Cloutet, Georges Hadziioannou, and Hamid Kellay. Delamination and wrinkling of flexible conductive polymer thin films. *Advanced Functional Materials*, 31(21):2009039, 2021. doi: https://doi.org/10.1002/adfm.202009039. URL https://onlinelibrary.wiley.com/doi/abs/10.1002/adfm.202009039.

[323] Jérôme Colin, Christophe Coupeau, and Jean Grilhé. Plastic folding of buckling structures. *Phys. Rev. Lett.*, 99:046101, Jul 2007. doi: 10.1103/PhysRevLett.99.046101. URL https://link.aps.org/doi/10.1103/PhysRevLett.99.046101.

[324] Shaoting Lin, Yunwei Mao, Raul Radovitzky, and Xuanhe Zhao. Instabilities in confined elastic layers under tension: Fringe, fingering and cavitation. *Journal of the Mechanics and Physics of Solids*, 106:229–256, 2017. ISSN 0022-5096. doi: https://doi.org/10.1016/j.jmps.2017.05.011. URL https://www.sciencedirect.com/science/article/pii/S0022509617302892.

[325] S. Ghosh, I. Calizo, D. Teweldebrhan, E. P. Pokatilov, D. L. Nika, A. A. Balandin, W. Bao, F. Miao, and C. N. Lau. Extremely high thermal conductivity of graphene: Prospects for thermal management applications in nanoelectronic circuits. *Applied Physics Letters*, 92(15):151911, 2008. doi: 10.1063/1.2907977. URL https://doi.org/10.1063/1.2907977.

[326] Lucie Ducloué, Andrew L. Hazel, Draga Pihler-Puzović, and Anne Juel. Viscous fingering and dendritic growth under an elastic membrane. *Journal of Fluid Mechanics*, 826:R2, 2017. doi: 10.1017/jfm.2017.468.

[327] Irmgard Bischofberger, Radha Ramachandran, and Sidney R. Nagel. Fingering versus stability in the limit of zero interfacial tension. *Nature Communications*, 5(1):5265, Oct 2014. ISSN 2041-1723. doi: 10.1038/ncomms6265. URL https://doi.org/10.1038/ncomms6265.

[328] Todd M. Squires and Stephen R. Quake. Microfluidics: Fluid physics at the nanoliter scale. *Rev. Mod. Phys.*, 77:977–1026, Oct 2005. doi: 10.1103/RevModPhys.77.977. URL https://link.aps.org/doi/10.1103/RevModPhys.77.977.

[329] Elena Blundo, Alessandro Surrente, Davide Spirito, Giorgio Pettinari, Tanju Yildirim, Carlos Alvarado Chavarin, Leonetta Baldassarre, Marco Felici, and

Antonio Polimeni. Vibrational properties in highly strained hexagonal boron nitride bubbles. *Nano Letters*, 22(4):1525–1533, 2022. doi: 10.1021/acs.nanolett.1c04197. URL https://doi.org/10.1021/acs.nanolett.1c04197. PMID: 35107287.

[330] E. Blundo, E. Cappelluti, M. Felici, G. Pettinari, and A. Polimeni. Strain-tuning of the electronic, optical, and vibrational properties of two-dimensional crystals. *Applied Physics Reviews*, 8(2):021318, 06 2021. ISSN 1931-9401. doi: 10.1063/5.0037852. URL https://doi.org/10.1063/5.0037852.

[331] C. N. Berger, M. Dirschka, and A. Vijayaraghavan. Ultra-thin graphene–polymer heterostructure membranes. *Nanoscale*, 8:17928–17939, 2016. doi: 10.1039/C6NR06316K. URL http://dx.doi.org/10.1039/C6NR06316K.

[332] Guorui Wang, Zhepeng Zhang, Yanlei Wang, Enlai Gao, Xiangzheng Jia, Zhaohe Dai, Chuanxin Weng, Luqi Liu, Yanfeng Zhang, and Zhong Zhang. Out-of-plane deformations determined mechanics of vanadium disulfide (vs2) sheets. *ACS Applied Materials & Interfaces*, 13(2):3040–3050, 2021. doi: 10.1021/acsami.0c19835. URL https://doi.org/10.1021/acsami.0c19835. PMID: 33400503.

[333] Chengpeng Ma, Yingchao Zhang, Shuping Jiao, and Mingchao Liu. Snap-through of graphene nanowrinkles under out-of-plane compression. *Nanotechnology*, 34(1):015705, oct 2022. doi: 10.1088/1361-6528/ac9418. URL https://dx.doi.org/10.1088/1361-6528/ac9418.

[334] Leo Yu, Minda Deng, Jingyuan Linda Zhang, Sven Borghardt, Beata Kardynal, Jelena Vučković, and Tony F. Heinz. Site-controlled quantum emitters in monolayer mose2. *Nano Letters*, 21(6):2376–2381, 2021. doi: 10.1021/acs.nanolett.0c04282. URL https://doi.org/10.1021/acs.nanolett.0c04282. PMID: 33689386.

[335] Steffen Michaelis de Vasconcellos, Daniel Wigger, Ursula Wurstbauer, Alexander W. Holleitner, Rudolf Bratschitsch, and Tilmann Kuhn. Single-photon emitters in layered van der waals materials. *physica status solidi (b)*, 259 (4):2100566, 2022. doi: https://doi.org/10.1002/pssb.202100566. URL https://onlinelibrary.wiley.com/doi/abs/10.1002/pssb.202100566.

[336] Jae-Pil So, Ha-Reem Kim, Hyeonjun Baek, Kwang-Yong Jeong, Hoo-Cheol Lee, Woong Huh, Yoon Seok Kim, Kenji Watanabe, Takashi Taniguchi, Jungkil Kim, Chul-Ho Lee, and Hong-Gyu Park. Electrically driven strain-induced deterministic single-photon emitters in a van der waals heterostructure. *Science Advances*, 7(43):eabj3176, 2021. doi: 10.1126/sciadv.abj3176. URL `https://www.science.org/doi/abs/10.1126/sciadv.abj3176`.

[337] Salvatore Cianci, Elena Blundo, Federico Tuzi, Giorgio Pettinari, Katarzyna Olkowska-Pucko, Eirini Parmenopoulou, Djero B. L. Peeters, Antonio Miriametro, Takashi Taniguchi, Kenji Watanabe, Adam Babinski, Maciej R. Molas, Marco Felici, and Antonio Polimeni. Spatially controlled single photon emitters in hbn-capped ws2 domes. *Advanced Optical Materials*, 11(12): 2202953, 2023. doi: https://doi.org/10.1002/adom.202202953. URL `https://onlinelibrary.wiley.com/doi/abs/10.1002/adom.202202953`.

[338] Wenxiang Wang, Xiaojie Ma, Zhaohe Dai, Shuai Zhang, Yuan Hou, Guorui Wang, Qunyang Li, Zhong Zhang, Yueguang Wei, and Luqi Liu. Mechanical behavior of blisters spontaneously formed by multilayer 2d materials. *Advanced Materials Interfaces*, 9(12):2101939, 2022. doi: https://doi.org/10.1002/admi.202101939. URL `https://onlinelibrary.wiley.com/doi/abs/10.1002/admi.202101939`.

[339] Yaodong Li, Shirui Weng, Rui Niu, Weili Zhen, Feng Xu, Wenka Zhu, and Changjin Zhang. Poly(vinyl alcohol)-assisted exfoliation of van der waals materials. *ACS Omega*, 7(43):38774–38781, 2022. doi: 10.1021/acsomega.2c04409. URL `https://doi.org/10.1021/acsomega.2c04409`.

[340] Animangsu Ghatak, L. Mahadevan, Jun Young Chung, Manoj K. Chaudhury, and Vijay Shenoy. Peeling from a biomimetically patterned thin elastic film. *Proceedings of the Royal Society of London. Series A: Mathematical, Physical and Engineering Sciences*, 460(2049):2725–2735, 2004. doi: 10.1098/rspa.2004.1313. URL `https://royalsocietypublishing.org/doi/abs/10.1098/rspa.2004.1313`.

[341] Panayiotis Gialamas, Benjamin Völker, Rachel R. Collino, Matthew R. Begley, and Robert M. McMeeking. Peeling of an elastic membrane tape adhered to a substrate by a uniform cohesive traction. *International Journal of Solids and Structures*, 51(18):3003–3011, 2014. ISSN 0020-7683. doi: https://doi.org/10.

1016/j.ijsolstr.2014.04.001. URL https://www.sciencedirect.com/science/article/pii/S0020768314001504.

[342] Yuanbo Zhang, Tsung-Ta Tang, Caglar Girit, Zhao Hao, Michael C. Martin, Alex Zettl, Michael F. Crommie, Y. Ron Shen, and Feng Wang. Direct observation of a widely tunable bandgap in bilayer graphene. *Nature*, 459 (7248):820–823, Jun 2009. ISSN 1476-4687. doi: 10.1038/nature08105. URL https://doi.org/10.1038/nature08105.

[343] Katherine Smith, Aidan Retallick, Daniel Melendrez, Aravind Vijayaraghavan, and Matthias Heil. Modeling graphene–polymer heterostructure mems membranes with the föppl–von kármán equations. *ACS Applied Materials & Interfaces*, 15(7):9853–9861, 2023. doi: 10.1021/acsami.2c21096. URL https://doi.org/10.1021/acsami.2c21096. PMID: 36748982.

[344] David Lloyd, Xinghui Liu, Narasimha Boddeti, Lauren Cantley, Rong Long, Martin L. Dunn, and J. Scott Bunch. Adhesion, stiffness, and instability in atomically thin mos2 bubbles. *Nano Letters*, 17(9):5329–5334, 2017. doi: 10.1021/acs.nanolett.7b01735. URL https://doi.org/10.1021/acs.nanolett.7b01735. PMID: 28762748.

[345] Andrew Kozbial, Xiao Gong, Haitao Liu, and Lei Li. Understanding the intrinsic water wettability of molybdenum disulfide (mos2). *Langmuir*, 31(30):8429–8435, 2015. doi: 10.1021/acs.langmuir.5b02057. URL https://doi.org/10.1021/acs.langmuir.5b02057. PMID: 26172421.

[346] Zhesheng Chen, Johan Biscaras, and Abhay Shukla. Optimal light harvesting in 2d semiconductor heterostructures. *2D Materials*, 4(2):025115, jun 2017. doi: 10.1088/2053-1583/aa736f. URL https://dx.doi.org/10.1088/2053-1583/aa736f.

[347] J.S. Bunch and M.L. Dunn. Adhesion mechanics of graphene membranes. *Solid State Communications*, 152(15):1359–1364, 2012. ISSN 0038-1098. doi: https://doi.org/10.1016/j.ssc.2012.04.029. URL https://www.sciencedirect.com/science/article/pii/S0038109812002359. Exploring Graphene, Recent Research Advances.

[348] Meagan B Elinski, Zhuotong Liu, Jessica C Spear, and James D Batteas. 2d or not 2d? the impact of nanoscale roughness and substrate interactions on the tribological properties of graphene and mos2. *Journal of Physics D: Applied*

Physics, 50(10):103003, feb 2017. doi: 10.1088/1361-6463/aa58d6. URL https://dx.doi.org/10.1088/1361-6463/aa58d6.

[349] Zhixing Lu and Martin L. Dunn. van der waals adhesion of graphene membranes. *Journal of Applied Physics*, 107(4):044301, 2010. doi: 10.1063/1.3270425. URL https://doi.org/10.1063/1.3270425.

[350] Teng Cui, Kevin Yip, Aly Hassan, Guorui Wang, Xingjian Liu, Yu Sun, and Tobin Filleter. Graphene fatigue through van der waals interactions. *Science Advances*, 6(42):eabb1335, 2020. doi: 10.1126/sciadv.abb1335. URL https://www.science.org/doi/abs/10.1126/sciadv.abb1335.

[351] Zachary H. Aitken and Rui Huang. Effects of mismatch strain and substrate surface corrugation on morphology of supported monolayer graphene. *Journal of Applied Physics*, 107(12):123531, 2010. doi: 10.1063/1.3437642. URL https://doi.org/10.1063/1.3437642.

[352] Felix Carrascoso, Hao Li, Riccardo Frisenda, and Andres Castellanos-Gomez. Strain engineering in single-, bi- and tri-layer mos2, mose2, ws2 and wse2. *Nano Research*, 14(6):1698–1703, Jun 2021. ISSN 1998-0000. doi: 10.1007/s12274-020-2918-2. URL https://doi.org/10.1007/s12274-020-2918-2.

[353] Zhiwei Li, Yawei Lv, Liwang Ren, Jia Li, Lingan Kong, Yujia Zeng, Quanyang Tao, Ruixia Wu, Huifang Ma, Bei Zhao, Di Wang, Weiqi Dang, Keqiu Chen, Lei Liao, Xidong Duan, Xiangfeng Duan, and Yuan Liu. Efficient strain modulation of 2d materials via polymer encapsulation. *Nature Communications*, 11(1):1151, Mar 2020. ISSN 2041-1723. doi: 10.1038/s41467-020-15023-3. URL https://doi.org/10.1038/s41467-020-15023-3.

[354] Liangliang Zhu and Xi Chen. Delamination-Based Measurement and Prediction of the Adhesion Energy of Thin Film/Substrate Interfaces. *Journal of Engineering Materials and Technology*, 139(2):021021, 02 2017. ISSN 0094-4289. doi: 10.1115/1.4035497. URL https://doi.org/10.1115/1.4035497.

[355] Shikai Deng, Enlai Gao, Zhiping Xu, and Vikas Berry. Adhesion energy of mos2 thin films on silicon-based substrates determined via the attributes of a single mos2 wrinkle. *ACS Applied Materials & Interfaces*, 9(8):7812–7818, 2017. doi: 10.1021/acsami.6b16175. URL https://doi.org/10.1021/acsami.6b16175. PMID: 28124892.

[356] Lei Meng, Yang Li, Tian Sheng Liu, Chongyang Zhu, Qun Yang Li, Xianjue Chen, Shuai Zhang, Xu Zhang, Lihong Bao, Yuan Huang, Feng Xu, and Rodney S. Ruoff. Wrinkle networks in exfoliated multilayer graphene and other layered materials. *Carbon*, 156:24–30, 2020. ISSN 0008-6223. doi: https://doi.org/10.1016/j.carbon.2019.09.035. URL `https://www.sciencedirect.com/science/article/pii/S0008622319309406`.

[357] Krishna Sampathkumar, Charalampos Androulidakis, Emmanuel N. Koukaras, Jaroslava Rahova, Karolina Drogowska, Martin Kalbac, Aliaksei Vetushka, Antonin Fejfar, Costas Galiotis, and Otakar Frank. Sculpturing graphene wrinkle patterns into compliant substrates. *Carbon*, 146:772–778, 2019. ISSN 0008-6223. doi: https://doi.org/10.1016/j.carbon.2019.02.041. URL `https://www.sciencedirect.com/science/article/pii/S0008622319301654`.

[358] Siwei Luo, Guolin Hao, Yinping Fan, Liangzhi Kou, Chaoyu He, Xiang Qi, Chao Tang, Jin Li, Kai Huang, and Jianxin Zhong. Formation of ripples in atomically thin mos2 and local strain engineering of electrostatic properties. *Nanotechnology*, 26(10):105705, feb 2015. doi: 10.1088/0957-4484/26/10/105705. URL `https://dx.doi.org/10.1088/0957-4484/26/10/105705`.

[359] Zheling Li, Robert J Young, Dimitrios G Papageorgiou, Ian A Kinloch, Xin Zhao, Cheng Yang, and Sijia Hao. Interfacial stress transfer in strain engineered wrinkled and folded graphene. *2D Materials*, 6(4):045026, jul 2019. doi: 10.1088/2053-1583/ab3167. URL `https://doi.org/10.1088/2053-1583/ab3167`.

[360] David Maeso, Sahar Pakdel, Hernán Santos, Nicolás Agraït, Juan José Palacios, Elsa Prada, and Gabino Rubio-Bollinger. Strong modulation of optical properties in rippled 2d GaSe via strain engineering. *Nanotechnology*, 30(24):24LT01, mar 2019. doi: 10.1088/1361-6528/ab0bc1. URL `https://doi.org/10.1088/1361-6528/ab0bc1`.

[361] Rongliang Yang, Haizhou Song, Zheng Zhou, Shaodian Yang, Xin Tang, Junkai He, Shaoyong Liu, Zhiping Zeng, Bo-Ru Yang, and Xuchun Gui. Ultra-sensitive, multi-directional flexible strain sensors based on an mxene film with periodic wrinkles. *ACS Applied Materials & Interfaces*, 15(6):8345–8354, 2023. doi: 10.1021/acsami.2c22158. URL `https://doi.org/10.1021/acsami.2c22158`. PMID: 36725839.

[362] Shikai Deng, Enlai Gao, Yanlei Wang, Soumyo Sen, Sreeprasad Theruvakkattil Sreenivasan, Sanjay Behura, Petr Král, Zhiping Xu, and Vikas Berry. Confined, oriented, and electrically anisotropic graphene wrinkles on bacteria. *ACS Nano*, 10(9):8403–8412, 2016. doi: 10.1021/acsnano.6b03214. URL `https://doi.org/10.1021/acsnano.6b03214`. PMID: 27391776.

[363] Yong Ju Park, Seoung-Ki Lee, Min-Seok Kim, Hyunmin Kim, and Jong-Hyun Ahn. Graphene-based conformal devices. *ACS Nano*, 8(8):7655–7662, 2014. doi: 10.1021/nn503446f. URL `https://doi.org/10.1021/nn503446f`. PMID: 25073058.

[364] Giwon Lee, Mohammad Zarei, Qingshan Wei, Yong Zhu, and Seung Goo Lee. Surface wrinkling for flexible and stretchable sensors. *Small*, 18(42): 2203491, 2022. doi: https://doi.org/10.1002/smll.202203491. URL `https://onlinelibrary.wiley.com/doi/abs/10.1002/smll.202203491`.

[365] Xinyue Tang, Weidong Yang, Shuran Yin, Guojun Tai, Min Su, Jin Yang, Haofei Shi, Dapeng Wei, and Jun Yang. Controllable graphene wrinkle for a high-performance flexible pressure sensor. *ACS Applied Materials & Interfaces*, 13(17):20448–20458, 2021. doi: 10.1021/acsami.0c22784. URL `https://doi.org/10.1021/acsami.0c22784`. PMID: 33899475.

[366] Jun Yang, Qincui Ran, Dapeng Wei, Tai Sun, Leyong Yu, Xuefen Song, Lichun Pu, Haofei Shi, and Chunlei Du. Three-dimensional conformal graphene microstructure for flexible and highly sensitive electronic skin. *Nanotechnology*, 28(11):115501, feb 2017. doi: 10.1088/1361-6528/aa5b56. URL `https://dx.doi.org/10.1088/1361-6528/aa5b56`.

[367] Bowen Zhu, Zhiqiang Niu, Hong Wang, Wan Ru Leow, Hua Wang, Yuangang Li, Liyan Zheng, Jun Wei, Fengwei Huo, and Xiaodong Chen. Microstructured graphene arrays for highly sensitive flexible tactile sensors. *Small*, 10(18):3625–3631, 2014. doi: https://doi.org/10.1002/smll.201401207. URL `https://onlinelibrary.wiley.com/doi/abs/10.1002/smll.201401207`.

[368] Shuhuan Zhang, Changfeng Ge, and Rui Liu. Mechanical characterization of the stress-strain behavior of the polydimethylsiloxane (pdms) substate of wearable strain sensors under uniaxial loading conditions. *Sensors and Actuators A: Physical*, 341:113580, 2022. ISSN 0924-4247. doi: https://doi.org/10.1016/j.sna.2022.113580. URL `https://www.sciencedirect.com/science/article/pii/S0924424722002187`.

[369] Charalampos Androulidakis, Emmanuel N. Koukaras, Jaroslava Rahova, Krishna Sampathkumar, John Parthenios, Konstantinos Papagelis, Otakar Frank, and Costas Galiotis. Wrinkled few-layer graphene as highly efficient load bearer. *ACS Applied Materials & Interfaces*, 9(31):26593–26601, 2017. doi: 10.1021/acsami.7b07547. URL https://doi.org/10.1021/acsami.7b07547. PMID: 28722403.

[370] Shikai Deng and Vikas Berry. Wrinkled, rippled and crumpled graphene: an overview of formation mechanism, electronic properties, and applications. *Materials Today*, 19(4):197–212, 2016. ISSN 1369-7021. doi: https://doi.org/10.1016/j.mattod.2015.10.002. URL https://www.sciencedirect.com/science/article/pii/S1369702115003119.

[371] Monika Moun, Aastha Vasdev, Rajashekhar Pujar, K. Priya Madhuri, U. Mogera, Neena S. John, G. U. Kulkarni, and Goutam Sheet. Enhanced electrical transport through wrinkles in turbostratic graphene films. *Applied Physics Letters*, 119(3):033102, 2021. doi: 10.1063/5.0056212. URL https://doi.org/10.1063/5.0056212.

[372] Sungwoo Chun, Yeonhoi Choi, and Wanjun Park. All-graphene strain sensor on soft substrate. *Carbon*, 116:753–759, 2017. ISSN 0008-6223. doi: https://doi.org/10.1016/j.carbon.2017.02.058. URL https://www.sciencedirect.com/science/article/pii/S0008622317301872.

[373] Tao Liang, Wanting Hou, Jiuxiang Ji, and Yuehua Huang. Wrinkled reduced graphene oxide humidity sensor with fast response/recovery and flexibility for respiratory monitoring. *Sensors and Actuators A: Physical*, 350:114104, 2023. ISSN 0924-4247. doi: https://doi.org/10.1016/j.sna.2022.114104. URL https://www.sciencedirect.com/science/article/pii/S0924424722007397.

[374] Liu Wang, Shutao Qiao, Shideh Kabiri Ameri, Hyoyoung Jeong, and Nanshu Lu. A Thin Elastic Membrane Conformed to a Soft and Rough Substrate Subjected to Stretching/Compression. *Journal of Applied Mechanics*, 84(11):111003, 09 2017. ISSN 0021-8936. doi: 10.1115/1.4037740. URL https://doi.org/10.1115/1.4037740.

[375] Liu Wang and Nanshu Lu. Conformability of a Thin Elastic Membrane Laminated on a Soft Substrate With Slightly Wavy Surface. *Journal of Applied Mechanics*, 83(4):041007, 01 2016. ISSN 0021-8936. doi: 10.1115/1.4032466. URL https://doi.org/10.1115/1.4032466.

[376] Wei Gao and Rui Huang. Effect of surface roughness on adhesion of graphene membranes. *Journal of Physics D: Applied Physics*, 44(45):452001, oct 2011. doi: 10.1088/0022-3727/44/45/452001. URL `https://dx.doi.org/10.1088/0022-3727/44/45/452001`.

[377] Wenjuan Zhu, Tony Low, Vasili Perebeinos, Ageeth A. Bol, Yu Zhu, Hugen Yan, Jerry Tersoff, and Phaedon Avouris. Structure and electronic transport in graphene wrinkles. *Nano Letters*, 12(7):3431–3436, 2012. doi: 10.1021/nl300563h. URL `https://doi.org/10.1021/nl300563h`. PMID: 22646513.

[378] Zhao Zhang and Teng Li. Determining graphene adhesion via substrate-regulated morphology of graphene. *Journal of Applied Physics*, 110(8):083526, 2011. doi: 10.1063/1.3656720. URL `https://doi.org/10.1063/1.3656720`.

[379] Scott Scharfenberg, D. Z. Rocklin, Cesar Chialvo, Richard L. Weaver, Paul M. Goldbart, and Nadya Mason. Probing the mechanical properties of graphene using a corrugated elastic substrate. *Applied Physics Letters*, 98(9):091908, 2011. doi: 10.1063/1.3553228. URL `https://doi.org/10.1063/1.3553228`.

[380] Scott Scharfenberg, Nikhita Mansukhani, Cesar Chialvo, Richard L. Weaver, and Nadya Mason. Observation of a snap-through instability in graphene. *Applied Physics Letters*, 100(2):021910, 2012. doi: 10.1063/1.3676059. URL `https://doi.org/10.1063/1.3676059`.

[381] Till J. W. Wagner and Dominic Vella. The sensitivity of graphene "snap-through" to substrate geometry. *Applied Physics Letters*, 100(23):233111, 2012. doi: 10.1063/1.4724329. URL `https://doi.org/10.1063/1.4724329`.

[382] Teng Li and Zhao Zhang. Substrate-regulated morphology of graphene. *Journal of Physics D: Applied Physics*, 43(7):075303, feb 2010. doi: 10.1088/0022-3727/43/7/075303. URL `https://dx.doi.org/10.1088/0022-3727/43/7/075303`.

[383] Teng Li and Zhao Zhang. Snap-through instability of graphene on substrates. *Nanoscale Research Letters*, 5(1):169, Oct 2009. ISSN 1556-276X. doi: 10.1007/s11671-009-9460-1. URL `https://doi.org/10.1007/s11671-009-9460-1`.

[384] Michael Gomez, Derek E. Moulton, and Dominic Vella. Critical slowing down in purely elastic 'snap-through' instabilities. *Nature Physics*, 13(2):142–145, Feb 2017. ISSN 1745-2481. doi: 10.1038/nphys3915. URL `https://doi.org/10.1038/nphys3915`.

[385] M. Neek-Amal and F. M. Peeters. Strain-engineered graphene through a nanostructured substrate. i. deformations. *Phys. Rev. B*, 85:195445, May 2012. doi: 10.1103/PhysRevB.85.195445. URL https://link.aps.org/doi/10.1103/PhysRevB.85.195445.

[386] Xin He, Qingshun Bai, Rongqi Shen, Feihu Zhang, and Yongbo Guo. The evolution of configuration and final state of graphene on rough iron surface. *Applied Surface Science*, 530:147084, 2020. ISSN 0169-4332. doi: https://doi.org/10.1016/j.apsusc.2020.147084. URL https://www.sciencedirect.com/science/article/pii/S0169433220318419.

[387] Emmanuel Okogbue, Jung Han Kim, Tae-Jun Ko, Hee-Suk Chung, Adithi Krishnaprasad, Jean Calderon Flores, Shraddha Nehate, Md Golam Kaium, Jong Bae Park, Sei-Jin Lee, Kalpathy B. Sundaram, Lei Zhai, Tania Roy, and Yeonwoong Jung. Centimeter-scale periodically corrugated few-layer 2d mos2 with tensile stretch-driven tunable multifunctionalities. *ACS Applied Materials & Interfaces*, 10(36):30623–30630, 2018. doi: 10.1021/acsami.8b08178. URL https://doi.org/10.1021/acsami.8b08178. PMID: 30059199.

[388] Y. Jin, Q. Ren, J. Liu, Y. Zhang, H. Zheng, and P. Zhao. Stretching graphene to 3.3% strain using formvar-reinforced flexible substrate. *Experimental Mechanics*, 62(5):761–767, Jun 2022. ISSN 1741-2765. doi: 10.1007/s11340-021-00817-3. URL https://doi.org/10.1007/s11340-021-00817-3.

[389] Chaochen Xu, Tao Xue, Jiangang Guo, Qinghua Qin, Sen Wu, Haibin Song, and Haimei Xie. An experimental investigation on the mechanical properties of the interface between large-sized graphene and a flexible substrate. *Journal of Applied Physics*, 117(16):164301, 2015. doi: 10.1063/1.4918899. URL https://doi.org/10.1063/1.4918899.

[390] Seunghun Lee, Eunyeon Byeon, Sunghoon Jung, and Do-Geun Kim. Heterogeneity of hard skin layer in wrinkled pdms surface fabricated by ar ion-beam irradiation. *Scientific Reports*, 8(1):14063, Sep 2018. ISSN 2045-2322. doi: 10.1038/s41598-018-32378-2. URL https://doi.org/10.1038/s41598-018-32378-2.

[391] Hae-Chang Jeong, Hong-Gyu Park, Yoon Ho Jung, Ju Hwan Lee, Byeong-Yun Oh, and Dae-Shik Seo. Tailoring the orientation and periodicity of wrinkles using ion-beam bombardment. *Langmuir*, 32(28):7138–7143, 2016. doi: 10.

1021/acs.langmuir.6b01473. URL https://doi.org/10.1021/acs.langmuir.6b01473. PMID: 27322365.

[392] Hae-Chang Jeong, Hong-Gyu Park, Ju Hwan Lee, and Dae-Shik Seo. Localized ion-beam irradiation-induced wrinkle patterns. *ACS Applied Materials & Interfaces*, 7(41):23216–23222, 2015. doi: 10.1021/acsami.5b07147. URL https://doi.org/10.1021/acsami.5b07147. PMID: 26430969.

[393] Sk. Faruque Ahmed, Geon-Ho Rho, Kwang-Ryeol Lee, Ashkan Vaziri, and Myoung-Woon Moon. High aspect ratio wrinkles on a soft polymer. *Soft Matter*, 6:5709–5714, 2010. doi: 10.1039/C0SM00386G. URL http://dx.doi.org/10.1039/C0SM00386G.

[394] Vivek Pachchigar, Mukesh Ranjan, and Subroto Mukherjee. Role of hierarchical protrusions in water repellent superhydrophobic ptfe surface produced by low energy ion beam irradiation. *Scientific Reports*, 9(1):8675, Jun 2019. ISSN 2045-2322. doi: 10.1038/s41598-019-45132-z. URL https://doi.org/10.1038/s41598-019-45132-z.

[395] Yoon Ho Jung & Dae-Shik Seo Hong-Gyu Park, Hae-Chang Jeong. Control of the wrinkle structure on surface-reformed poly(dimethylsiloxane) via ion-beam bombardment. *Sci Rep*, 5(5):12356, 2015. doi: 10.1038/srep12356. URL https://doi.org/10.1038/srep12356. PMID: 33914542.

[396] Haixia Mei, Rui Huang, Jun Young Chung, Christopher M. Stafford, and Hong-Hui Yu. Buckling modes of elastic thin films on elastic substrates. *Applied Physics Letters*, 90(15):151902, 2007. doi: 10.1063/1.2720759. URL https://doi.org/10.1063/1.2720759.

[397] R. Mark Bradley and James M. E. Harper. Theory of ripple topography induced by ion bombardment. *Journal of Vacuum Science & Technology A*, 6(4):2390–2395, 1988. doi: 10.1116/1.575561. URL https://doi.org/10.1116/1.575561.

[398] Narasimha G Boddeti, Rong Long, and Martin L Dunn. Adhesion mechanics of graphene on textured substrates. *International Journal of Solids and Structures*, 97-98:56–74, 2016. ISSN 0020-7683. doi: https://doi.org/10.1016/j.ijsolstr.2016.07.043. URL https://www.sciencedirect.com/science/article/pii/S0020768316302049.

[399] Diming Ru, Chunhua Zhu, Shuhong Dong, and Junhua Zhao. Wrinkling behavior of graphene on substrates with different surface morphologies. *Mechanics of Materials*, 137:103144, 2019. ISSN 0167-6636. doi: https://doi.org/10.1016/j.mechmat.2019.103144. URL https://www.sciencedirect.com/science/article/pii/S0167663619305551.

[400] Zhongying Wang, Daniel Tonderys, Susan E. Leggett, Evelyn Kendall Williams, Mehrdad T. Kiani, Ruben Spitz Steinberg, Yang Qiu, Ian Y. Wong, and Robert H. Hurt. Wrinkled, wavelength-tunable graphene-based surface topographies for directing cell alignment and morphology. *Carbon*, 97:14–24, 2016. ISSN 0008-6223. doi: https://doi.org/10.1016/j.carbon.2015.03.040. URL https://www.sciencedirect.com/science/article/pii/S0008622315002377. BIOMEDICAL APPLICATIONS OF CARBON NANOMATERIALS.

[401] Edmund Han, Jaehyung Yu, Emil Annevelink, Jangyup Son, Dongyun A. Kang, Kenji Watanabe, Takashi Taniguchi, Elif Ertekin, Pinshane Y. Huang, and Arend M. van der Zande. Ultrasoft slip-mediated bending in few-layer graphene. *Nature Materials*, 19(3):305–309, Mar 2020. ISSN 1476-4660. doi: 10.1038/s41563-019-0529-7. URL https://doi.org/10.1038/s41563-019-0529-7.

[402] S. Viola Kusminskiy, D. K Campbell, A. H. Castro Neto, and F. Guinea. Pinning of a two-dimensional membrane on top of a patterned substrate: The case of graphene. *Phys. Rev. B*, 83:165405, Apr 2011. doi: 10.1103/PhysRevB.83.165405. URL https://link.aps.org/doi/10.1103/PhysRevB.83.165405.

[403] Hongzhi Du, Tao Xue, Chaochen Xu, Yilan Kang, and Wenbo Dou. Improvement of mechanical properties of graphene/substrate interface via regulation of initial strain through cyclic loading. *Optics and Lasers in Engineering*, 110:356–363, 2018. ISSN 0143-8166. doi: https://doi.org/10.1016/j.optlaseng.2018.04.026. URL https://www.sciencedirect.com/science/article/pii/S0143816618300836.

[404] T. M. G. Mohiuddin, A. Lombardo, R. R. Nair, A. Bonetti, G. Savini, R. Jalil, N. Bonini, D. M. Basko, C. Galiotis, N. Marzari, K. S. Novoselov, A. K. Geim, and A. C. Ferrari. Uniaxial strain in graphene by raman spectroscopy: g peak splitting, grüneisen parameters, and sample orientation. *Phys. Rev. B*, 79:205433, May 2009. doi: 10.1103/PhysRevB.79.205433. URL https://link.aps.org/doi/10.1103/PhysRevB.79.205433.

[405] Dongjoon Rhee, Jeffrey T. Paci, Shikai Deng, Won-Kyu Lee, George C. Schatz, and Teri W. Odom. Soft skin layers enable area-specific, multiscale graphene wrinkles with switchable orientations. *ACS Nano*, 14(1):166–174, 2020. doi: 10.1021/acsnano.9b06325. URL https://doi.org/10.1021/acsnano.9b06325. PMID: 31675210.

Mr. Mukesh Pandey

Department of Physics
Indian Institute of Technology (IIT) Ropar
Rupnagar
140001, Punjab
India

Mob. No. +91-8171451526
EMAIL: 2018phz0002@iitrpr.ac.in
mukeshpandey.physics@gmail.com
PUBLICATION: Google Scholar / ORCID
WEB: Mukesh Pandey (LinkedIn)

Personal Data

Date of Birth	1st July, 1995	**Marital Status**	Unmarried

WORK EXPERIENCE

09/2017-present	Chegg, Inc., Expert Q&A (Freelancing) in Advanced Physics
06/2021-12/2021 6 months	Graphene Research Labs (RI Instruments and Innovations) Pvt. Ltd., Bengaluru, India Visiting Laboratory Scientist • Worked on an industrial project, entitled: rGO/PVA composite based conductive ink for printed electronics. (06/2021-08/2021) • Worked on a six-month industrial consultancy project (Polymer-based scalable transfer technique to fabricate graphene-based flexible electronic devices) at IIT Ropar, partially funded by the industry.

EDUCATION

07/2018-12/2023	**Ph. D.** in Physics, Department of Physics Indian Institute of Technology (IIT) Ropar, Rupnagar, Punjab-140001, India Doctoral Thesis: "**Adhesion-driven mechanical instabilities in the blistering and buckling of polymer-supported 2D materials: Graphene and beyond**" Adviser: A/Prof. Rakesh Kumar Co-advisor: Prof. Rajeev Ahuja
08/2015-07/2017	**Master of Science** in Physics Grade: **66.66%** Specialization in: Advanced Solid-State Physics (76.5%) & Plasma Physics (72.5%) Department of Physics and Astrophysics, University of Delhi, India
08/2012-07/2015	**Bachelor of Science (Honors)** in Physics Grade: **88.58%**; Major: Physics Department of Physics, Sri Venkateswara College, South Campus, University of Delhi, India

SCHOLASTIC ACHIEVEMENTS

05/2023	International Travel Grant by SERB, Govt. of India for the participation in Graphene-2023 held at The University of Manchester, United Kingdom
03/2023	Best poster prize by the Director, IIT Ropar in Physics Day 2023
07/2019	Second Position in Summer School in Advanced Lithography for Device Fabrication SSALDF'19, IIT Mandi, India
06/2019,18	Qualified GATE, MoE, India
07/2018	Qualified Jawahar Lal Nehru Entrance Test (JNUEE) For Ph.D. in Physics
06/2012	INSPIRE Scholarship award for higher education, DST, India
06/2012,10	State Meritorious Student Award 2010 & 2012 for best performance in class 10th and 12th, Uttarakhand Board of School Education, Govt. of India.

SCIENTIFIC RESEARCH INTERESTS

Broad Experimental condensed/soft matter physics

Specific: Adhesion mechanics and strain engineering of 2D materials: graphene and beyond

- Adhesion mechanical behavior of 2D materials over diverse solid and soft substrates
- Surface and interface physics and engineering at the nanoscale
- Surface nanopatterning of 2D materials
- Strain engineering of 2D materials, blistering & buckling of 2D materials
- Micro/nano-fabrication of 2D material-based devices
- Micromechanical exfoliation of 2D materials, and their optical, vibrational, and mechanical characterizations
- Electrostatic deposition of 2D materials using 'anodic bonding approach'
- Polymer-assisted 2D material transfer techniques (dry and wet) to transfer 2D materials onto diverse solid and soft substrates (flat or rough)
- 2D material based heterostructure synthesis for straintronics and twistronics
- Liquid-phase exfoliation to produce graphene and its derivatives
- Membranes and Elastic wetting
- 2D material-based Micro/nanoelectromechanical sensors (NEMS/MEMS)
- 2D material blisters as quantum emitters
- Viscous fingering and Elastic solid-based instabilities

Instrumentation Skills

Instruments

- Optical/Interference Reflection Microscopy (Experience of Independent operation for 4+ years)
- AFM (Experience of Supervised operation for 2+ years + Experience of Independent operation for 2 years)
- RAMAN/PHOTOLUMIESCENCE Spectrometer (Experience of Supervised operation for 4+ years)
- FE-SEM (Experience of Independent operation for 6 months)
- Physical vapor deposition (Experience of Independent operation for 2 years)
- FTIR microscopy (Experience of Supervised operation for 3 months)
- XRD (Experience of Supervised operation for 3 months)
- Experience of working in Class 10 and Class 100 Cleanroom environment

'Supervised operation' means handling of the instrument in presence of a staff operator.

Softwares

- Expert in using IGOR-pro, ORIGIN, GWYDDION, WSxM, ImageJ, MS-Office
- Experience of working in LAMMPS, COMSOL Multiphysics, L-edit, AutoCAD

Programming Languages

- Experience of Mathematica, MATLAB, C^{++}, LaTeX, Python

Participation in organizations & other professional activities

Teaching

Master of Science in Physics, Department of Physics, IIT Ropar, India

- ***Experimental Methods (PH422):*** *6 months*
- ***Condensed Matter Physics: Theory Course (PH425):*** *6 months*
- ***Physics Lab-I: Optics Experiments (PH420):*** *12 months*
- ***Physics lab-II: Condensed Matter Experiments (PH510):*** *12 months*

Supervision and Leadership

- **Master's Thesis supervision:** Mr. Cheeranjiv Pandey (2021-2022), Mr. Muhammad Sayed (2023-2024)
- **Summer interns:** Ms. Aditi Sharma, M.Sc. Physics (2021), and Ms. Pukhrambam Manshika Devi, M.Sc. Physics (2023)
- **Leadership among Ph.D. students working in the group:** Mr. Vikas Singh (2021-2026), Mr. Gagandeep Singh (2023-2028)

Attended Conferences/Workshops/Schools and Awards

Conferences and Workshops:

1. Participated in International Workshop on 2D Materials (IW2DM'19) held at IISER TVM, India during July 22 – 23, 2019
2. Participated in a Short-Term Course on 2D materials: Physics and Applications held at IIT Madras, India during Sept. 21 – 26, 2019
3. Participated in a Familiarization Workshop on Nanofabrication at INUP, IISc Bengaluru, India during Oct. 14 – 16, 2019
4. Participated in a Short-Term Course on Advanced Functional Materials held at NIT Jalandhar, India during 30 Dec 2019 – 3 Jan 2020
5. Presented a poster at the International Virtual Conference on Advanced Nanomaterials Applications (VCAN 2020), CNR, VIT Vellore, India during June 17 – 20, 2020
6. Presented a poster in online mode at School on Advanced Light-Emitting and Optical Materials (SLALOM) held on June 29 – 30, 2020 at ITMO University, Russia
7. Presented a poster at International Union of Materials Research Societies – International Conference in Asia (IUMRS-ICA'22) held on Dec 19 – 23, 2022 at IIT Jodhpur, India
8. Participated in Advanced Hands-on Training on MEMS Devices held on March 17 – 23, 2023 at IIT Delhi, India
9. Participated and presented Research Poster in the International conference: GRAPHENE-2023 held on June 27 – 30, 2023 at The University of Manchester, UK
10. Participated and presented Research Poster in the International conference: Recent Progress in Graphene and 2D materials Research (RPGR)-2023 held on November 20 – 23, 2023 in India organized by IISc Bengaluru.

List of Publications (Peer-reviewed)

1. **Mukesh Pandey**, Cheeranjiv Pandey, Rajeev Ahuja*, Rakesh Kumar*, Straining techniques for strain engineering of 2D materials towards flexible straintronic applications, https://doi.org/10.1016/j.nanoen.2023.108278, **Nano Energy 109, 108278 (2023).**
2. **Mukesh Pandey**, Rakesh Kumar*, Polymer curing assisted formation of optically visible sub-micron blisters of multilayer graphene for local strain engineering,

https://doi.org/10.1088/1361-648X/ac61b4, **J. Phys.: Condens. Matter 34, 245401 (2022)**.

3. **Mukesh Pandey**, Rajeev Ahuja, Rakesh Kumar*, Hoop compression driven instabilities in spontaneously formed multilayer graphene blisters over a polymeric substrate, https://doi.org/10.1088/1361-6528/acaf33, **Nanotechnology 34, 175301 (2023)**.
4. **Mukesh Pandey**, B. K. Parida, M. Ranjan, Rajeev Ahuja, Rakesh Kumar*, Pinning of graphene for conformal wrinkling over a soft corrugated substrate through prestretch-release process, https://doi.org/10.1016/j.apsadv.2023.100433, **Applied Surface Science Advances, 16, 100433 (2023)**.
5. **Mukesh Pandey,** Rajeev Ahuja*, Rakesh Kumar*, Viscous fingering instabilities in spontaneously formed blisters of MoS_2 multilayers, https://doi.org/10.1039/D3NA00563A, **Nanoscale Adv., 5, 6617-6625 (2023).**

Publication Backlogs & ongoing works

1. **Mukesh Pandey***, Rajeev Ahuja*, Rakesh Kumar*, Electron beam irradiation-induced dense and giant atomically thin domes of two-dimensional crystals, **(submitted manuscript, under revision).**
2. **Mukesh Pandey**, Guorui Wang, Zhaohe Dai, Rajeev Ahuja, Rakesh Kumar, Instabilities in blistering of two-dimensional materials: A review, **(manuscript to be submitted)**
3. **Mukesh Pandey**, Gagandeep Singh, Sayed M. Mukhtadeer, Lakhan Bainsla, Saroj P. Dash, Rajeev Ahuja, Rakesh Kumar, Swollen polymer-induced gigantic bulging of two-dimensional materials, **(manuscript under preparation).**

References

- Dr. Rakesh Kumar

  Associate Professor, Department of Physics, IIT Ropar, India

  rakesh@iitrpr.ac.in
- Prof. Rajeev Ahuja

  Professor, Department of Physics and Astronomy, Uppsala University, Sweden

  rajeev.ahuja@iitrpr.ac.in

  Professor, Department of Physics, IIT Ropar, India

  rajeev.ahuja@physics.uu.se